



GRAN SASSO SCIENCE INSTITUTE

Nucleosynthesis of light and heavy elements across the Galaxy

CANDIDATE:
Diego Vescovi

THESIS ADVISOR:
Dr. Sergio Cristallo

THESIS ADVISOR:
Prof. Dr. Marica Branchesi

PHD IN ASTROPARTICLE PHYSICS

XXXIII cycle

Abstract

The synthesis of elements mostly takes place in stars. Elements up to iron peak are a by-product of thermonuclear fusion reactions sustaining the stellar structure itself. This is the case of the Sun, whose energy generation is provided by the pp chain and (to a lesser extent) by the CNO cycle. However, a precise evaluation of their relative contributions is still lacking. On the other hand, elements heavier than iron are almost entirely produced via the *slow* (*s*) and *rapid* (*r*) neutron capture processes. Low-mass stars during their Asymptotic Giant Branch (AGB) phase are the site of the so-called main component of the *s*-process. In those objects a ^{13}C *n*-source (the ^{13}C pocket), formed due to partial mixing of hydrogen from the convective envelope, operates. The physical mechanism responsible for such mixing is still a matter of debate. Binary neutron star mergers are instead primary sites for the production of heavy elements through the *r*-process. This was recently confirmed by the detection of the kilonova AT2017gfo as the electromagnetic counterpart of the gravitational wave signal GW170817. Interestingly, the production of *r*-process elements can be accompanied by the synthesis of light elements, which could be detected during the early kilonova emission.

With a *multi-messenger* approach, we investigate the nucleosynthesis occurring in these astrophysical scenarios by comparing results not only to stellar spectra, but also other observables: i.e. emission of neutrinos, isotopic measurements in primitive meteorites, and electromagnetic radiation emissions.

Regarding the Sun, we use solar models to study the impact of a different ^7Be electron-capture rate on the solar structure. We compare the results with the measured ^7Be and ^8B solar neutrino fluxes and find that the agreement with the Sudbury Neutrino Observatory measurements of the neutral current component of the ^8B neutrino flux is improved.

We then revise and generalize the relation connecting the measured solar photon luminosity and the total solar neutrino fluxes, namely the *luminosity constraint*. In particular, we study and determine the energy contributions due to non-equilibrium burning of ^3He and ^{14}N and due to solar expansion/contraction. We finally show the importance of such a relation for the search of CNO neutrinos by providing a specific relation that links CNO and pp neutrino fluxes.

For what concerns the nucleosynthesis in AGB stars, we examine the origins of now-extinct radioactivities that were alive in the solar nebula, as testified

by meteoritic measurements, in the light of most updated stellar models for intermediate-mass stars and massive stars. We find that, while the Galactic inheritance broadly explains most of the isotopes involved with lifetime $\tau \gtrsim 5$ Myr, shorter-lived isotopes require nucleosynthesis events close in time to the solar formation. We investigate the possibility that an Asymptotic Giant Branch or a Massive star could have contaminated the solar nebula. We find that both scenarios meet serious problems to reproduce the presence of isotopic anomalies measured in early solar system solids of the solar system.

In another work, we perform the first numerical simulations of the formation of a magnetically-induced ^{13}C pocket in a stellar evolutionary code with fully coupled nucleosynthesis. We find that magnetic fields of the order 10^5 G can induce the formation and the buoyant rise of magnetic flux tubes in the He-intershell of AGB stars. The ensuing mixing can account for the downward penetration of poorly magnetized H-rich material, necessary for the formation of the ^{13}C pocket. By adopting a single magnetic field configuration, new magnetic models provide a consistent explanation to the majority of the heavy-element isotope data detected in presolar SiC grains from AGB stars.

Finally, we study the production of light elements in the ejecta of binary neutron star mergers. The outcome of numerical relativity merger simulations is combined with detailed r -process nucleosynthesis calculations performed with the Skynet nuclear reaction network. We find that hydrogen and helium are the most abundant light elements. However, despite their high abundance, the possibility of detecting hydrogen and helium features in kilonova spectra is very unlikely.

Acknowledgments

The research presented in this thesis is the result of close collaborations with many people I met and worked with during these three years. I am undoubtedly grateful to my advisors, Sergio and Marica, for their guidance through this work, which would not have been possible without their precious knowledge and expertise. A special thank goes to Francesco for his continuous support and scientific guidance during my research activity at GSSI. I thank Luciano, Carlo, and Oscar for the many fruitful discussions and scientific collaborations. A heartfelt thank is addressed to Maurizio and Sara, for a fruitful and long-lasting collaboration and for having encouraged me to pursue a scientific career. Many thanks also go to Albino for the insightful discussions, his time and interest, and for hosting me at Trento University. Finally, all my gratitude is devoted to my family and friends, for the great motivation and support they provided to me, and to Giovanna, for her extraordinary patience and love.

List of publications

Part of this PhD thesis has been already published on referenced journals and conference proceedings and/or presented in conferences and workshops.

Articles

- Vescovi, D., Busso, M., Palmerini, S., Trippella, O., Cristallo, S., Piersanti, L., Chieffi, A., Limongi, M., Hoppe, P., and Kratz, K. L. (2018). On the Origin of Early Solar System Radioactivities: Problems with the Asymptotic Giant Branch and Massive Star Scenarios. *ApJ*, 863(2):115. doi: [10.3847/1538-4357/aad191](https://doi.org/10.3847/1538-4357/aad191)
- Vescovi, D., Piersanti, L., Cristallo, S., Busso, M., Vissani, F., Palmerini, S., Simonucci, S., and Taioli, S. (2019). Effects of a revised ${}^7\text{Be}$ e^- -capture rate on solar neutrino fluxes. *A&A*, 623:A126. doi: [10.1051/0004-6361/201834993](https://doi.org/10.1051/0004-6361/201834993)
- Colonna, N., Tsinganis, A., Vlastou, R., Patronis, N., Diakaki, M., Amaducci, S., Barbagallo, M., Bennett, S., Berthoumieux, E., Bacak, M., Cosentino, G., Cristallo, S., Finocchiaro, P., Heyse, J., Lewis, D., Manna, A., Massimi, C., Mendoza, E., Mirea, M., Moens, A., Nolte, R., Pirovano, E., Sabaté-Gilarte, M., Sibbens, G., Smith, A. G., Sosnin, N., Stamatopoulos, A., Tarrío, D., Tassan-Got, L., Vanleeuw, D., Ventura, A., Vescovi, D., Wright, T., Žugec, P., and n_TOF Collaboration (2020). The fission experimental programme at the CERN n_TOF facility: status and perspectives. *European Physical Journal A*, 56(2):48. doi: [10.1140/epja/s10050-020-00037-8](https://doi.org/10.1140/epja/s10050-020-00037-8)
- Mazzone, A., Cristallo, S., Aberle, O., and other 128 authors including Vescovi, D. (2020). Measurement of the ${}^{154}\text{Gd}(n,\gamma)$ cross section and its astrophysical implications. *Physics Letters B*, 804:135405. doi: [10.1016/j.physletb.2020.135405](https://doi.org/10.1016/j.physletb.2020.135405)
- Vescovi, D., Cristallo, S., Busso, M., and Liu, N. (2020). Magnetic-buoyancy-induced mixing in AGB stars: Presolar SiC grains. *ApJL*, 897(2):L25. doi: [10.3847/2041-8213/ab9fa1](https://doi.org/10.3847/2041-8213/ab9fa1)
- Perego, A., Vescovi, D., Fiore, A., Benetti, S., Bernuzzi, S., Branchesi, M., Cristallo, S., Cappellaro, E., and Radice, D. (2020). Production of very light elements in kilonovae. *arXiv e-prints*, page arXiv:2009.08988. <https://arxiv.org/abs/2009.08988>

Vescovi, D., Mascaretti, C., Vissani, F., Piersanti, L., and Straniero, O. (2021). The luminosity constraint in the era of precision solar physics. *Journal of Physics G Nuclear Physics*, 48(1):015201. doi: [10.1088/1361-6471/abb784](https://doi.org/10.1088/1361-6471/abb784)

Conferences

Magnetic fields in AGB stars. XXX National Seminar of Nuclear and Subnuclear Physics “Francesco Romano”, June 5-12 2018, Serra degli Alimini, Italy

The Effects of a Late Single-Star Contamination of the Solar Nebula on the Early Solar System Radioactivities. 15th International Symposium on Nuclei in the Cosmos, June 24-29 2018, Laboratori Nazionali del Gran Sasso, Assergi, Italy. Appeared in *Nuclei in the Cosmos XV*, volume 219, pages 461–464. doi: [10.1007/978-3-030-13876-9_90](https://doi.org/10.1007/978-3-030-13876-9_90).

The major neutron source in AGB stars. Low metallicity *s*-process, November 30 2018, Heidelberg, Germany

Modeling the formation of the ^{13}C neutron source in AGB stars. Nuclear Physics in Astrophysics IX, September 15-20 2019, Castle Waldthausen, Frankfurt, Germany. Appeared in *Journal of Physics: Conference Series*, 1668:012047. doi: [10.1088/1742-6596/1668/1/012047](https://doi.org/10.1088/1742-6596/1668/1/012047)

Nucleosynthesis across the Galaxy: AGB Stars and Neutron Stars Mergers. GIANTS X, October 23-25 2019, Genova, Italy

Mescolamento magnetico in stelle AGB e grani presolari. 106° Congresso Nazionale della Società Italiana di Fisica, September 14-18 2020, Milano, Italy

Other work (not part of this thesis)

Palmerini, S., Trippella, O., Busso, M., Vescovi, D., Petrelli, M., Zucchini, A., and Frondini, F. (2018). *s*-Processing from MHD-induced mixing and isotopic abundances in presolar SiC grains. *GeoCoA*, 221:21–36. doi: [10.1016/j.gca.2017.05.030](https://doi.org/10.1016/j.gca.2017.05.030)

Cristallo, S., La Cognata, M., Massimi, C., Best, A., Palmerini, S., Straniero, O., Trippella, O., Busso, M., Ciani, G. F., Mingrone, F., Piersanti, L., and Vescovi, D. (2018). The Importance of the $^{13}\text{C}(\alpha, n)^{16}\text{O}$ Reaction in Asymptotic Giant Branch Stars. *ApJ*, 859(2):105. doi: [10.3847/1538-4357/aac177](https://doi.org/10.3847/1538-4357/aac177)

D’Agata, G., Pizzone, R. G., La Cognata, M., Indelicato, I., Spitaleri, C., Palmerini, S., Trippella, O., Vescovi, D., et al. (2018). The $^{19}\text{F}(\alpha, p)^{22}\text{Ne}$ Reaction at Energies of Astrophysical Relevance by Means of the Trojan Horse Method and Its Implications in AGB Stars. *ApJ*, 860:61. doi: [10.3847/1538-4357/aac207](https://doi.org/10.3847/1538-4357/aac207)

Cristallo, S., Nanni, A., Cescutti, G., Minchev, I., Liu, N., Vescovi, D., Gobrecht, D., and Piersanti, L. (2020). Mass and metallicity distribution of parent AGB stars of presolar SiC. *A&A*, 644:A8. doi: [10.1051/0004-6361/202039492](https://doi.org/10.1051/0004-6361/202039492)

Busso, M., Vescovi, D., Palmerini, S., Cristallo, S., and Antonuccio Delogu, V. (2020). s-Processing in AGB Stars Revisited. III. Neutron captures from MHD mixing at different metallicities and observational constraints. *arXiv e-prints*, page arXiv:2011.07469. <https://arxiv.org/abs/2011.07469>

Contents

Contents	xi
1 Introduction	1
1.1 Stellar evolution	1
1.1.1 Pre-main sequence	1
1.1.2 Main sequence	2
1.1.3 Red giant branch phase and core He-burning	3
1.1.4 Asymptotic giant branch phase	4
1.2 Nucleosynthesis	7
1.2.1 Nucleosynthesis in main sequence stars	7
1.2.2 Solar models and solar neutrinos	10
1.2.3 Nucleosynthesis up to the iron peak	12
1.2.4 Nucleosynthesis of the heavy elements	13
1.2.5 The <i>s</i> -process	14
1.2.6 Mixing processes in AGB stars	19
1.2.7 The <i>r</i> -process	21
1.2.8 Neutron star mergers and kilonovae	25
2 Updating stellar models	29
2.1 Equation of state, solar mixture, opacity tables, and mass loss	29
2.2 Nuclear network	32
2.3 The ^{13}C pocket formation	33
3 <i>s</i>- and <i>r</i>-process data at the n_TOF facility	39
3.1 <i>s</i> -process capture measurements	39
3.1.1 <i>s</i> -only isotopes: the case of ^{154}Gd	40
3.2 <i>r</i> -process fission measurements	42
4 Effects of a revised ^7Be e^--capture rate on solar neutrino fluxes	47
4.1 Introduction	47
4.2 Standard solar model	50
4.3 Electron-capture on ^7Be	51
4.4 Solar neutrino fluxes	54
4.5 Impact of a revised $^7\text{Be} + e^-$ on the ^8B neutrino flux	56

4.6	Conclusions	59
5	The luminosity constraint in the era of precision solar physics	61
5.1	Introduction	61
5.2	Experimental status of solar neutrinos	63
5.3	The standard luminosity constraint	65
5.3.1	A critical examination of the standard luminosity constraint	66
5.3.2	A derivation of the standard luminosity constraint	67
5.4	A new version of the luminosity constraint	69
5.4.1	The departure from the local nuclear equilibrium	70
5.4.2	Non-stationary luminosity constraint	73
5.4.3	Summary	74
5.5	Luminosity constraint and the search for CNO neutrinos	75
5.6	Conclusive remarks	78
6	On the origin of the early solar system radioactivities.	
	Problems with the AGB and massive star scenarios	83
6.1	Short-lived radioactivities in the ESS	83
6.2	Constraints from isotopic anomalies in meteorites	88
6.3	Contributions from galactic evolution	90
6.4	Constraints and models for <i>r</i> -process nucleosynthesis	92
6.4.1	Observed constraints and <i>r</i> -process sources	92
6.4.2	Reconciling the ESS abundances of ¹²⁹ I and ¹⁸² Hf	96
6.5	The reference models for intermediate mass stars	100
6.5.1	Effects of a late AGB star. I. Models with MHD-induced mixing	103
6.5.2	Effects of a late AGB star. II. Models with opacity-induced mixing	107
6.6	Nucleosynthesis in massive stars and the role of late supernovae .	111
6.7	Conclusions	119
7	Magnetic-buoyancy-induced mixing in AGB Stars: presolar SiC grains	123
7.1	Introduction	123
7.2	Updated FRUITY models	124
7.2.1	Convective overshooting	125
7.3	Mixing triggered by magnetic buoyancy in AGB stars	128
7.4	Presolar SiC grains	132
7.5	Conclusions	133
8	Production of very light elements in kilonovae	135
8.1	Introduction	135
8.2	Methods	136
8.3	Synthesis of hydrogen and helium in BNS mergers	137
8.4	Discussion and conclusions	142

8.A	<i>r</i> -process nucleosynthesis calculations	143
8.B	Numerical relativity simulations of binary neutron star mergers .	143
8.C	Conditions of the dynamical and spiral-wave wind ejecta from BNS merger simulations	144
8.D	Helium and heavy elements production in low and high entropy ejecta	145
9	Summary and conclusions	151
	Bibliography	155

Introduction

In this thesis, we investigate the nucleosynthesis of light elements occurring in the Sun and the production of heavy elements in asymptotic giant branch stars. This is done with the FUNS stellar evolutionary code. In addition, we study r -process nucleosynthesis in neutron star mergers with the SkyNet nuclear reaction network. In this introduction, we briefly summarize the characteristics of stars in the main evolutionary phases of their life and the nuclear and mixing processes at work in their interiors. These aspects are covered to provide the reader with a complete picture concerning the current understanding of the physical and nuclear processes responsible for the formation of light and heavy elements in Stars. In Chapter 2 we present the updates made to the FUNS code. In Chapter 3 we discuss some neutron capture measurements of interest for nuclear astrophysics carried out at the n_TOF facility at CERN. We use FUNS in Chapters 4 and 5 to study the correlation between solar neutrinos and solar models. In Chapters 6 and 7 we discuss s -process nucleosynthesis in AGB stars, and in Chapter 8, we consider the r -process in the mass outflow following a neutron star merger using the SkyNet code. The main results of the thesis are summarized and discussed in Chapter 9. Few appendices are included at the end of Chapter 8 in order to provide more exhaustive information about the physical results discussed therein.

1.1 Stellar evolution

1.1.1 Pre-main sequence

A star is a self-gravitating structure in hydrostatic and thermal equilibrium that originates from a gas cloud, essentially composed of hydrogen, helium, and a small amount of heavier elements, which are generally called metals. During the first phase of formation, the evolution is controlled by the quasi-free collapse of the cloud. This occurs in an isothermal way, being the cloud very rarefied. As the density in the regions where the matter is concentrated reaches sufficiently large values, the gas starts to heat up; at the same time the opacity of the cloud

increases. Then the cloud becomes optically thick and part of the radiation is trapped; the evolution shifts from dynamic time scales to thermal time scales. The star evolves through states of quasi-equilibrium governed by the virial theorem, which establishes that the energy associated with the gravitational contraction of the cloud increases the thermal energy of matter; the time it takes to lose energy by thermal emission is the time scale on which contractions occur.

In these early stages, the structure is cold enough for opacity to be high. Since the photon flow is unable to carry enough energy outside, an additional energy transport mechanism is activated, the *convection* (see Section 1.2.6), affecting the entire stellar structure. During this phase, which lasts for $10^5 \div 10^6$ years, the star appears to be completely convective, and therefore chemically homogeneous. Fusion processes are triggered by nuclear energy involving the most fragile elements (lithium, beryllium, and boron) and, in particular, by deuterium, which generates enough energy to partially slow down the contraction of the star. Convection causes deuterium to be completely destroyed throughout the entire structure. As the contraction goes on, however, the innermost regions heat up, the opacity of matter decreases, and a radiative core is formed. However, there are no nuclear reactions sufficiently efficient to produce a significant chemical change in the core. Therefore, apart from the abundance of light elements, the structure can be still considered homogeneous from a chemical point of view. As the star does not yet have sufficiently efficient energy processes, the contraction continues on thermal timescales, until the core temperature reaches typical hydrogen burning (H-burning) temperatures. From this point on, the evolution proceeds differently depending on the mass of the star.

1.1.2 Main sequence

Stars with a mass lower than about $0.08 M_{\odot}$ are too cold to reach the minimum ignition temperature of the hydrogen fusion ($\sim 6 \times 10^6$ K). Since these are very dense structures, the contraction favors the formation of a core in which the pressure of the degenerate electrons counterbalances gravity. These stars will never undergo hydrogen fusion and will slowly cool down. Instead, stars with higher mass succeed in triggering hydrogen fusion. Two possible reaction chains lead to the transformation of hydrogen into helium: the *pp* chain and the CNO cycle. Since the efficiencies of the two cycles depend on the temperature in different ways ($\propto T^4$ for the *pp* chain, and $\propto T^{18}$ for the CNO cycle), H-burning mainly occurs through the *pp* chain in stars with a mass lower than $\sim 1.2 - 1.3 M_{\odot}$ (the exact value depending on the initial chemical composition). The CNO cycle is instead dominant in higher mass stars ¹.

It is common to refer to stars belonging to the *Upper Main Sequence* (UMS) as those which fuse hydrogen into helium primarily through the CNO cycle, and to *Lower Main Sequence* (LMS) stars as those in which the main H-burning mechanism is the *pp* chain. When the hydrogen fusion reaction is triggered,

¹In those objects, the *pp* chain is still active, but the efficiency is lower compared to CNO cycle.

however, the star does not yet have reached the equilibrium of the secondary fusion reaction elements (especially ${}^3\text{He}$ and ${}^{12}\text{C}$); when this occurs the star reaches the *Zero Age Main Sequence* (ZAMS) phase. Starting from this moment the star enters the Main Sequence (MS), the longest evolutionary phase of stars, during which central hydrogen is transformed into helium. Since then, the evolution shifts from thermal timescales to the typical nuclear timescales of central hydrogen burning. In this phase, more massive stars are also hotter and brighter and thus have shorter evolutionary timescales.

The different kinds of central hydrogen-burning cause variations in the characteristics of the stars. In the case of LMS stars, the reactions do not have a strong temperature dependency, so the active burning in the core does not generate too high energy flows, and therefore the core is radiative. Instead, the outer envelope is relatively cold, opaque, and thus convective.

In the UMS, on the other hand, the stars are rather warm when leaving the Pre-main Sequence, so they have a radiative envelope, while in the core, given the strong dependence of the fusion reactions from the temperature, the energy flow is very large. This triggers convection in the inner regions, even though the material is not particularly opaque. Because of convection, even if the burning takes place in a very narrow area, hydrogen is exhausted in a much wider region. This has significant consequences for the subsequent evolution.

An LMS star depletes hydrogen in a small region of the core and, in order to counterbalance the decrease in efficiency caused by the lower amount of hydrogen central, slightly contracts to increase the temperature; this process continues until there is no more hydrogen in the core, and a helium-rich central region is formed, slowly growing. As the star begins to raise the central temperature, it continues to burn hydrogen in the surrounding shell above the core, which has sufficient hydrogen abundance to trigger fusion processes.

In the case of a UMS star, instead, due to the onset of convection in the core, once the central hydrogen has run out, it has a larger helium core, and a small contraction is not enough to trigger the fusion in the shell. As a result, all UMS stars undergo what is known as *overall contraction*, i.e. a contraction of the internal areas of the star, occurring on timescales shorter than nuclear ones. The contraction leads to a further increase in temperature until the hydrogen shell is turned on.

1.1.3 Red giant branch phase and core He-burning

The ignition of the hydrogen shell², for both LMS and UMS stars, causes an expansion of the external regions, which then cool. As a consequence, in the Hertzsprung-Russell (H-R) diagram the star moves towards lower effective temperatures and larger luminosities (Red Giant Branch, RGB). Since it is relatively cold, the convective envelope manages to penetrate into the deeper layers where

²In this case, the burning of hydrogen into helium in the shell always takes place via the CNO cycle.

the material has undergone H-burning. The ensuing mixing causes an enrichment of the envelope with the H-burning products. As a result of this phenomenon, called first dredge-up (FDU), the surface He abundance increases, while the H abundance and $^{12}\text{C}/^{13}\text{C}$ and C/N ratios decrease. The H-shell then continues to accumulate helium on the core, growing in mass. Depending on the mass, stars follow different evolutionary paths.

Stars with a mass lower than about $2.5 M_{\odot}$ develop a partially degenerate helium core as they evolve through the RGB phase. As a consequence, the central helium ignition phase is delayed until critical mass about $0.5 M_{\odot}$ for the helium core is reached. These stars experience the so-called *helium flash*, during which a large amount of energy is produced. When the central helium-burning (He-burning) is triggered in a non-degenerate environment, normal equilibrium conditions are restored. A significant point in the evolution of stars with $M < 2.5 M_{\odot}$ is the mass loss: in the RGB phase, given the low surface gravity due to the expansion of the outer envelope and the energy generated in the shell, which gives rise to strong radiation pressure, the star is subject to mass loss (through stellar winds) which can also be very pronounced. Stars with a mass less than about $0.5 M_{\odot}$, being unable to trigger He-burning, end their life as white helium dwarfs, cooling continuously. The evolution of these stars occurs on timescales much longer than the age of the universe. Stars with masses in the range $1.8 - 2.5 M_{\odot}$ burn helium more quickly, and therefore develop a lower degree of degeneration in the RGB phase. This also involves a faster evolution and a lower mass loss.

Finally, stars with mass $M > 2.5 M_{\odot}$ do not develop a degenerate core at the end of H-burning and can trigger the central helium in a quiescent way.

When the star triggers the fusion of central helium (through the 3α reaction, $3\alpha \rightarrow ^{12}\text{C} + \gamma$ and, toward the end of the He-burning, the $^{12}\text{C} + \alpha \rightarrow ^{16}\text{O} + \gamma$ reaction), the H-burning shell around the core remains active so that the star evolves with two energy sources: the He-burning in the core and the H-burning in the shell. Given the great temperature dependence of the efficiency of He-burning ($\epsilon \propto T^{40}$ for $T \sim 10^8$ K), the helium core is convective, similarly to the case of the hydrogen core in the UMS stars.

1.1.4 Asymptotic giant branch phase

Once the central helium is exhausted, the star contracts until it reaches the temperatures required to trigger the 3α in the shell around the core.

Massive stars ($M \gtrsim 10 M_{\odot}$) manage to trigger the fusion of carbon in a non-degenerate environment and the subsequent fusion chains, up to the production of ^{56}Fe , in an exoenergetic way. These stars then explode as supernovae enriching the interstellar medium (ISM) with nuclear-processed matter.

On the other hand, low- and intermediate-mass stars, with a mass lower than about $8 M_{\odot}$, do not manage to trigger the central carbon burning. In this case, once the He in the central areas has exhausted and electron degeneracy has been achieved in the C-O core, the star loses energy and cools thanks to an

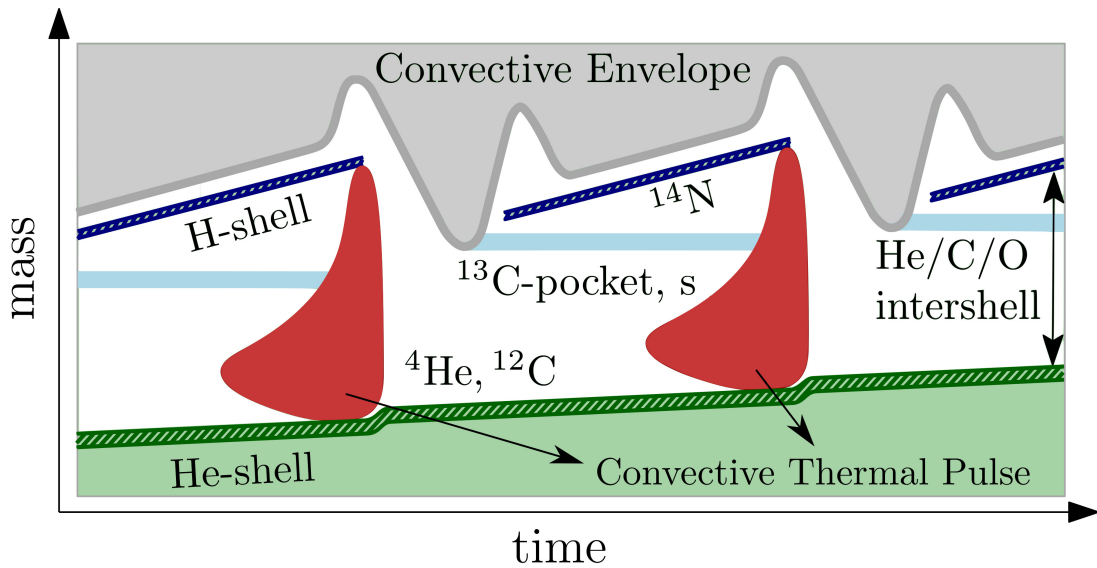


Figure 1.1: Schematic sketch of the mixing episodes during thermal pulses.

efficient neutrino flow emission. As a consequence, the region below the H-burning shell contracts until the activation of He-burning in a shell above the core. The energy released by the burning of He determines an expansion and cooling of the overlying layers. In stars with mass $M \gtrsim 4 M_{\odot}$ the hydrogen shell, which was previously active, is turned off and a second dredge-up (SDU) episode occurs, allowing the convective envelope to deeply penetrate the He-rich layers. Instead, stars of lower masses maintain a thin active H-burning shell. This phase, called Early Asymptotic Giant Branch (E-AGB) corresponds to the initial part of the asymptotic giant branch in the H-R diagram. The cooling of the envelope then induces its contraction and the consequent re-ignition of the H-burning shell. At the end of this phase, the star consists of a degenerate nucleus of C-O that grows in mass, by two shells of helium and hydrogen, separated from a He-rich intermediate zone in radiative equilibrium (He-intershell), and by an extended convective envelope. The helium produced by the H-burning shell accumulates, causing an increase of density and temperature in the innermost zones. As a consequence, on a timescale of tens of thousand years, the He-burning switches on in semi-explosive conditions. The increase in energy induces convective motions in the entire He-intershell region, homogenizing it with the freshly synthesized products of He-burning. The energy released in this *thermal pulse* causes an expansion, and thus a cooling of the hydrogen shell. As a consequence, the latter switches off, while He starts burning radiatively. Later, the structure contracts again, heating up and leading to the re-ignition of the H-shell. This alternate series of burnings repeats until the complete erosion of the envelope by stellar winds and characterize the thermally pulsing AGB (TP-AGB) phase of the star (see Figure 1.1). During the expansion of the envelope, convection penetrates deep into the H-He discontinuity beyond the region where the hydrogen shell was active.

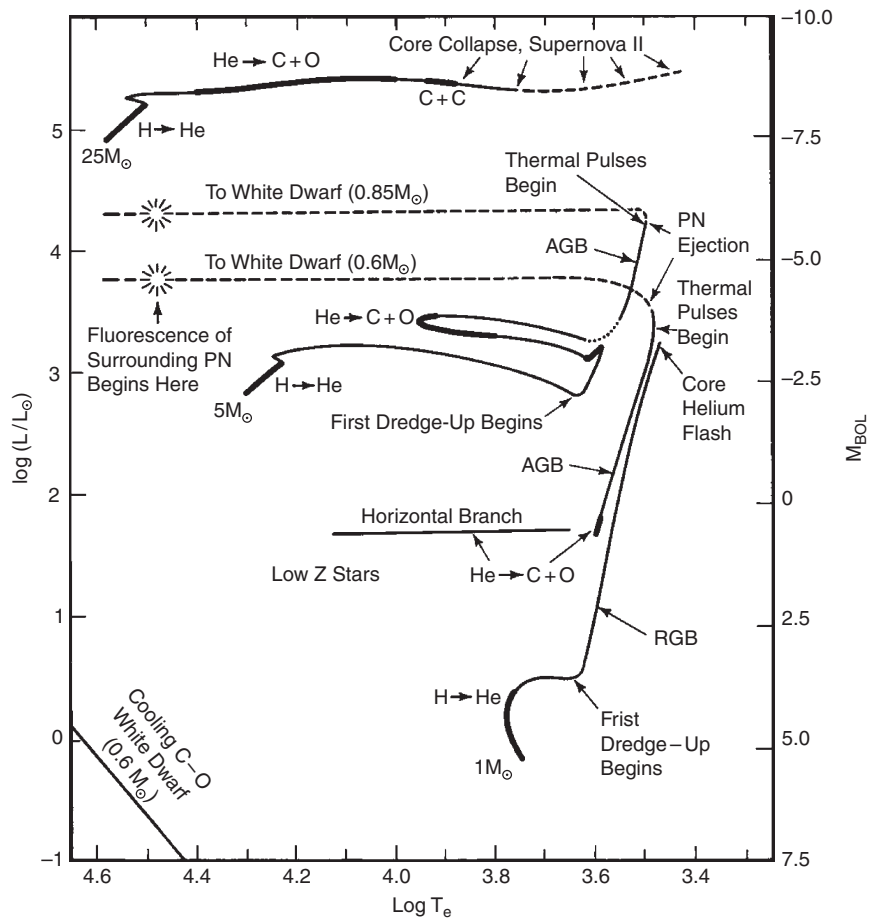


Figure 1.2: Evolutionary tracks of theoretical model stars in the H-R diagram. Figure from Iben (1985); see that reference for details. © 1985 Royal Astronomical Society

Consequently, the by-products of the fusion reactions are carried to the surface by convective motions, thereby modifying the surface abundances of the star. This phenomenon is known as third dredge-up (TDU). At each TDU, protons penetrate into the He-intershell, thanks to mixing phenomena at the base of the envelope. Later, following the re-ignition of the H-shell, a ^{13}C -enriched layer forms: the so-called ^{13}C pocket (Figure 1.1). The latter is essential to the production of free neutrons necessary for the synthesis of heavy elements through the so-called *s*(low)-process (see Section 1.2.5). When, under the action of strong stellar winds the star has lost almost all its H-rich envelope, thus revealing the underlying hot helium shell, it will pass to the post-AGB phase, moving horizontally along the H-R diagram towards the blue region. In the end, the progressive extinguishing of thermonuclear reactions, and neutrino and thermal losses, will lead the star to cool as a carbon-oxygen white dwarf.

Stars with a mass between about $8 - 10 M_{\odot}$ trigger the central carbon-burning in a degenerate environment, developing nuclei of oxygen and neon, and possibly exploding as electron capture supernovae (see, e.g., Nomoto 1984).

A diagram of the key evolutionary phases discussed so far for stars with different mass is reported in Figure 1.2.

1.2 Nucleosynthesis

The formation and evolution of stellar objects is a process characterizing the history of the entire universe. Stars, with different times and modes, represent “forges” for the synthesis of almost all known chemical elements, converting hydrogen into helium and helium into heavier elements. The synthesized elements are recycled into the interstellar medium, leading to the gradual enrichment of heavy elements in subsequent generations of stars. Many stellar generations have created the abundances pattern observed in the present interstellar medium and celestial bodies (including the Earth). These abundances trends are provided by the spectroscopic analysis of the stellar atmospheres, which must preserve - with a few exceptions - the chemical composition of the material from which those stars were born. Similar observations can be obtained directly for the interstellar medium, the local terrestrial sample, meteorites, and various bodies of the solar system.

By taking these data into account, matter in the Universe seems to have preserved over time a typical distribution of the various nuclear species which does not differ significantly from that obtained for the Sun (reported in Figure 1.3). Keeping in mind the sequence of nuclear reactions in the stellar structure, it is not difficult to recognize the fingerprint of stellar nucleosynthesis in this distribution. For instance, the low abundance of light elements like Li, Be, and B is a consequence of thermonuclear reactions (mainly destruction) and cosmic ray spallation processes (production).

The distribution up to the iron (Fe) peak shows the occurrence of progressive α -captures (see Figure 1.3). The iron-peak abundance is instead the direct result of the processes governing the last phases of massive stars’ life. The origin of nuclei beyond iron, which cannot be produced in that thermonuclear charged particle fusion reactions that sustain stellar structures, is almost entirely due to neutron captures (*s*- and *r*-process, see Sections 1.2.5 and 1.2.7).

1.2.1 Nucleosynthesis in main sequence stars

Hydrogen-burning regulates the evolution of main sequence stars. Overall, this process consists of a chain of reactions culminating in the transformation of four protons into a helium nucleus (α particle), plus two positrons and two electron neutrinos:



Actually, in this sequence, the reaction products on the right can be obtained through two chains of nuclear reactions: the pp chain and the CNO cycle, in which carbon, nitrogen, and oxygen act as catalysts. The Q value of the reaction (1.1) is 26.731 MeV, although not all of this energy is always made available to

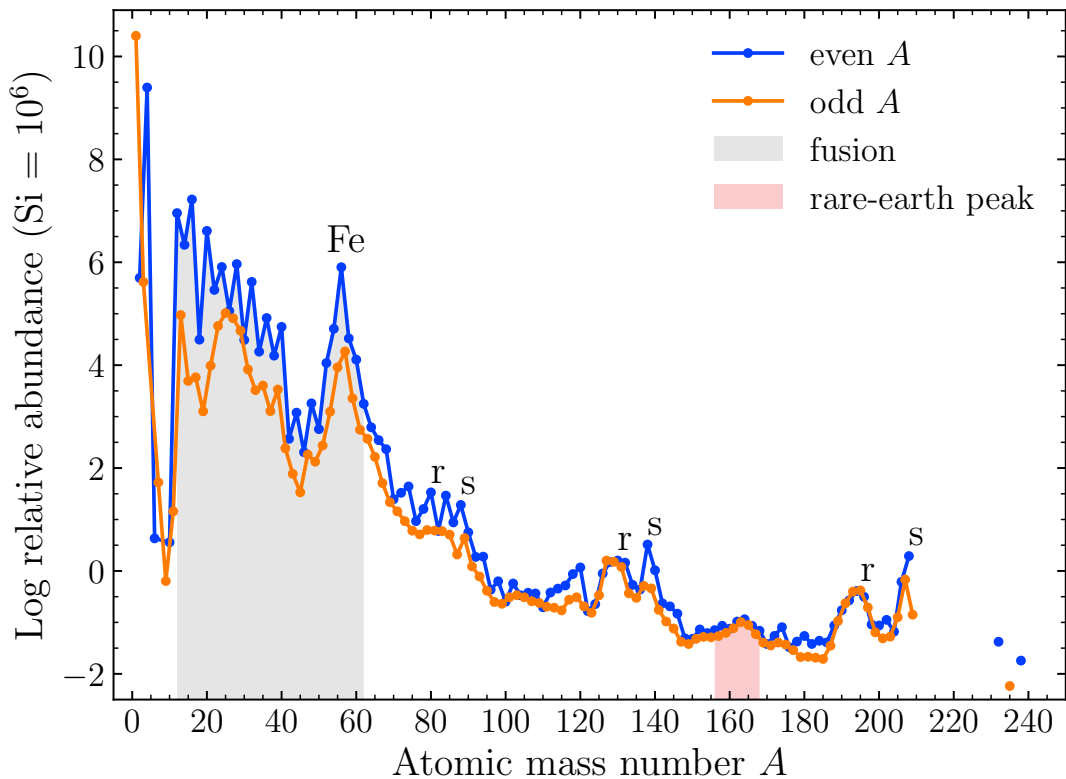


Figure 1.3: Isotopes abundances in our solar system as a function of mass number A . The lightest elements were created in the Big Bang. The gray area marks the elements created by fusion reactions up to the iron peak regions. Elements beyond the iron peak are synthesized by the slow (s) and rapid (r) neutron capture processes. These processes produce three distinct double peaks (see Sections 1.2.5 and 1.2.7). Abundance data from Lodders (2019).

the star and depends on the reaction in which the neutrinos are emitted (see Chap. 5).

The pp chain is the most effective at temperatures of the order of 10^7 K and is the one that largely dominates in the Sun. The two protons can fuse and form a deuteron, only if their distances are of the order of a few fm. Their approach is hampered by the coulombian repulsion, but the fusion process can proceed through quantum tunneling (Gamow 1928). The energy needed to trigger the nuclear reaction is provided by the gravitational contraction. During the contraction process, the gas temperature increases until the kinetic energies of the protons reach sufficient values for the onset of nuclear reactions. The reactions produce energy that tends to expand the gas, so counterbalancing the gravitational contraction. The star thus achieves a state of equilibrium and emits energy with constant power, especially in the form of electromagnetic radiation, but also of neutrinos.

Figure 1.4 shows the reactions that are part of the pp chain. All the various

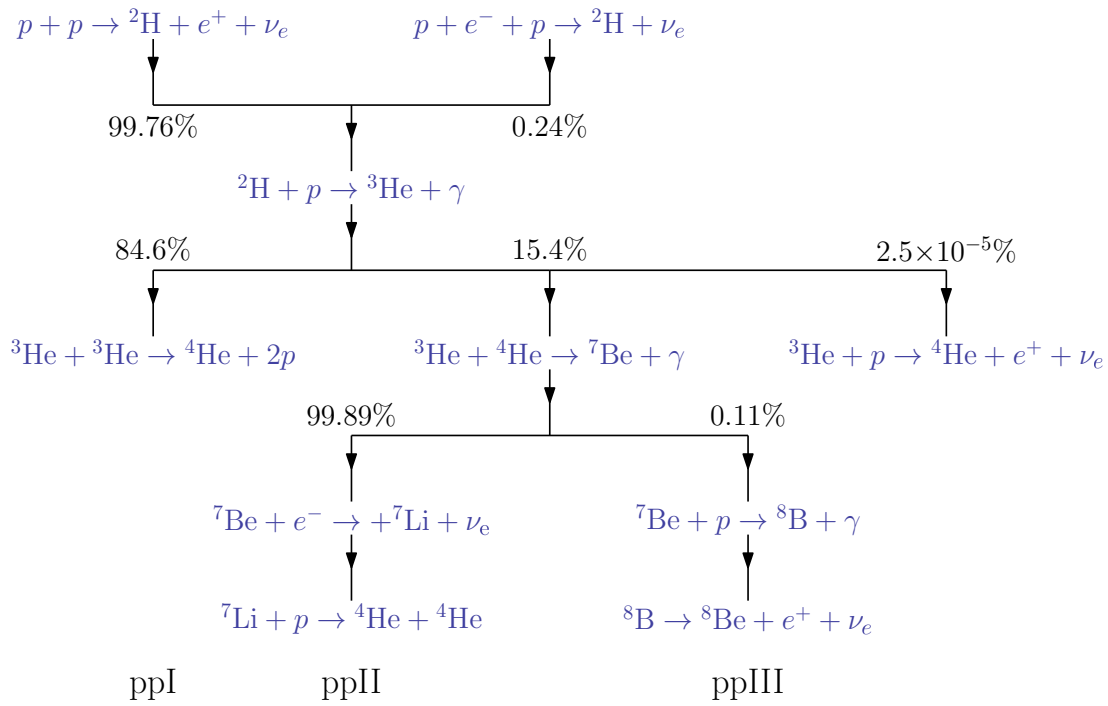


Figure 1.4: The pp chain. The numbers next to the individual branches indicate the percentage probabilities of the reactions.

branches end with the production of helium nuclei. The first step of the pp reaction chain consists of the formation of the deuteron, with a Q value of 1.442 MeV. The process is mediated by the weak interaction that changes a proton into a neutron. The related cross section is therefore very small and other reactions have to “wait” until this reaction occurs. That is why this reaction is referred to as the *bottleneck* of the pp chain.

The first (and now extinct) generation stars, (Population III) are thought to be pure hydrogen-helium stars since the material that emerged from the Big Bang was free of heavy elements. Conversely, the condensed gas cloud from which the following generation stars (Population II and to a greater extent Population I) were formed also included elements that are heavier than hydrogen and helium; these elements are typically referred to as metals. Metals participate in nuclear reactions by acting as catalysts in the fusion process. The presence of these nuclei in reaction processes implies the overcoming of coulombian barriers higher than those present in the pp chain. For this reason, these reactions effectively occur at temperatures typical of stars more massive than the Sun. Those nuclei with a low coulombian barrier and a high relative abundance would be favored to participate in nuclear reactions. Since C and N nuclei are more abundant than nuclei between ${}^4\text{He}$ and ${}^{12}\text{C}$ the chain of reactions necessary for H-burning can take place via the so-called CN cycle, with carbon and nitrogen acting as catalysts for the conversion of hydrogen into helium (see Figure 1.5).

As in the pp chain, the cycle velocity is limited by the slower reaction. In

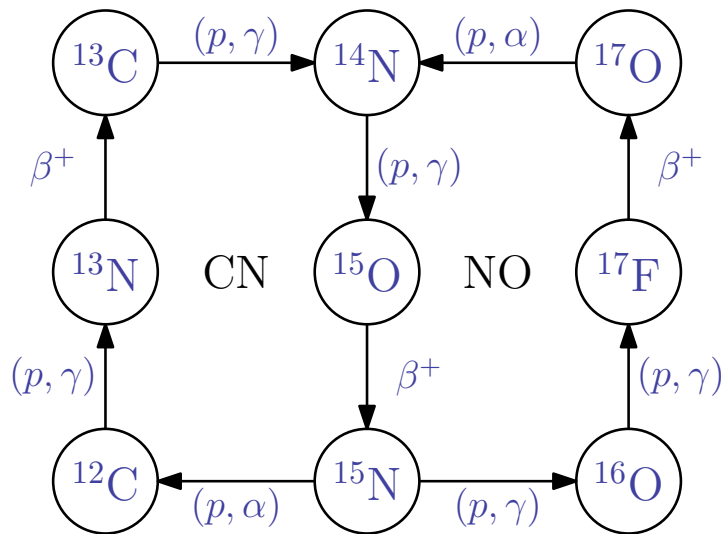


Figure 1.5: The bi-cycle CN-NO.

this case, the problem consists in overcoming the coulombian barrier. From this point of view, the $^{14}\text{N}(p, \gamma)^{15}\text{O}$ and $^{15}\text{N}(p, \alpha)^{12}\text{C}$ reactions are equal, since it is still a proton that must overcome the barrier of a nitrogen nucleus. However, the reaction $^{15}\text{N}(p, \alpha)^{12}\text{C}$, being mediated by the strong nuclear interaction, is faster than the reaction $^{14}\text{N}(p, \gamma)^{15}\text{O}$, which is mediated by the electromagnetic interaction. The latter is therefore the bottleneck that controls the rate with which the CN cycle occurs. Once formed, the ^{15}N nucleus, after absorbing a proton, it can decay in $\alpha + ^{12}\text{C}$ or it may form ^{16}O and trigger another cycle, named NO (see again Figure 1.5), which produces the fuel for the $^{14}\text{N}(p, \gamma)^{15}\text{O}$ reaction. The two combined cycles constitute the CNO cycle. The NO cycle is predicted to occur once every thousand CN cycles. It is therefore not of great significance for energy production, even though it is important for nucleosynthesis.

1.2.2 Solar models and solar neutrinos

Although the energy transported by neutrinos is only a small fraction of the energy released inside the Sun (about 2% for the pp chain), neutrinos are a clear testimony to the validity of stellar and solar models. Nuclear reactions occurring in the stars' core also emit high-energy photons. These photons are susceptible to different diffusion mechanisms, with relatively large cross-sections and thus a very small mean free path. Neutrinos, on the other hand, escape from the Sun without almost interacting with the plasma and reach the Earth. In Figure 1.6 the spectra of solar neutrinos at the Earth are shown. These fluxes are estimated using the so-called Standard Solar Model (SSM). SSM accounts for the energy generation through the pp chain and the CNO cycle. It is also constructed to reproduce the observed values of the present-day solar luminosity L_{\odot} , radius R_{\odot} ,

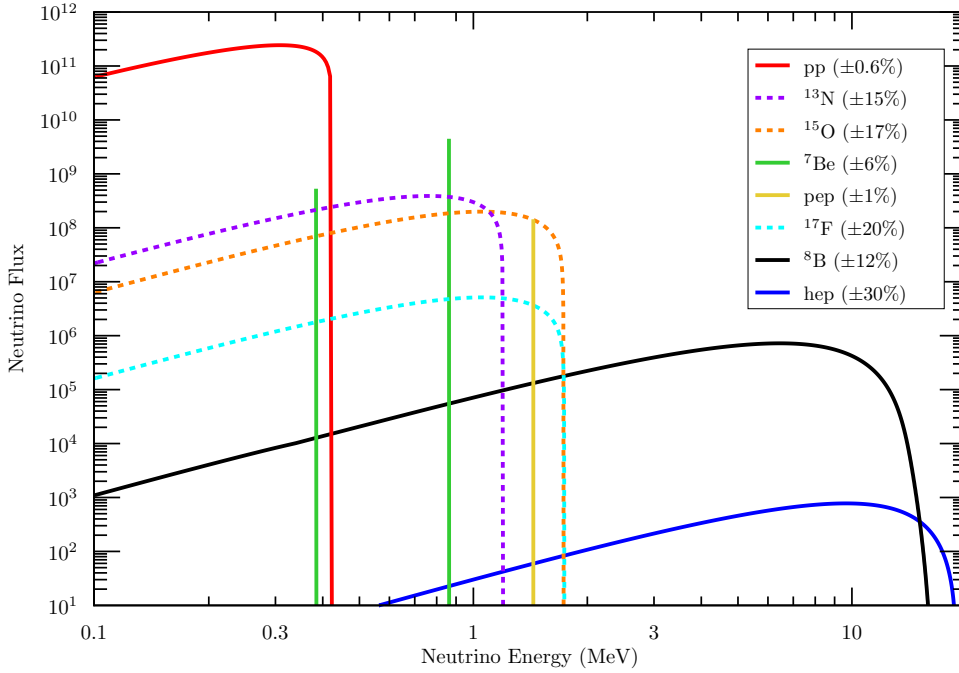


Figure 1.6: Energy dependence of the neutrino fluxes produced by the different nuclear processes in the Sun, according to the B16-GS98 Standard Solar Model from Vinyoles et al. (2017). Continuous spectra are expressed in units of $\text{cm}^{-2} \text{s}^{-1} \text{MeV}^{-1}$, while mono-energetic neutrino (${}^7\text{Be}$ and pep neutrinos) are in units of $\text{cm}^{-2} \text{s}^{-1}$. The dashed lines highlight the CNO-cycle contribution to the solar neutrino flux. Figure adapted from Gallo Rosso et al. (2018); see that reference for details. © 2018 Springer Nature

and surface metal to hydrogen abundance ratio $(Z/X)_{\odot}$ (see Chapters 4 and 5). In the past years, special attention has been devoted to the validation of the SSM, as neutrino observations from the Sun suggested fluxes lower than expected. This discrepancy, initially recorded by Homestake (Davis et al. 1968; Cleveland et al. 1998) and then verified by GALLEX (Hampel et al. 1999), SAGE (Abdurashitov et al. 1999), Kamiokande (Hirata et al. 1989) and Super-Kamiokande (Cravens et al. 2008), caused the so-called *solar neutrino problem*. A solution for the missing solar neutrinos was found in 2002 when the SNO experiment (Ahmad et al. 2002) obtained clear proof of flavor oscillations of solar neutrinos.

Nowadays, we have a solid understanding of solar neutrino oscillations and direct experimental determination of most solar neutrino fluxes. Over the last twenty years, big efforts have been made to measure neutrino fluxes by Super-Kamiokande (Abe et al. 2016), SNO (Bellerive et al. 2016), and Borexino (Bellini et al. 2014; Agostini et al. 2018) experiments, which have provided very high precision measurements of pp, ${}^7\text{Be}$, pep, ${}^8\text{B}$ neutrino spectra. Borexino has also recently obtained the first direct measurement of CNO neutrinos (Agostini et al. 2020a). In this context, solar neutrinos are a powerful instrument with which the

solar interior can be tested with high accuracy, also because the production of solar neutrinos is very sensitive to the temperature at which nuclear reactions take place. This is e.g. the case of ^8B neutrino flux, which is greatly sensitive to thermodynamic conditions of the solar core (Bahcall and Ulmer 1996; Haxton and Serenelli 2008), and in particular to its temperature. Therefore it acts as a “thermometer”. For this reason, SNO and Super-Kamiokande measurements of the ^8B neutrino flux, which are by the far the most precise available, pose a major constraint for solar modeling (see Chapter 4). Another example is the measurement of CN neutrino fluxes, recently announced by the Borexino Collaboration (Agostini et al. 2020a). Observation of CNO neutrinos, despite the large uncertainty affecting the measurement, is of utmost relevance. On the one hand, it is an important experimental confirmation of our understanding of how the Sun works; on the other, it demonstrates that an improved future measurement could determine the combined C+N abundance in the solar core independently of the solar model. Such a measurement would then result in a direct determination of the core admixture of the Sun (and any other star) and would be a major asset for understanding mixing processes in stars (see Chapter 5).

Summarizing, the Sun can be used to calibrate stellar models and explore neutrino physics, but also to test the effects of neutrino interactions with matter, i.e. the propagation of neutrinos in the Sun’s interior.

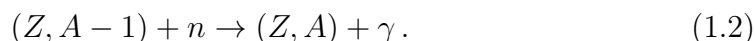
1.2.3 Nucleosynthesis up to the iron peak

When the hydrogen fuel runs out, the star undergoes the transformations described in Section 1.1.3 and a red giant star is formed. As the mass of the helium core becomes high enough, ^4He is burned throughout the core. The fusion process occurs thanks to the formation of the unstable ^8Be system that immediately captures another α particle so producing a nucleus of ^{12}C . This process can take place thanks to the presence of a resonance of ^{12}C nucleus (the *Hoyle state*), which allows the fusion of three α . In the center of red giants, temperatures are sufficient to trigger the $^{12}\text{C} + \alpha \rightarrow ^{16}\text{O} + \gamma$ reaction. Stars with masses lower than $\simeq 10 M_{\odot}$ pass through the AGB phase and, later, cool as white dwarves. At this stage, nucleosynthesis processes are halted. Nuclei heavier than ^{12}C and ^{16}O are formed, at least in non-negligible amount, only in more massive stars. In these stars, the carbon burning is activated by temperature rise caused by the contraction of the star itself. From an energy point of view, the carbon burning phase is very short and of little relevance for the hydrodynamic balance, provided that most of the energy produced leaves the star in the form of neutrinos. As the star shrinks after the exhaustion of the ^{12}C , the temperature goes up ($\sim 1.5 \times 10^9$ K), and Ne photodisintegration is expected. At $\sim 2 \times 10^9$ K the burning of oxygen becomes efficient and, if the temperature reaches $\sim 3 \times 10^9$ K, the nucleosynthesis processes continue with the silicon burning phase. At this point, the various nuclear production reactions and their inverse (photodissociations) are in equilibrium, thus ensuring the so-called nuclear-statistical equilibrium (NSE),

which implies a complete chemical balance between all the nuclear reactions involved. In this scenario, the more stable nuclei around ^{56}Fe are favored and therefore more abundant. These nucleosynthesis processes can explain, even quantitatively, the elemental abundances around the iron peak.

1.2.4 Nucleosynthesis of the heavy elements

Starting from the initial abundances, the synthesis of the elements continues via nuclear fusion in the stars until the production of iron (in sufficiently massive stars). From this point on, fusion no longer occurs spontaneously since it would become endothermic: namely, it would require energy from the environment instead of producing it. If we look at the binding energy per nucleon curve (the main indicator of the stability of a nucleus) as a function of the mass number, we actually see a peak in correspondence of iron. The synthesis of elements beyond the iron peak therefore mostly takes place through processes other than charged particle reactions, i.e. through neutron captures (*s*- and *r*-process):



These processes are determined by the intensity of the neutron flux, the neutron capture cross section and the β -decay constant of the isotope produced. Under these assumptions, the equation that defines the number abundance of an isotope as a function of time is as follows:

$$\frac{dN_A(t)}{dt} = [-N_n(t)N_A(t)\langle\sigma v\rangle_A + N_n(t)N_{A-1}(t)\langle\sigma v\rangle_{A-1}] - \lambda_A N_A(t), \quad (1.3)$$

where N_A and N_n are the number densities of nucleus A and of free neutrons, respectively; $\langle\sigma v\rangle_A$ is the neutron capture rate per particle pair of nucleus A, and λ_A is the decay constant of nucleus A. The process of neutron capture occurs when the term in square brackets is positive and dominant over the decay term, i.e. when the difference between these two terms is positive. The distinction between *s*- and *r*-process is strictly linked to this difference.

It can be shown that the cross section for thermal neutrons follows the trend $\sigma \sim v^{-1}$. In this way we can define a Maxwellian averaged cross-section (MACS) as :

$$\langle\sigma\rangle \equiv \frac{\langle\sigma v\rangle}{v_T}, \quad (1.4)$$

where $v_T = (2k_B T/\mu)^{1/2}$ is the thermal velocity of the Maxwell-Boltzmann distribution, while μ is the reduced mass of the system, T the absolute temperature, and k_B the Boltzmann constant. We find that, in the case of a heavy nucleus, the reduced mass can be replaced in good approximation with the mass of the neutron, with the notable benefit of having $\langle\sigma\rangle$ fully independent of the properties of the single nucleus. The Equation 1.3 can then be re-written as

$$\frac{dN_A(t)}{dt} = v_T N_n(t) [-N_A \langle\sigma\rangle_A + N_{A-1} \langle\sigma\rangle_{A-1}] - \lambda_A N_A(t). \quad (1.5)$$

For a given isotope, the cross sections σ_{A-1} and σ_A , and the decay constant λ_A are fixed. The factor that allows or prevents nucleus formation is the neutron flux $\phi_n \propto N_n(t)v_T$. Low neutron fluxes are attained in the core He-burning and shell C-burning of a massive star or the thermally-pulsing phase of AGB stars, whereas intense neutron fluxes are produced during the explosive phase of a supernova or a neutron merger event. The difference between the two neutron capture processes is the time scale on which they occur with respect to the corresponding β -decay. There are three kinds of such decays:

- β^- . A neutron decays in an electron-proton pair, plus an electron antineutrino. It is the most important decay in the path of synthesis of heavy elements;
- β^+ . A proton decays into a neutron-positron pair plus an electron neutrino;
- e^- -capture. A proton and an electron produce a neutron with the emission of an electron neutrino. It represents a key process in the collapse of massive stars resulting in a supernova explosion and the formation of a compact object.

In the s -process the neutron capture occurs on a timescale longer than that of the corresponding β decay. Therefore the s -process path on the nuclide charts will always evolve close to the beta stability valley (see Figure 1.7).

On the contrary, the r -process proceeds on timescales shorter than β -decay timescales, and the path significantly departs from the stability valley, so producing strongly β -unstable nuclei, up to the neutron dripline (see again Figure 1.7). The physical dynamics of these nucleosynthesis processes are responsible for abundance peaks of the nuclei with more stable configurations, i.e. in correspondence to the so-called magic neutron numbers 50, 82, 126 (see Figure 1.3), according to the nuclear shell model. The trend of observed abundances represents, together with the spectral properties of the astrophysical sites of interest, the key observable for the nucleosynthesis analysis. From Figure 1.3 we can see the three peaks of the s -process and the r -process in a mutually offset position, a phenomenon closely related to the physics of these synthesis mechanisms, as discussed in the next sections. Furthermore, between the second and third peaks, there is the so-called rare-earth peak (at $A \sim 160$), corresponding to a nuclear region produced in the competition between neutron captures and decays, following the freezing-out phase of the r -process (see Section 1.2.7).

1.2.5 The s -process

In the *slow* process, neutrons are captured and form nuclei which, if unstable, decay before capturing another neutron. For this reason, the decay term in Equation (1.5) is dominant in the case of an unstable nucleus. On the opposite, in the case of a stable nucleus, or with a mean lifetime much longer than the average time for the capture of another neutron, the decay term is negligible

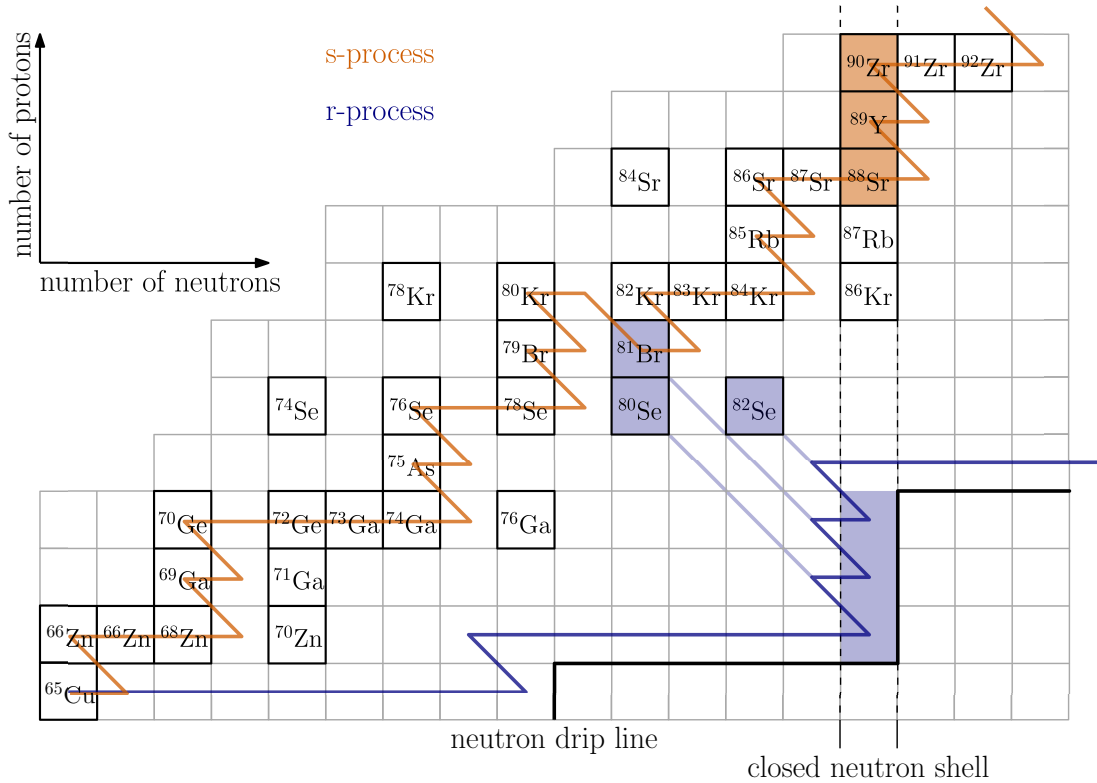


Figure 1.7: Schematic representation of the s - and r -processes on a section of the chart of nuclides. The s -process (orange) proceeds along the valley of stability and the r -process (blue) along the neutron drip line. At the closed neutron shell $N = 50$, the neutron capture cross section drops by several orders of magnitude, resulting in a pile up of material there that produces the double-peak features shown in Figure 1.3. Figure adapted from Lippuner (2018).

relative to the others. As a consequence, nuclei produced through s -process are located very close to the stability valley. Considering the equation Equation 1.5 we have that, for stable nuclei (far from magic nuclei), the equilibrium condition is reached when

$$\sigma_{A-1}N_{A-1} = \sigma_A N_A. \quad (1.6)$$

The abundances observed in nature for s -process nuclei indicate that there is a clear correlation between abundances and cross sections for neutron capture. The product $\sigma_A N_A$ is a fairly smooth function of A (see Figure 1.8), despite the irregularity of the trend of σ_A , as shown in Figure 1.9.

The process takes place under relatively low neutron density conditions ($N_n \sim 10^7 \div 10^{11}$ neutrons cm^{-3}). In this case, the time scale for neutron capture is much longer than the β -decay time scale of radioactive isotopes, thus explaining the adjective *slow*. The process is therefore going to produce isotopes along the so-called β -stability valley (see Figure 1.7). This is because, given the velocity of β -decays, one can ignore the abundance of radioactive species and assume that the nucleus will instantly decay to a more stable state. There are also abundance

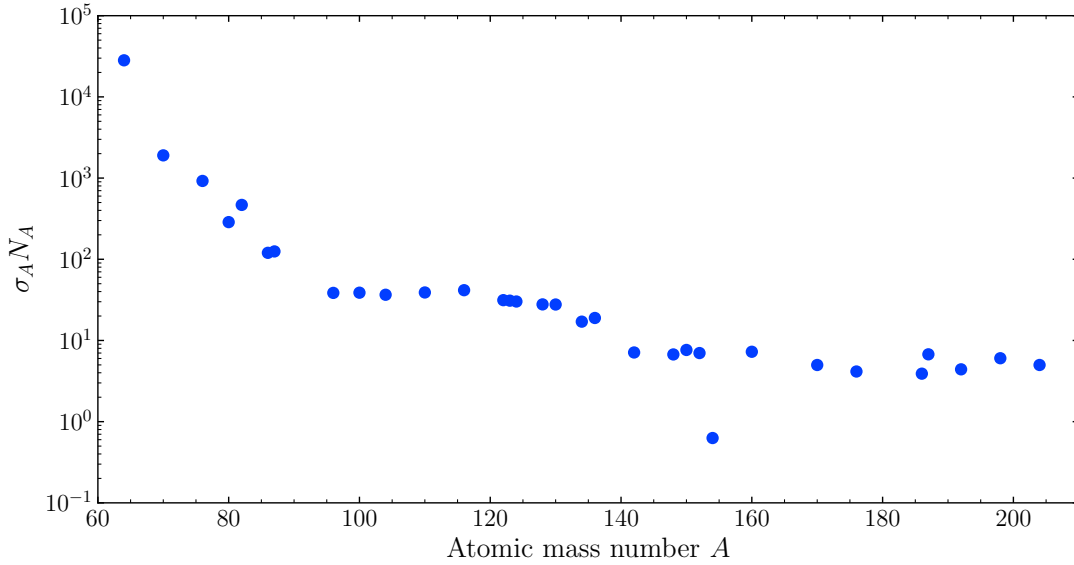


Figure 1.8: The solar-system $\sigma_A N_A$ curve. The product of the neutron-capture cross sections for $kT = 30$ keV times the nuclide abundance per 10^6 silicon atoms is plotted versus the atomic mass number A . The symbols denote the empirical products for the s -only nuclei. Some important branchings of the neutron capture chain are indicated as well. Note that reaction flow equilibrium has only been achieved for the main component in mass regions between magic neutron numbers (where $\sigma_A N_A$ values are nearly constant).

peaks of certain isotopes formed by slow neutron capture. Nuclei with a magic number of neutrons are very stable against neutron capture and have small cross sections. These nuclei therefore cause a *bottleneck* effect with the corresponding formation of abundance peaks (see Figure 1.3).

The result of an s -process calculation, solving Equation (1.5), depends solely on the neutron exposure τ for constant (not temperature-dependent) $\langle\sigma v\rangle$ -values. Historically, the neutron exposure is defined to also contain the thermal velocity v_T as:

$$\tau = \int v_T N_n(t) dt. \quad (1.7)$$

Seeger et al. (1965) has shown that an adequate fit to the solar s -process abundance distribution could be obtained on the assumption of an exponential distribution of neutron exposures of the form

$$\rho(\tau) \propto \exp(-\tau/\tau_0). \quad (1.8)$$

Such a superposition gives a much better fit to the slightly decreasing σN_s -curve, as compared to a constant one for a complete steady flow between magic neutron numbers. The best overall fit to the s -process σN_s curve was found to be given by a combination of three different components (see, e.g., Kappeler et al. 1989). The majority of s -process nuclei in the mass range $90 < A < 204$ can be produced by

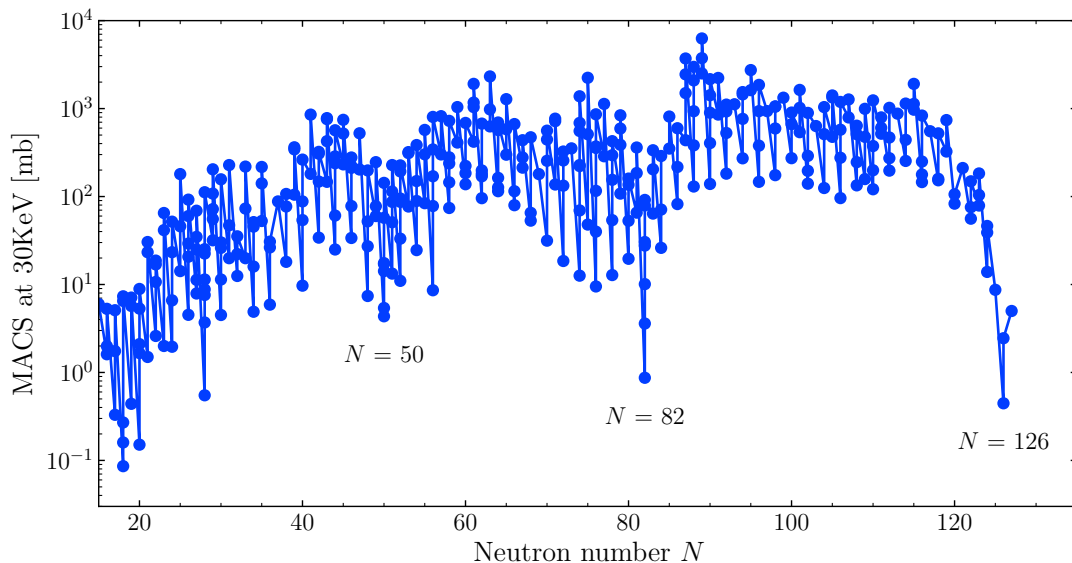


Figure 1.9: Stellar (n,γ) cross-sections at 30 keV as a function of the neutron number N . The compilation is taken from the KADoNiS v1.0 database (Dillmann 2014). Highlighted are the minimums corresponding to nuclei with magic neutron numbers $N = 50, 82, 126$.

the main s -process component, with an approximate mean exposure parameter $\tau_0 \sim 0.3 \text{ mb}^{-1}$. As we shall discuss, this component is usually attributed to the combined action of the ^{13}C and ^{22}Ne neutron sources in the thermally pulsing shells of low- and intermediate-mass AGB stars. The abundances of s -process isotopes with $A \leq 90$ are instead associated with a weak exposure of order $\tau_0 \sim 0.06 \text{ mb}^{-1}$, typical of those encountered in massive stars by iron seed nuclei during core helium burning and shell carbon burning. Finally, a strong s -process component appears to be required, with $\tau_0 \sim 7 \text{ mb}^{-1}$, to match the abundances of the heavy lead isotopes and bismuth. However, it was later found that this component does not exist, as it is not related to some other astrophysical environment, but it is due to low-mass and low-metallicity AGB stars (Arlandini et al. 1999).

In this regard, an important factor in determining the temperature and neutron density conditions typical of the s -process nucleosynthesis site is represented by the analysis of the so-called branching points. Along the s -process nucleosynthesis path, there exist particular isotopes that are unstable to beta-decay, with β -decay timescale comparable to the neutron capture:

$$\tau_\beta \sim \tau_n. \quad (1.9)$$

In correspondence with those nuclei, the flow bifurcates and proceeds either through more neutron-poor and or more neutron-rich isotopes. Accurate determinations of the s -process contributions to shielded s -only isotopes, which cannot have an r -process contribution, can then reveal which is the critical neutron number density and temperature conditions that set the lifetimes of branch point isotopes (see, e.g., Bisterzo et al. 2015; see also Section 3.1).

Neutron capture processes require a source of free neutrons, always taking into account that neutrons are unstable and decay within ≈ 10 minutes. *s*-process nucleosynthesis occurs in two distinct environments: the helium-burning cores and carbon-burning shells of massive stars ($M \geq 10 M_{\odot}$) and the helium-burning shells of AGB stars. The first site accounts for the weak *s*-process component, while the second one accounts for the main component.

In massive stars, the main neutron source is represented by the $^{22}\text{Ne}(\alpha, n)^{25}\text{Mg}$ reaction, with ^{22}Ne produced through the chain $^{14}\text{N}(\alpha, \gamma)^{18}\text{F}(\beta^+\nu)^{18}\text{O}(\alpha, \gamma)^{22}\text{Ne}$.

The main reactions that enrich AGB stars with neutrons develop in the helium-burning shell during the TP-AGB phase and are:

- $^{14}\text{N}(\alpha, \gamma)^{18}\text{F}(\beta^+\nu)^{18}\text{O}(\alpha, \gamma)^{22}\text{Ne}(\alpha, n)^{25}\text{Mg}$
- $^{12}\text{C}(\text{p}, \gamma)^{13}\text{N}(\beta^+\nu)^{13}\text{C}(\alpha, n)^{16}\text{O}$

During the interpulse phase, the region between the two burning shells (see Figure 1.1) is largely enriched in ^{14}N produced by the hydrogen-burning shell in its outward progression. This ^{14}N is then converted into ^{22}Ne through α -captures, when mixed downward into the helium shell during the ensuing convective thermal pulse and, if the temperature is high enough ($T \gtrsim 3 \times 10^8$ K), the $^{22}\text{Ne}(\alpha, n)^{25}\text{Mg}$ reaction is activated. The neutron production through this channel is efficient only in intermediate AGB stars, with masses of $M \geq 4 M_{\odot}$, due to the high temperature required for this reaction to occur (Cristallo et al. 2015b). These temperatures can also be reached during some thermal pulses in less massive AGB stars, but the neutrons produced in this way have only a marginal influence on the final distribution of the *s*-elements abundance (Cristallo et al. 2015b).

The main neutron source in AGB stars is actually provided by ^{13}C nuclei, which are burned via the $^{13}\text{C}(\alpha, n)^{16}\text{O}$ reaction. This requires both proton and α capture reactions to occur in the helium intershell. One of the issues with modeling this neutron production channel is due to the abundance of ^{13}C . The ^{13}C left in the ashes of the H-burning shell is not sufficient to explain the observed neutron enrichments. Then, there must exist some mixing which brings hydrogen from the envelope down to the ^{12}C -rich region during a TDU (see again Figure 1.1). Protons would then be captured by ^{12}C nuclei to form ^{13}C . This ^{13}C -enriched region, known as the ^{13}C pocket, provides the required neutrons. This reaction efficiently produce neutrons at about $T \approx 9 \times 10^7$ K. The $^{13}\text{C}(\alpha, n)^{16}\text{O}$ reaction is the dominant neutron source for low mass AGB stars, $M \leq 3 M_{\odot}$ (see, e.g, Busso et al. 1999).

To date, the mechanism through which the ^{13}C pocket forms is still debated. While classical post-process models typically assume an artificial ad-hoc ^{13}C pocket (Gallino et al. 1998), many physically-based approaches have been recently developed in order to model the penetration of proton-rich material from the convective envelope to the He-intershell (see Section 1.2.6).

1.2.6 Mixing processes in AGB stars

The transport of matter in stars is strictly related to the transport of energy. Radiation and, in degenerate conditions, electron conduction, are the most important forms of energy transport. To these, we must add a third form of contribution to the energy flow, namely convection. Convection is an energy and chemical element transport mechanism that involves large-scale motions of matter in stellar interiors. By imagining that bubbles of matter move within the star, then the creation and destruction of these bubbles will be mediated by turbulence. However, in computational terms, a detailed treatment of the convective mixing phenomenon turns out to be too expensive. For this reason so a phenomenological theory called *Mixing Length Theory* (MLT) is usually adopted (Böhm-Vitense 1958; see also Section 2.3). Convection is the only process considered for transporting chemical elements in standard stellar models. However, it has been shown that standard stellar models with pure convection are not capable of reproducing AGB isotopic and elemental distributions (Gallino et al. 1998; Busso et al. 1999; Nollett et al. 2003; Herwig 2005; Busso et al. 2010; Karakas and Lattanzio 2014). The latter can provide constraints on the velocity, and possibly on the nature, of the dynamical mixing phenomena taking place. This is so in particular for the enrichment in neutron-rich elements (Cristallo et al. 2009, 2011, 2015b; Trippella et al. 2016) occurring in the TP-AGB phases. One of the most challenging open problems actually concerns the formation of the ^{13}C pocket, whose solution is strictly connected to understanding the physical processes governing mass-exchange at the interface between the convective envelope and the radiative core. Recent research has then focused on studying non-convective transport mechanisms, from diffusive to relatively fast dynamical and magneto-hydrodynamical mixing processes, usually ignored by the canonical theory of stellar structure and evolution.

One kind of additional transport process is represented by *convective overshooting* (Herwig et al. 1997). When the convective envelope penetrates the H-exhausted region during a TDU, its innermost layers become unstable due to the formation of a sharp chemical discontinuity (see, e.g. Frost and Lattanzio 1996). Because of this chemical gradient, the turbulent eddies of the convective envelope have a large average radial velocity and may overshoot beyond the Schwarzschild limit, thus penetrating the underlying stable layer and producing some extra-mixing. In stellar evolution calculations, convective overshooting is modeled as an exponential decay of the diffusion coefficient (Herwig et al. 1997; Herwig 2000) or of the convective velocities (Straniero et al. 2006; Cristallo et al. 2009), depending on the numerical algorithm adopted for the chemical transport of elements. Such an exponential decay has been tuned on hydrodynamical calculations (e.g., Freytag et al. 1996). Based on two-dimensional hydrodynamical simulations (Herwig et al. 2007), Battino et al. (2016, 2019) applied a double exponential decreasing profile to account for both Kelvin-Helmholtz instabilities and internal gravity waves (IGWs) mixing (Denissenkov and Tout 2003) at the bottom of the convective envelope. Such convective-boundary-mixing model leads

to the formation of a wider ^{13}C pocket compared to the one obtained in the models not accounting for IGWs. The ensuing model results agree with most of the observational data but fail in reproducing the full ranges of some isotopic ratios measured in presolar grains, unless invoking some rotation-induced mixing (Battino et al. 2019).

Rotation may also influence the dynamic processes at play in stellar interiors (e.g., Maeder 2009). Many constraints on these processes have been obtained with helioseismology and asteroseismology studies (see, e.g., Aerts 2019). In addition, rotation, and especially differential rotation, generates several instabilities that produce mixing processes able to transport elements from inner layers to the surface. There are several *rotationally-induced instabilities*. The most important among them is the *Eddington-Sweet circulation* which arises due to large-scale meridional currents of material, resulting from the thermal imbalance between pole and equator characteristic of rotating stars. Others are the *dynamical shear instability*, the *secular shear instability*, the *Solberg-Hoiland instability*, the *Goldreich-Schubert-Fricke instability*. Although it is clear that stars rotate and that rotation can trigger certain instabilities which may lead to mixing, it is not well understood how efficient these processes are and how the different instabilities interact with each other (see, e.g., Maeder 2009). Concerning AGB stars, the possibility that rotation-induced mixing can be active has been widely investigated (see Langer et al. 1999; Herwig et al. 2003; Siess et al. 2004). These studies put in doubt that rotation alone could produce a sizable ^{13}C pocket. Nonetheless, a variation in the initial rotational velocity can lead to a spread in the final surface *s*-process enhancements and spectroscopic indexes (Piersanti et al. 2013). On the other hand, AGB models rotating at a rate that matches the asteroseismic measurements, show an *s*-process production comparable to that of the non-rotating model (Piersanti et al. 2013; den Hartogh et al. 2019b), questioning that mixing induced by rotation may still play a significant role in *s*-process nucleosynthesis in low-mass AGB stars.

Another phenomenon strictly connected to rotation is stellar magnetism. The latter is often neglected in the computation of stellar evolutionary models. However, the interaction between convection and stellar differential rotation can generate complex internal magnetic fields that may play a major role in the evolution of stars. Such internal magnetic fields can be grouped into two different categories. The first deals with fossil fields, remnants of the star formation process that have somehow survived in a stable configuration. The other type is related to time-dependent magnetic fields created and maintained by some kind of dynamo process, which take advantage of sources of energy, i.e. convection and/or differential rotation; the latter could produce a self-sustained small-scale magnetic field in a radiative zone (see, e.g., Braithwaite and Spruit 2017) which could also be responsible for the transport of angular momentum and chemical elements (Busso et al. 2007; Aerts et al. 2019). This is e.g. the case of the *magnetic-buoyancy-induced* mixing proposed by Busso et al. (2007) (see also Nucci and Busso 2014). These authors suggested that dynamo-produced buoyancy of magnetized materials could provide a physical mechanism to transport material

from the radiative regions to the above convective envelope during the RGB and AGB phases of low-mass stars. In this scenario, the original poloidal field of a rotating star generates a strong toroidal field developing various instabilities (Parker 1960; Spruit 1999) among which the buoyancy of magnetized structures (e.g., Schuessler 1977). Such magnetic instabilities may also supply a sufficient transport rate capable to explain the formation of the ^{13}C pocket in TP-AGB stars (Trippella et al. 2014, 2016; see also Chapters 6 and 7). Such ^{13}C pocket was shown to be able to account for both the solar distributions of s -only isotopes (Trippella et al. 2016) and isotopic ratios of s -elements measured in presolar SiC grains (Palmerini et al. 2018 and Chapter 7).

Therefore, the presence of magnetic fields adds new transport mechanisms, some of which could compete with or suppress purely hydrodynamic processes and could change the surface distribution of elements.

1.2.7 The r -process

The r -process requires temperatures and free neutron densities higher than in the environments where slow capture occurs, i.e. $T > 10^9$ K and $n_n > 10^{20}$ cm $^{-3}$. Under these conditions, the neutron capture time scale is about 10^{-4} s, clearly lower than the half-lives of the β -decay of unstable isotopes, which are on average between 10^{-1} s and 10^{-3} s (see Figure 1.10). Neutron fluxes of this magnitude cause neutron-rich nuclei (located on the right of the valley of stability) to be rapidly synthesized, with paths very different from those of the s -process. There are basically two approaches to quantify abundances in the context of the *rapid* neutron capture process. The first is the *empirical* approach according to which the distribution of the r -process is obtained as

$$N_r = N_{\odot} - N_s, \quad (1.10)$$

i.e. by subtracting from the measured solar system abundances the contributions calculated for the s -process. We plot the solar r -process and s -process abundance patterns in Figure 1.11. An important distinguishing feature of s -process and r -process nucleosynthesis is clearly evident in this figure: s -process abundances show pronounced odd-even variations, while such effects are substantially reduced or largely absent in the r -process abundance pattern. It is generally believed that the reduced odd-even variations in the r -process abundances are partly a consequence of the effects of beta-delayed neutron emission, as the nuclei formed along the r -process path approach the valley of beta stability via β -decay (see, e.g., Kratz et al. 1993).

From Figure 1.11 it can be seen that the r -process peaks are always close to those due to the s -process, but shifted to lower mass numbers. This behavior suggests that the peaks are, as in the case of slow capture, due to a particular stability in correspondence to the magic numbers. The shifts are justified by considering that the magic nuclei produced with the rapid capture are located to the right of the stability valley and are strongly proton-deficient. When the neutron flux ends, they are therefore subjected to a series of β^- decays

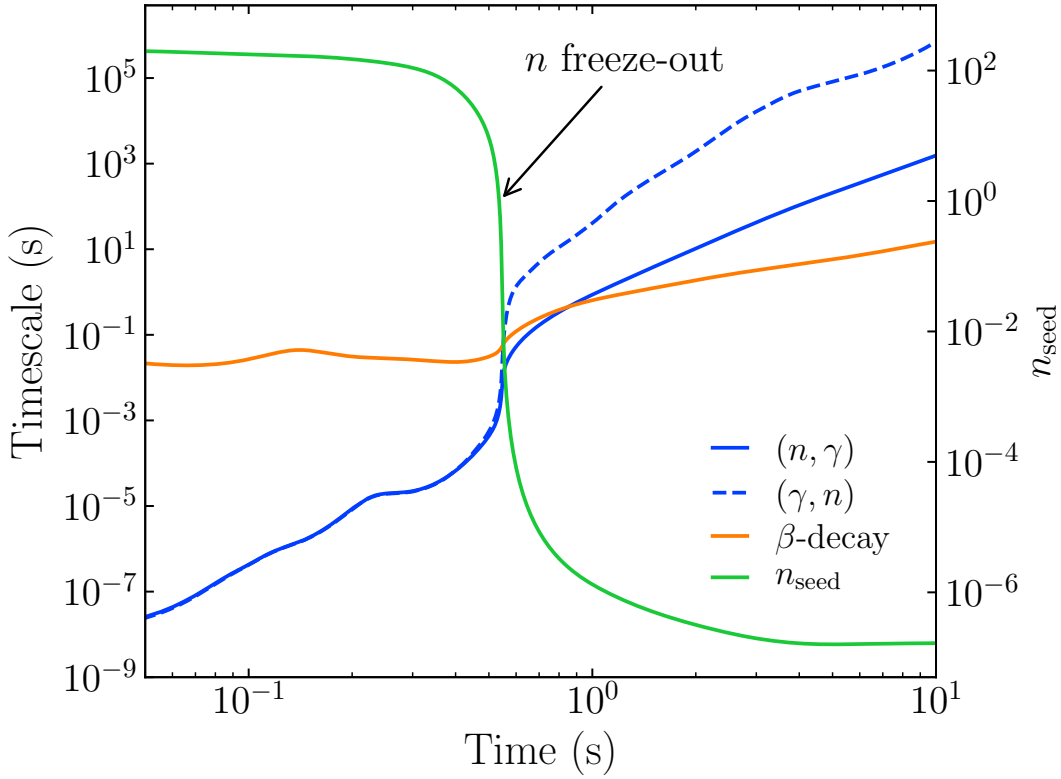


Figure 1.10: Evolution of the neutron-to-seed ratio and average timescales for neutron captures, photodissociation and β -decays for typical conditions of matter ejected in neutron star merger. The early r -process is characterized by $(n, \gamma) - (\gamma, n)$ equilibrium. As neutron freeze-out occurs, a competition between neutron capture and β -decay arises. At this stage, the neutron-to-seed ratio drops rapidly below unity. Nucleosynthesis calculations were performed with the SkyNet code (see Chapter 8).

along isobaric chains, namely keeping A constant, until stability is reached (see Figure 1.7). It should also be emphasized that the observed abundances are completely uncorrelated from the radiative capture cross sections, but strongly dependent on the properties of the radionuclides synthesized on the neutron-rich side of the table.

The second approach is the *canonical* r -process and is based again on an analytic description of the phenomenon starting from some fundamental considerations. Suppose we are in an environment in which the neutron temperature and density of neutrons are constant and high enough to trigger a rapid capture process. In this situation, the decay time scale is higher than both the neutron capture timescale and the inverse photodisintegration reaction (see Figure 1.10), so that each isotopic chain for any Z will be populated by an equilibrium abundance. The transport of abundances between nucleus (Z, A) and $(Z, A + 1)$ determines the rate of change

$$\dot{Y}(Z, A) = \lambda_{\gamma, n}(A + 1)Y(Z, A + 1) - \langle \sigma v \rangle_{n, \gamma}(A)Y(Z, A)n_n, \quad (1.11)$$

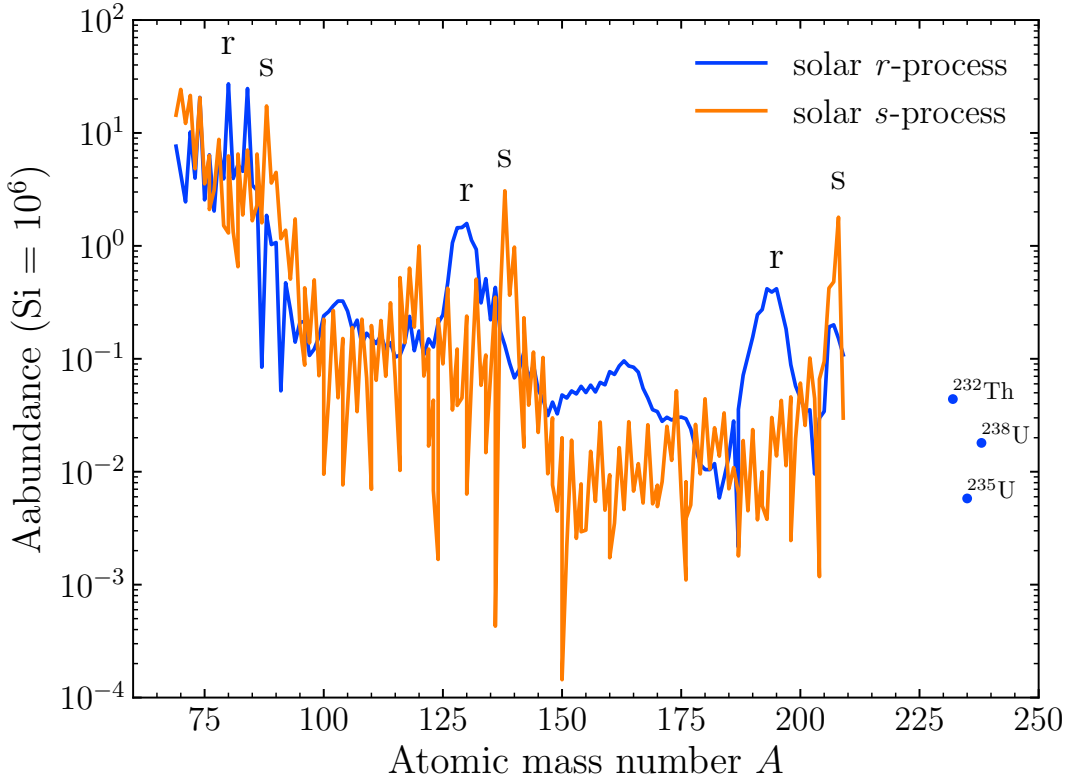


Figure 1.11: Decompositions of s -process and r -process abundances based upon the work of Prantzos et al. (2020). Notice the opposite behavior of the two processes with respect to odd-even staggering.

where $\lambda_{\gamma,n}$ is the photodisintegration rate. The large nuclear rates will ensure an equilibrium, i.e. $\dot{Y}(Z, A) = 0$ and an abundance ratio

$$\frac{Y(Z, A + 1)}{Y(Z, A)} = \frac{\langle \sigma v \rangle_{n,\gamma}(A)}{\lambda_{\gamma,n}(A + 1)} n_n \quad (1.12)$$

in this $(n, \gamma) \rightleftharpoons (\gamma, n)$ equilibrium or waiting-point approximation, since the abundance flow waits for the waiting-point nucleus, i.e. the nucleus with maximum abundance in each isotopic chain, decay to proceed to higher atomic numbers. When the waiting point nucleus decays, a beta-flow establishes between isotopic chains. When the decay terms begin to dominate, the transition to the next isotope chain occurs. The physical situation is the following: the r -process creates, from a nucleus with Z protons, isotopes increasingly rich in neutrons until the equilibrium between neutron capture and photodisintegration is reached and a β -decay bridges the isotopic chain $Z + 1$, where a new balance is reached, and so on.

Neutron captures end when neutrons run out and this can happen in different ways, depending on the characteristics of the astrophysical environment in which the process takes place (expansion time scale τ , electron fraction Y_e , entropy

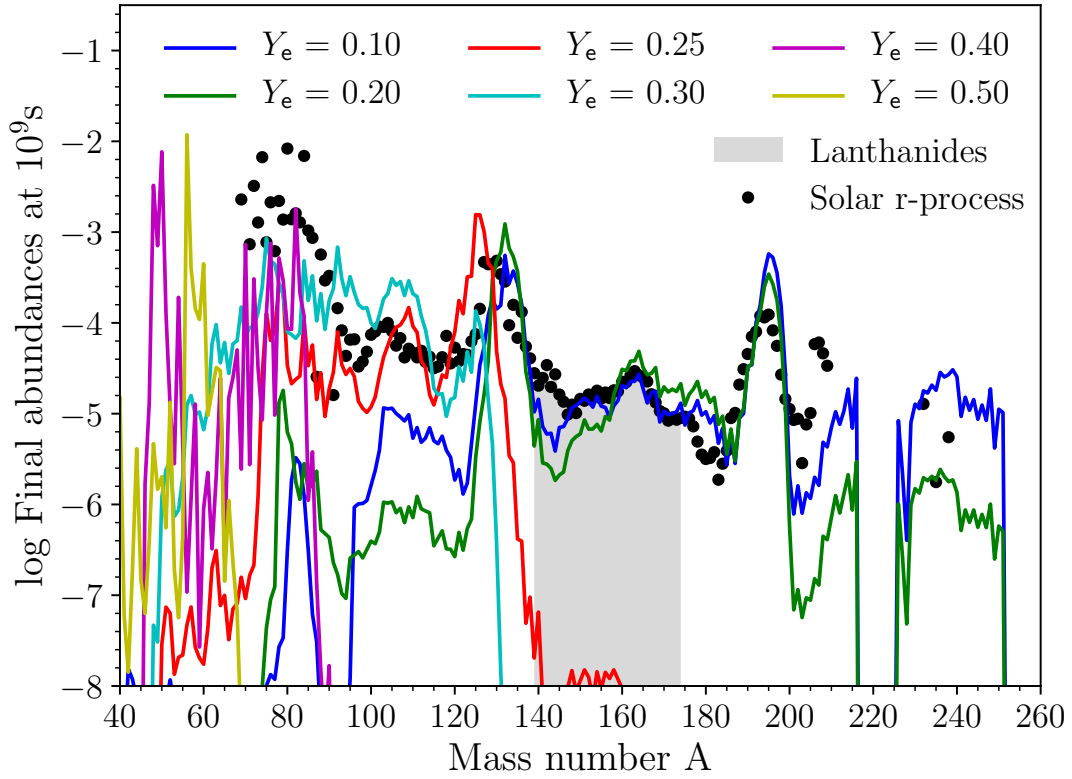


Figure 1.12: Dependence of nucleosynthesis on the electron fraction Y_e . The physical conditions (s, Y_e, τ) adopted are typical for matter ejected in neutron star merger. Colored lines label the resulting abundances, black symbols refer to the solar system r -process. Beyond $Y_e \simeq 0.25$ hardly any heavy elements beyond the second r -process peak ($A = 130$) are produced. Nucleosynthesis calculations were performed with the SkyNet code (see Chapter 8). Solar r -process residuals are taken from Prantzos et al. (2020).

specific s). The most immediate way to study the various cases is based on the neutron-to-seed ratio (n_{seed}), namely the neutrons captured per seed nucleus. In this way, four classes of environments emerge:

1. $n_{\text{seed}} \sim 50$, weak r -process: it can synthesize nuclei up to $A \sim 125$;
2. $n_{\text{seed}} \sim 100$, main r -process: synthesis reaches the two abundance peaks at $A = 130$ and $A = 195$;
3. $n_{\text{seed}} \sim 150$, production of actinides.
4. $n_{\text{seed}} \sim 1000$, r -process with fission cycle: the synthesis path proceeds along the dripline until it reaches $A \sim 300$, the region in which nuclear fission is extremely efficient.

The nucleosynthesis process stops at the so-called neutron freeze-out, i.e. when $n_{\text{seed}} \simeq 1$ (see Figure 1.10). In this phase, the availability of free neutrons is

drastically reduced and this leads the β -decay timescale to become comparable and even smaller than the neutron capture's one. In the case of low-entropy environments, like in the merger of a neutron star with a black hole or the merger of two neutron stars, the n_{seed} ratio becomes essentially entropy-independent, $n_{\text{seed}} \approx A_{\text{seed}} [Z_{\text{seed}} / (A_{\text{seed}} Y_e) - 1]$ such that only very neutron-rich matter ($Y_e \lesssim 0.15$) can support a strong r -process. Figure 1.12 shows such a case of low entropies per nucleon adopting $s = 10 k_B$ baryon $^{-1}$, a typical value for matter ejected in neutron star mergers. Lanthanides are produced for $Y_e \lesssim 0.25$.

The search for an astrophysical environment suitable for the occurring of the r -process is more delicate, as the physical conditions required are extreme. There are, however, numerous theoretical candidates, even if not all of them have been equally supported by the observations. Today, the most promising candidates are thought to be associated with the birth of a neutron star (NS) in a supernova explosion or to ejecta from a compact binary merger involving a neutron star (see Cowan et al. 2019), namely:

1. neutrino-driven winds from core-collapse supernovae (CCSN);
2. neutron-rich polar jets of magneto-rotational supernovae (MHD-SNe) or accretion disk outflows of collapsars;
3. ejecta from binary neutron star mergers (BNS) or neutron star black hole (NS-BH) systems.

1.2.8 Neutron star mergers and kilonovae

Given the stringent conditions required to synthesize heavy elements up to the third r -process peak in CCSN and MHD-SNe, compact binary mergers appear to be the most favorable site for the occurrence of a full r -process nucleosynthesis. In particular, if the weak component of the r -process (up to the second r -process peak, see Roberts et al. 2010; Arcones and Montes 2011) can be produced both in CCSN and in compact binary mergers, the fission cycles that allow the synthesis up to and beyond the third r -process peak can develop only in the latter environment, thanks to the very high n_{seed} that can be achieved (see, e.g., Shibagaki et al. 2016). Even the peculiar case of MHD-SNe represents a viable astrophysical environment in which a full r -process might occur. However, for this to happen high initial magnetic fields combined with high rotation rates are needed to promptly eject neutron-rich matter. Matter later ejected can in fact experience neutrino-interactions, enhancing Y_e and weakening the strength of the r -process (see, e.g., Nishimura et al. 2017).

In a binary system of compact objects, which originated from the collapse of two massive stars, energy is released through the emission of gravitational waves. As a consequence, the loss of energy gradually shrinks the binary orbit, and the inspiral of the two compact objects ends with their merger. Numerical simulations show that, during the last phase of the coalescence, the matter is dynamically ejected on timescales of milliseconds into two components: a cold and

very neutron-rich ($Y_e \sim 0.1$) tidal ejecta mainly distributed on the orbital plane and a more isotropic shock-heated ejecta originating from the contact interface between the two objects. The former can be observed both in BNS and BH-NS systems and they are constituted by material from the tidal disruption of the neutron star. This material is not gravitationally bound to the merger remnant and is widespread in the surrounding space. The latter is typically associated with a NS-NS system. In this case the ejecta, especially at high latitudes, is subject to pair processes and neutrino irradiation from the central remnant that increase Y_e from the very low initial value. The mass of *dynamical ejecta* typically ranges from $10^{-4}M_\odot$ to $10^{-2}M_\odot$, up to $0.1M_\odot$ in the case of a BH-NS system, while the characteristic ejection speed is $0.1 - 0.3c$ (see Radice et al. 2020 for a review).

Compact binary mergers can result both in a prompt formation of a BH or a massive neutron star (MNS), which survives for a short time before collapsing in turn into a BH. Around the merger remnant, an accretion disk is formed, from which material can be ejected again. This happens when the disk inflates due to an increase of the internal energy and, consequently, the matter is no longer bound; in this case, we speak of *wind*. The main heating mechanisms of the disk are the deposition of neutrinos emitted from the surface of the central body during deleptonization, viscous friction, and α -recombination. The *neutrino-driven wind* is ejected mainly in the polar direction with velocities $v \lesssim 0.08c$ and has a moderately neutron-rich ($Y_e \gtrsim 0.25$) mass of a few $10^{-3}M_\odot$ (Perego et al. 2014). The viscous-driven ejecta (also known as *secular ejecta*) is launched in the equatorial direction with a velocity $v \sim 0.05 - 0.1c$ and contains up to 40% of the disk mass with a Y_e distribution in the range $0.1 - 0.4$, depending on the lifetime of the MNS (Lippuner et al. 2017; Fujibayashi et al. 2018). The secular ejecta is thought to constitute the bulk of the outflow since accretion disks formed from NS mergers have masses up to $\sim 0.2M_\odot$ (Radice et al. 2020).

The ejected material in the various components can undergo different r -process nucleosynthesis, depending on the electron fraction Y_e from which it is characterized. The regions where a higher neutrino deposition occurs have a higher Y_e due to the action of weak interactions. This factor inhibits a significant neutron capture, not allowing the synthesis of the heaviest elements. On the contrary, the part of ejected material with low $Y_e \lesssim 0.25$ is likely to produce a full r -process. The Y_e enhancement in the ejected material is favored if the MNS produced in the merger has a considerable lifetime before collapsing into a black hole due to prolonged neutrino irradiation. An agreement with the solar system abundance pattern has been found for MNS models with lifetimes $\lesssim 10$ ms (see, e.g., Lippuner et al. 2017). The resulting chemical composition in the ejected material is, therefore, closely related to properties of the progenitor system and the properties of the merger remnant and can be studied through the electromagnetic counterpart of the event. Moreover, the detection of an electromagnetic signal is of great importance to localize the gravitational-waves source (the gravitational-wave detectors typically enable a poor sky-localization). The host galaxy can be identified making possible studies of the source environment.

Electromagnetic signals associated with a merger of compact objects are short

gamma-ray burst and kilonova (or macronova) emission (e.g., Metzger 2019). A kilonova is an electromagnetic transient powered by the release of nuclear energy due to the radioactive decay of freshly synthesized r -process elements in the ejecta. In particular, in the case of BNS mergers, the neutron-rich matter ejected through different channels expands into space and hosts the production of radioactive heavy elements. The decay products then thermalize with the ejecta, keeping it warm. The ensuing thermal radiation escapes from the (radioactively-heated) expanding ejecta, powering the kilonova emission. In general, the peak luminosity is proportional to the quantity of radioactive isotopes synthesized, while the emission color is red or blue depending on whether the ejecta contains lanthanide/actinide nuclei or only lighter nuclei.

The first phenomenon of this kind to be observed was the electromagnetic counterpart (AT2017gfo) of the gravitational wave detection GW170817 of a BNS merger (Abbott et al. 2017a). The transient was found to be significantly less luminous and faster than that typical of supernovae. The early emission (~ 1 days) of AT2017gfo was featureless, blue, and peaked at UV frequencies (e.g., Nicholl et al. 2017; Evans et al. 2017) while, few days later, it showed a spectral peak in the optical/near-infrared (e.g., Shappee et al. 2017; Pian et al. 2017; Tanvir et al. 2017). The luminosity and bolometric light curve evolution of AT2017gfo are in agreement with the heating rate and opacity expected from a distribution of freshly synthesized r -process elements (see Metzger 2019 for a review). In addition, analyses of the AT2017gfo spectrum revealed absorption features qualitatively compatible with the forest of lines expected for matter rich in actinides and lanthanides. In particular, absorption features around 1.5 and 1.75 μm were associated with the presence of light r -process elements like Cs and Te (Smartt et al. 2017). Recently, the multi-epoch analysis of the early spectrum (especially at 1.5 days) suggested the presence of absorption lines of Sr (Watson et al. 2019). In synthesis, the observation of GW170817/AT2017gfo provided the first direct indication that r -process elements are produced in neutron-star mergers. However, as often observed in astrophysical transients also light elements can be produced giving rise to recognizable features if synthesized in a considerable amount. We investigate the production of light elements in the ejecta of binary neutron star mergers by performing extensive nucleosynthesis calculations using the publicly available nuclear network SkyNet (Lippuner and Roberts 2017, see also Section 3.2). This work is discussed in Chapter 8.

Updating stellar models

The stellar models presented in this thesis have been computed using the FUNS code (**F**ull **N**etwork **S**tellar evolution; Straniero et al. 2006; Piersanti et al. 2007; Cristallo et al. 2009) with the state of the art of the input physics available in the literature. In this section, we will briefly describe the update of the input physics. Note that much data have just recently been made available. For this reason, only the models presented in Chapter 7 have been calculated with these latest inputs. Part of these updates has been presented in Mazzone et al. (2020). The inputs used to calculate the models presented in the remaining chapters will be specified from time to time.

2.1 Equation of state, solar mixture, opacity tables, and mass loss

Solving the system of equations that defines the stellar structure requires the knowledge of the equation of state (EOS), opacity, and energy losses/gains as a function of temperature, density, and chemical composition for the typical conditions of stellar interiors. In fact, during their evolution, stars with different masses span a wide range of temperatures and densities, and thus, to compute stellar models, it is important to use an accurate EOS for the entire range of temperatures and densities covered by the calculations. The accuracy of the EOS becomes particularly important in regions characterized by partially ionized regimes. Given the complexity of the EOS computation, generally, the EOS is provided as pre-computed tables to be interpolated. In general, the calculation of EOS tables is a very delicate point in the treatment of the physics of an interacting gas, which strongly affects the theoretical predictions of stellar models. For these reasons, in its latest version, FUNS adopts two different EOS valid in different physical conditions. For $\log T$ [K] ≥ 6.5 the electron degeneracy, relativistic effects, electron-positron pair creation, and Coulomb interactions are taken into account by using the EOS for fully ionized given by Straniero (1988), in the form updated by Prada Moroni and Straniero (2002). Instead, for $\log T$

$[K] < 6.5$ the most recent version of the OPAL EOS (Rogers et al. 1996) (updated in 2005) is adopted, which at present is the most reliable, accurate, and complete equation of state available. Actually, the OPAL EOS alone is not sufficient for a correct treatment of stellar gas, since it does not allow to correctly describe high-density plasma in which electrons must be treated as degenerate particles. In addition, the OPAL EOS is calculated for mixtures of H and He with traces of heavy elements and is therefore not applicable to those evolutionary phases in which configurations where hydrogen is absent are reached, such as He, C, and O cores during RGB and AGB phases where this state equation cannot be used; in these cases the EOS as given by Straniero (1988) is more suitable.

Another important ingredient in stellar modeling is the heavy element mixture, i.e. the abundances distribution of the chemical elements heavier than helium. Usually, the heavy element distribution of the Sun is adopted for solar-metallicity stars (Population I), while for metal deficient objects a given amount of α enhancement is adopted, to take into account enrichment of the ISM due to Type II Supernovae. The adopted solar mixture affects both the radiative opacity coefficients (and so the transport of energy, see below) and the nuclear burning efficiency of stars. The Sun's composition also represent a good average composition of the elements within the entire Solar System (Lodders 2019). In this respect, because the convective envelope of the Sun is almost decoupled from the core where nuclear burning occurs, the above photosphere should give a good representative composition for the Sun (and therefore the Solar System) at the time of its formation. However, during its lifetime helium and all other heavy elements diffuse for gravitational settling from the convective zone into the solar interior (see Chapters 4 and 5). Thus the photosphere is not representative of the original proto-solar composition. In the present-day convective envelope, the heavy element abundances are about 10 – 20% lower than at the time of the Sun's formation (e.g., Bahcall et al. 1995; Piersanti et al. 2007). For this reason, the proto-solar composition is usually inferred from meteoritic measurements (e.g., Lodders 2019), except for highly volatile elements such as H, C, N, O, and noble gases. The most reliable abundances for the solar photosphere are obtained from absorption spectra which can be analyzed through detailed 3D hydrodynamical atmospheric models (Asplund et al. 2005). Instead, the abundances of noble gases like He, Ne, Ar, Kr, and Xe, which have no lines in the photospheric spectrum, can be derived from observations of coronal sources such the solar wind, solar flares, or solar energetic particles (Lodders 2019). The He abundance can be derived by SSMS (indirectly) and helioseismological observations (directly) (e.g., Christensen-Dalsgaard 2020). However, matching the seismic observations for the primordial helium abundance, which is a free parameter in the solar models, depends on the details of the SSMS (see Chapters 4 and 5). In the FUNS code, we adopt as a reference for the solar-scaled metals distribution the one given by Lodders (2019).

Also the calculation of opacity, especially in the cool outer stellar envelopes, plays an important role in stellar evolution modeling. The opacity coefficients determine the transparency level of the matter to the radiation. Indeed, photons

are continuously absorbed and re-emitted (scattered) therefore transporting energy from hotter to cooler layers. In this sense the opacity determines the mean free path of photons crossing the stellar interior and thus the resulting temperature gradient. In addition to hydrogen and helium, the opacity in the outer zones is affected by the presence of metals, and in particular to C, N, O, and Fe which are the most abundant species and allow many possible atomic transitions. The opacity is therefore strongly dependent on relative abundances of the various elements and so on the specific solar mixture adopted. Similarly to the EOS, the opacity coefficients are given as pre-computed tables, covering a wide range of densities and temperatures. In the more advanced phases (RGB and AGB) when the stellar structure develops a core with partial degenerate electrons (helium or carbon core), electron conduction becomes the predominant mechanism for energy transport and must be considered to total opacity. Conversely, in the cool external layers of stars the formation of molecules ($T \lesssim 4500 - 4000$ K), which have many absorption lines, increases the radiative opacity. In the present version of the FUNS code, we adopt the most recent version of the OPAL radiative opacity tables (see, e.g., Iglesias and Rogers 1996) released in (2005) for $\log T[\text{K}] > 4.05$. The final radiative opacity tables has then been obtained by adding the conductive opacity computed by Potekhin et al. (1999); Shternin and Yakovlev (2006). Thus, the mean opacity $\bar{\kappa}$ has the contribution of both radiative (κ_r) and conductive (κ_c) opacity, being, $1/\bar{\kappa} = 1/\kappa_r + 1/\kappa_c$. For lower temperatures ($\log T [\text{K}] \leq 4.05$), typical of the external layers of stars, we used the \mathcal{A} ESOPUS tool (Marigo and Aringer 2009) to compute the opacity tables. In this way, many continuum and discrete sources, including atomic opacities, molecular absorption bands, and collision-induced absorption are accounted for. In particular, \mathcal{A} ESOPUS allows us to take into account the chemical composition variations of the envelope. For instance, during the TP-AGB phase, at each TDU the stellar envelope is enriched with the ashes of the He-burning, mainly ^{12}C . This C dredge-up, along with the conversion of C into N due to the CNO cycle, substantially affects the molecular contribution to the opacity for temperatures lower than ~ 4000 K, leading to larger opacity coefficients which deep influence the physical evolution of AGB stars (Marigo 2002; Cristallo et al. 2007; Ventura and Marigo 2010). The present opacity tables have been calculated for the updated solar mixture of Lodders (2019) and used, along with the updated EOS, to compute a SSM (with the procedure described in Chapter 4). As a result, we obtain a value for the initial abundance of helium in the Sun of $Y = 0.267$ and a total initial metallicity of $Z = 0.0167$. Accordingly, the value of mixing length parameter is $\alpha_{\text{MLT}} = 1.86$. Such a value is adopted in the close-to-solar metallicity models presented in Chapter 7.

One of the major uncertainties in stellar evolution modeling is mass loss. Stars lose mass during their evolution at different rates. Even if for some stars the mass-loss rate is so low (like for the Sun, $10^{-14} M_{\odot} \text{ yr}^{-1}$) that can be safely neglected, this is not at all the case. For instance, in the late stage of low- and intermediate-mass stars evolution, mass loss induce important changes in the stellar properties. During the AGB phase, the helium shell periodically reignites

in semi-explosive conditions, producing large amounts of energy for a few years. Such thermal pulses are followed by convective stirrings that modify the initial composition of the envelope bringing to the surface the products of H- and He-burning. At the same time, these pulsations cause the compression of the outer atmospheric layers and the formation of molecules and dusty particles leading the star to lose mass conspicuously due to strong stellar winds (Höfner and Olofsson 2018). Such mass loss directly affects the duration of the AGB phase, the strength of the pulse, and the efficiency of the TDU (see Straniero et al. 2006; Karakas and Lattanzio 2014; Ventura et al. 2015 for detailed discussions). The available observational data indicate that the AGB mass-loss rate spans from $10^{-8} M_{\odot} \text{ yr}^{-1}$ for Mira variables up to $10^{-4} M_{\odot} \text{ yr}^{-1}$ for the “superwind” phase during which the H-envelope is rapidly eroded. For the practical purposes of stellar evolution computations, the effect of mass loss is usually included by means of empirical or semi-empirical formulae. In particular, the AGB mass-loss rate can be estimated from the observational correlation with the pulsation period (e.g., Vassiliadis and Wood 1993). In FRUITY models (Straniero et al. 2006), the mass-loss law was obtained by fitting the mass-loss rate versus period for a sample of Galactic O-rich and C-rich giants. The stellar period is computed employing the relation between absolute magnitude and period provided by Whitelock et al. (2003). The absolute magnitude is derived from the bolometric magnitude of the model and a K-band bolometric correction (BC_K) vs T_{eff} relation. In this work we have adopted the new fit given by Abia et al. (2020), who considered an updated T_{eff} dataset of O-rich red giants from Buzzoni et al. (2010) and a new BC_K vs T_{eff} relation. For $T_{\text{eff}} < 3500 \text{ K}$, the new relation implies a reduction of the mass-loss rate and therefore a longer C-rich phase for AGB models (see Abia et al. 2020 for a detailed discussion).

2.2 Nuclear network

The calculation of nuclear processes in stellar plasma is another fundamental aspect for the integration of a stellar model: in addition to defining the energy generated and thus establishing the balance of a stellar structure, nuclear reactions are also responsible for the chemical evolution of the star. The current version of FUNS code can follow the chemical evolution of almost 500 isotopes (from hydrogen to bismuth) linked by more than 700 reactions (charged particle reactions, neutron captures, and β -decays). The baseline nuclear network is essentially the same already described in Cristallo et al. (2009) with the inclusion of some recent updated reaction rates. All the updated charged particle reactions and neutron capture reactions are shown in Table 2.1 and Table 2.2, respectively. In addition, (n, γ) reaction rates for ^{61}Ni , ^{74}Se , ^{79}Kr , ^{81}Kr , ^{83}Kr , ^{84}Sr , ^{93}Nb , ^{94}Nb , ^{103}Rh , ^{109}Ag , ^{119}Sn , ^{121}Sn , ^{122}Sb , ^{125}Te , ^{129}I , ^{129}Xe , ^{142}Pr , ^{147}Pm , ^{151}Eu , ^{152}Eu , ^{153}Eu , ^{154}Eu , ^{158}Gd , ^{158}Dy , ^{169}Tm , ^{171}Tm , ^{170}Yb , ^{181}Hf , ^{181}Ta , ^{182}Ta , ^{182}W , ^{183}W , ^{189}Os , ^{192}Ir , ^{193}Ir , ^{193}Pt , ^{205}Pb , and ^{210}Bi have been recomputed by using the updated *Stellar Enhancement Factor* (SEF, see e.g. Bao et al. 2000) from KADoNiS v0.3

Table 2.1: Updated charged particle reactions included in the nuclear network of FUNS.

Reaction	Reference	Reaction	Reference
${}^7\text{Li}(p, \alpha){}^4\text{He}$	1	${}^{26}\text{Al}^g(p, \gamma){}^{27}\text{Si}$	5
${}^{15}\text{N}(p, \gamma){}^{16}\text{O}$	2	${}^{27}\text{Al}(p, \gamma){}^{28}\text{Si}$	5
${}^{17}\text{O}(p, \gamma){}^{18}\text{F}$	3	${}^{27}\text{Al}(p, \alpha){}^{24}\text{Mg}$	5
${}^{17}\text{O}(p, \alpha){}^{14}\text{N}$	4	${}^4\text{He}(2\alpha, \gamma){}^{12}\text{C}$	14
${}^{14}\text{C}(p, \gamma){}^{15}\text{N}$	5	${}^{12}\text{C}(\alpha, \gamma){}^{16}\text{O}$	15
${}^{18}\text{O}(p, \gamma){}^{19}\text{F}$	6	${}^{13}\text{C}(\alpha, n){}^{16}\text{O}$	16
${}^{18}\text{O}(p, \alpha){}^{15}\text{N}$	7	${}^{14}\text{C}(\alpha, \gamma){}^{18}\text{O}$	17
${}^{19}\text{F}(p, \alpha){}^{16}\text{O}$	8	${}^{14}\text{N}(\alpha, \gamma){}^{18}\text{F}$	5
${}^9\text{Be}(p, \alpha){}^6\text{Li}$	9	${}^{16}\text{O}(\alpha, \gamma){}^{20}\text{Ne}$	18
${}^{10}\text{B}(p, \alpha){}^7\text{Be}$	9	${}^{18}\text{O}(\alpha, \gamma){}^{22}\text{Ne}$	5
${}^{20}\text{Ne}(p, \gamma){}^{21}\text{Na}$	5	${}^{22}\text{Ne}(\alpha, n){}^{25}\text{Mg}$	19
${}^{21}\text{Ne}(p, \gamma){}^{22}\text{Na}$	5	${}^{22}\text{Ne}(\alpha, \gamma){}^{26}\text{Mg}$	19
${}^{22}\text{Ne}(p, \gamma){}^{23}\text{Na}$	10	${}^{14}\text{N}(\alpha, p){}^{17}\text{O}$	20
${}^{22}\text{Na}(p, \gamma){}^{23}\text{Mg}$	11	${}^{15}\text{N}(\alpha, \gamma){}^{19}\text{F}$	5
${}^{23}\text{Na}(p, \gamma){}^{24}\text{Mg}$	12	${}^{17}\text{O}(\alpha, \gamma){}^{21}\text{Ne}$	21
${}^{23}\text{Na}(p, \alpha){}^{20}\text{Ne}$	5	${}^{17}\text{O}(\alpha, n){}^{20}\text{Ne}$	21
${}^{24}\text{Mg}(p, \gamma){}^{25}\text{Al}$	5	${}^{18}\text{O}(\alpha, n){}^{21}\text{Ne}$	22
${}^{25}\text{Mg}(p, \gamma){}^{26}\text{Al}^g$	13	${}^{19}\text{F}(\alpha, p){}^{22}\text{Ne}$	23
${}^{25}\text{Mg}(p, \gamma){}^{26}\text{Al}^m$	13	${}^{20}\text{Ne}(\alpha, \gamma){}^{24}\text{Mg}$	5
${}^{26}\text{Mg}(p, \gamma){}^{27}\text{Al}$	5	${}^{24}\text{Mg}(\alpha, \gamma){}^{28}\text{Si}$	5

References. (1) Lamia et al. (2012); (2) LeBlanc et al. (2010); (3) Di Leva et al. (2014); (4) Bruno et al. (2016); (5) Iliadis et al. (2010); (6) Best et al. (2019); (7) Bruno et al. (2019); (8) Indelicato et al. (2017); (9) Lamia et al. (2015); (10) Depalo et al. (2016); (11) Sallaska et al. (2013); (12) Cesaratto et al. (2013); (13) Straniero et al. (2013); (14) Angulo et al. (1999); (15) Kunz et al. (2002); (16) Trippella and La Cognata (2017); (17) Johnson et al. (2009); (18) Costantini et al. (2010); (19) Adsley et al. (2020); (20) Buckner et al. (2015); (21) Best et al. (2013); (22) Best et al. (2013); (23) D’Agata et al. (2018).

(Dillmann et al. 2009). The β -decay rate for ${}^{60}\text{Fe}$ is from Rugel et al. (2009). The ${}^{60}\text{Fe}(n, \gamma)$ cross section is from Uberseder et al. (2009) renormalized to take into account the new half-life of ${}^{60}\text{Fe}$ from Rugel et al. (2009). For ${}^7\text{Be}$ electron-capture rate we use that computed by Simonucci et al. (2013) (see also Chapter 4).

2.3 The ${}^{13}\text{C}$ pocket formation

The surface enrichment of C- and *s*-process elements AGB stars is related to the complex coupling between convective mixing and nuclear processes. The problem of the source of neutrons in AGB stars, and in particular the physical process driving the formation of a ${}^{13}\text{C}$ pocket in the He-rich and ${}^{12}\text{C}$ -rich intershell is still

Table 2.2: Updated neutron capture reactions included in the nuclear network of FUNS.

Reaction	Reference	Reaction	Reference	Reaction	Reference
$^{13}\text{C}(n, \gamma)^{14}\text{C}$	1	$^{79}\text{Br}(n, \gamma)^{80}\text{Br}$	23	$^{174}\text{Hf}(n, \gamma)^{175}\text{Hf}$	41
$^{14}\text{N}(n, p)^{14}\text{C}$	1	$^{81}\text{Br}(n, \gamma)^{82}\text{Br}$	23	$^{176}\text{Hf}(n, \gamma)^{177}\text{Hf}$	42
$^{17}\text{O}(n, \alpha)^{14}\text{C}$	2	$^{78}\text{Kr}(n, \gamma)^{79}\text{Kr}$	24	$^{177}\text{Hf}(n, \gamma)^{178}\text{Hf}$	42
$^{19}\text{F}(n, \gamma)^{20}\text{F}$	3	$^{80}\text{Kr}(n, \gamma)^{81}\text{Kr}$	24	$^{178}\text{Hf}(n, \gamma)^{179}\text{Hf}$	42
$^{20}\text{Ne}(n, \gamma)^{21}\text{Ne}$	4	$^{84}\text{Kr}(n, \gamma)^{85}\text{Kr}$	24	$^{179}\text{Hf}(n, \gamma)^{180}\text{Hf}$	42
$^{21}\text{Ne}(n, \gamma)^{22}\text{Ne}$	4	$^{84}\text{Kr}(n, \gamma)^{85}\text{Kr}$	24	$^{180}\text{Hf}(n, \gamma)^{181}\text{Hf}$	42
$^{22}\text{Ne}(n, \gamma)^{23}\text{Ne}$	4	$^{86}\text{Kr}(n, \gamma)^{87}\text{Kr}$	24	$^{182}\text{Hf}(n, \gamma)^{183}\text{Hf}$	41
$^{23}\text{Na}(n, \gamma)^{24}\text{Na}$	5	$^{85}\text{Rb}(n, \gamma)^{86}\text{Rb}$	23	$^{180}\text{W}(n, \gamma)^{181}\text{W}$	38
$^{24}\text{Mg}(n, \gamma)^{25}\text{Mg}$	6	$^{87}\text{Rb}(n, \gamma)^{88}\text{Rb}$	23	$^{184}\text{W}(n, \gamma)^{185}\text{W}$	43
$^{25}\text{Mg}(n, \gamma)^{26}\text{Mg}$	7	$^{88}\text{Sr}(n, \gamma)^{89}\text{Sr}$	25	$^{186}\text{W}(n, \gamma)^{187}\text{W}$	43
$^{26}\text{Mg}(n, \gamma)^{27}\text{Mg}$	6	$^{89}\text{Y}(n, \gamma)^{90}\text{Y}$	26	$^{184}\text{Os}(n, \gamma)^{185}\text{Os}$	38
$^{35}\text{Cl}(n, \gamma)^{36}\text{Cl}$	8	$^{90}\text{Zr}(n, \gamma)^{91}\text{Zr}$	27	$^{186}\text{Os}(n, \gamma)^{187}\text{Os}$	44
$^{40}\text{Ar}(n, \gamma)^{41}\text{Ar}$	9	$^{91}\text{Zr}(n, \gamma)^{92}\text{Zr}$	28	$^{187}\text{Os}(n, \gamma)^{188}\text{Os}$	44
$^{41}\text{K}(n, \gamma)^{42}\text{K}$	10	$^{92}\text{Zr}(n, \gamma)^{93}\text{Zr}$	29	$^{188}\text{Os}(n, \gamma)^{189}\text{Os}$	44
$^{40}\text{Ca}(n, \gamma)^{41}\text{Ca}$	11	$^{93}\text{Zr}(n, \gamma)^{94}\text{Zr}$	30	$^{190}\text{Os}(n, \gamma)^{191}\text{Os}$	39
$^{45}\text{Sc}(n, \gamma)^{46}\text{Sc}$	10	$^{94}\text{Zr}(n, \gamma)^{95}\text{Zr}$	31	$^{192}\text{Os}(n, \gamma)^{193}\text{Os}$	39
$^{54}\text{Fe}(n, \gamma)^{55}\text{Fe}$	12	$^{96}\text{Zr}(n, \gamma)^{97}\text{Zr}$	32	$^{190}\text{Pt}(n, \gamma)^{191}\text{Pt}$	38
$^{58}\text{Fe}(n, \gamma)^{59}\text{Fe}$	13	$^{96}\text{Ru}(n, \gamma)^{97}\text{Ru}$	33	$^{192}\text{Pt}(n, \gamma)^{193}\text{Pt}$	45
$^{59}\text{Co}(n, \gamma)^{60}\text{Co}$	13	$^{102}\text{Ru}(n, \gamma)^{103}\text{Ru}$	33	$^{194}\text{Pt}(n, \gamma)^{195}\text{Pt}$	45
$^{58}\text{Ni}(n, \gamma)^{59}\text{Ni}$	14	$^{104}\text{Ru}(n, \gamma)^{105}\text{Ru}$	33	$^{195}\text{Pt}(n, \gamma)^{196}\text{Pt}$	45
$^{60}\text{Ni}(n, \gamma)^{61}\text{Ni}$	15	$^{102}\text{Pd}(n, \gamma)^{103}\text{Pd}$	34	$^{196}\text{Pt}(n, \gamma)^{197}\text{Pt}$	45
$^{62}\text{Ni}(n, \gamma)^{63}\text{Ni}$	16	$^{120}\text{Te}(n, \gamma)^{121}\text{Te}$	34	$^{198}\text{Pt}(n, \gamma)^{199}\text{Pt}$	32
$^{63}\text{Ni}(n, \gamma)^{64}\text{Ni}$	17	$^{130}\text{Ba}(n, \gamma)^{131}\text{Ba}$	34	$^{197}\text{Au}(n, \gamma)^{198}\text{Au}$	46
$^{64}\text{Ni}(n, \gamma)^{65}\text{Ni}$	13	$^{132}\text{Ba}(n, \gamma)^{133}\text{Ba}$	34	$^{196}\text{Hg}(n, \gamma)^{197}\text{Hg}$	38
$^{63}\text{Cu}(n, \gamma)^{64}\text{Cu}$	18	$^{139}\text{La}(n, \gamma)^{140}\text{La}$	35	$^{202}\text{Hg}(n, \gamma)^{203}\text{Hg}$	39
$^{65}\text{Cu}(n, \gamma)^{66}\text{Cu}$	19	$^{151}\text{Sm}(n, \gamma)^{152}\text{Sm}$	36	$^{204}\text{Hg}(n, \gamma)^{205}\text{Hg}$	39
$^{64}\text{Zn}(n, \gamma)^{65}\text{Zn}$	20	$^{154}\text{Gd}(n, \gamma)^{155}\text{Gd}$	37	$^{204}\text{Pb}(n, \gamma)^{205}\text{Pb}$	47
$^{70}\text{Zn}(n, \gamma)^{71}\text{Zn}$	20	$^{156}\text{Dy}(n, \gamma)^{157}\text{Dy}$	34	$^{206}\text{Pb}(n, \gamma)^{207}\text{Pb}$	48
$^{73}\text{Ge}(n, \gamma)^{74}\text{Ge}$	21	$^{168}\text{Yb}(n, \gamma)^{169}\text{Yb}$	38	$^{207}\text{Pb}(n, \gamma)^{208}\text{Pb}$	49
$^{74}\text{Ge}(n, \gamma)^{75}\text{Ge}$	22	$^{174}\text{Yb}(n, \gamma)^{175}\text{Yb}$	39	$^{209}\text{Bi}(n, \gamma)^{210}\text{Bi}$	50
$^{76}\text{Ge}(n, \gamma)^{77}\text{Ge}$	22	$^{176}\text{Yb}(n, \gamma)^{177}\text{Yb}$	39		
$^{75}\text{As}(n, \gamma)^{76}\text{As}$	22	$^{176}\text{Lu}(n, \gamma)^{177}\text{Lu}$	40		

References. (1) Wallner et al. (2016); (2) Guardo et al. (2017); (3) Uberseder et al. (2007); (4) Heil et al. (2014); (5) Uberseder et al. (2017); (6) Massimi et al. (2012); (7) Massimi et al. (2017); (8) Pavetich et al. (2019); (9) Beer et al. (2002); (10) Heil et al. (2016); (11) Dillmann et al. (2009); (12) Wallner et al. (2017); (13) Heil et al. (2008b); (14) Žugec et al. (2014); (15) Guber et al. (2010); (16) Lederer et al. (2015); (17) Lederer et al. (2013); (18) Weigand et al. (2017); (19) Prokop et al. (2019); (20) Reifarh et al. (2012); (21) Lederer-Woods et al. (2019); (22) Marganiec et al. (2009b); (23) Heil et al. (2008a); (24) Tessler et al. (in preparation); (25) Koehler et al. (2000); (26) Tagliente et al. (in preparation); (27) Tagliente et al. (2008a); (28) Tagliente et al. (2008b); (29) Tagliente et al. (submitted); (30) Tagliente et al. (2013); (31) Tagliente et al. (2011b); (32) Tagliente et al. (2011a); (33) Rapp et al. (2002); (34) Dillmann et al. (2010); (35) Terlizzi et al. (2007); (36) Marrone et al. (2006); (37) Mazzone et al. (2020); (38) Marganiec et al. (2010); (39) Marganiec et al. (2014); (40) Roig et al. (2016); (41) Vockenhuber et al. (2007); (42) Wisshak et al. (2006); (43) Marganiec et al. (2009a); (44) Mosconi et al. (2010); (45) Koehler and Guber (2013); (46) Massimi et al. (2014); (47) Domingo-Pardo et al. (2007a); (48) Domingo-Pardo et al. (2007b); (49) Domingo-Pardo et al. (2006b); (50) Domingo-Pardo et al. (2006a).

a matter of debate (see Section 1.2.5). In past FRUITY models, the partial mixing of hydrogen from the envelope necessary to produce fresh ^{13}C is accounted for by the so-called *opacity-induced overshoot* (Straniero et al. 2006; Cristallo et al. 2009). According to the MLT, the average convective velocity (v_c) is proportional to the difference between the radiative (∇_{rad}) and the adiabatic (∇_{ad}) temperature gradients. This quantity abruptly drops to 0 at the convective boundary and so the average velocity. Actually, some convective plumes may penetrate the radiative stable layer, thus producing some extra-mixing. During a TDU the envelope (H-rich) is more opaque than the underlying H-exhausted (and He-rich) region. Because of this sharp chemical gradient, $\nabla_{\text{rad}} - \nabla_{\text{ad}} > 0$ at the inner border of the convective envelope, so that the average vertical velocity of the plumes is $v_c \gg 0$ and the convective border becomes unstable. This scenario can be simply seen as the convective plumes, pushed by their inertia, overshoot beyond the formal Schwarzschild border. The opacity-induced overshoot powers an extra-mixing and a formation of a chemically smooth transition zone between the fully convective envelope and the radiative region. In FUNS, the mixing exerted by convective overshooting is calculated by solving a time-dependent mixing equation as in Chieffi et al. (2001); Straniero et al. (2006), in which the average convective velocity is calculated according to the mixing-length theory (Cox and Giuli 1968). The convective boundary is determined according to the Schwarzschild criterion. At the inner border of the convective envelope, the velocity of the descending material accelerated by convection is estimated as

$$v = v_{\text{cb}} \exp\left(-\frac{\delta r}{\beta H_P}\right), \quad (2.1)$$

where v_{cb} is the velocity at the convective border, δr is the distance from the border, H_P is the pressure scale height at the convective border, and β is a free parameter whose value is set to 0.1 (see Cristallo et al. 2009; Guandalini and Cristallo 2013 for more details).

In this work, we consider mixing triggered by magnetic fields as the mechanism responsible for the formation of the ^{13}C pocket (see Chapter 7). In particular, the *magnetic-buoyancy-induced* mixing is implemented in the FUNS hydrostatic stellar evolutionary code, starting from the treatment of magnetic buoyancy given by Nucci and Busso (2014). In the Nucci and Busso (2014) magnetic buoyancy model, it is assumed that a toroidal magnetic field is present in the radiative zone of an RGB/AGB low-mass star. Here we assume that a toroidal field is present in the radiative He-intershell at the beginning of the TDU and triggers the buoyant rise of magnetic flux tubes (see also Trippella et al. 2016). As a consequence, a matter flow is pushed to the envelope. This induces, for mass conservation, a matter downflow of H-rich material to He-intershell. To derive the downflow velocity profile, we hypothesize that a magnetic flux torus, of radius $a(r_p)$, which formed in the He-intershell region due to the kink-mode buoyancy instability, starts to buoy at a distance r_p from the stellar center and reaches the H-rich material of the envelope at r_h . Its volume is $V(r_p) = 2\pi^2 a^2(r_p) r_p$. For the mass conservation within the flux tube (isolated matter) $\rho(r_p)V(r_p) = \rho(r_h)V(r_h)$, one

has

$$\rho(r_h) = \rho(r_p) \frac{V(r_p)}{V(r_h)} = \rho(r_p) \frac{a^2(r_p) r_p}{a^2(r_h) r_h}. \quad (2.2)$$

From the magnetic flux conservation one derives

$$\frac{B_\varphi(r_h)}{B_\varphi(r_p)} = \frac{a^2(r_p)}{a^2(r_h)}. \quad (2.3)$$

If the density of radiative layers below the convective envelope of an evolved star drops with the radius as a power law (i.e. $\rho(r) \propto r^k$, with an exponent k that is negative and has a modulus larger than unity), then the toroidal magnetic field can be expressed as $B_\varphi(r) = B_\varphi(r_p)(r/r_p)^{k+1}$ (see Appendix in Nucci and Busso 2014). From Equation (2.3), it follows that

$$\frac{B_\varphi(r_h)}{B_\varphi(r_p)} = \frac{a^2(r_p)}{a^2(r_h)} = \left(\frac{r_h}{r_p}\right)^{k+1}. \quad (2.4)$$

Thus Equation (2.2) becomes

$$\rho(r_h) = \rho(r_p) \left(\frac{r_h}{r_p}\right)^k. \quad (2.5)$$

If we consider that the magnetized regions will occupy a fraction $f(r)$ of the total mass of a stellar layer of radius r (Trippella et al. 2016), the rate of the total rising mass is $\dot{M}(r_p) = 4\pi r_p^2 \rho(r_p) v(r_p) f(r_p)$. Let's assume that the velocity of the rising flux tubes varies as (Nucci and Busso 2014)

$$v(r) = v(r_p) \left(\frac{r_p}{r}\right)^{k+1}. \quad (2.6)$$

Then, the mass flow at r_h would be

$$\dot{M}(r_h) = 4\pi r_h^2 \rho(r_h) v(r_h) f(r_h) = 4\pi r_h^2 \rho(r_p) \left(\frac{r_h}{r_p}\right)^k v(r_p) \left(\frac{r_p}{r_h}\right)^{k+1} f(r_h). \quad (2.7)$$

Being the rising mass conserved in its upward motion ($\dot{M} = \text{constant}$), this implies that $r \cdot f(r) = \text{constant}$, and therefore

$$f(r_h) = f(r_p) r_p / r_h. \quad (2.8)$$

Maintaining mass conservation across the envelope requires that $v(r_h) f(r_h) = v_d$, where $v(r_h)$ is the velocity of the buoyant flux tubes at r_h , and v_d is the initial velocity of envelope material injected into the He-rich layers. From Equations (2.5), (2.6), and (2.8), one obtains

$$v_d = v(r_p) f(r_p) \left(\frac{r_p}{r_h}\right)^{k+2}. \quad (2.9)$$

Since the density of radiative layers below the convective envelope has a density distribution of the form $\rho(r) \propto r^k$, considering mass conservation, it is possible to write the velocity dependency on the radius as $v_d(r) = v_d(r_h/r)^{k+2}$. We finally derive

$$v_d(r) = u_p \left(\frac{r_p}{r} \right)^{k+2}, \quad (2.10)$$

where we set $u_p \equiv v(r_p)f(r_p)$.

The updated input physics parameter, network, and mixing algorithm described in this chapter were used to calculate the evolutionary sequence of $2 M_\odot$ ad close-to-solar metallicity presented in Chapter 7.

s- and *r*-process data at the n_TOF facility

Nuclear astrophysics is an interdisciplinary field at the crossing of various branches, from experimental and theoretical studies of nuclear cross sections to stellar evolutionary models of high complexity. The physics of stellar interiors can be constrained only if the adopted inputs in stellar modeling are known with high accuracy. For the nucleosynthesis of heavy elements, neutron capture cross sections and neutron-induced fission cross section are among the major sources of uncertainty and, thus, any improvement in their estimates represents a progress toward a better comprehension of stellar processes. At the n_TOF facility at CERN (Guerrero et al. 2013), data on neutron-induced reactions for nuclear astrophysics have been collected for almost two decades. A wealth of important results has been obtained so far, both on capture and on fission reactions. The experimental program aims at determining and improving cross sections for several isotopes relevant to *s*- and *r*-process nucleosynthesis.

3.1 *s*-process capture measurements

The key nuclear physics quantity for *s*-process modeling is the Maxwellian-averaged capture cross section (MACS). At n_TOF, the experimental determination of the MACS is performed with the Time-of-flight technique by measuring the energy-dependent capture cross section $\sigma_\gamma(E)$. The MACS then is obtained by folding it with the neutron energy distribution, thus enabling the determination of the MACS as a function of the temperature. Many studies were carried out at n_TOF, about the role of branch-point isotopes, *s*-only isotopes, bottlenecks in the *s*-process path (see Section 1.2.5) and neutron source reactions.

Despite their importance, some few measurements of (n,γ) cross sections on unstable isotopes are present in literature in the energy region of interest. For instance, among the 21 relevant cases (Käppeler et al. 2011) only 8 isotopes have been studied so far. And among them, the cross section of 5 isotopes has been

measured as a function of neutron energy via time-of-flight at n_TOF. The results of $^{151}\text{Sm}(n,\gamma)$ and $^{171}\text{Tm}(n,\gamma)$ provided new information for the characterization of the pulsed *s*-process nucleosynthesis in AGB stars and for the production of ^{171}Yb (Marrone et al. 2006; Guerrero et al. 2020). (n,γ) cross section measurements for ^{62}Ni and ^{63}Ni , supplied new details on the production of ^{63}Cu , ^{64}Ni , and ^{65}Zn in massive stars (Lederer et al. 2013, 2015). The preliminary results of the isotopes with half-lives of a few years, i.e. ^{147}Pm and ^{204}Tl , indicate that their capture cross sections are smaller than theoretical predictions and therefore important consequences are expected. For the future, the n_TOF collaboration is preparing the detector setup for the measurement campaign on the branching at ^{79}Se , which can constrain the temperature of the *s*-process nucleosynthesis in massive stars, and at ^{94}Nb , with interesting consequences for the galactic production of ^{94}Mo .

The particularly stable configuration of nuclei with a magic number of neutrons ($N = 50, 82$ and 126) strongly reduce their neutron capture cross sections. As a consequence, the *s*-process distributions around those isotopes present peaks. The three peaks of the *s*-process are in correspondence of Sr-Y-Zr ($N = 50$), Ba-La-Ce-Pr-Nd ($N = 82$) and Pb ($N = 126$) (see discussion in Section 1.2.5). At the n_TOF facility, neutron capture cross section on some of those isotopes have already been measured, i.e. ^{90}Zr (Tagliente et al. 2008a) and ^{139}La (Terlizzi et al. 2007). Others are currently under analysis (^{88}Sr , ^{89}Y and ^{140}Ce). The latter, whose *n* capture cross will be soon published, is of particular interest to understand the origin of heavy elements in globular clusters belonging to our galaxy (Straniero et al. 2014).

3.1.1 *s*-only isotopes: the case of ^{154}Gd

There is a class of isotopes which completely owe their production to the *s*-process, since they are shielded by their stable isobars from the *r*-process contribution (see Section 1.2.5). Those nuclei, named *s*-only, are extremely helpful to calibrate *s*-process nucleosynthesis theoretical models. In fact, the latter must fulfill the condition to obtain a flat distribution of *s*-only isotopes for the solar distribution (see, e.g., Cristallo et al. 2015a; Prantzos et al. 2018). Among the isotopes with larger theoretical discrepancies, we list ^{134}Ba , ^{136}Ba , ^{152}Gd and ^{154}Gd . The latter has been recently measured at n_TOF, with new experimental values sensibly different from the literature (Mazzone et al. 2020). A new determination of the ^{154}Gd neutron capture cross section was motivated by a discrepancy between stellar models and observations, as highlighted by Cristallo et al. (2015a) and confirmed by Prantzos et al. (2020), where a lower theoretical $^{154}\text{Gd}/^{150}\text{Sm}$ ratio with respect to that measured in the Sun (and derived for the early-solar system) was found. In fact, theoretical values, which include yields from the Asymptotic Giant Branch (AGB) phase of low- and intermediate-mass stars (taken from the FRUITY database of AGB star nucleosynthesis (Cristallo et al. 2011, 2015b), show an underproduction of ^{154}Gd with respect to ^{150}Sm : $^{154}\text{Gd}/^{150}\text{Sm} = 0.70$. As a consequence, one can argue that a reason for the disagreement should be attributed to problems in the cross section of ^{154}Gd itself.

The use of the present cross section leads to an increase of the theoretical solar ^{154}Gd abundance by 10% on average¹. The difference in the ^{154}Gd surface abundances is lower than the change of the neutron capture cross sections (on average 15% compared to KaDoNiS v0.3). This is because the ^{154}Gd production/destruction strongly depends on the branching at ^{154}Eu , which is an unstable isotope (its decay lifetime in the terrestrial condition is 8.6 y). This branching is by-passed when the major neutron source in AGB stars (the $^{13}\text{C}(\alpha, n)^{16}\text{O}$ reaction) is activated, due to its short lifetime for the timescale characterizing neutron captures in this regime. The situation may be different during thermal pulses when the higher temperature can efficiently activate the $^{22}\text{Ne}(\alpha, n)^{25}\text{Mg}$ neutron source (which produces a definitely higher neutron flux). In such a case, the neutron capture channel is competitive compared to the β -decay channel and, as a consequence, the main s -process path may by-pass ^{154}Gd . The delicate balance between neutron captures on ^{154}Gd and β -decays from ^{154}Eu determines the final abundance of ^{154}Gd .

In summary, the present experimental value leads to a better agreement between model calculations and observations, although it is not able to completely remove the mismatch. In 2009, Lodders and collaborators (Lodders and Palme 2009) estimated the uncertainty in the determination of the solar gadolinium abundance to be $\pm 15\%$ (and $\pm 5\%$ for samarium). The adoption of the present ^{154}Gd neutron capture cross section, eventually leads to a new $^{154}\text{Gd}/^{150}\text{Sm}$ ratio of 0.77 in FRUITY models. When taking into consideration the lower limit of the present neutron capture cross section, we obtain $^{154}\text{Gd}/^{150}\text{Sm} \sim 0.81$. As a consequence, the ratios obtained in FRUITY models are now compatible with the observed abundances, within observational uncertainties ($\pm 20\%$).

When the present cross section is used in the models by Trippella et al. (2014, 2016), it is interesting to notice that while the discrepancy with respect to ^{142}Nd , ^{148}Sm and ^{152}Gd is completely erased (due to the larger production of ^{154}Gd), at the same time, the ratio $^{154}\text{Gd}/^{150}\text{Sm}$ attains a value (1.15) consistent with observations, within uncertainties. In general, it appears that the approach in Trippella et al. (2016) produces a flatter distribution of s -process isotopes, although this was obtained in post-process computations and not in full stellar models. Therefore, a clear suggestion emerging from the present $^{154}\text{Gd}(n, \gamma)$ cross section measurement is that some of the remaining model ambiguities might be solved by a merging of the mixing approaches presented in FRUITY and Trippella et al. (2016) (see Chapter 7 for more details).

Another important outcome from this combined experimental and theoretical study is related to the ^{154}Gd abundance, which largely depends on the branching at ^{154}Eu . For this isotope, no experimental data are available for both the neutron capture cross section and the temperature-dependent β -decay rate. Therefore, s -process calculations are based on purely theoretical estimations (see Rauscher and Thielemann 2000 and Takahashi and Yokoi (1987), respectively). A lower

¹Note that only a limited number of AGB models have been investigated with the present cross section. The evaluation of the effect in a full GCE model will be published separately.

$^{154}\text{Eu}(n,\gamma)$ cross section or a faster $^{154}\text{Eu}(\beta^-)^{154}\text{Gd}$ decay would lead to a larger ^{154}Gd surface abundance with respect to ^{150}Sm (and vice-versa). Therefore, the present result suggests that additional efforts should be spent in this direction from the experimental side, to provide experimental values as detailed as possible to stellar modelers.

3.2 r -process fission measurements

Neutron-induced fission reactions play a crucial role in a variety of fields of fundamental and applied nuclear science. In basic nuclear physics, they provide important information on properties of nuclear matter, while in nuclear technology they are at the basis of present and future reactor designs. Finally, there is a renewed interest in fission reactions in nuclear astrophysics due to the multi-messenger observation of neutron star mergers and the important role played by fission recycling in r -process nucleosynthesis (see Section 1.2.7). Although studied for several decades, many fundamental questions still remain on fission reactions, while modern applications and the development of more reliable nuclear models require high-accuracy and consistent experimental data on fission cross sections and other fission observables. To address these needs, an extensive fission research program has been carried out at the n_TOF neutron time-of-flight facility at CERN during the last 18 years, taking advantage of the high energy resolution, high luminosity and wide energy range of the neutron beam, as well as of the detection and data acquisition systems designed for this purpose. While long-lived isotopes are studied on the 185 m long flight-path, the recent construction of a second experimental area at a distance of about 19 m paved the way to challenging measurements of short-lived actinides.

In explosive scenarios like NSMs, the extremely high neutron densities available lead to the formation of nuclei heavier than iron, all the way up to unstable actinides. Spontaneous, β -delayed and, to a lesser extent, neutron-induced fission of these actinides produce fission fragments that in turn act as seeds for a new cycle of rapid neutron capture reactions. This process, referred to as "fission recycling", is predicted to play an important role in shaping the r -process abundance distribution of heavy elements. The effect of fission recycling is illustrated in Figure 3.1, which shows the final abundances expected from an expanding material that experiences r -process nucleosynthesis. The calculations have been performed with the SkyNet code (Lippuner and Roberts 2017) with a reasonable value of the electron fraction Y_e of 0.1 (such value is representative of neutron-rich matter, as the one dynamically ejected from a NSM event). Compared with the observed solar system r -process abundances (Goriely 1999), the calculation clearly demonstrates the fundamental role of fission recycling, generally believed to be responsible for an important component of the observed r -process heavy element abundances.

The r -process nucleosynthesis is computed by means of theoretical models that couple the physical evolution of the environment to a very large nuclear

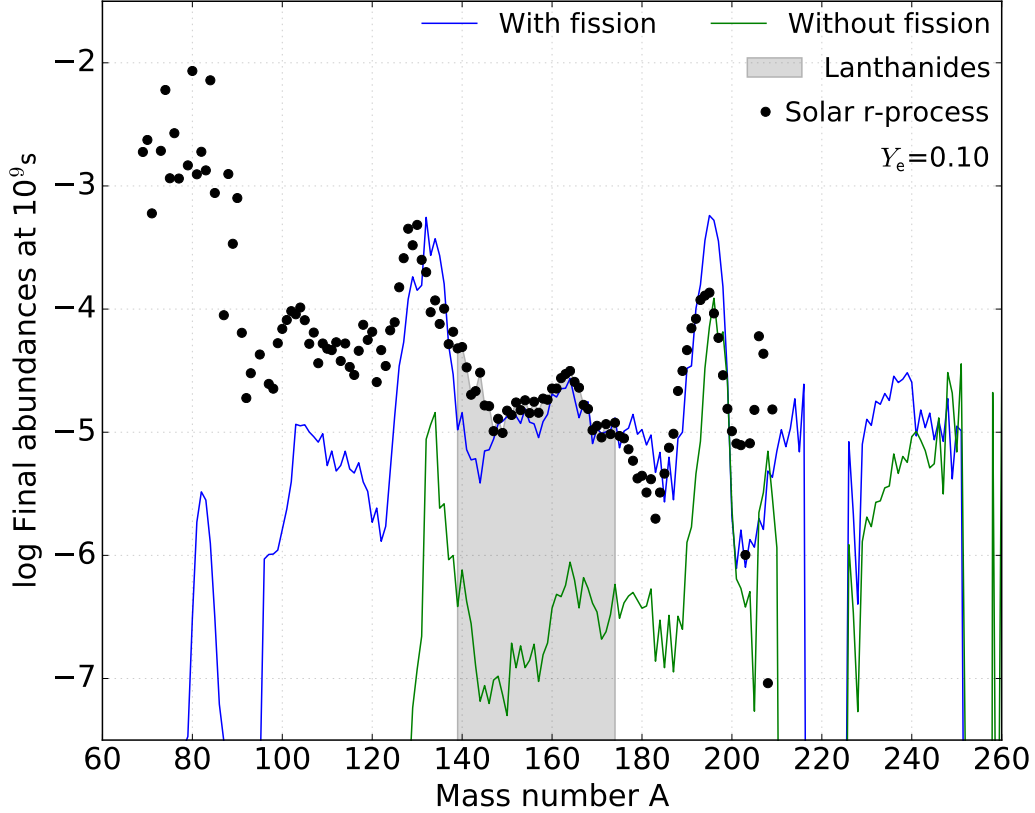


Figure 3.1: The r -process abundances in the solar system (solid symbols) are compared to SkyNet calculations performed assuming an electron fraction $Y_e = 0.1$, with and without fission recycling. Fission processes are fundamental to reproduce the observed abundance distribution, in particular in the peak at $A \sim 130$ and in the lanthanides region (shaded area).

network (see for example Goriely and Martínez Pinedo 2015; Eichler et al. 2015; Shibagaki et al. 2016; Mumpower et al. 2018). The calculations of the various nucleosynthesis processes at play during those powerful events require detailed and reliable nuclear inputs. In particular, fission recycling relies on the fission rates and the mass distribution of fission fragments for a number of heavy and highly unstable actinides. Current efforts aim at refining those nuclear models so that they can provide a comprehensive and self-consistent description of the fission process, and can be used by stellar modelers to predict the behavior of super-heavy actinides. Research activity is concentrating on the optimization of various nuclear physics parameters, such as fission barriers, nuclear level densities etc., that are at the basis of most fission models. In this respect, new fission data on a variety of actinides are needed, as the predictive power of current nuclear models can only be improved by comparison with a large set of experimental results. We recall here that, apart from neutron-induced fission cross sections,

β -delayed fission and spontaneous fission probabilities, models are needed to predict the fission yield, i.e. the mass and charge distribution of fission fragments that strongly affect the abundance distribution, in particular in the mass region between the second and third r -process peak ($130 < A < 180$). New experimental data on fission are therefore essential for optimizing these nuclear models and increasing the predictive power of nucleosynthesis models that use their output.

Current knowledge of r -process nucleosynthesis does not allow one yet to unambiguously identify the dominating fission channel(s) in r -process nucleosynthesis following a NSM (see for example Zhu et al. 2018). However, while β -delayed and spontaneous fission cannot be extensively studied in laboratories (Colonna et al. 2018), neutron-induced fission reactions are experimentally accessible at neutron facilities around the world. In particular, thanks to the high luminosity of the neutron beam, a wealth of fission data on actinides spanning from ^{230}Th to ^{245}Cm have been collected at the CERN n_TOF facility in its 18 years of operation. The higher flux expected in the second experimental area (EAR-2) after the installation of the new spallation target in the near future will give a further boost to fission studies at n_TOF, allowing the collaboration to study actinides with half-lives as short as a few years.

Stronger constraints on fission models may come in particular from measurements of neutron-induced fission cross sections and fission yields of an entire isotopic chain. In fact, a combination of data for various isotopes of the same element allows one to simultaneously study multiple-chance fission, thus better defining relevant model parameters. One of these chains regards curium. While ^{245}Cm has already successfully been measured at n_TOF in the past, new measurements can be performed in the future on all other isotopes of the chain, from ^{244}Cm to ^{248}Cm . Such data would represent a unique opportunity to refine fission models to be used for calculations of fission recycling in r -process nucleosynthesis. Another chain that has already been partially investigated at n_TOF regards plutonium, with ^{240}Pu and ^{242}Pu already measured in recent years. These two isotopes could be complemented with the short-lived ^{238}Pu and ^{241}Pu after the installation of the new spallation target, providing data on a rather long isotopic chain. It should be noted that available data are scarce and affected by large uncertainties on all mentioned isotopes. In particular, very few data are available on the fission yield. The use of a sophisticated $2E2v$ device (the STEFF apparatus; see Colonna et al. 2020 for more details), in combination with the unique features of the n_TOF neutron beam, allows the collaboration to measure fission fragment distributions with high resolution on the atomic mass and charge, thus providing crucial data for model optimization.

In the next future, we plan to exploit fission data collected at n_TOF to further study the role of fission in r -process nucleosynthesis. This will be done by means of the open-source nuclear reaction network SkyNet. SkyNet evolves the abundances of nuclear species under the influence of nuclear reactions. At present, the network contains 7843 nuclear species, spanning from free neutrons and protons to ^{337}Cn ($Z = 112$). Various different types of nuclear reactions are supported. The default version of SkyNet uses forward strong and weak rates

from the JINA REACLIB database (Cyburt et al. 2010), while strong inverse rates are computed assuming detailed balance. Spontaneous and neutron-induced fission rates are taken from Frankel and Metropolis (1947) and Panov et al. (2010), adopting fission barriers and fission fragment distributions from Mamdouh et al. (2001) and Wahl (2002), respectively. β -delayed fission reactions are not included. Nuclear masses are from the REACLIB database, which includes experimental values when available and theoretical masses from the finite-range droplet macroscopic model (FRDM) (Möller et al. 2016) otherwise. SkyNet is however modular so that new nuclear reactions can easily be added or modified. This will allow us to investigate the effect of new neutron-induced fission rates and fission yields.

Part of this chapter has already been published in Massimi et al. (2019)²; Cristallo and Vescovi (2019)³; Mazzone et al. (2020)⁴; Colonna et al. (2020)⁵. For all the papers, I performed s- and r-process calculations and data analysis to evaluate the nucleosynthesis. I significantly contributed to the paper writing, interpretation of the results, and figure creation.

²Data for the s Process from n_TOF. In *Nuclei in the Cosmos XV*, volume 219, pages 63–70. doi: [10.1007/978-3-030-13876-9_11](https://doi.org/10.1007/978-3-030-13876-9_11). Copyright © Springer Nature Switzerland AG

³Nuclear astrophysics at the n_TOF facility: Some key cases in low mass star evolution and Neutron Star Mergers. *Nuovo Cim. C*, 42(2-3-3):117. doi: [10.1393/ncc/i2019-19117-7](https://doi.org/10.1393/ncc/i2019-19117-7). Licensed under [CC BY 4.0](https://creativecommons.org/licenses/by/4.0/)

⁴Measurement of the $^{154}\text{Gd}(n,\gamma)$ cross section and its astrophysical implications. *Physics Letters B*, 804:135405. doi: [10.1016/j.physletb.2020.135405](https://doi.org/10.1016/j.physletb.2020.135405). Licensed under [CC BY 4.0](https://creativecommons.org/licenses/by/4.0/)

⁵The fission experimental program at the CERN n_TOF facility: status and perspectives. *European Physical Journal A*, 56(2):48. doi: [10.1140/epja/s10050-020-00037-8](https://doi.org/10.1140/epja/s10050-020-00037-8). Licensed under [CC BY 4.0](https://creativecommons.org/licenses/by/4.0/)

Effects of a revised ${}^7\text{Be}$ e^- -capture rate on solar neutrino fluxes

Electron-capture on ${}^7\text{Be}$ is the main production channel for ${}^7\text{Li}$ in several astrophysical environments. Theoretical evaluations have to account for not only the nuclear interaction, but also the processes in the plasma in which ${}^7\text{Be}$ ions and electrons interact. In recent decades several estimates were presented, pointing out that the theoretical uncertainty in the rate is in general of a few percent. In the framework of fundamental solar physics, we consider a recent evaluation for the ${}^7\text{Be}+e^-$ rate, which has not been used up to now, in the estimate of neutrino fluxes. We analyze the effects of the new assumptions on standard solar models (SSMs) and compare the results obtained by adopting the revised ${}^7\text{Be}+e^-$ rate to those obtained by that reported in a widely used compilation of reaction rates (ADE11). We find that new SSMs yield a maximum difference in the efficiency of the ${}^7\text{Be}$ channel of about -4% with respect to what is obtained with the previously adopted rate. This fact affects the production of neutrinos from ${}^8\text{B}$, increasing the relative flux up to a maximum of 2.7% . Negligible variations are found for the physical and chemical properties of the computed solar models. The agreement with the Sudbury Neutrino Observatory measurements of the neutral current component of the ${}^8\text{B}$ neutrino flux is improved.

4.1 Introduction

Solar models and their comparisons with observations are a powerful tool for probing the solar interiors with high accuracy, describing the trend of the sound speed, and predicting how neutrinos are distributed among the various channels (see, e.g., Bahcall et al. 2001, for a review).

Solar neutrino measurements in particular those from the ${}^8\text{B}$ channel (Aharmim et al. 2013; Abe et al. 2016) yielded information on fundamental neutrino properties; nowadays these properties are measured with an increasing accuracy and detailed knowledge of neutrino fluxes is also important to this aim.

Very recently the Borexino collaboration presented the first global analysis of three individual neutrino components of the proton-proton (pp) chain, namely pp, ${}^7\text{Be}$, and pep neutrinos, also putting an upper limit for those from CNO, over an energy range from 0.19 MeV to 2.93 MeV (Agostini et al. 2018).

These new data on neutrino fluxes can be used to improve our knowledge of the solar interiors (Vinyoles et al. 2017), which is still beset with problems; among these, of special relevance are those raised by the compilations of solar abundances based on 3D atmospheric models (Asplund 2005), which lead to disagreements with the measured sound speed (Bahcall et al. 2005b).

Standard solar model predictions for neutrino fluxes are then very sensitive to the reaction rates adopted, obviously including electron-captures in the plasma (which are also of great importance for several other astrophysical problems). The electron-capture rate on ${}^7\text{Be}$ itself is strongly dependent on the density and temperature distribution in the stellar structure (Simonucci et al. 2013); in solar conditions, in particular, this destruction channel of ${}^7\text{Be}$ dominates over proton captures (Adelberger et al. 1998). From this latter branching, through ${}^8\text{B}$ -decays, further neutrinos are emitted and can be detected by experiments such as Super-Kamiokande, Sudbury Neutrino Observatory (SNO), and KamLand. The observed flux of ${}^8\text{B}$ neutrinos is expected to be inversely proportional to the electron-capture rate on ${}^7\text{Be}$ because the counting rate in experiments is determined by the number of proton-capture reactions occurring per unit of time (Bahcall and Moeller 1969). Despite many different estimates presented (Bahcall 1962; Bahcall and Moeller 1969; Johnson et al. 1992; Gruzinov and Bahcall 1997), the accuracy in our knowledge of the relative importance of these two channels is not yet satisfactory and improvements have been limited over the years.

In this work we make a step forward by using a new estimate of the electron-capture rate on ${}^7\text{Be}$ (Simonucci et al. 2013, hereafter STPB13) to compute standard solar models (SSMs). The results are then compared with those obtained by the widely used rate by Adelberger et al. (2011) (hereafter ADE11), focusing our attention on solar neutrino fluxes. We make use of a tabulated version of the decay rate by STPB13. The aforementioned table, available at the CDS¹, contains the following information. Column 1 lists the density over the mean molecular weight for electrons in units of g cm^{-3} , Column 2 gives the temperature in units of K, and Column 3 provides the value of the electron-capture rate in units of s^{-1} . All the quantities are expressed in logarithmic scale. We also present an analytical approximation to the electron-capture rate. Our work is organized as follows. In Section 4.2 the main features of the adopted stellar evolutionary code and of SSMs are described. Section 4.3 illustrates the calculation of the electron-capture rate on ${}^7\text{Be}$ and presents a comparison with the previous estimate.

Table 4.1: Major reaction rates included in the SSMs presented in this work.

Reaction	Reference
${}^1\text{H}(\text{p}, \beta^+ \nu_e){}^2\text{H}$	1
${}^1\text{H}(\text{e}^- \text{p}, \nu_e){}^2\text{H}$	2
${}^2\text{H}(\text{p}, \gamma){}^3\text{He}$	2
${}^3\text{He}(\text{p}, \beta^+ \nu_e){}^4\text{He}$	2
${}^3\text{He}({}^3\text{He}, \alpha)2\text{H}$	2
${}^3\text{He}(\alpha, \gamma){}^7\text{Be}$	2
${}^7\text{Li}(\text{p}, \alpha){}^4\text{He}$	3
${}^7\text{Be}(\text{p}, \gamma){}^8\text{B}$	4
${}^7\text{Be}(\text{e}^-, \nu_e){}^7\text{Be}$	2, 5
${}^{12}\text{C}(\text{p}, \gamma){}^{13}\text{N}$	2
${}^{13}\text{C}(\text{p}, \gamma){}^{14}\text{N}$	2
${}^{14}\text{N}(\text{p}, \gamma){}^{15}\text{O}$	6
${}^{15}\text{N}(\text{p}, \gamma){}^{16}\text{O}$	2
${}^{15}\text{N}(\text{p}, \alpha){}^{12}\text{C}$	2
${}^{16}\text{O}(\text{p}, \gamma){}^{17}\text{F}$	2
${}^{17}\text{O}(\text{p}, \gamma){}^{18}\text{F}$	7
${}^{17}\text{O}(\text{p}, \alpha){}^{14}\text{N}$	8
${}^{14}\text{C}(\text{p}, \gamma){}^{15}\text{N}$	9
${}^{18}\text{O}(\text{p}, \gamma){}^{19}\text{F}$	10
${}^{18}\text{O}(\text{p}, \alpha){}^{15}\text{N}$	11
${}^{19}\text{F}(\text{p}, \gamma){}^{20}\text{Ne}$	12
${}^{19}\text{F}(\text{p}, \alpha){}^{16}\text{O}$	13
${}^6\text{Li}(\text{p}, \gamma){}^7\text{Be}$	12
${}^6\text{Li}(\text{p}, {}^3\text{He}){}^4\text{He}$	12
${}^9\text{Be}(\text{p}, \gamma){}^{10}\text{B}$	12
${}^9\text{B}(\text{p}, \alpha){}^6\text{Li}$	14
${}^{10}\text{B}(\text{p}, \gamma){}^{11}\text{C}$	12
${}^{10}\text{B}(\text{p}, \alpha){}^7\text{Be}$	14
${}^{11}\text{B}(\text{p}, \gamma){}^{12}\text{C}$	12
${}^{11}\text{B}(\text{p}, \alpha\alpha){}^4\text{He}$	12
${}^{14}\text{C}(\beta^-, \bar{\nu}_e){}^{14}\text{N}$	15
${}^{18}\text{F}(\beta^+, \nu_e){}^{18}\text{O}$	16
${}^{18}\text{O}(\beta^-, \bar{\nu}_e){}^{18}\text{F}$	16

References. (1) Marcucci et al. (2013); (2) Adelberger et al. (2011); (3) Lamia et al. (2012); (4) Zhang et al. (2015); (5) Simonucci et al. (2013); (6) Marta et al. (2011); (7) Di Leva et al. (2014); (8) Bruno et al. (2016); (9) Iliadis et al. (2010); (10) Buckner et al. (2012); (11) La Cognata et al. (2010); (12) Angulo et al. (1999); (13) Indelicato et al. (2017); (14) Lamia et al. (2015); (15) Rauscher and Thielemann (2000); (16) Oda et al. (1994).

4.2 Standard solar model

A SSM represents the mathematical way of fitting the present-day Sun status, provided some boundary conditions as luminosity, radius, mass, and composition are available. Other important features such as temperature, pressure, sound-speed profiles, solar photospheric abundances, and neutrino fluxes can then be predicted. Each of these quantities strictly depends on the nuclear reactions at work in the Sun's interiors, whose main outcome is helium production by hydrogen burning. This occurs through the pp-chain ($\sim 99\%$) and, to a much lesser extent, through the CN-cycle ($\sim 1\%$). Although the latter is not very important for the energy production in our Sun, it is relevant for the details of the neutrino production and as a test of the correctness of the predictions. Other ingredients of the input physics, such as equation of state (EoS), opacity, and chemical composition are also crucial for predicting the solar quantities mentioned above.

The essentials of a SSM include the full evolution of a $1 M_{\odot}$ star from the pre-main sequence to the present solar age $t_{\odot} = 4.566$ Gyr, usually by considering that mass loss is negligible. In addition, a SSM is required to reproduce, once the presolar composition is fixed, the present-day solar mass M_{\odot} , age, radius R_{\odot} , and luminosity L_{\odot} as well as the observed metal-to-hydrogen ratio $(Z/X)_{\odot}$ at the surface of the Sun. In order to do this, in our models we calibrated accordingly, with an iterative procedure, the initial helium and metal mass fractions Y_{ini} and Z_{ini} , respectively, as well as the mixing-length parameter (α_{MLT}). Our solar models have been calculated with the FUNS code (FULL Network Stellar evolution code) (Straniero et al. 2006; Piersanti et al. 2007; Cristallo et al. 2011). All the models assume a present solar luminosity of $L_{\odot} = 3.8418 \times 10^{33}$ erg s $^{-1}$, a present solar radius $R_{\odot} = 6.9598 \times 10^{10}$ cm, and a solar mass $M_{\odot} = 1.989 \times 10^{33}$ g (Allen 1963; Bahcall et al. 2005a).

The input physics is basically the same adopted by Piersanti et al. (2007), but includes a few recent updates as listed below. We adopted the nuclear reaction rates presented in Table 4.1, except for the case of the ${}^7\text{Be}$ electron-captures, for which we used either the rate suggested by Adelberger et al. (2011) or that computed by Simonucci et al. (2013). Concerning the mean energy loss in the individual branches of neutrino production, we used the experimental values suggested by Vissani (2019) (see their Table 2). For electron screening effects in the solar plasma we adopted the Salpeter formula for the weak-screening, as recommended by Gruzinov and Bahcall (1998) and Bahcall et al. (2002). The EoS is the same as that described by Straniero (1988) for fully ionized matter, in the form updated by Prada Moroni and Straniero (2002) for $\log T$ [K] ≥ 6.0 and a Saha equation for $\log T$ [K] < 6.0 . Atomic diffusion has been included, taking into account the effects of gravitational settling and thermal diffusion, by inverting the coupled set of Burgers equations (Thoul et al. 1994; Piersanti et al. 2007). For radiative opacities, we used the OPAL tables (Iglesias and Rogers 1996) for

¹<https://cdsarc.unistra.fr/viz-bin/cat/J/A+A/623/A126>

high temperatures ($\log T$ [K] ≥ 4.0) and the Ferguson et al. (2005) molecular opacities for low temperatures ($\log T$ [K] < 4.0), corresponding to the scaled-solar composition given either by Grevesse and Sauval (1998) or by Palme et al. (2014) (hereafter GS98 and PLJ14, respectively). Different choices of $(Z/X)_\odot$ correspond to different metal distributions in the solar structure, which, in their turn, change the calculated depth of the convective zone. Indeed, it was pointed out that SSMs with low metal abundances (i.e., with low $(Z/X)_\odot$ values) disagree with the helioseismologically measured sound speed, the depth of the convective zone, and the surface helium abundance (see, e.g., Bahcall et al. 2004). Solving this disagreement, known as the “solar abundance problem”, is an issue not related to ${}^7\text{Be}$ decay and is therefore beyond the scope of this work. We show that the effects of using the new rate are independent from the solar mixture assumed and can be stated in a general way.

Finally, we have to mention that all the analyses presented in the various cases of this work were performed by keeping all the physical parameters fixed, except for the ${}^7\text{Be}$ electron-capture rate, to evaluate the specific role of this rate and to minimize the effects related to other inputs. The results obtained with the updated estimate of the ${}^7\text{Be}$ electron-capture rate given by STPB13 were compared with those obtained with the evaluation given by ADE11 for the two mentioned stellar choices of the chemical composition. In principle, different assumptions for the composition, i.e., for the metal abundances, may lead to differences in the solar core temperature, hence also in the solar structure and in neutrino fluxes; see Section 4.4 for a quantitative discussion.

4.3 Electron-capture on ${}^7\text{Be}$

The deep stellar interiors are characterized by high densities and high temperatures. This implies that atoms are almost completely ionized; therefore, when describing the stellar core matter, it is necessary to apply the methods of plasma physics. The radioactive decay of a particular radioisotope (and its mean lifetime τ) is strongly dependent in such plasma conditions on the density ρ and temperature T of the plasma itself. In short, to provide an estimate of decay rates in stellar conditions we have to rely on accurate models for the plasma.

Many contributions, developed between the 1960s and 1980s, considered a ionized plasma, whose degree of ionization is described through the Saha equation. Free electrons, acting as a screen inside the Debye radius, are treated as a Maxwellian gas (Takahashi and Yokoi 1987). Concerning the specific case of ${}^7\text{Be}$ electron-captures, the first detailed calculation from continuum states was done by Bahcall (1962). Subsequently, estimates of the bound-electron contributions were also made (Iben et al. 1967; Bahcall and Moeller 1969; Bahcall 1994). A recommended resulting rate, based on all these calculations, was proposed by Adelberger et al. (1998) and Adelberger et al. (2011). More general treatments have also been developed over the years (Gruzinov and Bahcall 1997; Brown and Sawyer 1997; Sawyer 2011), but always referring to solar core conditions

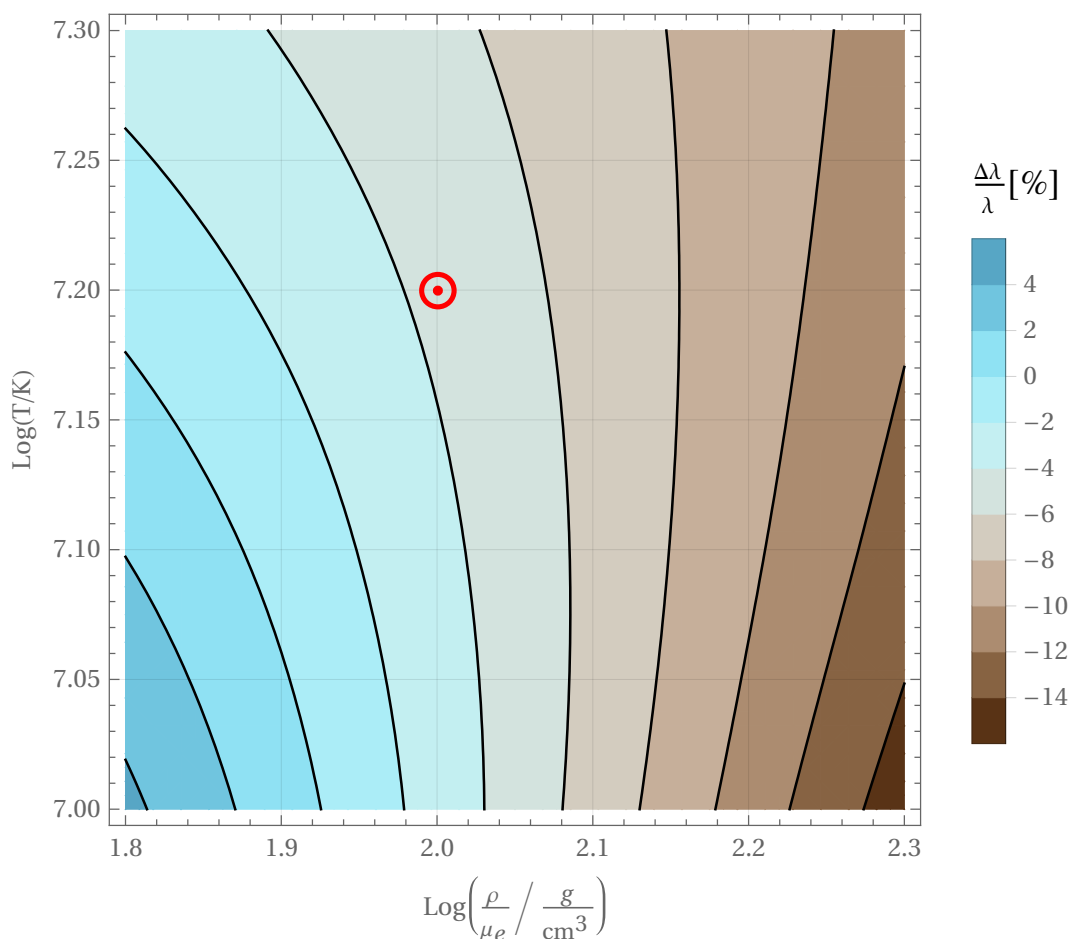


Figure 4.1: Fractional variation of the ${}^7\text{Be}$ electron-capture rate, $\Delta\lambda/\lambda[\%] = 100 \cdot (R_{\text{STPB13}} - R_{\text{ADE11}})/R_{\text{ADE11}}$, as a function of ρ/μ_e and T , adopting the Simonucci et al. (2013) rate, as compared to that of Adelberger et al. (2011) for the PLJ14 solar composition (see Section 4.2). The solar core conditions are highlighted with the common solar symbol.

and maintaining an approach resembling the Born-Oppenheimer (BO) one. In addition to this, it was recognized that the major uncertainty affecting the decay rate arises from possible deviations from a pure Debye screening. Indeed, Johnson et al. (1992) estimated these possible corrections to the Debye-Hückel (DB) approximation by means of self-consistent thermal Hartree calculations, concluding that the proposed rate was correct within an accuracy of about 2%. In this regard, it has to be remarked that the temperature at the center of the Sun ($T \simeq 15.5$ MK) is too high for electron degeneracy to set in. Hence, the classical approximation used, for example, by Bahcall to derive his rate is well founded for the solar conditions.

Recently, Simonucci et al. (2013) developed a first-principles approach to derive the ${}^7\text{Be}$ electron-capture rate by modeling the electron-capture as a two-body scattering process ${}^7\text{Be}-e^-$. To this aim, the e^- -capture process is assumed to be proportional to the electronic density at the nucleus $\rho_e(0)$, which is screened

and modified by the presence of the surrounding particles. We notice in passing that the DB approximation used by Bahcall represents the high-temperature classical limit of the approach developed by Simonucci et al. (2013), which provides the e^- -capture rate on ${}^7\text{Be}$ over a range of plasma densities and temperatures definitively wider than that in the solar core conditions. In this approach, the plasma is assumed hot and is modeled as a homogeneous *Fermi* gas made by ${}^7\text{Be}$ atoms, surrounded by N_p protons (hydrogen nuclei) and N_e electrons, at various temperatures T and densities ρ . The motion of quantum Fermi gases is ruled by the Schrödinger equation and described in a reference frame fixed on the Be nucleus. Because of the adopted non-inertial frame, the Hamiltonian of the system contains non-inertial terms, coupling the motion of particles of the different species. As Be is definitively more massive, all these terms can be safely neglected, so that a factorization of the eigenfunctions can be performed and separable eigensolutions can be found. This procedure is reminiscent of the conditions for the adiabatic theorem, and thus it represents an adiabatic approximation. In this way the many-body scattering problem is reduced to a screened two-body problem. As such, $\rho_e(0)$ is computed by solving a coupled Hartree-Fock (HF) self-consistent system of equations for both protons and electrons in the electric field generated by a ${}^7\text{Be}$ nucleus located at the origin of the reference frame. The HF treatment of the Coulomb repulsion is satisfactory and accurate enough to comply with the electron correlation in stellar conditions (see Simonucci et al. 2013).

The mean lifetime, resulting from this method, is in general compatible with estimates by Bahcall (1962), Bahcall and Moeller (1969), Bahcall (1994), Adelberger et al. (1998), and Adelberger et al. (2011); however, the mean lifetime has values that in solar conditions are smaller by $\sim 3 - 4\%$ with respect to those estimated in the mentioned works. Far from these conditions, the differences can be much more pronounced (see Figure 4.1). Details of the calculations are provided in Simonucci et al. (2013). The total reaction rate λ for ${}^7\text{Be}(e^-, \nu_e){}^7\text{Li}$ by STPB13 can also be expressed analytically in an approximate formula, as a function of temperature, density, and composition.

An expression that agrees with an accuracy of 2% to the tabulated results for the rate λ [s^{-1}], in the region of relevance for solar physics, i.e., $35 \lesssim \rho/\mu_e$ [g cm^{-3}] $\lesssim 105$ and $10 \leq T_6$ [MK] ≤ 16 , is written as

$$\lambda\left(\frac{\rho}{\mu_e}, T_6\right) = \frac{\rho}{\mu_e} \frac{\kappa}{\sqrt{T_6}} \left[1 + \alpha (T_6 - 16) + \beta \frac{\rho}{\mu_e} \left(1 + \gamma (T_6 - 16) \right) \right]. \quad (4.1)$$

In this equation, μ_e is the mean molecular weight per electron, T_6 is the temperature in units of 10^6 K, and ρ is the density in units of [g cm^{-3}]. Thus, the electron density is $n_e = \rho/(m_p \mu_e)$, where m_p is the proton mass. The values of the four coefficients $\kappa, \alpha, \beta, \gamma$, whose units ensure the correct dimension of Equation (4.1), are reported in Table 4.2. We notice that a nonlinear term in the density is present, while it was absent in Bahcall's calculations. In fact, this term results from the Coulomb repulsion (electron screening) acted upon the electrons, which modifies the density close to the nucleus. Taking into account such a nonlinearity

Table 4.2: Coefficients for the analytical approximation to the STPB13 and ADE11 electron-capture rates.

	κ	α	β	γ
this work	5.9065×10^{-9}	-1.3614×10^{-2}	-9.2042×10^{-4}	-1.5334×10^{-1}
ADE11	5.6×10^{-9}	$+4 \times 10^{-3}$	0	0

requires the introduction of a higher number of polynomial terms. We recall, however, that in this work we make use of a tabulated version of the decay rate by STPB13: in fact, the adopted fine resolution allows us to compute highly accurate solar models without adding further uncertainties deriving from the use of an analytical formula. We note that in our discussion, none of the nuclear reaction rates relevant for the standard solar model has been modified, so that expected variations are entirely a consequence of the new approach adopted in computing ${}^7\text{Be}$ electron-capture rate. Nevertheless, the change in the electron density, due to the formalism introduced by Simonucci et al. (2013) to describe e^- -capture on ${}^7\text{Be}$, might also be relevant for other charged-particle interactions, leading to a correction in the screening factor. An investigation of this possibility and the quantitative estimation of this effect deserves dedicated analyses and future work.

4.4 Solar neutrino fluxes

Stars with initial mass $M \lesssim 1.2 M_\odot$ primarily burn hydrogen through the pp-chain. The latter has three main branches, namely the ppI-, ppII-, and ppIII-cycles. The pp, ${}^8\text{B}$ β -decay, and hep reactions produce neutrino spectra with characteristic shapes and with energies from zero up to a maximum energy q . In particular, the neutrinos coming from the weak hep branch are the most energetic neutrinos produced by the Sun ($q \leq 18.773$ MeV) and, thus, are observed in the SNO and Super-Kamiokande event distributions because they populate energy bins above the ${}^8\text{B}$ neutrino endpoint. The electron-capture reactions $p + e^- \rightarrow n + \nu$ and ${}^7\text{Be} + e^- \rightarrow {}^7\text{Li} + \nu$ produce, on the contrary, emission lines, possibly broadened by thermal effects. Concerning the ${}^7\text{Be}$ neutrinos, they form two distinct lines, corresponding to population of both the ground state (89.5%) and the first excited state (10.5%) in ${}^7\text{Li}$ (Vissani 2019).

The ppI, ppII, and ppIII contributions to solar energy generation can be determined from measurements of the pp/pep, ${}^7\text{Be}$, and ${}^8\text{B}$ neutrino fluxes. Because the relative rates are very sensitive to the solar core temperature T_c , it is possible to infer important information about the physics of the solar interior from neutrino fluxes. Nowadays the pp, ${}^7\text{Be}$, and ${}^8\text{B}$ fluxes are well known, while the measured pep neutrino flux is strongly model-dependent. In particular, this flux depends on the metallicity assumed for estimating the competing CNO neutrinos (Agostini et al. 2018). The solar core physics is sensitive to metallicity effects

Table 4.3: Main relevant quantities for the solar models adopting the ADE11 rate, as defined in the text. The models using the STPB13 rate show negligible variations for the same quantities. The value R_{CE} is the radius at the base of the convective envelope, T_c and ρ_c are the central temperature and density, and α_{MLT} is the value of the mixing-length parameter. The values X_{ini} , Y_{ini} , Z_{ini} and $(Z/X)_{\text{ini}}$ are the initial hydrogen, helium and metal abundances by mass and the initial metal-to-hydrogen ratio, while X_{\odot} , Y_{\odot} , Z_{\odot} and $(Z/X)_{\odot}$ are the corresponding present-day photospheric values.

	GS98	PLJ14
R_{CE}/R_{\odot}	0.71628	0.72294
T_c [10^7K]	1.55031	1.54286
ρ_c [g cm^{-3}]	149.377	148.325
α_{MLT}	2.31832	2.30317
X_{ini}	0.70428	0.71092
Y_{ini}	0.27703	0.27256
Z_{ini}	0.01868	0.01653
$(Z/X)_{\text{ini}}$	0.02653	0.02325
X_{\odot}	0.73656	0.74412
Y_{\odot}	0.24656	0.24103
Z_{\odot}	0.01688	0.01485
$(Z/X)_{\odot}$	0.02292	0.01995

because of the free-bound/bound-free transitions in metals, which are important contributors to the opacity. This means that metallicity variations alter the solar core temperature and, in turn, the fluxes of temperature-sensitive neutrinos, such as those from ^8B β -decay. Heavier metals (Mg, Si, and Fe) also affect the predicted neutrino fluxes (see Bahcall et al. 1982). Even if not very abundant, they are important opacity sources at the Sun center, as they are highly ionized. Instead, in the region just below the convective zone, at temperatures of a few millions kelvins, they are small contributors to the opacity. On the contrary, abundant, lighter, volatile heavy elements (C, N, O, Ne, and Ar) are partially ionized there and significantly affect the radiative opacities. This is the origin of discrepancies between helioseismological measurements and the predictions made using solar compositions with low (Z/X) , as discussed in Bahcall et al. (2005b) and Bahcall and Serenelli (2005). As a matter of fact, abundance variations of different metals influence different regions in the solar interior. Moreover, different CNO abundances also imply an effect on CNO burning efficiency (and corresponding neutrino fluxes) and a minor effect on the mean molecular weight and, in turn, on the thermodynamical quantities.

The net effect is that models using the GS98 compilation of abundances exhibit higher temperatures and higher densities with respect to those using that of PLJ14 (see Table 4.3). On the other hand, while pp and pep fluxes are only slightly

modified, ${}^7\text{Be}$, ${}^8\text{B}$, ${}^{13}\text{N}$, ${}^{15}\text{O}$, and ${}^{17}\text{F}$ neutrino fluxes are rather enhanced. Their fluxes are indeed strongly dependent on the central temperature T_c , with a power law of the form $\Phi \propto T_c^m$, where $m = 10.0, 24.0, 24.4, 27.1$, and 27.8 , respectively (see Bahcall and Ulmer 1996). CNO neutrino fluxes are also enhanced because of the increased burning efficiency caused by the higher CNO abundances in the GS98 compilation. As was already mentioned, using modern solar compositions such as that of PLJ14, with low surface metal abundances, solar models have been found to be in disagreement with helioseismological measurements (see Bahcall et al. 2004; Basu and Antia 2004; Bahcall et al. 2005a; Serenelli et al. 2011; Haxton et al. 2013; Vinyoles et al. 2017). We checked that the predicted sound speed profiles of our computed SSMs are in agreement with others in the literature. We found that for the PLJ14 abundance choice the prediction disagrees with that measured (Schou et al. 1998). Instead, the choice of the older GS98 composition gives a better match.

We recall however that this work is not aimed at giving the best prediction for the total neutrino fluxes nor at probing the solar metallicity problem, rather we want to probe the effects induced on solar neutrino fluxes by varying the ${}^7\text{Be}$ electron-capture rate alone, in the light of the mentioned evaluation by STPB13.

4.5 Impact of a revised ${}^7\text{Be} + e^-$ on the ${}^8\text{B}$ neutrino flux

In this section we want to evaluate the impact of using a revised rate for the ${}^7\text{Be}$ electron-capture, computed following the approach suggested by Simonucci et al. (2013), on the ${}^8\text{B}$ neutrino flux. While pp neutrinos originate in a wide range of the Sun, corresponding to the main energy-producing region, ${}^7\text{Be}$ and ${}^8\text{B}$ neutrinos are produced in a hotter and narrower zone, ranging from the solar center to about $0.15 - 0.2R_\odot$. The quantities R_{STPB13} and R_{ADE11} represent the electron-capture rate given by STPB13 and by ADE11, respectively. As shown in the top panel of Figure 4.2, there is an appreciable variation: the new rate is lower with respect to the ADE11 choice in solar core conditions, meaning that the ${}^7\text{Be}$ neutrino production channel is slightly suppressed in favor of all other channels. In particular, the solar neutrino fluxes from ${}^7\text{Be}$ and ${}^8\text{B}$, $\Phi({}^7\text{Be})$ and $\Phi({}^8\text{B})$ are proportional to the local density of ${}^7\text{Be}$ ions. The $\Phi({}^7\text{Be})$ flux depends on both the electron-capture (R_{ec}) and the proton-capture rate (R_{pc}) through

$$\Phi({}^7\text{Be}) \propto \frac{R_{\text{ec}}}{R_{\text{ec}} + R_{\text{pc}}}, \quad (4.2)$$

where $R_{\text{pc}} \approx 10^{-3} R_{\text{ec}}$ (see Adelberger et al. 1998). The flux $\Phi({}^7\text{Be})$ is therefore basically independent from the rates and dependent only upon the branching ratio of the reactions ${}^3\text{He} + {}^3\text{He} \rightarrow e + {}^3\text{He} + {}^4\text{He}$. On the contrary, $\Phi({}^8\text{B})$ can be written as

$$\Phi({}^8\text{B}) \propto \frac{R_{\text{pc}}}{R_{\text{ec}} + R_{\text{pc}}} \simeq \frac{R_{\text{pc}}}{R_{\text{ec}}}, \quad (4.3)$$

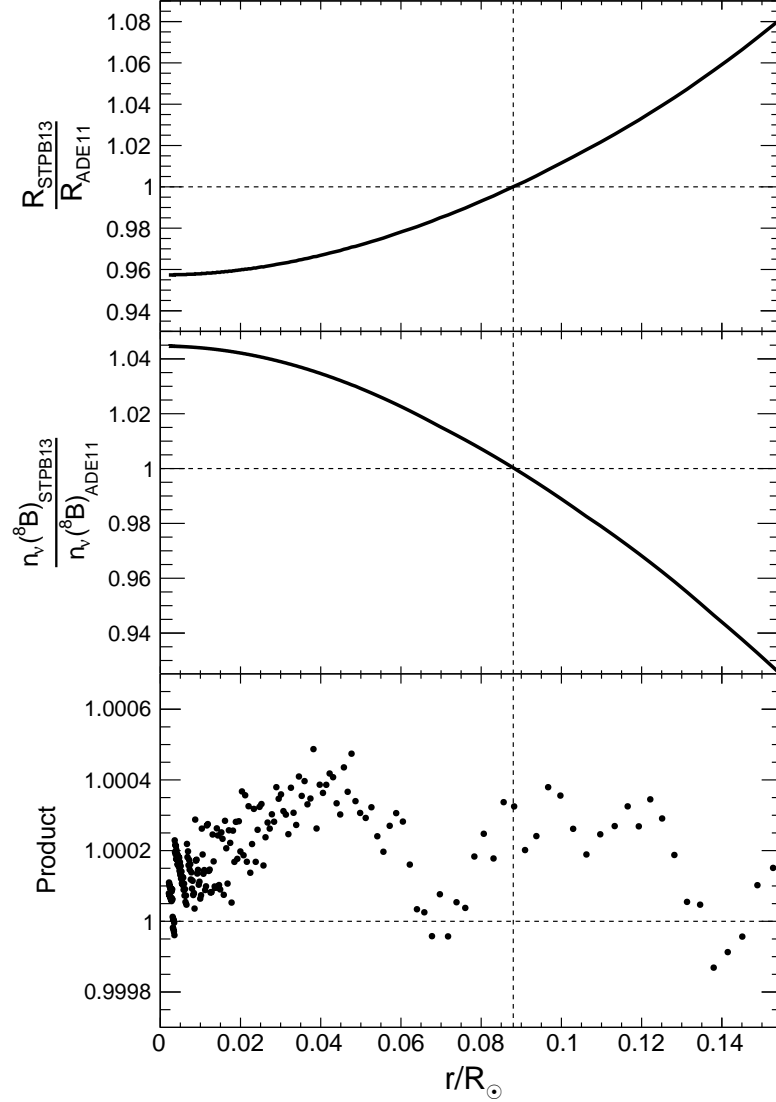


Figure 4.2: Top panel shows the ratio of the STPB13 electron-capture rate to that of ADE11 in the production region of ${}^8\text{B}$ neutrinos. These are both computed on the solar structure resulting from the ADE11 SSM, with a PLJ14 composition. The middle panel shows the ratio of the neutrinos fraction produced in STPB13 SSM to that of ADE11, both computed with a PLJ14 composition. In the bottom panel the product $n_\nu({}^8\text{B})_{\text{STPB13}} \cdot R_{\text{STPB13}} / (n_\nu({}^8\text{B})_{\text{ADE11}} \cdot R_{\text{STPB13}})$ is shown; we note, in comparison with the other two panels, the much finer vertical scale. The consistency of this value with the unity means that there is practically no difference in computing a SSM with the revised STPB13 rate or applying it directly on the solar structure of a ADE11 SSM.

meaning that it is inversely proportional to the electron-capture rate R_{ec} . This means that a variation of the R_{ec} should have a linear effect on neutrino flux of ${}^8\text{B}$ and negligible effects on other channels. Indeed, the STPB13 models present exactly the same physical and chemical features of the ADE11 models (see Table

Table 4.4: Predicted fluxes in units of 10^{10} (pp), 10^9 (${}^7\text{Be}$), 10^8 (pep, ${}^{13}\text{N}$, ${}^{15}\text{O}$), 10^6 (${}^8\text{B}$, ${}^{17}\text{F}$), and 10^3 (hep) $\text{cm}^{-2}\text{s}^{-1}$ for the reference ADE11 models, presented in Table 4.3, for the STPB13 models and relative differences. .

	GS98			PLJ14		
	ADE11	STPB13	relative differences	ADE11	STPB13	relative differences
$\Phi(\text{pp})$	5.99	5.99	+0.20‰	6.01	6.01	+0.01‰
$\Phi(\text{pep})$	1.42	1.42	+0.25‰	1.43	1.43	+0.01‰
$\Phi(\text{hep})$	8.09	8.09	+0.15‰	8.22	8.22	+0.01‰
$\Phi({}^7\text{Be})$	4.74	4.74	+0.38‰	4.54	4.54	-0.01‰
$\Phi({}^8\text{B})$	5.28	5.42	+2.70%	4.82	4.95	+2.60%
$\Phi({}^{13}\text{N})$	2.82	2.82	+0.67‰	2.55	2.55	+0.06‰
$\Phi({}^{15}\text{O})$	2.07	2.07	+0.71‰	1.82	1.82	+0.07‰
$\Phi({}^{17}\text{F})$	5.35	5.35	+0.80‰	3.95	3.95	+0.07‰

4.3). If we take into account neutrinos that originate in each fraction of the solar radius (Figure 4.2, middle panel), we thus deduce that the ${}^8\text{B}$ neutrino production channel becomes more efficient and so $\Phi({}^8\text{B})$ is increased because of the less efficient electron-capture on ${}^7\text{Be}$ rate. It is also possible to see that, in correspondence of a change from negative to positive values of the variations in the electron-capture rate, the neutrino flux variation shifts from positive to negative values, thus corroborating the hypothesis of linearity between the electron-capture rate on ${}^7\text{Be}$ and the ${}^8\text{B}$ neutrino flux. Furthermore, if relation (4.3) holds, then we see that

$$\frac{n_\nu({}^8\text{B})_{\text{STPB13}}}{n_\nu({}^8\text{B})_{\text{ADE11}}} = \frac{\Phi({}^8\text{B})_{\text{STPB13}}}{\Phi({}^8\text{B})_{\text{ADE11}}} \simeq \frac{R_{\text{ADE11}}}{R_{\text{STPB13}}}, \quad (4.4)$$

or alternatively,

$$\frac{n_\nu({}^8\text{B})_{\text{STPB13}} R_{\text{STPB13}}}{n_\nu({}^8\text{B})_{\text{ADE11}} R_{\text{ADE11}}} \simeq 1, \quad (4.5)$$

where $n_\nu({}^8\text{B})$ is the number of neutrinos coming from the ${}^8\text{B}$ decay. The bottom panel of Figure 4.2 shows the product in the left-hand side of relation (4.5). Its value is consistent with unity at less than one part per thousand, meaning that relation (4.3) is indeed valid and that an increase of the R_{ec} has the effect of linearly decreasing the flux of ${}^8\text{B}$ neutrinos. Finally, variations by +2.6% and +2.7% in $\Phi({}^8\text{B})$ are obtained for SSMs using a PLJ14 or a GS98 composition, respectively (see Table 4.4). The adoption of the STPB13 rate for electron-captures on ${}^7\text{Be}$ has negligible effects on all other neutrino fluxes because it induces no variation on the physics and chemistry of the SSM itself (see Table 4.3).

At the present moment we cannot tag our predicted fluxes with well-defined uncertainty estimates. We should construct Monte Carlo (MC) simulations of SSMs to provide statistical errors to our results (see Bahcall et al. 2006; Serenelli

et al. 2011; Vinyoles et al. 2017). Still we can estimate these uncertainties starting from known literature. Concerning the predicted ${}^8\text{B}$ neutrino flux, Bahcall et al. (2006) found that the 1σ theoretical uncertainty varies from 17% to 11%, depending on the adopted composition (see their Table 15 and Figure 6). Similar but lower values were also found by Serenelli et al. (2011) and Vinyoles et al. (2017). Then we can choose, in a conservative way, the higher value of 17% as our uncertainty on the predicted ${}^8\text{B}$ neutrino flux. Similarly we can adopt an error of 10% 1σ on the ${}^7\text{Be}$ neutrino flux, as predicted by Bahcall et al. (2006), which is the highest found in the literature. We also use, as correlation coefficient of the ${}^7\text{Be}$ - ${}^8\text{B}$ neutrino fluxes, that given by Bahcall et al. (2006) for the GS98 composition. In this way we only give a rough, but still reliable, estimate of the uncertainties affecting our neutrino flux predictions, to be compared with the measured values.

The final joint fit to all SNO data gave a total flux of neutrino from ${}^8\text{B}$ decays in the Sun of $\Phi({}^8\text{B}) = 5.25(1 \pm 0.04) \times 10^6 \text{ cm}^{-2}\text{s}^{-1}$ (Aharmim et al. 2013). The latest results of the Borexino collaboration (Agostini et al. 2018) provided a total flux of ${}^7\text{Be}$ neutrino flux of $\Phi({}^7\text{Be}) = 4.99(1 \pm 0.03) \times 10^9 \text{ cm}^{-2}\text{s}^{-1}$. Such a value is somehow model-dependent, being obtained from the measured rates assuming a specific mechanism of neutrino oscillations (see Agostini et al. 2018, for details). In fact, elastic scattering measurements, such as those performed by Borexino, are mainly sensitive to ν_e charged-current interactions. On the contrary, the neutral-current detection channel in SNO is sensitive to all neutrino flavors and so it is a direct model-independent observation of the ${}^8\text{B}$ solar neutrino flux. Figure 4.3 shows that adopting either the GS98 or PLJ14 compositions leads to a fair agreement with the total ${}^8\text{B}$ neutrino flux measured by the SNO neutral current experiments. The use of the revised electron-capture rate R_{STPB13} increases the old values of the predicted ${}^8\text{B}$ neutrino fluxes with respect to the measured value. The measured value of the ${}^8\text{B}$ neutrino flux is compatible with the solar model predictions for each of the two adopted solar compositions.

4.6 Conclusions

We have presented new SSMS for two different mixtures of solar abundances, GS98 and PLJ14. We performed the simulation with the FUNS code suite. We used recent values for the cross sections in our nuclear reaction network. In particular, we adopt the e^- -capture rate on ${}^7\text{Be}$ provided by Simonucci et al. (2013) based on a description of the physical conditions in the solar interior that is more accurate than previous works (e.g., ADE11) and is also applicable to more general stellar environments. The comparison with models computed with the ADE11 widely adopted electron-capture rate shows maximum differences of about 3 – 4% in solar conditions. The effects on the standard solar model calculations, along with the effects on neutrino fluxes, have been discussed. We found that variations in the solar structure and in neutrino fluxes are negligible, except for the ${}^8\text{B}$ neutrino flux. The estimated increase is 2.6 – 2.7%, depending on the

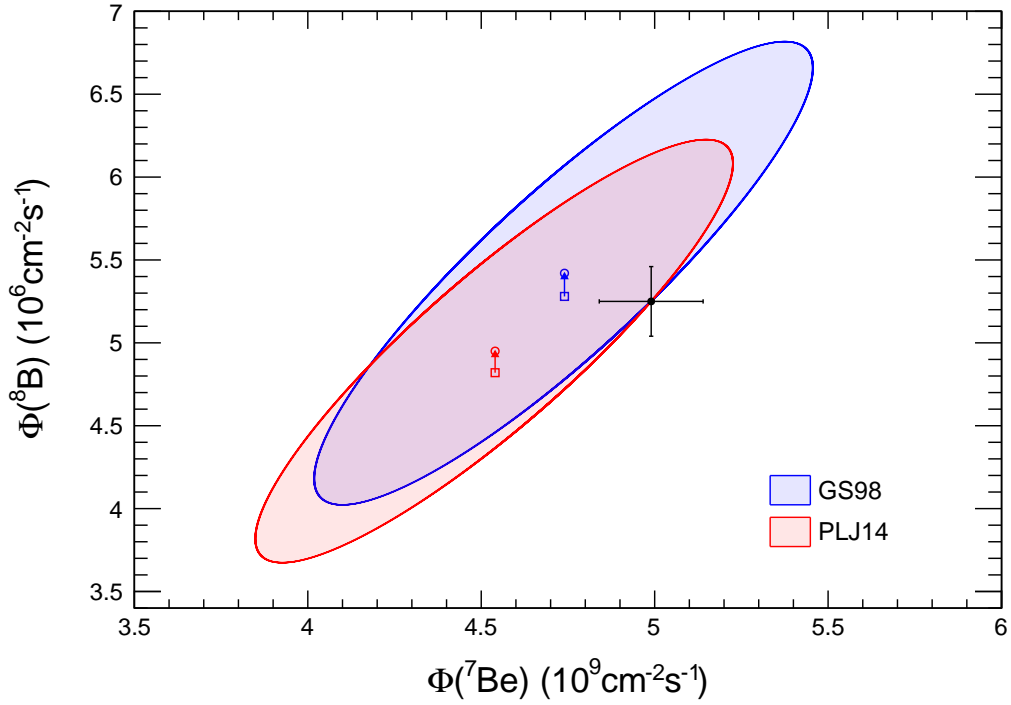


Figure 4.3: Fluxes of $\Phi(^8\text{B})$ and $\Phi(^7\text{Be})$ compared to solar values (Aharmim et al. 2013; Agostini et al. 2018). The black dot and error bars indicate solar values, while the squares and circles indicate the results obtained with the ADE11 electron-capture rate (older) and that of STPB13 (current), respectively. Ellipses denote theoretical 1σ confidence level (C.L.) for 2 degrees of freedom.

composition assumed. Finally, we have also shown that the solar ^8B neutrino flux is reproduced rather well, both using the GS98 and PLJ14 abundance sets.

The content of this chapter has been published in Vescovi et al. (2019)². As the first author, I performed all solar model calculations and data analysis, created all the figures, led data interpretation and paper writing.

²Effects of a revised ^7Be e^- -capture rate on solar neutrino fluxes. *A&A*, 623:A126. doi: [10.1051/0004-6361/201834993](https://doi.org/10.1051/0004-6361/201834993). Reproduced with permission from Astronomy & Astrophysics, © ESO

The luminosity constraint in the era of precision solar physics

The *luminosity constraint* is a very precise relationship linking the power released by the Sun as photons and the solar neutrino fluxes. Such a relation, which is a direct consequence of the physical processes controlling the production and the transport of energy in the solar interior, is of great importance for the studies of solar neutrinos and has a special role for the search of neutrinos from the CNO cycle, whose first detection with a 5σ significance has been recently announced by the Borexino collaboration. Here we revise the luminosity constraint, discussing and validating its underlying hypotheses, in the light of latest solar neutrino and luminosity measurements. We generalize the current formulation of the luminosity constraint relation so that it can be easily used in future analysis of solar neutrino data, and we provide a specific application showing the link between CNO and pp neutrino fluxes.

5.1 Introduction

The Sun, being the closest star, is a fundamental benchmark for our comprehension of the stellar physics and for the stellar evolution theory. The prediction of solar models that the CNO cycle actually contributes to the energy production in the Sun has never been observationally verified up to now (Agostini et al. 2020a). Although this contribution is small if compared to the total energy budget, its detection directly probes the physical conditions within the solar core. Hopefully, it may also help in solving the longstanding problem of the discrepancy between standard solar models (SSMs) and helioseismic measurements. In brief, the sound speed profile predicted by SSMs, as computed by using the most recent photospheric abundance determination of CNO and other volatile elements (Asplund et al. 2005, 2009; Caffau et al. 2011), are in tension with the sound speed profile obtained from helioseismic data (Basu and Antia 2004). In particular, the sound-speed profile allows a precise determination of the location of the internal

border of the solar convective envelope and this location is more external in standard solar models than the one derived from helioseismic measurement. This issue could be solved if the actual metallicity of the Sun would be larger than currently assumed. Indeed, the location of the convective boundary depends on the temperature gradient and, in turn on the radiative opacity. A larger opacity, as due to a higher metallicity, would imply a deeper convective envelope (Christensen-Dalsgaard et al. 2009; Villante 2010). This represents the so-called “solar metallicity problem” (Bahcall et al. 2005a). It is worth recalling that the solar system abundances currently used in solar model calculations are obtained by combining different sources, mainly spectroscopy of the solar photosphere and mass spectroscopy of pristine meteorites (Grevesse and Sauval 1998; Asplund et al. 2005; Palme et al. 2014). Note that this provides us only abundance ratios, rather than absolute abundances (Piersanti et al. 2007). In this context, an independent evaluation of the solar metallicity or of the abundances of its major constituents, i.e. C, N and O, through the measurement of the CNO burning rate, may provide this solution. Note that in this way we may evaluate the abundances of C, N and O in the *solar core*, rather than in the solar photosphere, as obtained from the standard spectroscopic abundance analysis

The CNO burning rate can be determined by measuring the neutrinos related to the β -decay of ^{13}N , ^{15}O , and ^{17}F . Those are produced in the innermost zone of the Sun, where the temperature is high enough to fully activate the CN cycle and partially the NO cycle. The importance of these measurements in our understanding of the present and the primordial Sun has been pointed out by Haxton and Serenelli (2008) (see also Zhang et al. 2019 for a recent discussion). In particular, Haxton and Serenelli (2008) show that the correlation between the core metallicity and the CNO fluxes is independent of other solar model input parameters at a high level of significance and use this information to infer the primordial metallicity of the Sun, provided that a reliable estimation of the diffusion coefficient is available (Christensen-Dalsgaard 2020). On an experimental point of view, one has to keep in mind that CNO neutrinos have so low energies (\sim MeV) that their detection is particularly difficult. Moreover, in the same energy region, neutrinos from the pp-chain are also emitted, thus requiring an independent determination of neutrinos from the $p + p \rightarrow {}^2\text{H} + e^+ + \nu$ and $p + p + e^- \rightarrow {}^2\text{H} + \nu$ reactions. As a consequence, only two of the solar neutrino telescopes currently working can be used to this aim, namely SAGE in Russia (Elliott et al. 1995) and Borexino in Italy (Bellini et al. 2014). The former provides information about the integrated neutrino flux for energies above 233 keV: in this case the CNO contribution to the total is smaller than the uncertainties in the detection cross section of the apparatus, thus the SAGE determination can be hardly used to constraint the CNO cycle rate. On the other hand, the detection cross section in Borexino is well known and, in addition, the contamination of the signal from non-CNO neutrinos reduces to the pep reaction only, whose contribution can not be measured directly, thus representing a limitation for any solar neutrino telescope evaluation of the CNO cycle rate.

However, an independent estimate of pep neutrinos can be derived from the

solar luminosity, by using a reliable (appropriately simplified) description of the solar structure at the current epoch, based on the assumption, already proved, that the main energy source in the Sun is provided by nuclear reactions (Bellini et al. 2014). According to this general scenario, the neutrinos emitted from the Sun are tightly related to its surface luminosity, by means of the so-called *luminosity constraint* whose current formulation is illustrated and discussed in Bahcall (2002). The relevance of such relation relies on the possibility to express the solar photon luminosity, which is measured very precisely, as a linear combination of the neutrino fluxes, so that the latter can be linked to each other with very high precision.

In the present work we review such a relation, by critically analyzing the uncertainties on the underlying assumptions and quantifying their contributions to the corresponding estimation of pp and pep neutrino fluxes. This kind of analysis has to be performed since neutrino measurements have now attained so high accuracy to require appropriate and very precise theoretical analysis tools. In this regard we recall that the luminosity constraint is already used for a model-independent analysis of neutrino data (Bergström et al. 2016). Moreover, recently the Borexino collaboration has announced officially the first detection with 5σ confidence level of CNO neutrinos (Agostini et al. 2020a), so it is of paramount importance to improve as possible the luminosity constraint and to establish to what extent it can be used to estimate pp and pep neutrino fluxes. Furthermore, it has recently been observed that there are inaccuracies in the formula currently in use for the luminosity constraint (Vissani 2019), which adds motivation to engage a new discussion of this topic.

5.2 Experimental status of solar neutrinos

The solar neutrino flux has been studied ever since the Homestake experiment (Cleveland et al. 1998), which has taken data between 1970 and 1994. Such experiment was based on the inverse β absorption of an electron neutrino by chlorine, namely: $\nu_e + {}^{37}\text{Cl} \rightarrow {}^{37}\text{Ar} + e^-$. Today, the most popular techniques of solar neutrino detection rely on Cherenkov emission of neutrino-induced charged particles and neutrino-induced scintillation (see, for reference, Alimonti et al. 2009; Fukuda et al. 2003; Boger et al. 2000). Generally, solar neutrino fluxes are expressed as:

$$\Phi_i = \varphi_i \times 10^{\gamma_i} \text{ cm}^{-2} \text{ s}^{-1}, \quad (5.1)$$

where the fluxes are labeled with $i = \text{pp, pep, Be, B, hep, N, O, F}$, according to their production mechanism. Not surprisingly, the γ_i exponents have been stable over time, while the adimensional φ_i factors have been improved and tested with experiments.

In Table 5.1 we compare the latest experimental determination of solar neutrino fluxes to the theoretical expectations based on SSMs, computed by adopting two different heavy metals distributions, namely GS98 (Grevesse and Sauval

Table 5.1: The predicted and measured solar neutrino fluxes in units of $10^{\gamma_i} \text{ cm}^{-2} \text{ s}^{-1}$. The CNO neutrino flux is the sum of the singular fluxes of N, O and F. Theoretical SSM predictions are from this work (see Section 5.4), for the GS98 (Grevesse and Sauval 1998) and PLJ14 (Palme et al. 2014) solar compositions. The results from Borexino (BX) are taken from Agostini et al. (2019, 2020a), that from Super-Kamiokande (SK) is taken from Abe et al. (2016), and that for the Sudbury Neutrino Observatory (SNO) is from Aharmim et al. (2013). We note that SNO has performed a notable oscillation-independent measurement of the Boron flux via the neutral current interaction channel $\nu_\ell + d \rightarrow n + p + \nu_\ell$: they obtained $\Phi_B = 5.25(1 \pm 0.04)$, which is compatible with the measurement by Super-Kamiokande. The error on Φ_{hep} as measured by Super-Kamiokande is not known, but it is presumably large. In a very recent work by SNO (Aharmim et al. 2020), they quote $\Phi_{\text{hep}} = (5.1 - 23) \times 10^3 \text{ cm}^{-2} \text{ s}^{-1}$ at 1σ .

Flux	γ_i	φ_i		Experimental results	Source
		GS98	PLJ14		
Φ_{pp}	10	5.99(1 ± 0.01)	6.01(1 ± 0.01)	6.1(1 ± 0.1)	BX
Φ_{pep}	8	1.42(1 ± 0.02)	1.43(1 ± 0.02)	1.27(1 ± 0.17) ^a	BX
Φ_{Be}	9	4.73(1 ± 0.12)	4.52(1 ± 0.12)	4.99(1 ± 0.03)	BX
Φ_B	6	5.52(1 ± 0.24)	5.01(1 ± 0.24)	5.41(1 ± 0.016)	SK ^b
Φ_{hep}	3	8.15(1 ± 0.30)	8.28(1 ± 0.30)	8(1 ± 2)	SNO
Φ_N	8	2.87(1 ± 0.30)	2.58(1 ± 0.29)	-	-
Φ_O	8	2.13(1 ± 0.36)	1.86(1 ± 0.35)	-	-
Φ_F	6	5.51(1 ± 0.37)	4.04(1 ± 0.36)	-	-
Φ_{CNO}	8	5.06(1 ± 0.32)	4.48(1 ± 0.31)	7.0 ^{+3.0} _{-2.0}	BX

^a Measured Φ_{pep} neutrino flux for the GS98 solar composition.

^b By including the SNO measurement mentioned in the caption, $\Phi_B = 5.39(1 \pm 0.015)$.

1998, high metallicity case) and PLJ14 (Palme et al. 2014, low metallicity case)¹. From Table 5.1 we can see that Φ_{Be} and Φ_B are measured with an accuracy better than that of the corresponding theoretical prediction. This fact, along with the upcoming first measurement of CNO neutrinos by Borexino, marks the beginning of precision solar neutrino flux measurements. The extraction of the CNO neutrino signal, however, is particularly difficult due to the presence of the background constituted by the decay of bismuth and by pep neutrinos (Villante et al. 2011). A precise determination of the bismuth contamination is possible, as it decays β^- in polonium in about 20 minutes, which is easily visible and measurable (Villante et al. 2011). On the other hand, the identification and separation of pep neutrinos represent a problem not only for Borexino but also for any other neutrino telescope. The precise observational knowledge of the solar luminosity can be used to overcome this last experimental difficulty. In fact, the solar luminosity can be used to constrain a linear combination of pp and CNO neutrino fluxes, which basically amounts to a precise determination of the pp flux

¹For details about the derivation of the theoretical uncertainties, see Section 5.4.1.

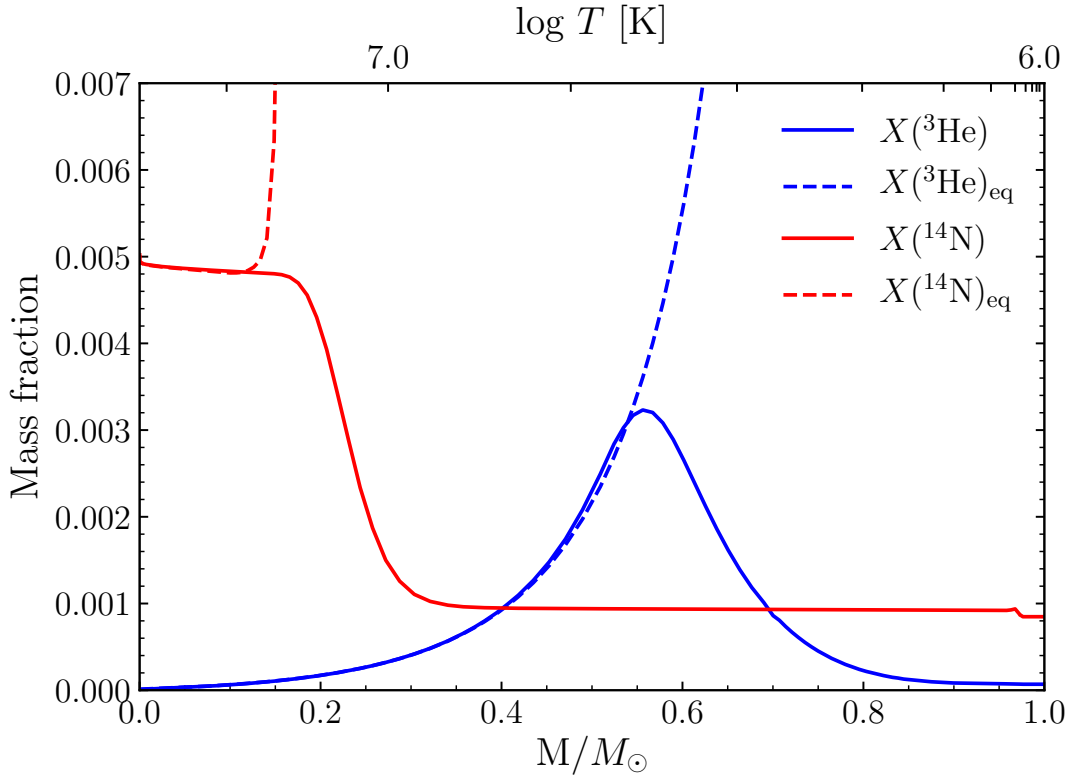


Figure 5.1: ${}^3\text{He}$ and ${}^{14}\text{N}$ abundances (solid lines) as a function of mass coordinate, for the GS98 SSM described in Section 5.4. In the innermost region, production and destruction channels, both for ${}^3\text{He}$ and ${}^{14}\text{N}$, equate and these isotopes attain their equilibrium abundances (dashed lines). At $\simeq 0.15 M_{\odot}$, p-captures on ${}^{12}\text{C}$ and ${}^{13}\text{C}$ becomes ineffective due to the low temperatures. ${}^3\text{He}$ shows a sharp peak at about $0.55 M_{\odot}$: in this region ${}^3\text{He}$ is continually produced by proton burning reactions but the temperature is too low to burn it at equilibrium rate via ${}^3\text{He} + {}^3\text{He}$ and ${}^3\text{He} + {}^4\text{He}$ reactions. In the outer region proton burning is ineffective in producing ${}^3\text{He}$.

(pep neutrinos are very closely related to pp neutrinos). We will discuss both points quantitatively later.

5.3 The standard luminosity constraint

The luminosity constraint is a relation linking the photospheric solar luminosity with the neutrino fluxes produced in nuclear reactions active in the innermost zones of the Sun, and it is obtained under some assumptions representing an excellent approximation of the real solar physical properties (Bahcall 2002). First of all, it is assumed that all the secondary isotopes involved in nuclear processes are in local nuclear equilibrium, i.e. that their abundances are fixed by the condition that their production rate is equal to the destruction one. Under this hypothesis, the net result of these nuclear processes is the conversion of four protons into one α particle mainly via the pp chain, to a small extent via the

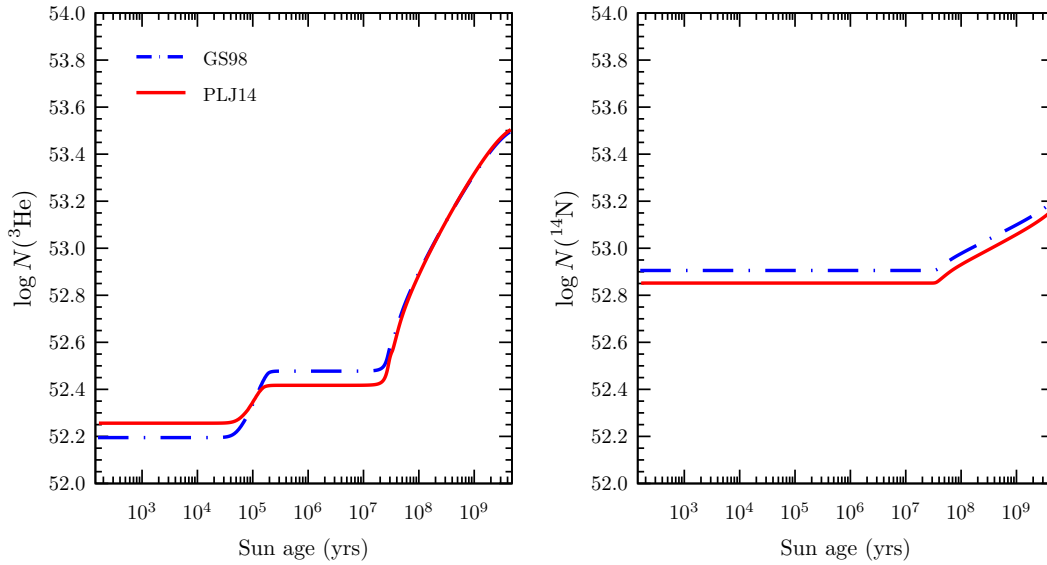


Figure 5.2: Temporal evolution of the total ${}^3\text{He}$ (left) and ${}^{14}\text{N}$ (right) abundances, adopting both GS98 (blue, dash-dotted line) and PLJ14 (red, solid line) solar compositions.

CNO I cycle, and, to a negligible extent, via the CNO II cycle. Every time four protons are destroyed (and a ${}^4\text{He}$ synthesized), two neutrinos are produced.

5.3.1 A critical examination of the standard luminosity constraint

However, the local nuclear equilibrium is exactly verified only in the innermost zones of the Sun, where the temperature is large enough that the production and destruction rates of intermediate isotopes attain nuclear equilibrium. For instance, in the standard formulation of the luminosity constraint (Bahcall and Krastev 1996; Bahcall 2002), it is assumed that ${}^3\text{He}$ is in local nuclear equilibrium in the whole Sun. As shown in Figure 5.1 the equilibrium abundance of ${}^3\text{He}$ (dashed blue line) changes along the structure as the temperature and density values change. In particular, the ${}^3\text{He}$ lifetime in the solar core is $\gtrsim 10^5$ yr, but it rapidly increases outward, resulting in an exponential increase of the equilibrium abundance. On the other hand in the real Sun, due to the temperature decrease, the cross section for ${}^3\text{He}$ production becomes lower and lower for mass coordinate above $M_r \sim 0.5 - 0.6 M_\odot$, thus its mass abundance rapidly goes to zero (solid blue line), largely departing from its local equilibrium abundance.

Similar considerations are valid also for the ${}^{14}\text{N}$: in the innermost zones of the Sun, below $M_r \sim 0.12 M_\odot$, its abundance is determined by the efficiency of the CNO cycle, while above this zone, where temperature is lower than $\sim 10^7$ K, it is not produced at all as p -captures can occur efficiently on neither ${}^{12}\text{C}$ nor ${}^{16}\text{O}$ (solid red line in Figure 5.1). At variance, the ${}^{14}\text{N}$ equilibrium abundance in this zone rapidly diverges (dashed red line). As a matter of fact, the total number of

both ${}^3\text{He}$ and ${}^{14}\text{N}$ nuclei in the whole Sun is expected to increase with the time, as currently obtained by computing SSMs (see Figure 5.2).

The other important assumption in deriving the luminosity constraint is that the release of energy in the Sun is due to nuclear reactions only. In the Sun (and more in general in real stars during the Main Sequence phase), however, part of the nuclear energy, the so-called “gravothermal energy”, is absorbed to produce an expansion against gravity on a timescale of few Myr. As a consequence, the surface solar luminosity is expected to be smaller than the energy produced in the central core by nuclear reactions per unit of mass. Relying on SSM calculations, Bahcall and Krastev (1996) argued that the gravothermal energy contribution to the solar photospheric luminosity is $\simeq 0.03\%$, substantially lower than the uncertainty of 0.4% for the value of $L_{\odot} = 3.844 \times 10^{33} \text{ erg s}^{-1}$ (Bahcall et al. 1995), available at that time. However, more recent determinations (Mamajek et al. 2015) are 10 times more precise and provide for the photospheric solar luminosity the value

$$L_{\odot} = 3.8275 (1 \pm 0.0004) \times 10^{33} \text{ erg s}^{-1}, \quad (5.2)$$

therefore, therefore, with an estimated uncertainty comparable with the gravothermal energy contribution to the solar luminosity.

We want to remark that usually in the computation of SSMs no simplifying assumptions are adopted, thus all the relevant physical and nuclear processes are consistently accounted for. The results of these computations, however, are based on many physical inputs (e.g. nuclear cross section, heavy elements initial abundances, radiative opacities, equation of state), simplifying hypotheses (e.g. approximate description of the convection, neglecting of mass loss processes, assumptions on primordial composition whose potential relevance was recently pointed out Zhang et al. 2019), and physical processes, such as gravitational settling of helium and heavy elements, whose uncertainties are definitively larger than those discussed above (for a review see Bahcall et al. 1995). For this reason, the luminosity constraint offers a unique tool to perform a model-independent analysis of the solar neutrino fluxes.

5.3.2 A derivation of the standard luminosity constraint

Before obtaining a more general formulation of the luminosity constraint, accounting for the small deviation from the local equilibrium assumption and for the gravothermal contribution to the surface solar luminosity, it is useful to begin by re-deriving this relation in its current “standard” form. To this aim we make use of just three assumptions², namely:

1. lepton number conservation: the nuclear fusion processes operating in the Sun inevitably produce neutrinos, which can be used to observe and “tag” such reactions;

²As discussed above, the last two hypotheses have only approximate validity and will be improved later.

2. source of the energy: the energy that goes into radiation (neutrinos and photons) comes entirely from nuclear reactions;
3. net effect of nucleosynthesis; hydrogen nuclei transform into ${}^4\text{He}$ while all other nuclear species remain unchanged.

The amount of energy delivered from the conversion of four protons into an α particle as a whole is equal to

$$Q_4 := M_4 - 4M_1 = 26.730\,97\text{ MeV}, \quad (5.3)$$

where M_1 and M_4 are the atomic mass of ${}^1\text{H}$ and ${}^4\text{He}$, respectively. In this way we automatically take into account the contribution due to the annihilation of the two positrons from β -decays with two electrons in the surrounding. Such energy eventually goes into photons and neutrinos, so that the solar luminosity (the power) can be expressed as

$$L_{\text{nuc}} = L_{\odot} + L_{\nu}. \quad (5.4)$$

Here L_{\odot} is the solar luminosity emitted in photons, L_{nuc} the contribution from nuclear reactions and L_{ν} is that emitted in neutrinos, i.e.

$$L_{\nu} = 4\pi\text{ au}^2 \sum_i \langle E_i \rangle \Phi_i, \quad (5.5)$$

where $\langle E_i \rangle$ is the average energy of neutrinos resulting from a certain reaction and “au” is the average Earth-Sun distance.

Considering ${}^4\text{He}$ as the sole synthesized nucleus, the conservation of energy relation reads

$$L_{\odot} + L_{\nu} = Q_4 \dot{N}({}^4\text{He}), \quad (5.6)$$

where $N({}^4\text{He})$ is the total number of ${}^4\text{He}$ nuclei in the Sun and $\dot{N}({}^4\text{He})$ is its time derivative.

As the synthesis of ${}^4\text{He}$ from ${}^1\text{H}$ requires the transformation of four protons into two protons and two neutrons, two neutrinos must be produced in the ensuing β^+ processes. We can then write the lepton number conservation as

$$4\pi\text{ au}^2 \sum_i \Phi_i = 2\dot{N}({}^4\text{He}), \quad (5.7)$$

as the rate of neutrino production is twice that of ${}^4\text{He}$ production. Solving Equation (5.7) for $\dot{N}({}^4\text{He})$ and substituting this expression and Equation (5.5) in Equation (5.6), we obtain

$$L_{\odot} + 4\pi\text{ au}^2 \sum_i \langle E_i \rangle \Phi_i = \frac{Q_4}{2} 4\pi\text{ au}^2 \sum_i \Phi_i, \quad (5.8)$$

thus the luminosity constraint relation becomes

$$\frac{L_{\odot}}{4\pi\text{ au}^2} = \sum_i \left(\frac{Q_4}{2} - \langle E_i \rangle \right) \Phi_i. \quad (5.9)$$

Table 5.2: The k_i factors, in units of $\text{MeV cm}^{-2} \text{s}^{-1}$, as defined in Equation (5.11).

i	k_i
pp	1.3099×10^{11}
Be	1.2552×10^{10}
pep	1.1920×10^9
B	6.6305×10^6
hep	3.7355×10^3
N	1.2658×10^9
O	1.2368×10^9
F	1.2365×10^7

Please, note that only now, when substituting the numerical values of Q_4 , $\langle E_i \rangle$ (on which we assume negligible uncertainty) as well as choosing which “kind” of neutrinos are produced, the nuclear physics details are needed. Throughout this work we adopt the values for $\langle E_i \rangle$ provided in Table 2 of Vissani (2019). As an example, let us assume that only neutrinos from the pp-chain are produced in the Sun: then, we would have $13.10 \text{ MeV} \times \Phi_{\text{pp}} = L_{\odot}/4\pi \text{ au}^2$, and so $\Phi_{\text{pp}} = 6.485 (1 \pm 0.0004) \times 10^{10} \text{ cm}^{-2} \text{ s}^{-1}$, the relative error descending directly from that on the solar luminosity value.

Including all the other solar neutrino components and dividing both sides of Equation (5.9) by $L_{\odot}/(4\pi \text{ au}^2) = 8.4946 \times 10^{11} \text{ MeV cm}^{-2} \text{ s}^{-1}$, we obtain

$$(1 \pm 0.04\%) = \frac{1}{8.4946 \times 10^{11}} \sum_i k_i \varphi_i, \quad (5.10)$$

where the k_i coefficients are defined as

$$k_i = \left(\frac{Q_4}{2} - \langle E_i \rangle \right) 10^{\gamma_i}. \quad (5.11)$$

The values of the k_i coefficients are listed in Table 5.2, while the γ_i factors, as defined in Equation (5.1), can be seen in Table 5.1.

From the argument above it follows that the luminosity constraint effectively links, within a very small 0.04% uncertainty, the pp, Be, pep, N and O neutrinos.

5.4 A new version of the luminosity constraint

The expression derived for the luminosity constraint can be generalized by relaxing the assumption that only ${}^4\text{He}$ is produced in the Sun and accounting for the deviation of ${}^3\text{He}$ and ${}^{14}\text{N}$ abundances from their equilibrium values in the region above the burning zone. This can be done by adding in Equation (5.6) new terms and weighting them accordingly to the corresponding produced neutrinos. In the same way, it is possible also to include energy term related to non-nuclear processes, such as the gravothermal energy. The resulting formulation of the luminosity constraint will be more refined and, most importantly, more accurate.

5.4.1 The departure from the local nuclear equilibrium

On a general ground, without any assumptions about the synthesized nuclei, the lepton number conservation as formulated in Equation (5.7) can be expressed as

$$4\pi \text{ au}^2 \sum_i \Phi_i = \sum_j c_j \dot{N}(j), \quad (5.12)$$

where c_j counts the number of electron neutrinos involved in the production of the nucleus j ; for example, as seen before, $c_{\text{He}} = 2$. The energy conservation (Equation (5.6)) would then become

$$L_\odot + L_\nu = \sum_j Q_j \dot{N}(j), \quad (5.13)$$

as now we are accounting for the production of more nuclei. As before, we can isolate $\dot{N}({}^4\text{He})$ from Equation (5.12) and substitute it into Equation (5.13), so that:

$$L_\odot + 4\pi \text{ au}^2 \sum_i \langle E_i \rangle \Phi_i = \frac{Q_4}{2} \left[4\pi \text{ au}^2 \sum_i \Phi_i - \sum_{j \neq {}^4\text{He}} c_j \dot{N}(j) \right] + \sum_{j \neq {}^4\text{He}} Q_j \dot{N}(j), \quad (5.14)$$

which results in

$$\frac{1}{4\pi \text{ au}^2} \left(L_\odot + \sum_{j \neq {}^4\text{He}} L_j \right) = \sum_i \left(\frac{Q_4}{2} - \langle E_i \rangle \right) \Phi_i, \quad (5.15)$$

having defined L_j as

$$L_j := \left(\frac{c_j Q_4}{2} - Q_j \right) \dot{N}(j). \quad (5.16)$$

These L_j terms represent the corrections to the power, that can be “tagged” by neutrinos (i.e. the right-hand-side of Equation (5.15)), due to the production of the intermediate isotope j other than ${}^4\text{He}$. As it is well known, the pp chain and the CNO cycle can be both naturally broken into two branches, each of them leading to the production of one intermediate isotopes and one neutrino, so it turns out $c_j = 1$. Therefore, the sign of the above quantities L_j depends on the energy released per neutrino, and, in the assumption that the abundance of the intermediate isotope increase with time (i.e., $\dot{N}(j) > 0$), it is positive if Q_j/c_j is less than $Q_4/c_{{}^4\text{He}}$.

The pp chain is broken into two parts: one corresponding to the first two reactions in the ppI chain ($\text{p}(\text{p}, \beta^+)^2\text{H}(\text{p}, \gamma){}^3\text{He}$), leading to the production of ${}^3\text{He}$, and the other, corresponding to the last reaction in ppI chain (${}^3\text{He}({}^3\text{He}, 2\text{p}){}^4\text{He}$) and those in ppII (${}^3\text{He}({}^4\text{He}, \gamma){}^7\text{Be}(e^-, \nu){}^7\text{Li}(\text{p}, \gamma){}^8\text{Be} \rightarrow {}^2{}^4\text{He}$)

Table 5.3: $\dot{N}(j)$ (units of 10^{35} s^{-1}) and L_j (units of $10^{30} \text{ erg s}^{-1}$) quantities, with relative uncertainties, involved in the formulation of the revised luminosity constraint, for GS98 ad PLJ14 models.

Models	$\dot{N}(^3\text{He})$	$\dot{N}(^{14}\text{N})$	$L_{^3\text{He}}$	$L_{^{14}\text{N}}$	L_g
GS98	$3.29(1 \pm 0.07)$	$2.15(1 \pm 0.13)$	$3.39(1 \pm 0.07)$	$0.57(1 \pm 0.13)$	$1.54(1 \pm 0.04)$
PLJ14	$3.42(1 \pm 0.07)$	$2.07(1 \pm 0.13)$	$3.53(1 \pm 0.07)$	$0.55(1 \pm 0.13)$	$1.52(1 \pm 0.04)$

and ppIII ($^3\text{He}(^4\text{He}, \gamma)^7\text{Be}(p, \gamma)^8\text{B} \rightarrow \beta^+ + ^8\text{Be} \rightarrow 2^4\text{He}$) chains, leading to the formation of one ^4He nucleus. On the other hand, the CNO I cycle is made by two branches as well, the CN and the NO; with ^{14}N acting as a bottleneck, due to the very low value of the p -capture cross section on this isotope as compared to those on C and O isotopes.

Broadly speaking, the time derivative of total number $\dot{N}(j)$ of a given isotopes j in Equation (5.16) can be expressed as

$$\dot{N}(j) = \frac{dN(j)}{dt} = \frac{N_A}{A_j} \int_0^{M_\odot} \frac{dX(j)}{dt} dM, \quad (5.17)$$

where N_A is the Avogadro number and $X(j)$ is mass fraction and A_j the relative atomic mass number of j -nucleus and the integration is performed on the whole mass of the Sun.

We estimated $\dot{N}(^3\text{He})$ and $\dot{N}(^{14}\text{N})$ by computing two different SSMS, adopting both GS98 and PLJ14 solar compositions, with the use of the FUNS evolutionary code (Piersanti et al. 2007; Vescovi et al. 2019). We used the same input physics as in Vescovi et al. (2019), except for the solar luminosity, for which we adopted the more precise and recent evaluation of Mamajek et al. (2015), and equation of state, for which we adopted the OPAL EOS2005 (Rogers et al. 1996). We also employed the p+p rate from Adelberger et al. (2011) (see also Marcucci et al. 2019). In Table 5.3 we show, for both GS98 and PLJ14 models, the ensuing predictions for $\dot{N}(^3\text{He})$ and $\dot{N}(^{14}\text{N})$.

In order to calculate the contribution to the luminosity constraint due to the non-equilibrium burning of ^3He and ^{14}N as described by Equation (5.15), we need also the energy released in the production of such nuclei, i.e., $Q_3 := M_3 - 3M_1 = 6.936 \text{ MeV}$ and $Q_{14} := M_{12} + 2M_1 - M_{14} = 11.710 \text{ MeV}$. Finally, as the production of ^3He and ^{14}N is always accompanied by the emission of one electron neutrino, their c_j factors are both equal to 1. In Table 5.3, we report also the corrective terms to the luminosity constraint due to the production of ^3He , ^{14}N , calculated from Equation (5.16). We find that these corrections are important and not negligible, being comparable or even larger than the present uncertainty on the solar luminosity.

We then estimated the uncertainty associated with the quantities L_j by considering that their sensitivity to the input parameters adopted in the computation of SSMS, β_k , can be expressed in terms of the logarithmic partial derivatives, $\lambda_{j,k}$

Table 5.4: Estimated 1σ uncertainties, for the GS98 (PLJ14) model, in solar (Bahcall and Pinsonneault 2004; Bahcall et al. 2006; Mamajek et al. 2015) and nuclear physics (Adelberger et al. 2011; Marta et al. 2011; Vinyoles et al. 2017), and their influence on L_j predictions, computed from the partial derivatives of Table 5.5.

β_j	Central value	$\frac{\Delta\beta}{\beta}$ (%)	$\frac{\Delta L_{^3\text{He}}}{L_{^3\text{He}}}$ (%)	$\frac{\Delta L_{^{14}\text{N}}}{L_{^{14}\text{N}}}$ (%)	$\frac{\Delta L_{\text{g}}}{L_{\text{g}}}$ (%)
L_{\odot}	3.8275×10^{33} erg s $^{-1}$	0.04	0.06 (0.07)	0.008 (0.009)	0.04 (0.04)
Opacity	1.0	2.5	1.54 (1.75)	0.41 (0.36)	0.75 (1.08)
Age	4.57 Gyr	0.44	0.73 (0.67)	0.15 (0.15)	0.15 (0.16)
Diffusion	1.0	15.0	2.68 (2.66)	3.17 (3.21)	1.80 (1.44)
Z/X	0.02292	15.0	5.04 (5.28)	12.83 (12.82)	3.62 (3.20)
$p+p$	4.01×10^{-25} MeV b	1.0	0.34 (0.43)	0.09 (0.09)	0.44 (0.51)
$^3\text{He}+^3\text{He}$	5.21 MeV b	5.2	2.17 (2.16)	0.25 (0.23)	0.55 (0.54)
$^3\text{He}+^4\text{He}$	0.56 MeV b	5.4	1.35 (1.13)	0.47 (0.44)	1.13 (1.10)
$p+^7\text{Be}$	21.3 eV b	4.7	0.008 (0.001)	0.0003 (0.0001)	0.01 (0.04)
$p+^{14}\text{N}$	1.59 keV b	7.5	0.46 (0.52)	0.14 (0.13)	0.34 (0.30)

(see e.g. Bahcall and Ulrich 1988), defined as

$$\lambda_{j,k} = \frac{\partial \ln L_j}{\partial \ln \beta_k}. \quad (5.18)$$

Hence, the total fractional uncertainty would be

$$\frac{\delta L_j}{L_j} = \left[\sum_k \left[\left(1 + \frac{\Delta\beta_k}{\beta_k} \right)^{\lambda_{j,k}} - 1 \right]^2 \right]^{1/2}, \quad (5.19)$$

where the contributions from individual uncertainties are quadratically combined. Standard deviations computed with this method, which relies on the assumption of linear response of solar models to changes in the input parameters, was shown to agree to better than 10% with those estimated by Monte Carlo simulations (Bahcall and Ulrich 1988). Due to the small uncertainties of the input parameters, in fact, linearity of solar models is usually a very good approximation (Villante and Ricci 2010).

Such input parameters, which are the major nuclear sources of uncertainties in calculating a SSM, and therefore affecting the predicted L_j , can be divided into two sets, corresponding to nuclear and “solar” β_k . The nuclear parameters are the astrophysical S -factors for $p+p$ (S_{11}), $^3\text{He}+^3\text{He}$ (S_{33}), $^3\text{He}+^4\text{He}$ (S_{34}), $p+^7\text{Be}$ (S_{17}), and $p+^{14}\text{N}$ (S_{114}) reactions. The most important “solar” uncertainties arise from the measured photon luminosity L_{\odot} , the mean radiative opacity, the solar age, the efficiency of He and metals gravitational settling, and the surface metallicity relative to the hydrogen abundance ($(Z/X)_{\odot}$). In order to estimate the percentage uncertainties $\delta L_j/L_j$ in Equation (5.19), we compute many SSMs by varying all the previous listed quantity inside their 1σ fractional uncertainties $\Delta\beta_k/\beta_k$ as given in Table 5.4. In the same Table, we also report the values of the fractional

Table 5.5: Partial derivatives $\lambda_{j,k}$ of relevant quantities involved in the formulation of the revised luminosity constraint, with respect to solar environmental parameters and S-factors. Table entries are the logarithmic partial derivatives $\lambda_{j,k}$ of the defined quantities L_j with respect to the indicated solar model parameter β_k , taken from the GS98 (upper row) and PLJ14 (lower row) SSM best values.

Source	β_k									
	L_\odot	Opacity	Age	Diffusion	Z/X	S_{11}	S_{33}	S_{34}	S_{17}	S_{114}
$L_{^3\text{He}}$	-1.504	-0.627	-1.676	-0.194	-0.370	0.337	-0.432	0.255	-0.002	0.063
	-1.678	-0.717	-1.533	-0.193	-0.388	0.435	-0.431	0.214	0.000	0.072
$L_{^{14}\text{N}}$	0.191	-0.166	-0.332	2.094	0.864	0.095	0.050	-0.089	0.000	-0.020
	0.233	-0.146	-0.336	2.119	0.863	0.095	0.045	-0.084	0.000	-0.018
L_g	1.062	0.303	0.333	0.127	0.255	-0.446	-0.110	0.213	-0.002	0.048
	1.118	0.434	0.364	0.102	0.225	-0.519	-0.106	0.208	-0.001	0.042

uncertainties on L_j , produced by a variation of the individual input β_k . Such errors are computed by means of $\lambda_{j,k}$ values listed in Table 5.5. Eventually, Table 5.3 summarizes our best estimates of L_j and their relative theoretical errors.

The correction to the solar luminosity due to the non-equilibrium burning of ^{14}N can also be evaluated according to the connection among $\dot{N}(^{14}\text{N})$, Φ_{O} and Φ_{N} , by assuming that the $^{12}\text{C} \rightarrow ^{14}\text{N}$ and $^{15}\text{O} \rightarrow ^{12}\text{C}$ branches of the CNO I cycle proceed fast (see, e.g., Vissani 2019). In fact, the emission of a “nitrogen neutrino” in the reaction $^{13}\text{N}(e^+ \nu_e)^{13}\text{C}$ precedes the production of ^{14}N , while, every time that a ^{14}N nucleus is destroyed, an “oxygen neutrino” is emitted in the reaction $^{15}\text{O}(e^+ \nu_e)^{15}\text{N}$. This means that the difference in the neutrino fluxes from $\Phi_{\text{N}} - \Phi_{\text{O}}$ keeps track of the accumulation of ^{14}N as

$$\dot{N}(^{14}\text{N}) \simeq 4\pi \text{ au}^2 (\Phi_{\text{N}} - \Phi_{\text{O}}). \quad (5.20)$$

Adopting Φ_{N} and Φ_{O} from Table 5.1, this results in $\dot{N}(^{14}\text{N}) \simeq 2.09 \times 10^{35} \text{ s}^{-1}$ and $\dot{N}(^{14}\text{N}) \simeq 2.02 \times 10^{35} \text{ s}^{-1}$ for the GS98 and the PLJ14 models, respectively. The difference with respect to the values reported in Table 5.3 arises from a (small) non-zero value for $\dot{N}(^{13}\text{C})$. Note that, in principle, $\dot{N}(^{14}\text{N})$ can be determined from experimental measured values for Φ_{N} and Φ_{O} , if available, or alternatively from $\Phi_{\text{CN}} = \Phi_{\text{N}} + \Phi_{\text{O}}$, given the stringent value for the $\Phi_{\text{N}}/\Phi_{\text{O}}$ ratio (see Section 5.5).

5.4.2 Non-stationary luminosity constraint

Due to hydrogen burning, the average molecular weight in the innermost zone of the Sun progressively increases. As a consequence, the solar structure must continually re-adjust on a new equilibrium configuration to preserve the hydrostatic equilibrium. This implies that the Sun steadily increases its inner temperature and its photospheric luminosity, getting prepared gradually to become a red giant. In order to account for these changes in the solar structure, the contribution of

gravothermal energy has to be included in Equation (5.13) as:

$$L_{\odot} + L_{\nu} = \sum_j Q_j \dot{N}(j) - L_g. \quad (5.21)$$

For a star evolving in time, L_g is defined as

$$L_g \doteq \int_0^{M_{\odot}} \left[-\frac{dU}{dt} + \frac{P}{\rho^2} \frac{d\rho}{dt} \right] dM, \quad (5.22)$$

where U (erg g^{-1}) is the local internal energy, P (dyne cm^{-2}) is the local pressure, and ρ ($g\ cm^{-3}$) is the local density. By adopting this formulation, we are neglecting the energy contribution due to the chemical potential of ions produced/destroyed in nuclear processes because this term is order of magnitudes lower than those related to the variation of the internal energy and to the pressure work. The quantity L_g represents the rate at which the changes in internal energy $\dot{E}_{\text{int}} = \int_0^{M_{\odot}} dU/dt\ dM$ and compressional work $\dot{E}_{\text{work}} = \int_0^{M_{\odot}} (P/\rho^2) (d\rho/dt) dM$ contribute to the stellar luminosity. The gravothermal luminosity L_g can be directly evaluated by approximating the derivative in Equation (5.22) with finite difference between two models, one at the epoch $t = t_{\odot}$ (see Table 5.4) and the other at the epoch $t = t_{\odot} - dt$, where dt is the last evolutionary time step. We computed L_g both for GS98 and PLJ14 models (see Table 5.3). Analogously to Section 5.4, we estimated the global uncertainty affecting L_g , by considering all the SSM-inputs with their errors, and computing the relative partial derivatives. Table 5.5 shows the partial derivatives $\lambda_{j,k}$. We remark once again that the estimated values of L_g are comparable with the present uncertainty for L_{\odot} and, therefore, should be included for a precise derivation of the luminosity constraint.

5.4.3 Summary

Basing on Equation (5.21) and Equation (5.15) we can now write the luminosity constraint in its general form as

$$\frac{1}{4\pi\ \text{au}^2} (L_{\odot} + L_{3\text{He}} + L_{14\text{N}} + L_g) = \sum_i \left(\frac{Q_4}{2} - \langle E_i \rangle \right) \Phi_i. \quad (5.23)$$

The values of the new quantities that appear in the equation above are given in Table 5.3, for the two SSMs considered in this work. We note that the first two terms $L_{3\text{He}}$ and $L_{14\text{N}}$ are both positive (see Section 5.4.1), the latter being particularly small because the energy released in the production of ^{14}N is only a bit less than $Q_4/2$. The rate of gravothermal energy production L_g , determined by the rate of change of the molecular weight in the innermost zones of the Sun, is gained at the expense of the energy delivered by nuclear reactions: as a consequence, the same amount of nuclear reactions (and of neutrinos) would correspond to a photon luminosity diminished by L_g . As the solar luminosity is

fixed by observations, and the three new terms are all positive, this means that their net effect is to increase the number of expected neutrinos. This is quite evident by putting Equation (5.23) in the same form of Equation (5.10), namely

$$(1 \pm \sigma) = \frac{1}{\mathcal{F}} \sum_i k_i \varphi_i, \quad (5.24)$$

where the values of the k_i are still the one given in Table 5.2, and

$$\mathcal{F} = \frac{L_\odot + L_{3\text{He}} + L_{14\text{N}} + L_{\text{g}}}{4\pi \text{ au}^2} \quad (5.25)$$

where

$$\mathcal{F}(\text{GS98}) = 8.5068 \times 10^{11} \quad \mathcal{F}(\text{PLJ14}) = 8.5070 \times 10^{11}$$

The error σ in the previous equation can be evaluated with simple error propagation from table 5.3: in both GS98 and PLJ14 composition models we obtain

$$\sigma = 0.04\%.$$

Summarizing the result of this discussion, the new contributions can be included by changing the value of the coefficient in the denominator of Equation (5.10) with the new coefficient \mathcal{F} .

5.5 Luminosity constraint and the search for CNO neutrinos

In view of the experimental state-of-the-art of solar neutrino measurements, it is interesting to illustrate the use of the luminosity constraint to improve the search for CNO neutrinos.

From Table 5.2 it is clear that neutrinos from CNO, in particular N and O neutrinos, play an important role in the determination of φ_{pp} in the context of the luminosity constraint, which helps linking φ_{pp} and φ_{CNO} to each other. In fact, the luminosity constraint by itself is not enough to improve our knowledge on these neutrino fluxes; however, when further theoretical information on the $\Phi_{\text{pep}}/\Phi_{\text{pp}}$ and on the $\Phi_{\text{O}}/\Phi_{\text{N}}$ ratios is provided, then a stringent relation between the pp and CNO fluxes can be obtained. At first glance, one could believe that the usage of this theoretical information would make this application model-dependent, but this is not the case.

The ratio of the pp and pep reaction rates is fixed by nuclear physics (Adelberger et al. 2011), and such rate is assumed also for the pp and pep neutrino fluxes which, *a priori*, could be different due to the impact of the whole ensemble of processes occurring in the Sun.

Comparing how the pep to pp neutrino fluxes change with different metallicities, we get: $\Phi_{\text{pep}}/\Phi_{\text{pp}}|_{\text{GS98}} = 2.375 \times 10^{-3}(1 \pm 0.012)$ and $\Phi_{\text{pep}}/\Phi_{\text{pp}}|_{\text{PLJ14}} = 2.383 \times 10^{-3}(1 \pm 0.012)$ The uncertainty of each ratio was obtained combined

quadratically the errors as discussed in Section 5.4.1. This result reinforces the assumption that such a ratio is largely model-independent and that it depends on nuclear physics only.

Regarding the ratio of N and O neutrinos, if we assume that only ${}^4\text{He}$ is produced, its value is exactly 1, due to the nuclear equilibrium of all nuclei in the CNO cycles. As discussed in Section 5.4.3, however, because of the slowness ${}^{14}\text{N}(p, \gamma){}^{15}\text{O}$, the CN cycle does not reach the equilibrium and ${}^{13}\text{N}$ neutrinos are slightly more abundant than the ${}^{15}\text{O}$ neutrinos. The ratio $\Phi_{\text{O}}/\Phi_{\text{N}}$ is then fixed to be < 1 , with a value depending upon the adopted SSM. For the two SSMs we calculated, the ratios are: $\Phi_{\text{O}}/\Phi_{\text{N}}|_{\text{GS98}} = 0.742(1 \pm 0.053)$ and $\Phi_{\text{O}}/\Phi_{\text{N}}|_{\text{PLJ14}} = 0.722(1 \pm 0.056)$. Such a variation due to different SSMs affects the luminosity constraint so slightly (less than 0.02%) that the model-dependence is not a significant issue also in this regard.

The same procedure can be used to link the F neutrinos to the N ones; in this case $\Phi_{\text{F}}/\Phi_{\text{N}}|_{\text{GS98}} = 0.019(1 \pm 0.085)$ and $\Phi_{\text{F}}/\Phi_{\text{N}}|_{\text{PLJ14}} = 0.016(1 \pm 0.086)$. Thanks to the arguments above, the required ratios of neutrino fluxes are

$$\Phi_{\text{pep}}/\Phi_{\text{pp}} = 2.379(1 \pm 0.012) \times 10^{-3} \quad (5.26)$$

$$\Phi_{\text{O}}/\Phi_{\text{N}} = 0.732(1 \pm 0.06) \quad (5.27)$$

$$\Phi_{\text{F}}/\Phi_{\text{N}} = 0.017(1 \pm 0.12) . \quad (5.28)$$

Such values are obtained by averaging the two results and keeping into account the theoretical errors and the difference between the two predictions, summing in quadrature these uncertainties. Note that the first uncertainty is similar, slightly smaller, to the value 1.4% adopted by Borexino collaboration (Agostini et al. 2020b,a).

Now, we proceed to derive of a constraint between the pp and N neutrino fluxes using these ratios and including the information on the fluxes which have been already measured. After Borexino phase-II (Agostini et al. 2019), ${}^7\text{Be}$ neutrinos are very well known and their flux is fixed with a precision better than the theoretical one to

$$\Phi_{\text{Be}} = (4.99 \pm 0.11_{-0.08}^{+0.06}) \times 10^9 \text{ cm}^{-2} \text{ s}^{-1} . \quad (5.29)$$

Also the boron neutrino flux, after four phases of Super-Kamiokande operation (Abe et al. 2016), is very well known to be

$$\Phi_{\text{B}} = 5.41(1 \pm 0.016) \times 10^6 \text{ cm}^{-2} \text{ s}^{-1} . \quad (5.30)$$

Note that, while the value of the beryllium flux is quite important for the luminosity constraint, the value of the boron flux has a very small relevance; therefore, the inclusion of the SNO measurement, given in Table (5.1), has no impact in practice.

Equation (5.10) can be rewritten as

$$\begin{aligned} (1 \pm 0.04\%) = & 0.15420 \varphi_{\text{pp}} + 0.01478 \varphi_{\text{Be}} + 0.00140 \varphi_{\text{pep}} \\ & + 0.00149 \varphi_{\text{N}} + 0.001456 \varphi_{\text{O}} + 1.46 \times 10^{-5} \varphi_{\text{F}} \\ & + 7.81 \times 10^{-6} \varphi_{\text{B}} . \end{aligned} \quad (5.31)$$

Table 5.6: The central value, in units of $10^{10} \text{ cm}^{-2} \text{ s}^{-1}$, of the constraint (with 0.2% precision) as described in Equation (5.34), including the various refinements of Section 5.4.

corrective terms	GS98	PLJ14	average
none	5.9936	5.9936	5.9936
$L_{3\text{He}}$	5.9994	5.9996	5.9995
$L_{3\text{He}} + L_{14\text{N}}$	6.0004	6.0006	6.0005
$L_{3\text{He}} + L_{14\text{N}} + L_g$	6.0030	6.0031	6.0031

Introducing the ratios obtained in Equations (5.26)–(5.28), we have:

$$(1 \pm 0.04\%) = 0.15453 \varphi_{\text{pp}} + 0.002556 \varphi_{\text{N}} + 0.01478 \varphi_{\text{Be}} + 7.81 \times 10^{-6} \varphi_{\text{B}} \quad (5.32)$$

and now we can subtract the beryllium and boron contribution:

$$(0.9262 \pm 0.0022) = 0.15453 \varphi_{\text{pp}} + 0.002556 \varphi_{\text{N}} \quad (5.33)$$

thus, isolating Φ_{pp} :

$$\Phi_{\text{pp}} + 1.654 \Phi_{\text{N}} = 5.994 (1 \pm 0.2\%) \times 10^{10} \text{ cm}^{-2} \text{ s}^{-1} \quad (5.34)$$

The main contribution to the 0.2% error is due to the experimental uncertainty in the beryllium neutrino flux; therefore, in principle, this can be decreased in the future. As already remarked, the contribution of the boron flux is much less relevant.

The impact of the uncertainties on the of ratios Equations (5.26)–(5.27) modify the prefactor of Φ_{N} in Equation (5.34), in that its 1σ range is $1.654(1 \pm 0.025)$. Given the fact that Φ_{pp} is roughly more than 200 times larger than Φ_{N} , we conclude that a 2.5% variation of the Φ_{N} prefactor induces an error of 0.02%, which is negligible for the purposes of Equation (5.34). We can then conclude that the uncertainties in Equations (5.26)–(5.28) do not introduce any significant model dependence in Equation (5.34).

In order to include the corrections described in Section 5.4, it is sufficient to replace the right-hand side value of the above equation with the values given in Table 5.6. Including the contribution due to the corrective terms $L_{3\text{He}}$, $L_{14\text{N}}$, and L_g one obtains:

$$\Phi_{\text{pp}} + 1.654 \Phi_{\text{N}} = 6.003 (1 \pm 0.2\%) \times 10^{10} \text{ cm}^{-2} \text{ s}^{-1}. \quad (5.35)$$

Note that, since the relative difference between the corrective terms for GS98 and PLJ14 models is about $\simeq 0.003\%$ (see last row of Table 5.6), this relation links pp and nitrogen neutrino fluxes without a significant impact on the assumptions for the solar core metallicity. Equation (5.35) can also be expressed in terms of $\Phi_{\text{CNO}} = \Phi_{\text{N}} + \Phi_{\text{O}} + \Phi_{\text{F}}$, as

$$\Phi_{\text{pp}} + 0.946 \Phi_{\text{CNO}} = 6.003 (1 \pm 0.2\%) \times 10^{10} \text{ cm}^{-2} \text{ s}^{-1}. \quad (5.36)$$

5.6 Conclusive remarks

In this work we derived an improved version the luminosity constraint, by relaxing two of the fundamental assumptions adopted in the original standard derivation of Bahcall (2002) as well as in Vissani (2019), i.e. the local nuclear equilibrium of all the isotopes involved in the trasformations of 4 protons into a ^4He and the stationarity of the solar structure. The relation we obtained represents the most straightforward, complete and useful one currently available.

In his seminal work (Bahcall 2002), Bahcall stated:

If nuclear fusion reactions among light elements are responsible for the solar luminosity, then a specific linear combination of solar neutrino fluxes must equal the solar constant [...]

$$\frac{L_{\odot}}{4\pi\text{au}^2} = \sum_i \left(\frac{\alpha_i}{10\text{MeV}} \right) \Phi_i$$

[...] The coefficient α_i is the amount of energy provided to the star by nuclear fusion reactions associated with each of the important solar neutrino fluxes, Φ_i .

In our formulation, as detailed in Section 5.3, the factors analogous to Bahcall's α_i are:

$$\alpha_i = 10^{-\gamma_i-1} k_i,$$

where the $\gamma_i + 1$ comes from the normalization of α_i factors to 10 MeV. For the neutrinos coming from the CNO cycles we obtain in our formalism:

$$\alpha_{\text{N}} = \frac{M_{12} + M_1 - M_{13} - \langle E_{\text{N}} \rangle}{10\text{MeV}} = 0.34570 \quad (5.37)$$

$$\alpha_{\text{O}} = \frac{3M_1 + M_{13} - M_4 - M_{12} - \langle E_{\text{O}} \rangle}{10\text{MeV}} = 2.157 \quad (5.38)$$

$$\alpha_{\text{F}} = \frac{M_{16} + M_1 - M_{17} - \langle E_{\text{F}} \rangle}{10\text{MeV}} = 0.2361 \quad (5.39)$$

where we make use of the updates values for the nuclear masses of the involved isotopes. We want to remark that such an approach does not distinguish the CNO bi-cycle at its slowest node, i.e. at ^{14}N , and this represents the main reason for the critical analysis performed in Vissani (2019).

In Table 5.7 we compare our results with those from Bahcall (2002) and, as it is quite evident, the factors are very close to each others. This demonstrates that our approach is fully consistent with that used in Bahcall (2002). There is, however, a notable exception regarding the α_{Be} value. In the computation of that factor, Bahcall stated:

[...] one must average over the two ^7Be neutrino lines with the appropriate weighting *and include the γ -ray energy from the 10.3% of the decays that go to the first excited state of ^7Li .*

Table 5.7: The matching of Bahcall’s formalism from Bahcall (2002) (α_i column) to ours.

i	α_i Bahcall (2002)	$10^{-\gamma_i-1}k_i$ this work
pp	1.309 87	1.309 87
pep	1.191 93	1.192 05
hep	0.373 70	0.373 55
Be	1.260 08	1.255 25
B	0.663 05	0.663 05

We believe that this procedure leads to double counting the largest energy that neutrinos can have in such a decay, as first noted in Vissani (2019).

In Equation (5.34) we provide a form of the luminosity constraint which is ready to be used in pp and CNO neutrino analyses, something impossible 20 years ago, by incorporating the neutrino fluxes from ${}^7\text{Be}$ and ${}^8\text{B}$, which are currently very well determined experimentally. This was envisioned by Bahcall in Bahcall (2002):

In the future, the generalized luminosity constraint can and should be implemented in analyses that determine solar neutrino parameters. The additional constraint provided by the measured solar luminosity will be especially important when pp and ${}^7\text{Be}$ neutrino fluxes are measured as well as the ${}^8\text{B}$ neutrino flux. As more experimental data become available, the analyses of neutrino oscillations will become more independent of the standard solar model and it will be natural and convenient to incorporate the luminosity constraint.

Our formulation of the luminosity constraint is more accurate, as it includes more precise values of the solar luminosity and of the atomic masses as compared to Bahcall (2002). Moreover, it is also more general, as it allow us to include the effects of non-equilibrium in nuclear processes as well as non-nuclear energy terms, as detailed in Equation (5.15).

In particular, we explicitly considered the effects of non-equilibrium abundances of ${}^3\text{He}$ and ${}^{14}\text{N}$ and the gravothermal energy contribution to the total energy budget, thus improving the constraint on the linear combination of all solar neutrino fluxes (see Equation (5.24)). Basing on such equation we derived a ready-to-use relation, linking the pp and CNO neutrino fluxes (see Equation (5.36)) and we presentd in Table 5.6 the impact of the considered corrective terms above.

The very high precision of the measured photospheric solar luminosity (Equation (5.2)) gives us the possibility to test the relevance of such corrections, even if in the final expression (Equation (5.34)) such refinements do not have a sizable impact. This is due to the fact that the current determination of the ${}^7\text{Be}$ flux is not sufficiently precise – compare Equations (5.32) and (5.33). This is the

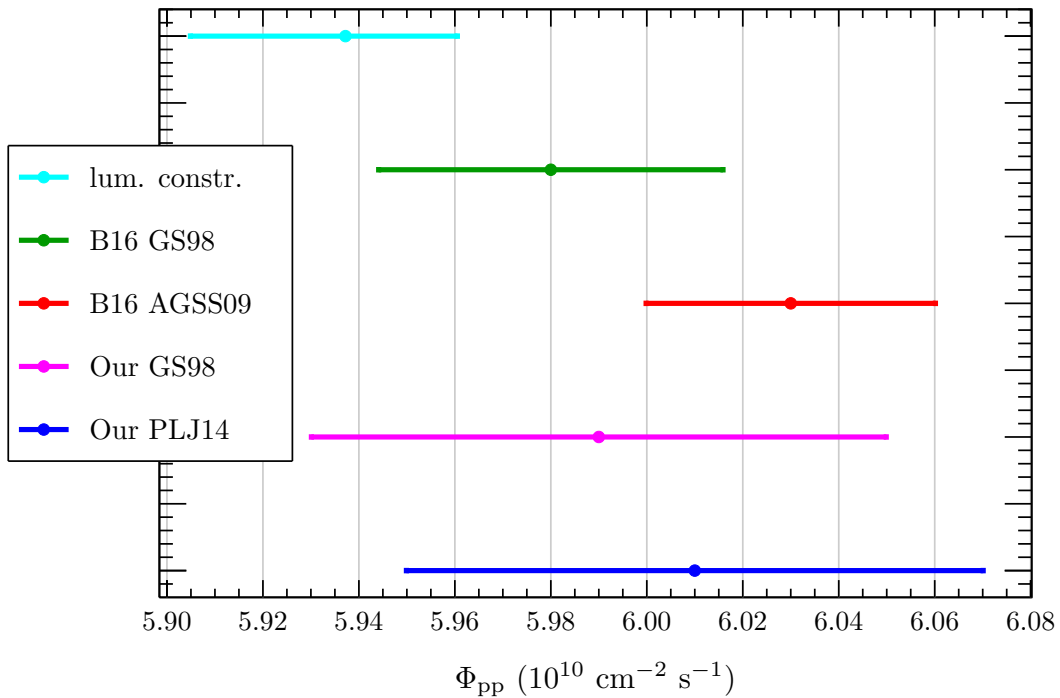


Figure 5.3: The comparison among the theoretical predictions on the pp neutrino flux from Vinyoles et al. (2017) (“B16”), our theoretical predictions (see Table 5.1), and the constrained value resulting from incorporating the CNO flux (as measured by Borexino in Agostini et al. 2020a) in Equation (5.36), in which all corrections are considered (blue cyan bar). The bars show the 1σ range.

limiting factor of the current numerical precision of the luminosity constraint, namely 0.2%.

As a final application, we make use of Equation (5.36) along with the very recent measurement of CNO neutrinos by Borexino collaboration (see Table 5.1), to derive the corresponding pp neutrino flux:

$$\Phi_{pp} = 5.937^{+0.023}_{-0.032} \times 10^{10} \text{ cm}^{-2} \text{ s}^{-1}. \quad (5.40)$$

The asymmetric range reflects the range for the CNO flux found by Borexino. Note that if we used the “naive” version of the luminosity constraint (the one that leads to Equation (5.34) rather than Equation (5.35)) the central value would decrease from 5.937 to 5.928, namely by 0.2%, the same amount of the uncertainty in the luminosity constraint. Moreover, is the uncertainty in the measurement of the CNO neutrinos that dominates the error in Φ_{pp} and not the 0.2% uncertainty in the luminosity constraint; thus, improved measurements will reduce this error.

The value of the flux in Equation (5.40) is compared in Figure 5.3 with several theoretical SSM predictions: see the value indicated with the label *lum. constr.*. Such a value is marginally consistent, within the estimated uncertainties, with theoretical predictions for models assuming an high abundance of heavy elements (B16 GS98, Our GS98) and, to a lesser extent, for Our PLJ14 model. A possible

explanation for such an evidence is that SSMs currently predict a too low CNO abundance in the solar core. This interpretation is in agreement with the analysis performed in Gough (2019) who suggested that the total metal content in the solar core (Z_c) where CNO neutrinos are produced linearly depends on Φ_{CNO} . In fact, by making use of the value measured by the Borexino collaboration for the CNO neutrino flux and the relation provided by Gough (2019) (see their Equation (1)), the estimated metallicity in the solar core should be $Z_c = 0.028^{+0.012}_{-0.008}$, whereas for the high metallicity SSM computed in the present work (GS98) we obtain $Z_c = 0.02024 \pm 0.00731$. This fact could give new insights and raise new questions regarding the metal content in solar core and/or possibly the approximations adopted in the current versions of the SSM.

The content of this chapter has been published in Vescovi et al. (2021)³. As the first author, I performed all solar model calculations and most of the data analysis. I wrote a large part of the text. I contributed significantly to the development of the equations, interpretation of the results, and figure creation.

³The luminosity constraint in the era of precision solar physics. *JPhG*, 48(1):015201. doi: [10.1088/1361-6471/abb784](https://doi.org/10.1088/1361-6471/abb784). Reproduced with permission from Journal of Physics G: Nuclear and Particle Physics, © IOP Publishing

On the origin of the early solar system radioactivities

Problems with the AGB and massive star scenarios

Recent improvements in stellar models for intermediate-mass and massive stars are recalled, together with their expectations for the synthesis of radioactive nuclei of lifetime $\tau \lesssim 25$ Myr, in order to re-examine the origins of now extinct radioactivities, which were alive in the solar nebula. The Galactic inheritance broadly explains most of them, especially if r -process nuclei are produced by neutron star merging according to recent models. Instead, ^{26}Al , ^{41}Ca , ^{135}Cs and possibly ^{60}Fe require nucleosynthesis events close to the solar formation. We outline the persisting difficulties to account for these nuclei by Intermediate Mass Stars ($2 \lesssim M/M_{\odot} \lesssim 7 - 8$). Models of their final stages now predict the ubiquitous formation of a ^{13}C reservoir as a neutron capture source; hence, even in presence of ^{26}Al production from Deep Mixing or Hot Bottom Burning, the ratio $^{26}\text{Al}/^{107}\text{Pd}$ remains incompatible with measured data, with a large excess in ^{107}Pd . This is shown for two recent approaches to Deep Mixing. Even a late contamination by a Massive Star meets problems. In fact, inhomogeneous addition of Supernova debris predicts non-measured excesses on stable isotopes. Revisions invoking specific low-mass supernovae and/or the sequential contamination of the pre-solar molecular cloud might be affected by similar problems, although our conclusions here are weakened by our schematic approach to the addition of SN ejecta. The limited parameter space remaining to be explored for solving this puzzle is discussed.

6.1 Short-lived radioactivities in the ESS

Measurements revealing that several radioactive species with half-lives ranging from less than one to hundreds of million years were present alive in solids of the

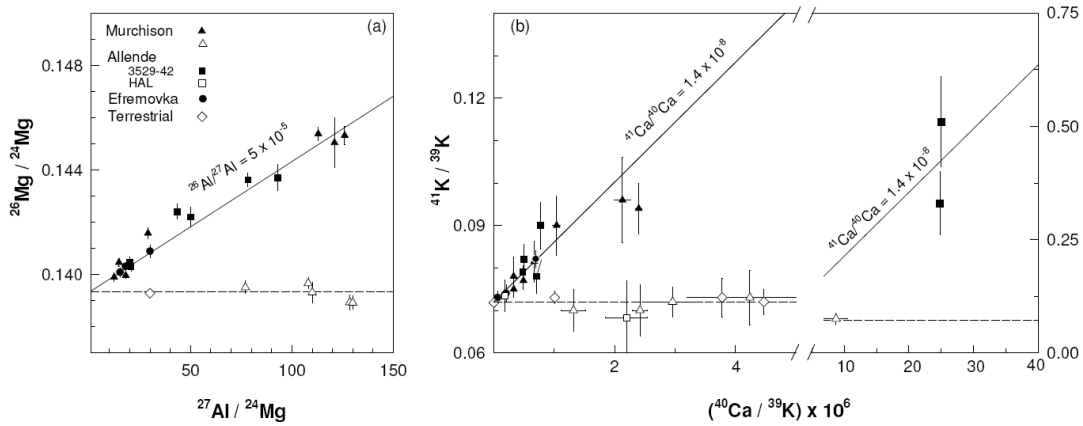


Figure 6.1: Panel a) shows the Al-Mg data from Calcium and Aluminum Inclusions (CAIs) in various meteorites; the straight-line fit to the filled symbols is for the so-called canonical value of $(^{26}\text{Al}/^{27}\text{Al})_0$ in the ESS, $\simeq 5 \cdot 10^{-5}$. Panel b) shows the Ca-K data from the same samples used for Panel a). First measurements and the line pointing to $(^{41}\text{Ca}/^{40}\text{Ca})_0 = 1.4 \cdot 10^{-8}$ were due to Srinivasan et al. (1994) and Srinivasan et al. (1996). The suggestion of a correlation with Al was due to Sahijpal et al. (1998). This figure is reproduced from these last authors and from Wasserburg et al. (2006). Copyright: Nature Publishing Group. (Note that subsequent work by Liu et al. 2012, proved that the initial ^{41}Ca abundance was lower, at the level of $(^{41}\text{Ca}/^{40}\text{Ca})_0 \sim 4.2 \cdot 10^{-9}$).

Early Solar System (ESS) gradually accumulated in the past decades, after the pioneering work by Reynolds (1960) on ^{129}I . These nuclei, in the present context, are referred to as *short-lived radioactivities* (SLRs).

Identification today of the stable decay product (and of its abundance) for a nucleus of this kind, permits then to extrapolate backwards, deriving the original abundance of the unstable isotope (Busso et al. 1999; Wasserburg et al. 2006; Davis and McKeegan 2014). A description of the procedure can be found, e.g., in Lee et al. (1976). Figure 6.1 shows this technique, as applied to ^{26}Al and ^{41}Ca ; the figure is taken from the work by Sahijpal et al. (1998).

The wealth of new measurements on ESS samples has now become impressive. It soon posed the crucial question of which was the astrophysical interpretation of their presence: this problem is still partly unsolved now. It is in any case evident that, although solid materials formed in a very short lapse of time (from a fraction of a Myr to a few Myrs), they somehow maintain the records of several phenomena, from the possible blend of various stellar nucleosynthesis processes (Busso 2011, 2018), to traces of spallation effects induced in the solar nebula itself (Sossi et al. 2017). For a detailed account of the science built in the last 60 years with short-lived nuclei we refer to dedicated reviews – see e.g. Busso et al. (1999); Kratz et al. (2004); Wasserburg et al. (2006); Wadhwa et al. (2007); Huss et al. (2007); Davies et al. (2014); Davis and McKeegan (2014).

Some of the experimental estimates for early SLR abundances are still uncertain and subject to discussions. This often occurs for nuclei of metals that are

Table 6.1: Short-Lived Nuclei in the ESS^a.

Rad.	Ref.	τ_R (Myr)	$[N^R/N^S]_{\text{Meas.}}$
¹⁰ Be	⁹ Be	2.0	$(8.8 \pm 0.6) \cdot 10^{-4}$
²⁶ Al	²⁷ Al	1.03	$(5.23 \pm 0.13) \cdot 10^{-5}$
³⁶ Cl	³⁵ Cl	0.43	$1.8 \cdot 10^{-5}$
⁴¹ Ca	⁴⁰ Ca	0.15	$4 \cdot 10^{-9}$
⁵³ Mn	⁵⁵ Mn	5.3	$(6.7 \pm 0.56) \cdot 10^{-6}$
⁶⁰ Fe	⁵⁶ Fe	3.75	$10^{-8} - 10^{-6}$
¹⁰⁷ Pd	¹⁰⁸ Pd	9.4	$(5.9 \pm 2.2) \cdot 10^{-5}$
¹²⁹ I	¹²⁷ I	23	$1.0 \cdot 10^{-4}$
¹³⁵ Cs	¹³³ Cs	3.3	$4.8 \cdot 10^{-4}$
¹⁸² Hf	¹⁸⁰ Hf	12.8	$(9.81 \pm 0.41) \cdot 10^{-5}$
²⁰⁵ Pb	²⁰⁴ Pb	22	10^{-3}
²⁴⁷ Cm	²³² Th	23	$(1.1 - 2.4) \cdot 10^{-3}$
¹⁴⁶ Sm	¹⁴⁴ Sm	148	$1.0 \cdot 10^{-2}$

^a For general references see Wasserburg et al. (2006) and Davis and McKeegan (2014). Among recently revised abundances, for ¹⁰Be see Chaussidon et al. (2006); for ⁶⁰Fe see Tang and Dauphas (2012); for ¹⁰⁷Pd see Schönbächler et al. (2008); for ¹³⁵Cs see Hidaka and Yoneda (2013); for ¹⁸²Hf see Burkhardt et al. (2008); for ²⁰⁵Pb see Baker et al. (2010); for ²⁴⁷Cm, see Brennecka et al. (2010).

extremely difficult or impossible to measure in pristine refractory condensates, so that their inferred initial abundances in the ESS require extrapolations from measurements made on subsequent, differentiated objects. In this field it is of particular importance the case of ⁶⁰Fe. The values derived for the initial abundance ratio ⁶⁰Fe/⁵⁶Fe wandered across the large range from a few 10^{-9} (Tang and Dauphas 2012) to about 10^{-6} (Mostefaoui et al. 2005). The review by Davis and McKeegan (2014) discusses in some detail how the inference of an initial ratio, based on absolute age determinations for the eucrite samples where it was early measured, are bound to suffer for large systematic uncertainties. Those authors privileged the lowest values presented in the literature; however, there does not seem to exist a general agreement on this, especially in view of the possible large internal modifications of the abundances in the samples, subsequent to the Solar System formation (Telus et al. 2016); see also Boss (2017). The most recent measurements by Trappitsch et al. (2018) stay in the lower part of the spread, but suggest an initial abundance considerably higher than the choice by Davis and McKeegan (2014). We shall therefore consider this isotopic ratio as being uncertain inside the wide range $10^{-8} - 10^{-6}$.

In Table 6.1 we try to fix reasonable ESS abundance ratios ($[N^R/N^S]_{\text{Meas.}}$) for SLRs with mean life (τ_R) lower than 25 Myr. We also include ¹⁴⁶Sm as an example of longer lived nuclei. We adopt mainly Davis and McKeegan (2014) as a reference; this will be in general adequate for our purposes, with the mentioned

exception of ^{60}Fe .

In the last 40 years a wealth of astrophysical models were presented in the attempt of accounting for the presence of short-lived nuclei in early solar materials. The first interpretation was advanced by Cameron and Truran (1977), who suggested that a supernova (SN), which occurred close in time and space to the solar nebula formation, might have introduced the required nucleosynthesis contaminations. After this seminal work, the idea of a close encounter with a dying star was re-explored by many authors and various stellar scenarios were examined, from that of a single SN, to the one of a less-massive object, namely a low or intermediate-mass star in its Asymptotic Giant Branch (or AGB) phase (Podosek and Nichols 1997; Wasserburg et al. 1998; Busso et al. 1999; Wasserburg et al. 2006; Gounelle et al. 2006; Takigawa et al. 2008; Huss et al. 2009).

Furthermore, also the evolution of the ejecta from massive stars was modelled by various authors. These works ranged from studies of cosmic ray processes inside supernova remnants, where even ^{10}Be can be produced (Tatischeff et al. 2014), to the reconstruction of the evolution of a molecular cloud possibly hosting the solar nebula, with its complex phenomena of nucleosynthesis from previous supernovae, mixing, and contributions from very massive stars in their Wolf-Rayet (WR) stage (see e.g. Gounelle and Meynet 2012; Dwarkadas et al. 2017, 2018, and references therein).

Various objections were raised to each of the models presented (for an inventory of them see e.g. Busso 2011, 2018). Basically, the most relevant ones can be divided in two categories, each affecting a different mass range of the proposed source. First of all, any idea involving a SN event, or a sequence of SN contributions in a molecular cloud, must keep in mind that these explosive phenomena are the main source of nucleosynthesis for most of the stable elements, and for α -rich ones in particular. As suggested by Wasserburg et al. (1998), materials coming from supernova nucleosynthesis and diluted sufficiently to account for the ^{26}Al and ^{60}Fe concentrations in the ESS are bound to contain large amounts of oxygen, neon, magnesium, silicon, etc. Their inclusion would affect the early solar nebula in completely different ways, depending on how they are added to the materials of the forming star. Let us consider in more detail this crucial point. A first possibility is that fresh Core Collapse Supernova (CCSN) ejecta are directly added to the forming Solar System by a single event (maybe also triggering the collapse), maintaining the typical, heterogeneous structure characterizing supernova remnants (Boss 2017; Loll et al. 2013). This non-homogeneous and clumpy kind of mixing was early modelled by Pan et al. (2012); in this case, the effects of the pollution should be now registered in pristine meteorites in the form of wide-spread anomalies in the abundance ratios of stable isotopes for such elements, at the level of a few percent (Wasserburg et al. 1998). The most important of these effects would concern oxygen, generally produced in large quantities by exploding stars leaving a neutron star as a remnant. However, observed oxygen isotope anomalies in primitive Solar System materials do not require the admixture of a distinct nucleosynthetic component (see Section 6.2). Anomalies in contrast with observations would also be predicted for the isotopes

of other α -rich nuclei and an important excess would be foreseen for the SLR ^{53}Mn , whose ratio to ^{55}Mn would be larger than observed by orders of magnitude (Wasserburg et al. 1998; Meyer and Clayton 2000); the whole scenario is therefore in doubt. Attempts at answering to these objections invoked very peculiar SN types, e.g. objects ejecting only external layers, not interested by manganese production (Meyer and Clayton 2000), and/or having a very particular mass (close to the lowest limit for CCSNe), to minimize the production of unwanted anomalies on oxygen and α -rich nuclei (Banerjee et al. 2016). In any case, whatever ad-hoc choice of parameters is adopted, these models do not really avoid the problems outlined above. An example is the recent work by Banerjee et al. (2016), where abundance shifts not acceptable by the present meteoritic measurements (i.e. at levels of 1-3 %) remain on various stable isotopes (see their Table 3 in the Supplement materials).

A very different scenario considers that, before being admixed into the presolar nebula, the ejecta of previous supernovae had time to mix and homogenize in the molecular cloud from which the Sun formed, presumably because they came from an appreciable number of explosive events in a sequential star formation process lasting for several million years. If this was the case for the solar formation, the addition of most stable nuclei would not cause any particular problem: they would simply modify slightly the “average” solar abundances, not introducing measurable isotopic variations with respect to the average composition in pristine meteorites. This type of scenario has been rather common in recent years (Gounelle and Meynet 2012; Dwarkadas et al. 2017). On one side, this scheme might appear rather realistic and is indeed interesting in itself, offering an alternative to the single-star contamination. Some versions of it indicate that a late WR star may have provided adequate amounts of ^{26}Al (and maybe ^{60}Fe) from stellar winds. The presence of other SLRs with different lifetimes would be simply the fossilized record of sequential star formation within a hierarchical interstellar medium. However, as we shall see, a major problem in this case emerges for the excess of unstable ^{53}Mn . While for a single event one might accept that the contaminant was a rare, peculiar SN, where Mn was not ejected, at the level of a whole molecular cloud this idea appears as untenable. We must notice that this kind of problems was not addressed in the papers invoking this explanation, which also did not include the effects of explosive nucleosynthesis (see e.g. Gounelle and Meynet 2012) and did not consider other crucial SLRs, like ^{135}Cs and ^{41}Ca . The very short-lived ^{41}Ca in particular would be completely extinct, in contrast with the striking correlation with ^{26}Al shown in Figure 6.1, which says it must have a stellar origin. Furthermore, these models assumed that the WR star itself does not give significant further contributions to nucleosynthesis, in addition to those from the wind. This is not supported by other works (Higdon et al. 2004). In any case, all the results on addition of SN debris, including ours, are somehow biased by oversimplifications in the treatments of the mechanism for the injection of fresh material, whose consequences still deserve detailed hydrodynamical studies of the type attempted by Boss (2017) and by Dwarkadas et al. (2017), but extended to all the measured SLRs.

On the other hand, the alternative origin in a (longer living) AGB star, early suggested by Wasserburg et al. (1994, 1995b) for several radioactivities has the weakness of requiring a chance stellar encounter at a level of probability that borders zero (Kastner and Myers 1994).

Despite the criticisms, it is clear that a considerable number of radioactive nuclei among those of Table 6.1 must be of stellar origin and cannot be attributed to endogenic phenomena in the solar nebula itself, like e.g. spallation processes induced by the solar wind (Sossi et al. 2017). In this respect, it was remarkable that the original suggestions by Wasserburg et al. (1994) on a possible AGB star origin, later specified by Busso et al. (2003); Wasserburg et al. (2006), were subsequently and independently confirmed by Trigo-Rodríguez et al. (2009) on the basis of models for slightly more massive stars, hosting hot bottom burning (HBB), i.e. hydrogen burning directly at the base of the convective envelope. In both these approaches it was assumed (with no real proof) that the parent star could produce elements from slow neutron captures (the *s*-process) only through the $^{22}\text{Ne}(\alpha, n)^{25}\text{Mg}$ source, avoiding the formation of the complementary and rather efficient source $^{13}\text{C}(\alpha, n)^{16}\text{O}$. Even the AGB models, therefore, did not come without drawbacks that go beyond their implausibility. They were however not a priori excluded only because of their apparent success in accounting contemporarily for several SLRs (^{26}Al , ^{60}Fe , ^{107}Pd , ^{135}Cs , ^{182}Hf , ^{205}Pb).

In recent years, the abundance measurements of stable isotopes in pristine meteorites were enormously improved, so that any possible scenario for a supernova origin of SLRs must now face more stringent constraints than envisaged by Wasserburg et al. (1998). On the other hand, also stellar models for both massive stars and AGB giants underwent important improvements. We have now safe predictions of nucleosynthesis from CCSNe, which include rotation in the hydrostatic phases and a full computation of explosive nucleosynthesis (Chieffi and Limongi 2013, 2015; Limongi and Chieffi 2018). For smaller masses ($M \lesssim 8 - 9 M_{\odot}$) attempts have been presented to address quantitatively, on the basis of known physical principles, the mixing of protons from the envelope into the He-shell that is preliminary to the activation of the reaction $^{13}\text{C}(\alpha, n)^{16}\text{O}$ and then to *s*-processing. These new kinds of models will be used here, in the attempt of limiting the free parameterizations and obtaining more secure indications. The same will be done for massive stars, adopting the mentioned computations where rotation and explosive phases were included. On these bases we shall also comment on the scenarios for the evolution of the presolar molecular cloud contaminated by a series of SN explosions and/or WR stars.

6.2 Constraints from isotopic anomalies in meteorites

As was indicated several years ago (Wasserburg et al. 1998), a supernova origin for SLRs present alive in the ESS would necessarily introduce in the parent nebula

also variations over the pre-existing record of abundances for stable isotopes. In case the mixing is not homogeneous, this might imply prediction of unobserved isotopic anomalies on elements typically produced by CCSNe. Any model of the solar contamination in SLRs by massive stars ending their evolution as CCSNe with inhomogeneous and clumpy ejecta must come with the guarantee that the isotopic abundance shifts introduced on the stable isotopes of major elements remain at a level low enough not to be in conflict with actual measurements.

In ancient meteorites, variations in the isotopic composition of oxygen (the most important product of SN nucleosynthesis) are rather large. However, they are, most likely, mainly the result of chemical processes and self-shielding in the solar nebula (Clayton 2003), and not the fingerprints of distinct nucleosynthetic components. More specifically, O-isotopic ratios of bulk chondrites vary by about 10‰/amu. Could this have an astrophysical origin, e.g. be the result of different abundances of presolar grains? The answer is no, as the most primitive meteorites have abundances of presolar O-rich grains of up to 500 ppm which, with the typical ^{17}O -enrichments of a factor of 2 in presolar grains, would shift the $^{17}\text{O}/^{16}\text{O}$ ratio by only 0.5 permil on a bulk scale.

Larger anomalies as compared to those in bulk chondrites are seen in specific components; notably, the most extreme cases are CAIs, with their enrichments in ^{16}O of up to 5%, as similarly inferred for the Sun by the Genesis mission (McKeegan et al. 2011) and for the so-called cosmic symplectite (formerly known as “new-PCP”), which shows enrichments in ^{17}O and ^{18}O of up to 20% and which is assumed to represent primordial water in the solar nebula (Sakamoto et al. 2007). The Genesis data suggest that CAIs have inherited mainly the O-isotopic composition of the gas in the solar nebula. Mixing the ^{16}O -rich gas of the ESS with ^{16}O -poor primordial water components in various proportions, along with mass fractionation effects, could easily account for the variations in O-isotopic compositions of planetary materials and there is no need to invoke a distinct nucleosynthetic component.

Much smaller isotopic variations are seen for the heavier elements on a bulk meteorite (planetary) scale, some of which may be of nucleosynthetic origin. For the rock-forming elements Mg, Si, and Fe isotopic anomalies are only at the sub-permil level (Teng 2017; Poitrasson 2017; Dauphas et al. 2017). The same holds for many other of the heavy elements on a bulk meteoritic scale (Dauphas and Schauble 2016). Interestingly, relatively large Si-isotopic anomalies (with large experimental uncertainties) were found by the Rosetta mission for the refractory Si component in comet 67P/Churyumov-Gerasimenko, which has $\delta(^{29}\text{Si}) = (-145 \pm 98)\text{‰}$ and $\delta(^{30}\text{Si}) = (-214 \pm 115)\text{‰}$. Note however that here errors are at 1- σ , so that within 2- σ the composition would be normal (Rubin et al. 2017).

In conclusion, on a bulk meteorite scale there is no unambiguous evidence for isotopic anomalies of nucleosynthetic origin in excess of a permil. Of course, if we include CAIs, and especially FUN (and hibonite) inclusions, as references, things get much more complicated. A useful compilation of isotope data for conventional CAIs and FUN (and hibonite) inclusions can be found in Dauphas

and Schauble (2016). For CAIs, isotopic anomalies of likely nucleosynthetic origin may reach up to a few permil *for certain isotopes*, and for FUN (and hibonite) inclusions anomalies can be even much larger, in excess of a percent. However, we are looking for widespread, global signatures, while FUN inclusions are rare and exhibit large mass fractionation effects. We believe they can be ignored in the present context, and we can consider only conventional CAIs along with meteoritic bulk compositions. For them, isotopic anomalies of putative nucleosynthetic origin are clearly much lower on this scale.

As a conclusion, we must verify that, in case the (typically clumpy and inhomogeneous) CCSN ejecta are assumed to be the source of SLRs in the solar nebula, the predicted shifts on the abundances of stable isotopes remain safely below a level of a few permil. Only when the above constraints are verified, one can consider nucleosynthesis processes in a close-by star as being a possible origin for radioactive nuclei in the protosolar cloud.

6.3 Contributions from galactic evolution

For a zero-order estimate of the contributions to SLRs from Galactic evolution, we consider the schematic model of an ISM behaving as a closed-box, enriched over a time duration T , following the approach by Wasserburg et al. (2006) and by Lugaro et al. (2014). Then, the inventory of a radioactive isotope R relative to a stable nuclide S produced in the same astrophysical site, at the moment in which production previous to the Solar System formation ceases, is:

$$[N^R(T)/N^S(T)]_{CE}^0 \simeq \frac{P^R p(T) \tau_R}{P^S \langle p \rangle T} \quad (6.1)$$

where CE means “Chemical Evolution”, the suffix “0” indicates that the estimate is for the moment in which nucleosynthesis ceases, $P^S \langle p \rangle$ is the *average* stellar production rate of the isotope S over the time interval T and $P^R p(T)$ is the production rate of R at the moment when the process ends. Whenever $p(T)$ can be considered as constant ($\simeq \langle p \rangle$), calling Δ the delay from the last nucleosynthesis episode after which the Sun forms, one has:

$$[N^R(T)/N^S(T)]_{CE}^\Delta \simeq \frac{P^R}{P^S} \cdot \frac{\tau_R}{T} \cdot e^{-\Delta/\tau_R}. \quad (6.2)$$

A problem with this treatment is that we need to apply it to nuclei produced by heterogeneous sources, e.g. by hydrostatic and explosive processes in stars of different mass and by slow and rapid neutron captures. For these last, Wasserburg et al. (1996) and Wasserburg et al. (2006) started simply from the assumption of the existence of a unique explosive scenario capable of reproducing the Solar System distribution of r -nuclei and derived the production ratios accordingly. Although in Equation (6.2) we now need only such ratios (P^R/P^S) for isotopes of the same element that are very close in mass, the problem of connecting the data for nuclides having different origins (like e.g. ^{53}Mn , the p -nucleus ^{146}Sm , the

Table 6.2: SLRs as synthesized by a uniform production model over $T = 10^{10}$ yr of Galactic evolution. Production factors from Wasserburg et al. (2006)

Rad.	Ref.	τ_R (Myr)	$[P^R/P^S]_{CE}$	$[N^R/N^S]_0$	$[N^R/N^S]_{10}$	$[N^R/N^S]_{20}$	$[N^R/N^S]_{Meas.}$
^{26}Al	^{27}Al	1.03	$5.4 \cdot 10^{-3}$	$5.6 \cdot 10^{-7}$	–	–	$(5.23 \pm 0.13) \cdot 10^{-5}$
^{41}Ca	^{40}Ca	0.15	$1.4 \cdot 10^{-3}$	$2.2 \cdot 10^{-8}$	–	–	$4 \cdot 10^{-9}$
^{53}Mn	^{55}Mn	5.3	0.189	$1.0 \cdot 10^{-4}$	$1.5 \cdot 10^{-5}$	$2.2 \cdot 10^{-6}$	10^{-6}
^{60}Fe	^{56}Fe	3.75	$2.3 \cdot 10^{-3}$	$8.0 \cdot 10^{-7}$	$5.6 \cdot 10^{-8}$	$3.8 \cdot 10^{-9}$	$10^{-8} - 10^{-6}$
^{107}Pd	^{108}Pd	9.4	0.66	$6.2 \cdot 10^{-4}$	$2.1 \cdot 10^{-4}$	$7.4 \cdot 10^{-5}$	$(5.9 \pm 2.2) \cdot 10^{-5}$
^{129}I	^{127}I	23	1.30	$3.0 \cdot 10^{-3}$	$1.9 \cdot 10^{-3}$	$1.3 \cdot 10^{-3}$	10^{-4}
^{135}Cs	^{133}Cs	3.3	0.724	$2.1 \cdot 10^{-4}$	$1.0 \cdot 10^{-5}$	$4.9 \cdot 10^{-7}$	$4.8 \cdot 10^{-4}$
^{146}Sm	^{144}Sm	148	0.675	$9.9 \cdot 10^{-3}$	$9.2 \cdot 10^{-3}$	$8.6 \cdot 10^{-3}$	10^{-2}
^{182}Hf	^{180}Hf	12.8	0.346	$4.5 \cdot 10^{-4}$	$2.1 \cdot 10^{-4}$	$9.4 \cdot 10^{-5}$	$(9.81 \pm 0.41) \cdot 10^{-5}$
^{247}Cm	^{235}U	23	3.95	$8.9 \cdot 10^{-3}$	$5.8 \cdot 10^{-3}$	$3.7 \cdot 10^{-3}$	$(1.1 - 2.4) \cdot 10^{-3}$
^{205}Pb	^{204}Pb	22	1.05	$2.3 \cdot 10^{-3}$	$1.5 \cdot 10^{-3}$	$9.3 \cdot 10^{-4}$	10^{-3}

s -process nucleus ^{205}Pb or the r -nucleus ^{247}Cm) remains, so that the results of the Galactic enrichment must be considered with a lot of caution and are affected by intrinsic strong uncertainties.

Should one accept the indications by Wasserburg et al. (2006), one would find that the ratio P^R/P^S is close to 1 for ^{107}Pd , ^{129}I and ^{135}Cs (the choices were 0.66, 1.3 and 0.724, respectively). This ratio is much smaller ($\simeq 1.4 \times 10^{-3}$) for ^{41}Ca . Also for ^{26}Al the production ratio to ^{27}Al is low. For example, in supernovae and massive stars P^R/P^S is expected to be between 10^{-2} and 10^{-3} : the adopted average value was then 5.4×10^{-3} . This last estimate might be suitable to explain the Galactic inventory of ^{26}Al ($2.8 \pm 0.8 M_\odot$, see e.g. Diehl et al. 2006). This corresponds to an average ratio $^{26}\text{Al}/^{27}\text{Al}$ of a few $\times 10^{-6}$, which is 10 times smaller than for the ESS (see also Higdon et al. 2004). For ^{60}Fe , the adopted production ratio to ^{56}Fe was 2.27×10^{-3} and for Hf, $P^{182}/P^{180} \simeq 0.346$. Table 6.2 gives a synthetic view of the abundance ratios that can be obtained with these hypotheses, either at the moment when nucleosynthesis episodes preceding the solar formation ceased ($\Delta = 0$), or after a delay of the order of the isolation times of cloud cores in star formation regions (Δ up to $1 - 2 \times 10^7$ yr).

The above general picture has not (and never had) the ambition of being really quantitative, both for the uncertainties in the production factors in stars and for the extremely elementary scheme of Chemical Evolution adopted for the Galaxy. It is only a general qualitative view to be improved by future models; in this respect, we cannot aim (in such a rough picture) to obtain an agreement with the measurements at levels better than a factor of 2–3; this is a minimum estimate for the uncertainty in the scheme adopted. Especially for Galactic Evolution one should actually consider more sophisticated models, like e.g. in Mathews et al. (2014); Bojazi and Meyer (2017); Dwarkadas et al. (2017); Bojazi and Meyer (2018)

Nevertheless, the above picture already provides relevant pieces of information. It turns out that nuclei of very different origins like ^{53}Mn , ^{107}Pd , ^{146}Sm , ^{182}Hf , ^{205}Pb and ^{247}Cm might actually find a proper explanation for an isolation time

between 10 and 20 Myr. Even the very uncertain ^{60}Fe might not be a problem, in case the most recent estimates for its abundance were to be confirmed (Trappitsch et al. 2018). The nuclides that are clearly underproduced by this simple and expected process of gradual Galactic enrichment are only limited to ^{26}Al , ^{41}Ca , ^{135}Cs and possibly ^{60}Fe (this last only in case its initial ESS ratio to ^{56}Fe should turn out to be larger than 10^{-7}).

However, in the case of heavy n-rich SLRs, the situation is more complex, as pointed out since the beginning by Cameron et al. (1993) and Wasserburg et al. (1996). Here one has to consider, aside to the *s*-process nuclide ^{205}Pb , also isotopes of possibly heterogeneous origin, like ^{107}Pd ; and ^{182}Hf , ^{247}Cm and others including ^{129}I , due to the *r*-process. While the stellar yields of slow neutron-capture nuclei are rather well understood, the situation is quite different for *r*-process isotopes, whose origin is not yet quantitatively established. SLRs make clear that ascribing it to a unique mechanism, taking place in some explosive event of non-specified nature, as done in Table 6.2, implies to find enormous overproductions for ^{129}I with respect to ^{107}Pd , ^{182}Hf and ^{247}Cm ; hence the works by Cameron et al. (1993) and Wasserburg et al. (1996) simply noticed that such a unique scenario was unlikely. Understanding heavy SLR abundances now, some 25 years later, requires to place them in the broader context of more recent observations and models for the *r*-process. We shall try to discuss these issues in the next Section.

6.4 Constraints and models for *r*-process nucleosynthesis

6.4.1 Observed constraints and *r*-process sources

In the *average* solar system abundances, the decay daughters of ^{129}I and of ^{182}Hf have a ratio $N(^{129}\text{Xe})/N(^{182}\text{W}) = 41.6$ (Lodders and Palme 2009); as ^{182}W is of *r*-process origin only for about 50% (Trippella et al. 2016), the abundance ratio between the *r*-components of these nuclei should be slightly larger than 80. Should we adopt the *s* and *r* components from Bisterzo et al. (2014), one would get a higher estimated ratio of 114. On the contrary, in the ESS, given the fact that the isotopic ratios $^{129}\text{I}/^{127}\text{I}$ and $^{182}\text{Hf}/^{180}\text{Hf}$ are essentially equal ($\simeq 10^{-4}$), the ratio between the two SLRs roughly equals the one of the stable references, i.e. $^{127}\text{I}/^{180}\text{Hf}$, which is about 20. There is a discrepancy by about a factor 4. With respect to the rough predictions of Table 6.2, referring to the continuous Galactic production of *r*-process nuclei from hypothetical sources of a unique nature, the discrepancy reaches up to a factor of 7 to 10 (see columns 6 and 7). This sharp contrast might probably be accounted for only if the two cases (average Solar System materials and anomalies in early solids) derive from different origins or different admixtures of *r*-process “components”. In particular, the average solar-system abundances were built through an elaborated blend of different processes, each accounting for one such “component” of the distribution. This blend was established by Galactic evolution over a time scale of $\simeq 10$ Gyr.

SLRs in the ESS produced through fast neutron captures might instead put in evidence the granularity of the Galactic mechanism on shorter time scales, possibly being controlled by only few contributions from specific sources (Cameron et al. 1993).

The work by Wasserburg et al. (1996) tried to infer the origins of the above contributions; although at that moment the reference sources were mainly assumed to be CCSNe, through neutron captures occurring in a neutrino-driven wind (Woosley et al. 1994), this assumption actually does not enter directly in the estimates of Table 6.2, which simply require a single mechanism reproducing the solar r -process abundances. The same approach was discussed by Busso et al. (1999). As a simple recipe for finding a way out, Wasserburg et al. (1996) guessed that the astrophysical source for the production of ^{129}I appeared for the last time in the solar neighborhood a long time before the last event producing ^{182}Hf and ^{247}Cm , thus implying a much longer decay of the first one, from which the low ESS ^{129}I abundance would derive. This was subsequently extrapolated by Qian and Wasserburg (2000), who assumed more explicitly a specific source for these nuclei (CCSNe) and proposed that two types of them were at play, one producing the lighter r -nuclei, up to $A \simeq 130$ (including iodine) and the second producing the heavier nuclei. The first kind of events was indicated with the letter L (*lower*, from their low expected rate of occurrence) and the second was indicated with H (*higher*). ^{107}Pd would be low in that hypothesis, but for it the help of the s -process can be invoked, see Section 6.5.

The above ideas generated extended debates and were in general criticized as being too simplistic. It was in particular underlined that, within CCSN models for the r -process, any *physically based* mechanism yielding enough ^{182}Hf to explain its ESS abundance, would most probably produce similarly also the nuclei at the $N = 82$ peak, including ^{129}I , thus leading to high values of their ratio (see e.g. Pfeiffer et al. 2001). In other words, the requirement of having “pure” r -process sources separately producing the two nuclei seemed to be too ad-hoc to be accepted. More plausible might be situations where they are produced together but at different efficiencies. This would be for example the case, using a rather recent mass model like the “finite-range droplet model” update of 2012, or FRDM(2012), by Möller et al. (2012), if a weakening of the $N = 82$ shell closure (often referred to as “shell quenching”) were to occur below the doubly-magic ^{132}Sn (Dillmann et al. 2003; Atanasov et al. 2015). This would anticipate the maximum of the peak, perhaps down to $A = 126$ (see Table 1 in Kratz et al. 2014a). Then ^{129}I would not stay at the peak, but after it, with a reduction of its abundance by a factor of 2–3 with respect to a standard solar r -component (Farouqi et al. 2010).

Subsequent research then clarified that other sources, different from CCSNe, might be crucial in producing the r -process nuclei (Freiburghaus et al. 1999). At the moment of this report, two main sites are often discussed to have excellent chances to contribute, in various proportions, to produce nuclei from fast neutron captures. They are the rare magneto-rotational types of supernova (MRS; see e.g. Nishimura et al. 2017, and references therein) and neutron star merger (NSM)

events; (see e.g. Freiburghaus et al. 1999). One has in particular to mention that this last paradigm received a now publicly famous observational support in the recent gravitational-wave event GW170817 (Abbott et al. 2017a). In the electromagnetic source AT2017gfo, the kilonova associated to it, qualitative evidence was recorded of the production of heavy n -rich elements at the second and/or third abundance peak (Pian et al. 2017; Tanvir et al. 2017; Troja et al. 2017). The possibility of having r -process nucleosynthesis in such an environment was early suggested by Lattimer et al. (1977), Meyer (1989), and Eichler et al. (1989). This kind of models was recently indicated to be in principle able to explain the whole solar-system distribution of nuclei coming from fast neutron captures (Wanajo et al. 2014; Thielemann et al. 2017). One has also to consider cautiously that the traditional CCSN models seem not to be completely out of the picture yet (Kajino and Mathews 2017). There have also been persisting suspects that CCSNe of a specific type (faint, ^{56}Ni -poor, type IIP events, showing enhanced Sr II and Ba II lines, like SN2009E and perhaps SN1987A, see e.g. Pastorello et al. 2012), can contribute to the r -process, as early suggested by Tsujimoto and Shigeyama (2001). Although the strength of Ba II lines might be affected by variable ionization and temperature issues (Utrobin and Chugai 2005; Pastorello et al. 2012), these effects should be valid in general and might not explain completely why in other CCSNe the Ba and Sr lines are significantly weaker (Branch and Wheeler 2017). The products of the above faint SN II sources might have been observed in dwarf galaxies (Ji et al. 2016a). In general, the real relative importance of the various contributors to heavy neutron capture nuclei, their frequency of occurrence and the amount of processed material returned to the Galaxy remain still unsecure, although NSMs, where high neutron excesses are found, are emerging as one of the most promising sites for r -processing (Thielemann et al. 2018).

Constraints on the zoo of present-day models can be found by considering real observed or measured element admixtures (Kratz et al. 1993). In our case, these include not only the solar system average abundances and ESS radioactivities, but also the pattern of r -nuclei observed at low metallicity, in our Galaxy and its neighbours, when the s -process has not yet started to appear and one has chances to see stars polluted by only part of the long-term r -process blend (Snedden et al. 2008). In this framework, it is by now ascertained that many old stars exist showing an almost solar distribution of elements across and beyond the $N = 82$ magic neutron number (Spite et al. 2018). The prototype of these objects is the famous CS22892-0052 source (Snedden et al. 1996), a supergiant in Aquarius. When in these stars one considers also lighter species (with $Z = 40$ to 50) one sees that for them the scatter is large, but on average the production of these elements is lower by a factor of 2-3 with respect to a scaled solar r -process distribution (see e.g. Honda et al. 2006, in particular their Figure 5). Completely different metal poor stars however exist, at even lower metallicity, the prototype being the subgiant/giant star HD 122563 (Honda et al. 2006). Here, the light r -nuclei at $N = 50$ are dominant with respect to heavier species across and beyond the $N = 82$ peak. We further note that the inventory of low-metallicity stars

differently enriched in the *light* and *heavy* r -nuclei seems to suggest that the former ones are actually more frequent than the latter ones, but also that the amount of r -processed matter ejected by events producing the lighter r -process elements be much smaller than for those producing preferentially the heavier nuclei, maybe by 2 orders of magnitude (Macias and Ramirez-Ruiz 2018). The two producing environments might be of heterogeneous origin (e.g. CCSNe and NSMs) or of the same type (e.g. NSMs only), but occurring in different conditions. For example it has been shown that NSM phenomena can give rise to light or heavy r -nuclei, depending on the extremely variable possible conditions. Anyhow, deriving absolute production factors like the $\langle p \rangle$ values needed in Equation (6.1) is certainly premature, so that we are obliged to stay at a purely qualitative discussion. Moreover, both HD 122563 and CS22892-0052 reflect situations probably not suited to explain the ESS $^{129}\text{I}/^{182}\text{Hf}$ ratio. Although the most relevant elements I, Xe ($Z = 53-54$) and Hf, W ($Z = 72-74$) were not observed, looking in general at the closest elements we see that, from both cases, we would expect a ratio much higher than observed in the ESS. Hence, if this last sample reflects the isotopic ratios typical of a specific r -process variety, then the two types of metal-poor stars (albeit offering a closer and different look at the granularity of the process) should be already the products of different forms of admixtures of heterogeneous components.

Although with caution, we can say that something better, more similar to the individual r -component revealed by ESS heavy SLRs, actually may exist, in some metal-poor stars. A few years ago it was shown, in Roederer et al. (2016), that three out of four stars observed in the dwarf Galaxy Reticulum 2, although in general similar to the Sneden's star, actually show rather large abundance ratios between the heavy elements before the third r -process peak (e.g. Dy) and those immediately after the second peak (e.g. Ba). In the mentioned stars the ratio Dy/Ba ranges from 7 to less than 24 (upper limit) times the average solar value. This last needs to be corrected for deriving a pure (solar) r -process component. This can be done using the r -residuals ($1-s$) from the models quoted in the next Section, in particular from Palmerini et al. (2018). With respect to previous computations, these models yield lower estimates for the Dy_r/Ba_r ratio in the Sun, in the range 2.7 to 5, with an average value depending on the Initial Mass Function adopted for the weighting, on mass loss rates etc. One can roughly evaluate it to be near 3.5 (against a previous estimate of 5.7, derived from Bisterzo et al. 2014). We underline that the new estimates are quite uncertain; despite this, they are closer to what can be found in HEW models with shell quenching (see e.g. Farouqi et al. 2010), where values down to 2.0 – 2.3 can be obtained. With the above correction (on average by a factor of 3.5) for the solar r -component normalization, the Dy/Ba ratios in the three stars of Reticulum 2 become 2, 4.5 and less than 6.8 (upper limit) times higher than in the solar r -process distribution. Can one roughly assume that this implies relatively large ratios also near the (unobserved) W and Xe (whose isotopes at $A = 182$ and $A = 129$ are decay daughters of the SLRs we are discussing)? As we illustrated, we need an enhancement factor in $^{182}\text{Hf}/^{129}\text{I}$ of about 4; if our extrapolation is

correct, the observations of Reticulum 2 early showed real stars where this might be achieved. A similar situation may apply to the more numerous stars recently observed by Hansen et al. (2018). In their Table 5, several measurements identify objects (called r -I) with negative values of $[\text{Eu}/\text{Ba}]$; some of them yield linear Ba/Eu ratios lower than in the solar r -distribution. Models accounting for this trend include the mentioned HEW cases with shell quenching, or certain NSM scenarios, like e.g. those by Goriely et al. (2013). Hence, two different sites, affected by r -process varieties similar to the one producing the heavy SLRs, would have been observationally confirmed. At present, NSMs seem to be the most probable sources to explain the above abundance distributions, due to their lower Y_e values with respect to CCSNe.

Anyhow, the abundance distributions of different metal-poor stars confirm that various r -process varieties must necessarily exist and that the blend shown by the average solar composition is certainly not “universal”, as also indicated by the extensive theoretical work of the last 25 years (see e.g. Roederer et al. 2010; Thielemann et al. 2018; Tsujimoto et al. 2017; Kajino and Mathews 2017, and references therein).

With the above scenario in mind, one can look for parameter studies, based both on site-independent and on site-specific models, to identify the astrophysical conditions requested for reproducing the observational evidence. From these conditions we can then try to figure out plausible scenarios accounting for the abundances of ^{129}I and ^{182}Hf in ESS samples, without violating other constraints from low-metallicity stars.

6.4.2 Reconciling the ESS abundances of ^{129}I and ^{182}Hf

In general it is recognized that a very promising general scheme for r -processing involves neutrino-driven interactions in neutrinospheres and/or neutrino winds (NWs), established in explosive conditions above a neutron star (Freiburghaus et al. 1999). It might be found in various astrophysical scenarios (CCSNe, NSMs, MRSe, see e.g. Kajino and Mathews 2017).

A few works some years ago criticized earlier attempts aimed at modelling its occurrence in CCSNe (see e.g. Fröhlich et al. 2006; Wanajo and Janka 2012), inferring that, for those conditions, the NW would remain proton-rich during its entire life, precluding any r -process nucleosynthesis, even simply for producing light nuclei up to the first magic neutron number $N = 50$ (Sr, Y, and Zr). However, Roberts et al. (2012) re-established this scenario as a possible one for the occurrence of neutron captures. The above authors showed that, with a more detailed treatment, including the nucleon potential energies and the collisional broadening of the response, the previous negative conclusions would have been considerably changed. In particular, for a reasonable period of time, the NW was predicted to remain moderately neutron rich. Interactions occurring in the NW were described, e.g., in Ott and Kratz (2008); Farouqi et al. (2010); Martínez-Pinedo et al. (2017); Thielemann et al. (2018). The main parameters controlling the nucleosynthesis products are the number of neutrons per nucleus $Y_n/Y_{r\text{-seed}}$,

the number of electrons Y_e , the expansion velocity, v_{exp} , and the entropy per nucleon, S (generally expressed in units of the Boltzmann’s constant, k_B). They are linked by the relation (Farouqi et al. 2008a,b; Kratz et al. 2008):

$$Y_n/Y_{r-seed} \simeq v_{exp} \cdot \left(\frac{S}{Y_e} \right) \quad (6.3)$$

In CCSNe only limited neutron enrichments seem to be achieved ($Y_e = 0.4 - 0.45$); in order to produce heavy nuclei, this requires that high values of the entropy S per nucleon are available ($S \geq 200$), which fact gives to the mechanism its same denomination: *High Entropy Wind*, or HEW. Nucleosynthesis induced by neutrino interactions can occur also in contexts different from CCSNe, in particular in NSMs, where the neutron excess is always much higher (with Y_e values down to 0.2); here, lower values of the entropy S are required ($S \lesssim 20$, *Low Entropy Winds*). These were some of the reasons why so much attention was dedicated to this scenario in recent years.

In the original work by Roberts et al. (2012) the values of Y_e and the maximum entropy S_{Max} for CCSNe were such ($Y_e \simeq 0.45$, $S_{Max} \leq 100$) that only relatively light trans-Fe elements, from Sr to maybe Ru, could be produced, in a process with a high proton abundance. A result of this kind had been previously discussed by Farouqi et al. (2009), in addressing the composition of presolar SiC grains of type “X” (Pellin et al. 2006).

However, after the indications by Roberts et al. (2012), a few groups showed that in some scenarios HEW models could still apply, reaching high values of S_{Max} (Kratz et al. 2014b; Thompson and ud-Doula 2018). As said, this is a necessary condition for the process to be effective at relatively high Y_e values, as in CCSN contexts. For example, explaining with these sources the observations of extremely metal poor stars like HD 122563 (Honda et al. 2006) with ejecta from a moderately neutron-rich wind ($Y_e = 0.45$, as in Roberts et al. 2012), would require $S_{Max} \simeq 220$. Should one try to account for other metal-poor stars richer in heavy r -nuclei, like CS22892-0052 (Snedden et al. 2008), in the same $Y_e = 0.45$ condition, then S_{Max} as high as 280–300 would be needed (Farouqi et al. 2010; Kratz et al. 2014b). If, instead, the game is played in more n-rich environments like NSMs, these requirements would be reduced by roughly a factor of ten (Thielemann et al. 2017).

One has also to notice that virtually any observed star, even at very low metallicity, contains an admixture of light and heavy r -nuclei. Just to make examples, r-poor stars like HD 122563 have Sr/Eu values from about 100 to about 550, whereas r-enriched stars like CS22892-0052 have Sr/Eu ratios from about 20 to about 30. Recent extreme cases were shown by Ji et al. (2016b) for stars enriched in heavy ($A > 130$) nuclei; they have Sr/Eu ratios lower than 10 and down to a minimum of about 3.5. If these numbers define a pure “main” r -component, this means that all other observed stars contain admixtures of different processes, i.e. are characterized by wider blends of Y_e and S values than obtained in individual calculations (Frebel and Beers 2018). This is so even at very low metallicities ($[Fe/H] \lesssim -2.5$), where the stars should have been

polluted by only very few SN events. If NSMs are at play, their potentially much lower Y_e values would allow all r -nuclei up to the heaviest ones to be produced in rather low entropy conditions (Goriely and Janka 2016; Thielemann et al. 2018).

In general, what we expect as a result of neutrino-wind driven nucleosynthesis phenomena for increasing values of S_{Max} can be outlined as follows.

- In CCSNe, for the lowest values of S_{Max} , in the dynamics of the mechanism a primary-like, rapid nucleosynthesis process can start, mainly controlled by charged particle (CP) interactions, where Y_n/Y_r is lower than unity. In these conditions SiC grains of type “X” might find their production site (Pellin et al. 2006; Farouqi et al. 2009). This requires S_{Max} to be up to 100 for typical Y_e values of 0.45 (Farouqi et al. 2009). This condition is not met in NSM environments, where the material is always neutron rich.
- For increasing values of S_{Max} and of Y_n/Y_r , neutrons start to dominate and we find various varieties of rapid n-capture processes. These variants have been called *weak*, *incomplete*, or, for higher S values, *main* and *actinide – boost r -processes*. Typically, the same regions of A can be reached in NSM models for S values smaller by an order of magnitude, due to the generally much lower Y_e .
- In CCSNe, for values of S_{Max} around 150 and in the range of free-neutron abundances $1 \lesssim Y_n/Y_r \lesssim 15$ one would find what was called by stellar modelers the “weak” r -process. Although light r -nuclei are produced, these are not the conditions for explaining the star described by Honda et al. (2006), as this last includes, as said, some heavy nuclei, while here the production stops at the rising wing of the $A = 130$ peak, producing iodine at the low level of a few percent. Similar results can be obtained with NSM models at values of S_{Max} at least ten times smaller (Siegel and Metzger 2017).
- There might be a following, more effective, r -process mechanism, for larger values of Y_n/Y_r and for S_{Max} values ranging between 200 and about 220 in CCSNe (and again smaller by an order of magnitude in NSMs, with Y_e values smaller by typically a factor of 2). Its existence is certified by stars where nuclei in the region from Sr to Cd dominate, but are accompanied by variable abundances of heavier species, like Ba and Eu. Examples of such stars with a rather scattered composition are abundant. Aside to the one quoted by Honda et al. (2006), new measurements have been presented by Hansen et al. (2012): this was called “limited r -process”, repeating suggestions advanced by Roederer et al. (2010) and others.
- A main n -capture mechanism follows, responsible for the top of the $A \simeq 130$ peak, including most of Xe, the Rare Earth Elements and the $A \simeq 195$ third r -peak. This process is often referred to as the “Snedden-like” r -process, as it would account for stars with a solar-system distribution of elements

above $A \geq 130$, like those described in Sneden et al. (2008), plus a variable proportion of lighter nuclei. This kind of process might occur in CCSNe for values of Y_n/Y_r up to about 150 and values of S_{Max} above 220. Again, in NSM scenarios suitable conditions require much smaller values of S_{Max} , due to the low Y_e . In this process the enhancement factor for iodine would traditionally reach up to more than 90% of the most effectively produced elements, like Eu. However, its abundance can be considerably reduced if a weakening of the $N = 82$ shell closure (often referred to as “shell quenching”) occurs below the doubly-magic ^{132}Sn (Dillmann et al. 2003; Atanasov et al. 2015). This would anticipate the maximum of the peak, perhaps down to $A = 126$ (see Table 1 in Kratz et al. 2014a). In those conditions the ratio I/Hf would be considerably reduced. The same effect would be obtained also by further increasing S_{Max} . Models of the *main* component with a low I/Hf ratio seem to be possible also in NSM models with high efficiency, like e.g. in Goriely et al. (2013); Goriely and Janka (2016); Bauswein et al. (2013).

- There might be a further, limited contribution from a very efficient n -capture process (that would explain the “actinide-boost” stars). Some of the stars observed by Roederer et al. (2009) might have these characteristics.

Depending on the ambient conditions, any site might be characterized by a specific range of S values; their superposition, from many different events, gives rise to the robust distribution of r -process nuclei observed in young Galactic stars; in the specific case of the *main* component, nuclei with $A \geq 135$, $Z \geq 56$ are produced with abundance ratios that look remarkably constant, since their early appearance in low metallicity stars (see e.g. Sneden et al. 2008; Hill et al. 2017, and references therein).

We have then two possible ways out for the I/Hf ratio. On one side, the same *main* component might produce a much lower abundance of iodine than previously found in CCSN models. This is obtained in certain NSM scenarios producing rather heavy r -nuclei (Goriely et al. 2013; Bauswein et al. 2013) and might also be found in CCSNe, where very high entropies and shell-quenching effects substantially reduce the previously expected I/Hf predictions. In both cases, the observed ESS ratios might be the direct outcome of only one specific r -process site, possibly the same producing the abundance patterns observed in some halo stars by Hansen et al. (2018) and in Reticulum 2 by Roederer et al. (2016). In view of the fact that NSM models show a high number of free neutrons, this scenario is probably the most promising one for yielding the required $^{129}\text{I}/^{182}\text{Hf}$ ratio. Another variety of NSM phenomena, with a lower number of neutrons per seed, might then be at the origin of ^{107}Pd , in a weaker r -process. As mentioned, this *weak* component might also come from CCSNe in suitable conditions. Table 6.2 would still be broadly similar to reality, but the production factor $\langle p \rangle$ for ^{129}I should be reduced by a large factor, maybe of the order of 5 (\pm a factor of two, trusting the few data from Reticulum 2).

Alternatively, the ESS ^{129}I might derive from the averaging over time scales much shorter than 10 Gyr of the contributions from different sources; a very limited number of them with a *traditional* main *r*-mechanism and a much larger number with a *weak* mechanism, with a poor efficiency (a few percent) in ^{129}I production. ^{182}Hf , instead, would be fully produced by the *main r*-process, with negligible contributions from the sources responsible for weaker components. In this second case, the productions of I and Hf would be essentially decoupled; however, in that case we would have the problem of obtaining the correct relative efficiencies (in frequency and mass ejected) of different producing sites for explaining Pd, I and Hf in an admixture of different sources. This seems a prohibitive fine-tuning task now; we therefore tentatively indicate the first possibility as the more probable.

We mention here that ^{182}Hf is well accounted for by the Galactic enrichment of *r*-process elements. We therefore do not feel any need to increase its *s*-process fraction, as done in Lugaro et al. (2014), following the revision of the level scheme and of the decay rate of ^{181}Hf , ensuing by a single estimate (Bondarenko et al. 2002). On this point we prefer to maintain a cautious approach, waiting for possible confirmations of this individual measurement.

6.5 The reference models for intermediate mass stars

When a radioactive nucleus is not accounted for by the chemical evolution of the Galaxy and requires a late event of nucleosynthesis to explain its abundance in early solids of the Solar System a formalism slightly different from Equation (6.1) applies to it. As discussed in Wasserburg et al. (2006), if a nearby star produced a radioactive nucleus R , of mean life τ_R , introducing for it in the ESS an abundance ratio $\alpha^{R,S}$ with respect to a stable isotope S of the same element, the following relation holds between the $\alpha^{R,S}$ value and the abundance ratio N^R/N^S (radioactive versus stable) in the stellar envelope:

$$\alpha^{R,S} = d \cdot \frac{N^R}{N^S} q^S e^{-\tau_R/\Delta} \quad (6.4)$$

Here q^S is the enhancement factor of the stable isotope S in the same envelope. The parameter d represents a dilution factor that measures the fraction of the ejected wind that is incorporated into the forming solar cloud, while Δ has the same meaning as in Equation (6.2).

In considering the stellar sources suitable for a late contamination of the solar nebula with SLRs, in this Section we start with an estimate of the possible role played by an Intermediate Mass Star (IMS). This issue was recently addressed also by Wasserburg et al. (2017). They assumed that below an initial mass of about $5M_{\odot}$ a ^{13}C pocket could be formed during the AGB phases, inducing the reaction $^{13}\text{C}(\alpha,n)^{16}\text{O}$ and producing neutrons efficiently through it. Above this limiting mass they instead considered only neutrons from the $^{22}\text{Ne}(\alpha,n)^{25}\text{Mg}$ reaction.

These more massive models were found to experience HBB at the base of the convective envelope, producing efficiently ^{26}Al . Contrary to previous indications by Trigo-Rodríguez et al. (2009), those authors could not find an explanation for SLRs in their models. In the lower mass range ^{26}Al was insufficiently produced with respect to *s*-elements; for the higher masses the reverse was true. They suggested that a compromise solution might be found mid-way between the two cases, but did not present a detailed model for it. One has to notice that in these computations the ^{13}C source was introduced ad hoc and without a physical model for it, as was common in many computations of the last 20 years or so. Moreover, also for HBB the model-dependency is large, so that these calculations cannot be considered as conclusive.

The approach we want to follow here is different. Whenever possible, we would like to base our considerations on physical models that avoid (as far as it is possible today) the free parameterizations. This attempt must address first of all the chemical peculiarities of light elements and CNO isotopes observed in stellar photospheres (see e.g. Gilroy 1989) and not directly accounted for by traditional stellar models. These peculiarities trace the existence, in stars below $7\text{--}8 M_{\odot}$, of non-convective transport phenomena. In particular, for low mass red giants, several authors (see e.g. Busso et al. 2010; Palmerini et al. 2017, and references cited therein) have shown that the known episodes of convective mixing that occur after the star enters its Red Giant Branch (RGB) stage and that carry to the envelope materials previously processed by nuclear reactions, are not sufficient to explain their isotopic abundance observations from ^7Li up to ^{26}Mg . The most important mixing episodes of this kind are called the “first dredge-up” (hereafter FDU), and the “third dredge-up” (hereafter TDU). The first one is induced by the inward expansion of the envelope after the main sequence; in solar-metallicity stars its main effect is a reduction of the $^{12}\text{C}/^{13}\text{C}$ ratio at the start of the RGB stage to 25–30 (from the initial solar value around 90), and a contemporary increase of the ^{14}N surface abundance. The second mixing episode is a similar envelope penetration occurring repeatedly, after runaways of the He-burning shell called “thermal pulses” (TP), during the final AGB phase. It mixes to the envelope mainly helium, carbon, and *s*-process elements. Stars more massive than about $2.2 M_{\odot}$ also experience a “second dredge-up” (SDU) in early phases of the AGB, carrying up materials polluted by extensive H-burning processes, including He and ^{14}N . In Subection 6.5.2 we shall see that further consequences of interest for the present study may also emerge.

For understanding the further mechanisms of mixing and nucleosynthesis that must be at play in evolved low- and intermediate-mass stars, stellar spectroscopic data were crucially supplemented by the record of isotopic abundances accurately measured in presolar grains found in pristine meteorites, as most of these grains were actually formed in the circumstellar envelopes of AGB stars. Wasserburg et al. (1995a) suggested that the peculiar isotopic composition of oxygen found in a large number of presolar corundum (Al_2O_3) grains could be explained assuming the presence of a deep matter circulation in the mentioned stellar sources; the same process would also be responsible for the presence of ^{26}Al in some of these grains

as well as for the high abundances of ^{13}C and the spread in the concentration of ^7Li observed in low mass red giant stars. These suggestions were then confirmed by Nollett et al. (2003) and later by Palmerini et al. (2011b,a).

Since then, several works have been presented by various groups to interpret those results, originally obtained with parameterized approaches, on the basis of models physically built on some fundamental properties of stellar plasmas. These last ranged from rotational mixing (Charbonnel and Lagarde 2010) to thermohaline diffusion (Eggleton et al. 2006, 2008; Charbonnel and Zahn 2007), to asteroseismic effects inducing gravity waves (Denissenkov and Tout 2003) and to the transport guaranteed by the buoyancy of magnetic flux tubes (Busso et al. 2007). Later, some of these mechanisms were found to be too slow to induce remarkable effects on the RGB (and even more on the shorter AGB phase): this was for example the case with thermohaline diffusion (Denissenkov and Merryfield 2011). Other mechanisms were not applied in detail to the interpretation of isotopic abundances on both the RGB and AGB and then compared to constraints coming from presolar grains.

Two remarkable exceptions however exist. On the basis of considerations concerning the physics of the inner border of the convective envelope of a red giant, and subsequently also the effects of rotation, Cristallo et al. (2009, 2011, 2015a,b) performed a general revision of the models, both for low mass stars (LMS, $M/M_{\odot} \lesssim 2 - 2.2$) and for IMS ($2 - 2.2 \lesssim M/M_{\odot} \lesssim 7 - 8$), where the effects of partial mixing were introduced along the whole evolutionary history and were extended to include the inner He-rich layers, where the presence of deep-mixing (DM) phenomena causes the formation of a ^{13}C -reservoir suitable to induce the activation of the $^{13}\text{C}(\alpha,n)^{16}\text{O}$ neutron source.

Independently of that, Nordhaus et al. (2008) and subsequently Nucci and Busso (2014) showed that the known mechanisms associated with magnetic stellar activity might induce circulations and transport phenomena in the external layer of a star that in specific circumstances might become quite fast (up to 100 m/s). Along the RGB and AGB sequences, their activation can carry materials modified by nucleosynthesis in H- and He-burning shells to the surface of the star. Detailed calculations of the consequences of such a suggestion were subsequently performed by Trippella et al. (2014); Wasserburg et al. (2015); Trippella et al. (2016); more recently, by Palmerini et al. (2017, 2018), comparing the results with a series of constraints ranging from the Solar System distribution of *s*-elements, to the record of oxygen isotopic anomalies and of ^{26}Mg excesses induced by the in-situ decay of ^{26}Al in presolar oxide grains, and up to the isotopic admixtures of trace *n*-rich elements in presolar SiC grains.

In the following two Subsections we shall briefly review what kind of predictions for SLRs in the early solar nebula can be derived by assuming that the forming Sun was contaminated by the slow winds of an AGB star of intermediate mass, hosting either of the two mentioned deep-mixing processes. The reference models we adopted have similar general input parameters. Those of Subsection 6.5.1 adopted the compilation by (Lodders and Palme 2009) for scaled solar abundances and that by Dillmann (2014) for neutron capture cross sections. For the models of

Subsection 6.5.2 the choices were Lodders (2003) and Bao et al. (2000); none of the small differences present in these databases has any effect on the results discussed here. In both cases, as mentioned previously, we did not adopt for ^{182}Hf the suggestions by Lugaro et al. (2014), indicating a revision of the decay rate for the precursor ^{181}Hf , which would substantially increase the *s*-process contribution to ^{182}Hf . This suggestion was based on a single measurement and, on the basis of our discussion of Section 6.3, this last SLR seems already well explained by the Galactic enrichment in *r*-process nuclei. We prefer in these conditions to cautiously wait for new experimental evidence.

6.5.1 Effects of a late AGB star. I. Models with MHD-induced mixing

Nucci and Busso (2014) demonstrated that the very complex MHD equations valid for a stellar plasma might simplify drastically in some specific geometries well approximating the radiative layers below the convective envelope of an evolved star. In this particular case, the equations can be solved analytically in an exact way, yielding simple formulae that can be introduced into stellar models to mimic the local effects induced by the magnetic field. In particular, the solution refers to the general process of buoyancy of magnetized zones early described by E.N. Parker in the fifties, leading to their emergence in the convective envelopes at a rather fast speed.

While this simple analytic solution to the MHD equations can be found under rather broad conditions, when we impose that the result must have a physical meaning applicable to stars, one is led to require that a number of constraints are satisfied. They can be summarized as follows:

1. The density must drop with radius as a power law ($\rho(r) \propto r^k$) with an exponent k that is negative and has a modulus larger than unity.
2. Also the pressure must follow a similar trend, but with a slightly larger negative exponent, so that a polytropic relation of the type $P(r) \propto \rho(r)^\delta$ with $\delta \lesssim 4/3$ holds.
3. The *magnetic Prandtl number* P_m (namely the ratio between the *kinematic* viscosity $\eta = \mu_d/\rho$ (where μ_d is the *dynamic* viscosity) and the magnetic diffusivity ν_m) is much larger than unity (see Spitzer 1956).
4. While the *kinematic* viscosity η cannot be neglected, the *dynamic* viscosity μ_d remains small due to the low density (at the level of one to few percent).

Once those conditions are verified, the radial velocity of magnetized structures turns out to be:

$$v_r = \Gamma r^{-(k+1)} \tag{6.5}$$

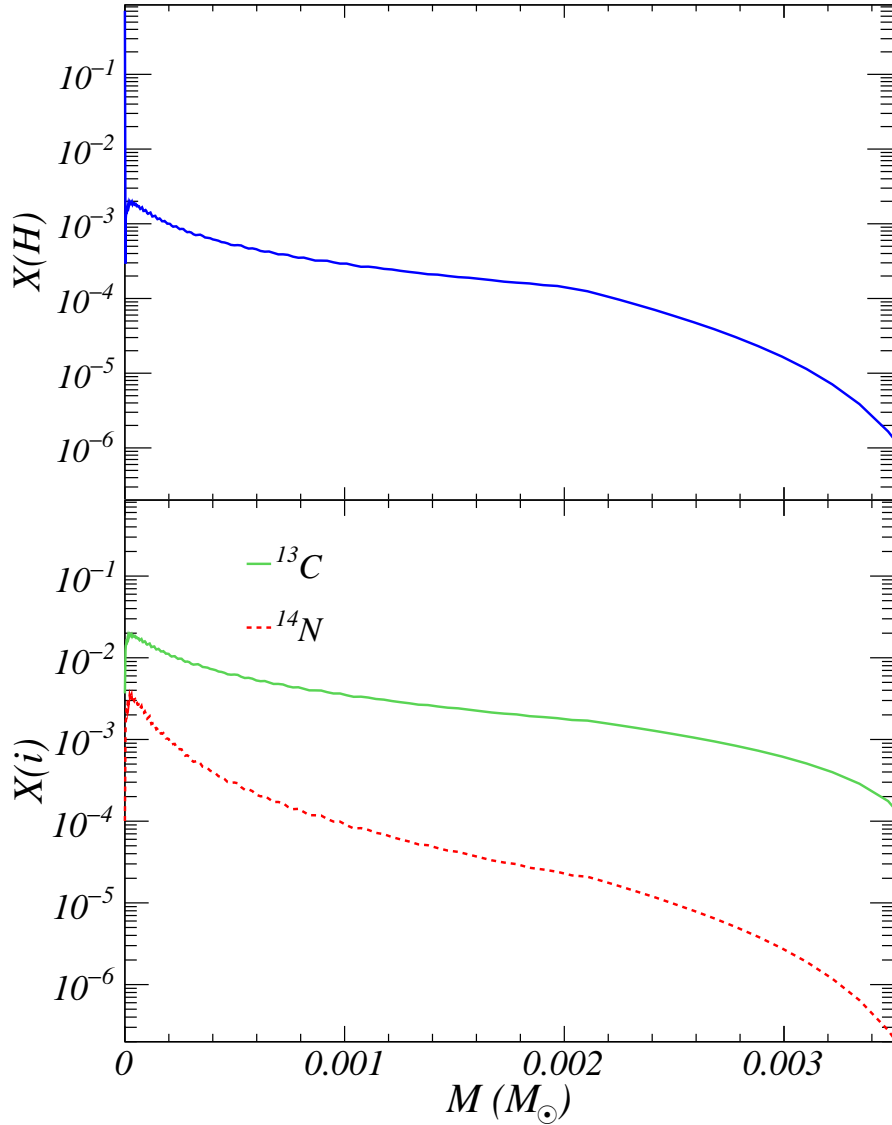


Figure 6.2: Upper panel: The proton profile established in the He-rich layers as a consequence of mass conservation, when magnetic buoyancy is occurring at a TDU episode. The case represented is for a $3 M_{\odot}$ star of solar metallicity, at the sixth TDU. The extension is about 60% of what was found by Trippella et al. (2016) for a $1.5 M_{\odot}$ model. Lower panel: The ensuing profiles of ^{13}C and ^{14}N formed after the H-shell reignition.

where $\Gamma = v_p r_p^{k+1}$. The parameters v_p and r_p refer to the buoyancy velocity and radial position of the innermost layer where the above-mentioned conditions start to be satisfied, while k is the exponent in the relation $\rho \propto r^k$.

Below a convective envelope k is always rather large in absolute value, but negative ($k \leq -3$); then Equation (6.5) yields an unstable condition, in which the buoyancy starts slowly but then gains speed rapidly for increasing radius. The

toroidal component of the magnetic field can be correspondingly written as:

$$B_\varphi = \Phi(\xi) \left(\frac{r_p}{r} \right)^{k+1} \quad (6.6)$$

where ξ is an adimensional variable and $\Phi(\xi)$ can be chosen with a lot of freedom; for a simple solution it might even be a constant ($\Phi(\xi) = B_{\varphi,p}$). Again, we use the suffix “ p ” to indicate the values of the parameters pertaining to the layer from which buoyancy (on average) starts. For more details on the solution and its stellar applications see Nucci and Busso (2014); Trippella et al. (2016); Palmerini et al. (2017, 2018).

During the occurrence of a TDU episode, while the H-burning shell is extinguished, the above procedure describes a mass upflow that forces a downflow of protons from the envelope for mass conservation. In the light of the above considerations, the mixing rate forced by magnetic buoyancy is:

$$\dot{M} = 4\pi\rho_e r_e^2 v_e f \quad (6.7)$$

Here v_e is the velocity of buoyant flux tubes at the envelope bottom and the filling factor f is of the order of 10^{-5} (Trippella et al. 2016). By applying this equation to AGB stars of masses up to $5 M_\odot$, \dot{M} values in the range 10^{-7} to $10^{-5} M_\odot/\text{yr}$ can be obtained.

The downflow of matter from the envelope, pushed down by the rising material, was analyzed in detail by Trippella et al. (2016) for the formation of a ^{13}C -pocket, and the subsequent neutron release via the $^{13}\text{C}(\alpha,n)^{16}\text{O}$ reaction. The ^{13}C reservoir varies in mass (by up to a factor of three) during the sequence of thermal pulses of an individual star. It varies more substantially as a function of the stellar mass.

A typical set of abundance profiles for protons, and subsequently for ^{13}C and ^{14}N , as obtained with our model in the He-rich layers is represented in Figure 6.2. Table 6.3, instead, shows the extension in mass of the pocket at the sixth TDU episode of different stellar models (the metallicity is indicated in the common logarithmic spectroscopic notation $[\text{Fe}/\text{H}]$ relative to solar, so that $[\text{Fe}/\text{H}] = 0$ means a solar metallicity, $[\text{Fe}/\text{H}] = -0.5$ means one-third solar). As is shown by the table, the size of the pocket is rather constant for low masses ($M \leq 2 M_\odot$) while it rapidly drops to very small values for higher-mass AGB stars. The extensions of the p -enriched reservoir are shown for two choices of the starting layer for buoyancy: (i) that characterized by a dynamical viscosity of $\mu_d = 0.01$ and (ii) the one where $\mu_d = 0.05$. This second value seems so far to be the one giving a more coherent interpretation of solar abundances (Trippella et al. 2016) and of isotopic anomalies in presolar grains (Palmerini et al. 2018). We shall therefore adopt it as a reference here.

The same basic mechanism drives DM in the H-rich layers below the convective envelope during H-shell burning. This mixes to the envelope, with the same process, products of proton captures, including the nucleus ^{26}Al , whose prediction is needed for our SLR calculations. Details on the determination of the ^{26}Al

Table 6.3: Mass of the ^{13}C pocket for different models

AGB Model	$\mu_d = 0.01$	$\mu_d = 0.05$
$1.5 M_{\odot}$, $[\text{Fe}/\text{H}] = 0.0$	$2.8 \cdot 10^{-3} M_{\odot}$	$4.9 \cdot 10^{-3} M_{\odot}$
$2.0 M_{\odot}$, $[\text{Fe}/\text{H}] = 0.0$	$2.6 \cdot 10^{-3} M_{\odot}$	$4.4 \cdot 10^{-3} M_{\odot}$
$3.0 M_{\odot}$, $[\text{Fe}/\text{H}] = -0.5$	$5.4 \cdot 10^{-4} M_{\odot}$	$1.4 \cdot 10^{-3} M_{\odot}$
$5.0 M_{\odot}$, $[\text{Fe}/\text{H}] = 0.0$	$1.5 \cdot 10^{-5} M_{\odot}$	$0.9 \cdot 10^{-4} M_{\odot}$

abundance in the envelope have been already published and can be found in Palmerini et al. (2017).

On the basis of the above procedures, we have computed the envelope abundances of ^{26}Al and of neutron-rich nuclei for several models; we shall discuss the results for a couple of typical cases among those indicated in Table 6.2.

One can apply the formula of Equation (6.4) to a couple of nuclei produced by a model star, thus fixing the two parameters d and Δ . Then one has to verify what kind of predictions this implies for the other radioactive nuclei in pristine solids.

For the reference nuclei we use ^{26}Al and ^{41}Ca . The motivation for this choice lays in the fact that it has been ascertained (Duprat and Tatischeff 2007; Villeneuve et al. 2009) that ^{26}Al cannot be produced by solar spallation, and needs to derive from a stellar source. Moreover, the correlation between ^{26}Al and ^{41}Ca established by Sahijpal et al. (1998) and reported here in Figure 6.1 suggests that the two nuclei may have the same origin. We underline that this constraint is not considered in several published scenarios among those quoted, but this appears to be a serious drawback: in fact, the mentioned correlation and the stellar origin for ^{26}Al represent important pieces of evidence and should be taken into account.

Tables 6.4 and 6.5 show the outcomes obtained by deriving the two free parameters from the mentioned nuclei (i.e. fixing d and Δ so that the measurements for ^{26}Al and ^{41}Ca in ESS solids are reproduced), adopting two typical models for IMSs from our calculations. They refer to a $3 M_{\odot}$ and a $5 M_{\odot}$ star, with solar metallicity. (We do not discuss here in detail results for significantly lower masses, because of their excessively long lifetimes, essentially inhibiting any chance encounter with the forming Sun).

The main result that can be derived from even a quick glance to Tables 6.4 and 6.5 is that, when a ^{13}C pocket is included (even of a minimal extension, as in the case of the $5 M_{\odot}$ model), accounting for the lighter radioactive isotopes ^{26}Al and ^{41}Ca always implies some large excesses on nuclei heavier than iron. This is a very big problem: a deficit on isotopes like ^{107}Pd , ^{135}Cs , or ^{182}Hf , which are not of purely s -process origin, might be compensated by some inheritance of r -process products from Galactic evolution; but large excesses, like those shown in the tables, cannot be accommodated.

As mentioned, the main difference between our models and those by Wasserburg et al. (2006), where a nice solution could be found for several SLRs, is the presence

Table 6.4: SLRs as predicted by a $3 M_{\odot}$ model with MHD mixing.

[Fe/H] = 0 – Dilution $d = 9.05 \cdot 10^{-3}$ – Delay time $\Delta = 0.87$ Myr						
Rad.	Ref.	τ_R (Myr)	N^R/N^S	q^S	$\alpha^{R,S}$	$[N^R/N^S]_{Meas.}$
^{26}Al	^{27}Al	1.03	$1.34 \cdot 10^{-2}$	1.004	$5.23 \cdot 10^{-5}$	$(5.23 \pm 0.13) \cdot 10^{-5}$
^{41}Ca	^{40}Ca	0.15	$1.48 \cdot 10^{-4}$	0.994	$4.00 \cdot 10^{-9}$	$4 \cdot 10^{-9}$
^{60}Fe	^{56}Fe	3.75	$2.18 \cdot 10^{-5}$	0.994	$1.55 \cdot 10^{-7}$	$10^{-8} - 10^{-6}$
^{107}Pd	^{108}Pd	9.4	$1.33 \cdot 10^{-1}$	6.198	$6.78 \cdot 10^{-3}$	$(5.9 \pm 2.2) \cdot 10^{-5}$
^{135}Cs	^{133}Cs	3.3	$6.77 \cdot 10^{-1}$	2.101	$5.53 \cdot 10^{-3}$	$4.8 \cdot 10^{-4}$
^{182}Hf	^{180}Hf	12.8	$1.18 \cdot 10^{-2}$	4.027	$4.01 \cdot 10^{-4}$	$(9.81 \pm 0.41) \cdot 10^{-5}$
^{205}Pb	^{204}Pb	22	$6.58 \cdot 10^{-1}$	2.552	$1.46 \cdot 10^{-2}$	10^{-3}

Table 6.5: SLRs as predicted by a $5 M_{\odot}$ model with MHD mixing.

[Fe/H] = 0 – Dilution $d = 3.27 \cdot 10^{-2}$ – Delay time $\Delta = 0.85$ Myr						
Rad.	Ref.	τ_R (Myr)	N^R/N^S	q^S	$\alpha^{R,S}$	$[N^R/N^S]_{Meas.}$
^{26}Al	^{27}Al	1.03	$3.65 \cdot 10^{-3}$	1.002	$5.23 \cdot 10^{-5}$	$(5.23 \pm 0.13) \cdot 10^{-5}$
^{41}Ca	^{40}Ca	0.15	$3.57 \cdot 10^{-5}$	0.996	$4.00 \cdot 10^{-9}$	$4 \cdot 10^{-9}$
^{60}Fe	^{56}Fe	3.75	$4.36 \cdot 10^{-4}$	0.995	$1.13 \cdot 10^{-5}$	$10^{-8} - 10^{-6}$
^{107}Pd	^{108}Pd	9.4	$2.24 \cdot 10^{-2}$	1.139	$7.61 \cdot 10^{-4}$	$(5.9 \pm 2.2) \cdot 10^{-5}$
^{135}Cs	^{133}Cs	3.3	$3.09 \cdot 10^{-2}$	1.011	$7.60 \cdot 10^{-4}$	$4.8 \cdot 10^{-4}$
^{182}Hf	^{180}Hf	12.8	$3.66 \cdot 10^{-4}$	1.026	$1.15 \cdot 10^{-5}$	$(9.81 \pm 0.41) \cdot 10^{-5}$
^{205}Pb	^{204}Pb	22	$4.42 \cdot 10^{-2}$	1.038	$1.44 \cdot 10^{-3}$	10^{-3}

of a ^{13}C pocket, which was instead excluded in that solution. Whatever the extension of the pocket is, the neutron flux remains always too large to find any consistency with ^{26}Al production. In the light of our MHD model for the formation of the neutron source ^{13}C , we have no way to solve this inconsistency and must admit that a solution for SLRs in the framework of our models for mixing and nucleosynthesis in AGB stars can no longer be found.

6.5.2 Effects of a late AGB star. II. Models with opacity-induced mixing

During a TDU, more than one physical mechanism can contribute to the downward diffusion of protons into the underlying He- and C-rich layer. Spectroscopic observations and pre-solar SiC grain measurements provide indications on the shape and extension of the ^{13}C pocket. Recent studies point to a flat ^{13}C profile in a region from one to a few $10^{-3} M_{\odot}$ thick (see e.g. Liu et al. 2014b, 2015; Palmerini et al. 2018); in this respect both the DM models considered in this work fulfil the basic requirements. Among the constraints to respect, there is also a need to limit the abundance by mass of ^{13}C in each layer, otherwise a

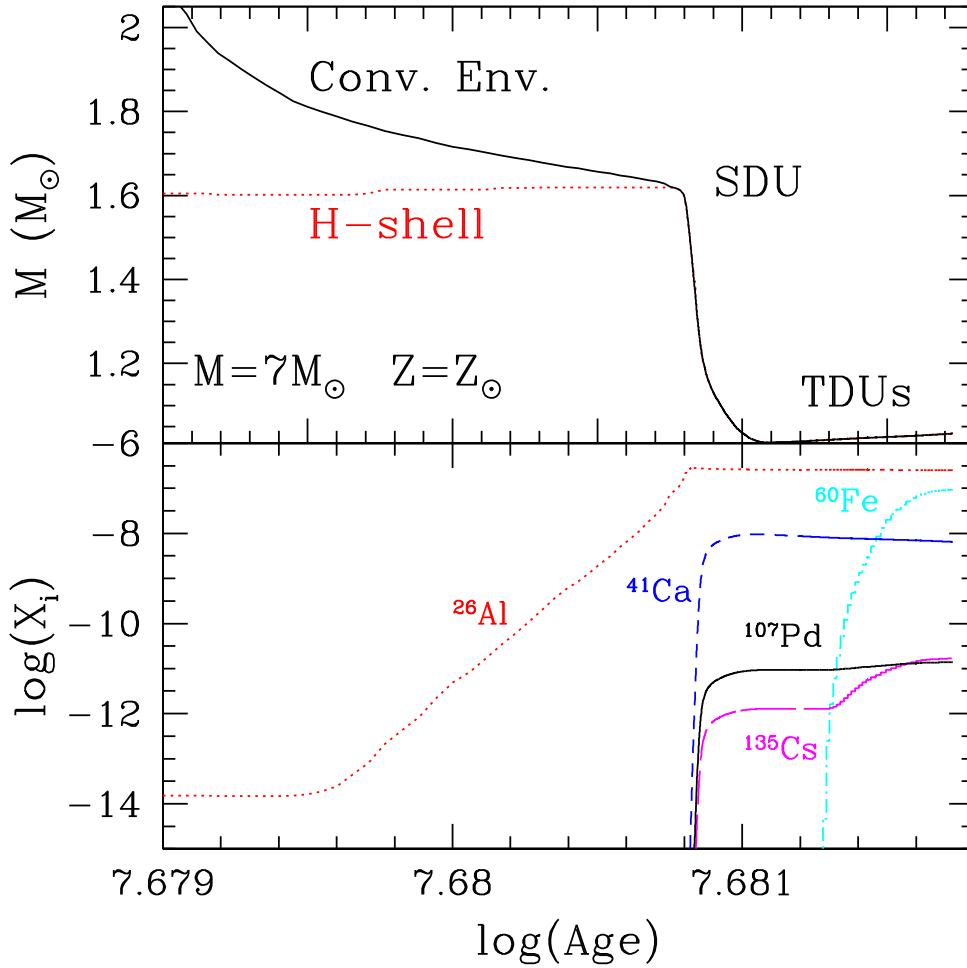


Figure 6.3: Upper panel: temporal evolution of the mass coordinates of the H-burning shell and of the inner border of the convective envelope for a $7 M_{\odot}$ model with solar metallicity. Lower panel: temporal evolution of surface abundances for some radioactive isotopes of interest.

too large production of ^{14}N (a neutron poison) would be obtained, hampering s -processing. In the so-called “FRUITY” models (Cristallo et al. 2011, 2015b, 2016), the approach first discussed by Becker and Iben (1979) was followed. It considers the effects on mixing of the opacity difference between the (opaque) H-rich envelope and the (more transparent) He-rich underlying region. During a TDU, such a difference produces a discontinuity in the temperature gradient at the inner border of the envelope, which leads to a consequent abrupt decrease of the convective velocities (see Straniero et al. 2006). This process is unbalanced and unstable: any perturbation of the convective/radiative interface tending to expand downward the boundary would grow, thus leading to an even deeper mixing. In such a condition, it is reasonable to hypothesize that the result is not an extension of the envelope as a whole, but rather that individual convective

elements with non-zero velocities penetrate beyond the limit defined by the Schwarzschild criterion (where the radiative gradient equals the adiabatic one). Those bubbles are decelerated by the steep pressure gradient immediately below the inner envelope border, which strongly limits the extent of their penetration. In order to mimic this behavior, we imposed that bubble velocities below the formal Schwarzschild border decline exponentially, namely:

$$v = v_{IN} \exp\left(-\frac{\Delta r}{\beta H_p}\right) \quad (6.8)$$

Here Δr is the distance from the Schwarzschild border, v_{IN} is the velocity of the most internal convective mesh, H_p is the pressure scale height at the border itself and β is a free parameter (usually set to $\beta=0.1$ on observational grounds: for its calibration see Cristallo et al. 2009). The introduction of this algorithm implies that:

1. the convective border becomes more stable;
2. the TDU efficiency is increased;
3. a profile of protons is left below the convective envelope.

As with MHD instabilities discussed in the previous Subsection, also in this approach the mass extension of the pocket does not remain constant along the AGB, but decreases steadily, following the shrinking of the He-intershell region with increasing core mass (Cristallo et al. 2009). A potential problem arising from this approach is that the exponential decline of convective velocities would proceed to the center of the star, unless a maximum penetration is fixed. This limit was initially set to $2H_p$ (Straniero et al. 2006). Later, a better match to isotopic ratios in pre-solar SiC grains (Liu et al. 2014b, 2015) suggested to fix the penetration limit in terms of the convective velocity, imposing that it stops at a certain small fraction (10^{-11}) of the value achieved at the Schwarzschild border. This corresponds to a depth $2.2 - 2.3H_p$.

The ^{13}C pockets obtained with the method outlined above are not remarkably different from those proposed by Trippella et al. (2016) and discussed in Subsection 6.5.1, although they are characterized by a larger amount of ^{14}N in the upper region. This feature is intrinsically connected to the approach followed, which yields a top-down flow of the material (and not a bottom-up movement, like for the magnetic tubes characterizing the models of Subsection 6.5.1).

We refer to Cristallo et al. (2015a, 2016) and references therein for a detailed description of the nucleosynthesis resulting from the assumptions outlined above. Here we recall simply that the models discussed are rather “cool” (e.g. cooler than those outlined in Subsection 6.5.1) and due to this do not experience HBB, a process that, as already mentioned, has a strong model dependence.

For the specific purposes of this work and in the framework of the approach just discussed, we integrated the FRUITY database by computing also more massive AGB models ($6.5 \leq M/M_\odot \leq 8$) at solar metallicity. The surface

isotopic distributions of those masses include the effects of SDU. This event has a considerable impact on radioactive isotope abundances. As already highlighted, SDU occurs during the early-AGB phase of IMSs; at that time, the switching off of the H-burning shell is followed by the inward penetration of the convective envelope in the H-depleted zone (upper panel of Figure 6.3). As widely reported in the literature, among the consequences of the SDU there is an increase of the surface ^4He , ^{14}N , and ^{26}Al abundances. A further effect present in our models induces enhancements for at least three more SLRs of interest, beyond ^{26}Al : they are ^{41}Ca , ^{107}Pd , and ^{135}Cs , ensuing from a marginal neutron-capture episode (see the lower panel of Figure 6.3, which also shows ^{60}Fe). Indeed, those isotopes are produced by the radiative burning of the amount of ^{13}C present in H-burning ashes (its CNO equilibrium abundance). This occurs because the layers beyond the H-burning shell are heated up to more than 10^8 K, i.e. to large enough temperatures to activate the $^{13}\text{C}(\alpha, n)^{16}\text{O}$ reaction. Later, surface abundances are further changed by TDUs (although not for all isotopes). Note that a similar finding has never been reported in the literature, because post-process calculations commonly ignore the nucleosynthesis of heavy elements before the TP-AGB phase. Our FRUITY stellar evolutionary models, instead, are computed with a full nuclear network, starting from the Main Sequence phase and up to the tip of the AGB.

Once all the above effects are considered, the final surface abundances of radioactive nuclei in our models can be used to estimate their possible contribution to their inventory in the ESS. Tables 6.6 and 6.7 summarize these results for two typical cases. Much like what we obtained in Subsection 6.5.1, also in this case there is no space for a compromise agreement. The predictions always include excesses of some heavy ($A > 56$) neutron-capture nuclei (especially ^{107}Pd) with respect to ^{26}Al and ^{41}Ca (from which, again, we deduce the time delay Δ and the dilution factor, d). We argue that this conclusion is not limited to the specific models considered in this work as examples: any DM model yielding proton penetration into the He-rich layers, inducing the formation of a ^{13}C pocket, will inevitably end up with excesses of ^{107}Pd and other neutron-rich isotopes with respect to the lighter ones.

Figure 6.4 summarizes the results of this Section, showing together the predictions from Subsections 6.5.1 and 6.5.2; they can be represented together thanks to the similarity of the findings, despite the different (complementary) starting hypotheses. Over the mass range from about 2 to about $8 M_{\odot}$, when one constrains the free parameters Δ and d through a fit of the measured ESS abundances of ^{26}Al and ^{41}Ca , heavier nuclei are not simultaneously accounted for and in all cases the most relevant problem resides in a huge overproduction of ^{107}Pd . This fact leads us to the conclusion that the scenario of the Solar System pollution by an AGB star of intermediate mass may be inadequate, although for the most massive models a window is still open. In particular, our models are rather cool and do not develop HBB. As mentioned, this process was examined by Wasserburg et al. (2017), with negative conclusions. However, HBB is still strongly model dependent. One would need an ad-hoc H-burning process at the base of the

Table 6.6: SLRs as predicted by a $6 M_{\odot}$ model.

[Fe/H] = 0 – Dilution $d = 5.18 \cdot 10^{-2}$ – Delay time $\Delta = 0.98$ Myr						
Rad.	Ref.	τ_R (Myr)	N^R/N^S	q^S	$\alpha^{R,S}$	$[N^R/N^S]_{Meas.}$
^{26}Al	^{27}Al	1.03	$2.64 \cdot 10^{-3}$	0.991	$5.23 \cdot 10^{-5}$	$(5.23 \pm 0.13) \cdot 10^{-5}$
^{41}Ca	^{40}Ca	0.15	$5.42 \cdot 10^{-5}$	0.980	$4.00 \cdot 10^{-9}$	$4 \cdot 10^{-9}$
^{60}Fe	^{56}Fe	3.75	$1.32 \cdot 10^{-5}$	1.008	$5.30 \cdot 10^{-7}$	$10^{-8} - 10^{-6}$
^{107}Pd	^{108}Pd	9.4	$2.31 \cdot 10^{-2}$	1.200	$1.29 \cdot 10^{-3}$	$(5.9 \pm 2.2) \cdot 10^{-5}$
^{135}Cs	^{133}Cs	3.3	$3.75 \cdot 10^{-2}$	1.007	$1.39 \cdot 10^{-3}$	$4.8 \cdot 10^{-4}$
^{182}Hf	^{180}Hf	12.8	$1.21 \cdot 10^{-2}$	1.271	$7.34 \cdot 10^{-4}$	$(9.81 \pm 0.41) \cdot 10^{-5}$
^{205}Pb	^{204}Pb	22	$1.73 \cdot 10^{-2}$	1.099	$9.39 \cdot 10^{-4}$	10^{-3}

Table 6.7: SLRs as predicted by a $7 M_{\odot}$ model.

[Fe/H] = 0 – Dilution $d = 3.32 \cdot 10^{-2}$ – Delay time $\Delta = 1.01$ Myr						
Rad.	Ref.	τ_R (Myr)	N^R/N^S	q^S	$\alpha^{R,S}$	$[N^R/N^S]_{Meas.}$
^{26}Al	^{27}Al	1.03	$4.31 \cdot 10^{-3}$	0.976	$5.23 \cdot 10^{-5}$	$(5.23 \pm 0.13) \cdot 10^{-5}$
^{41}Ca	^{40}Ca	0.15	$1.05 \cdot 10^{-4}$	0.980	$4.00 \cdot 10^{-9}$	$4 \cdot 10^{-9}$
^{60}Fe	^{56}Fe	3.75	$6.79 \cdot 10^{-5}$	1.008	$1.74 \cdot 10^{-6}$	$10^{-8} - 10^{-6}$
^{107}Pd	^{108}Pd	9.4	$1.21 \cdot 10^{-2}$	1.078	$3.88 \cdot 10^{-4}$	$(5.9 \pm 2.2) \cdot 10^{-5}$
^{135}Cs	^{133}Cs	3.3	$1.24 \cdot 10^{-2}$	0.963	$2.79 \cdot 10^{-4}$	$4.8 \cdot 10^{-4}$
^{182}Hf	^{180}Hf	12.8	$7.24 \cdot 10^{-3}$	1.132	$2.51 \cdot 10^{-4}$	$(9.81 \pm 0.41) \cdot 10^{-5}$
^{205}Pb	^{204}Pb	22	$1.03 \cdot 10^{-2}$	0.992	$3.23 \cdot 10^{-4}$	10^{-3}

envelope, to produce ^{26}Al in exactly the right amount to compensate for the excesses in n -rich isotopes induced by the presence of a ^{13}C pocket. The reality of this possibility must however be explored in detail. This will be the subject of a forthcoming work.

6.6 Nucleosynthesis in massive stars and the role of late supernovae

MSs are defined as those that can contract and heat up to several billions degrees, eventually reaching the conditions for the collapse of the core up to nuclear densities. Depending on the initial metallicity, the initial rotational velocity and the treatment of the convective borders, the minimum mass suitable to evolve up to the final stages ranges somewhere between 9 and $12 M_{\odot}$. This limit marks also the maximum mass of the so-called Super-AGB stars, i.e. those that form a strongly electron-degenerate core only after burning C and/or Ne. The evolution of these stars is characterized by repeated, weak but very frequent, thermal pulses and may end up with the formation of O-Ne white dwarfs or electron-capture supernovae (Denissenkov et al. 2013; Doherty et al. 2017). The

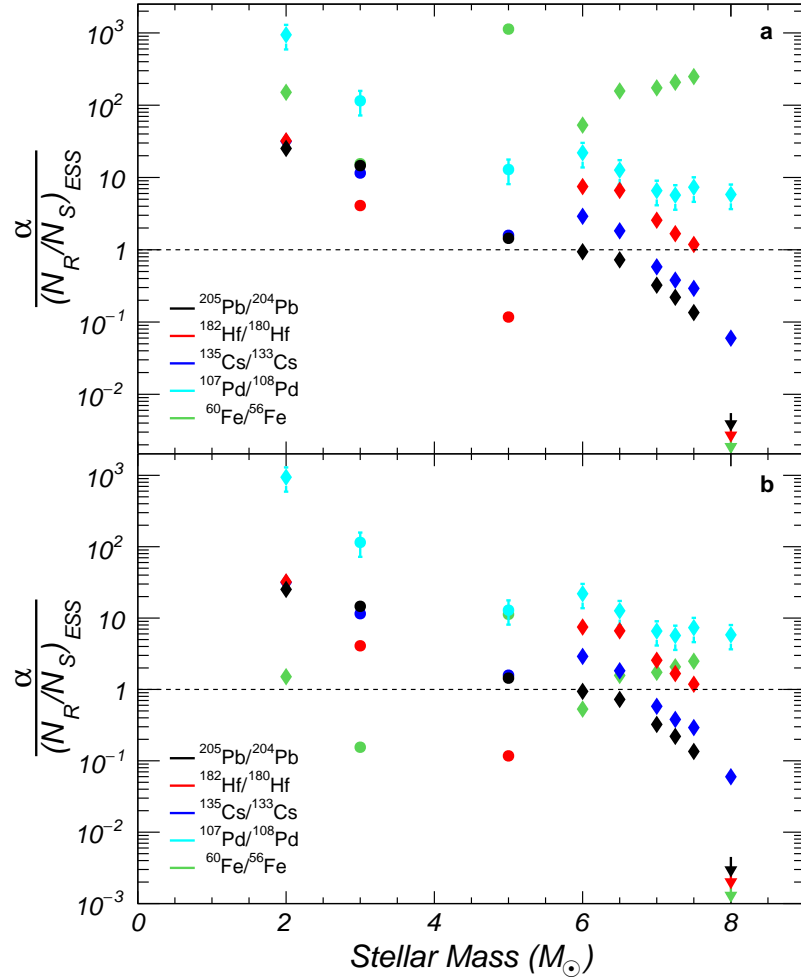


Figure 6.4: Prediction for heavy SLRs from AGB stars with the physical models for DM discussed in Subsections 6.5.1 and 6.5.2. In panel a) we adopt as a reference ESS ratio for $^{60}\text{Fe}/^{56}\text{Fe}$ the value 10^{-8} , while in panel b) the opposite extreme choice is made (10^{-6}). The picture shows that, when the free parameters Δ and d are fixed through a fit of the measured ESS abundances of ^{26}Al and ^{41}Ca , heavier nuclei are not satisfactorily accounted for. Just to make an example, even the models explaining well ^{60}Fe (those around $6-7 M_{\odot}$, in panel b) always imply excesses by a factor $8-20$ on ^{107}Pd . (In the plot circular dots indicate the models of Subsection 6.5.1, diamonds those of Subsection 6.5.2. The case of a $2 M_{\odot}$ illustrated here is not discussed explicitly in a table, due to its too long lifetime that would make a chance encounter with the forming Sun impossible. It is shown here only to illustrate the rather smooth and continuous sequence of behaviors characterizing the two series of models that, albeit different, converge to a rather unique and coherent view of AGB phases.)

possible contributions of Super-AGB stars to the inventory of ESS radioactivities was early analyzed by Lugaro et al. (2012); it will not be re-discussed here, in view of the large uncertainties and model-dependencies related to the very complex

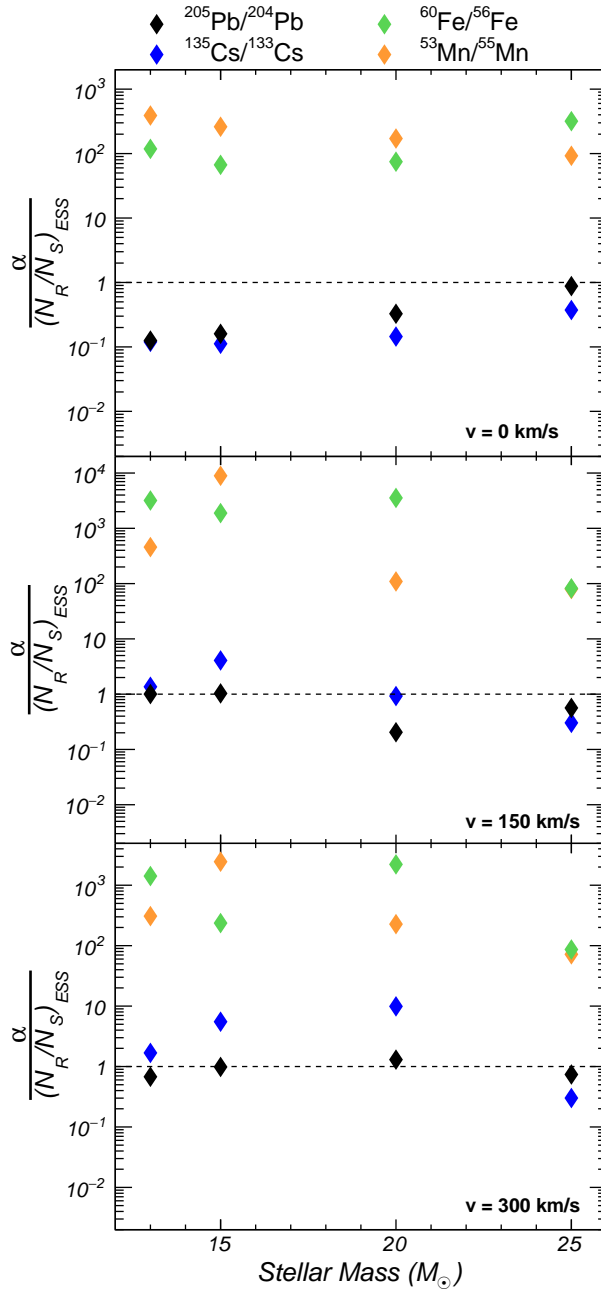


Figure 6.5: Predictions for SLRs from a late contamination by a CCSNe in the mass range 13–25 M_{\odot} , assuming as a reference a solar $^{60}\text{Fe}/^{56}\text{Fe}$ ratio of $1 \cdot 10^{-8}$. No one of the models shown can account acceptably for the measurements, once ^{26}Al and ^{41}Ca are used for fixing the free parameters. In particular, ^{60}Fe and ^{53}Mn would be in any case enormously overproduced.

physics still affecting this mass range.

Since massive stars avoid electron degeneracy and evolve towards higher and higher temperatures, they activate nuclear reactions that form increasingly heavier nuclei through the H-, He-, C-, Ne-, O-, and Si-burning phases. Once the

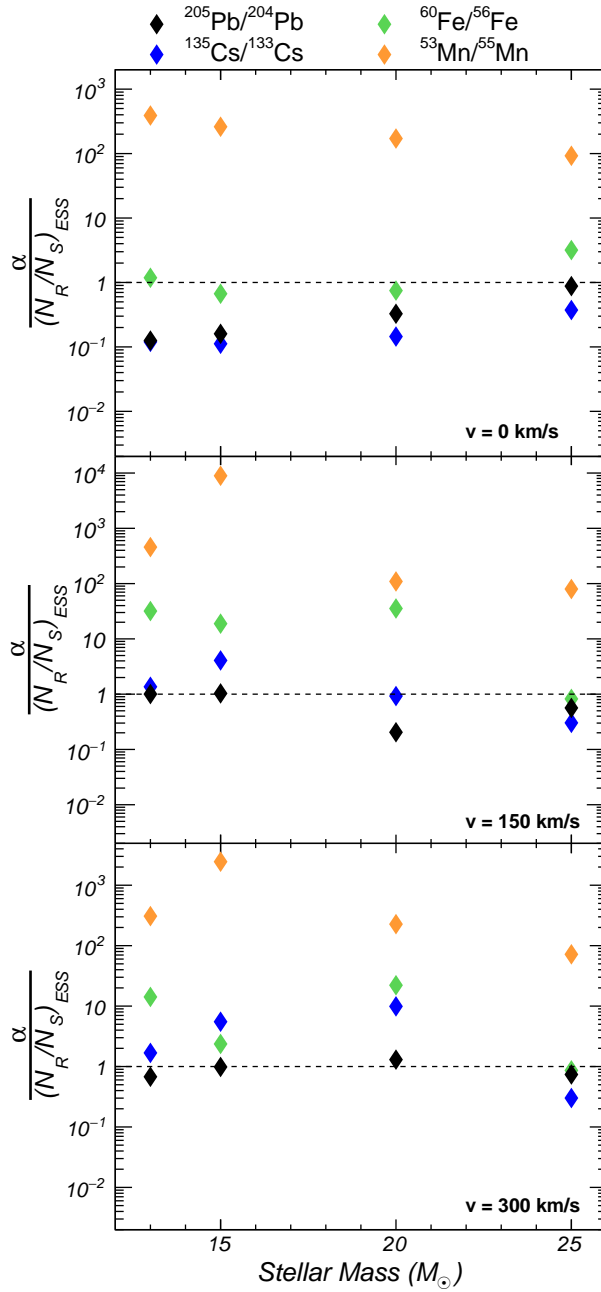


Figure 6.6: Predictions for SLRs from a late contamination by a CCSN in the mass range $13\text{-}25 M_{\odot}$ assuming as a reference a solar $^{60}\text{Fe}/^{56}\text{Fe}$ ratio of $1 \cdot 10^{-6}$. As the figure shows, in this second case the models with no rotation up to $20 M_{\odot}$ and the model of a $25 M_{\odot}$ with a rather large rotation rate (≥ 150 km/sec) would account reasonably for ^{60}Fe (in addition to ^{26}Al and ^{41}Ca that were used for fixing the parameters) avoiding overproductions for ^{107}Pd and ^{135}Cs . However, ^{53}Mn would remain, also in this case, overproduced by two orders of magnitude and would require a much larger mass cut, as in Meyer and Clayton (2000).

temperature reaches ~ 10 GK, electrons become relativistic and the contraction

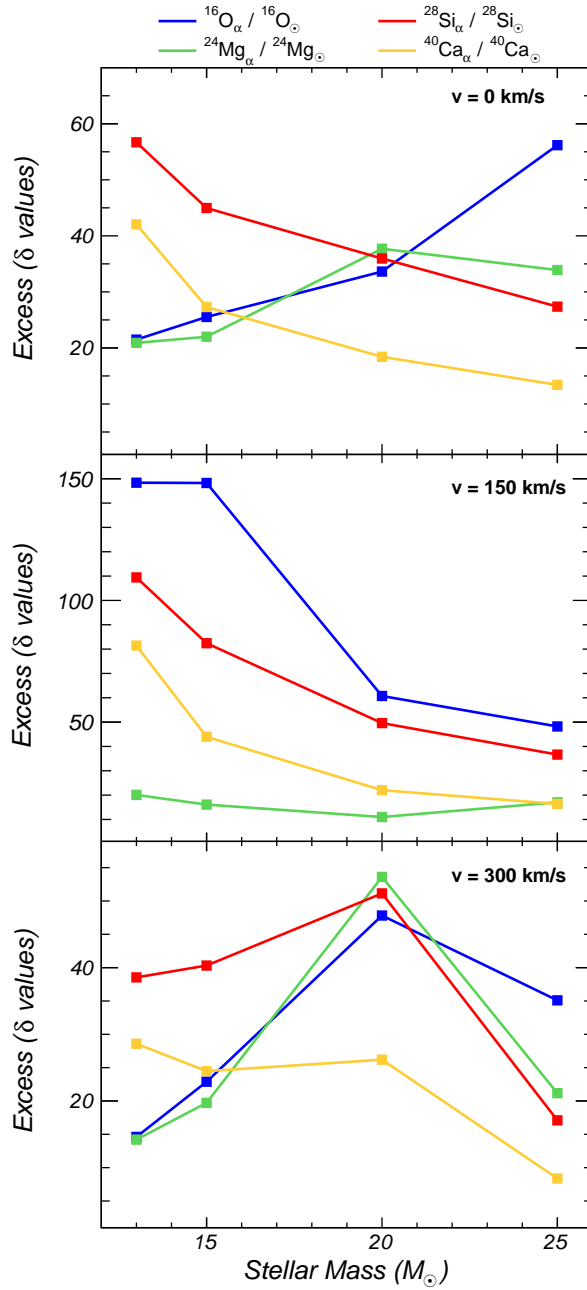


Figure 6.7: Values of the excesses introduced on α -rich isotopes of major stable elements by the CCSN models discussed so far, tuned to account for the $^{26}\text{Al}/^{27}\text{Al}$ and $^{41}\text{Ca}/^{40}\text{Ca}$ number ratios in the ESS. The plot shows the increase with respect to accepted average abundances. We recall that shifts in excess of a few permil are excluded by present-day measurements (see Section 6.2).

reverses into a collapse of the core. Here nuclear densities are reached, eventually driving the phenomenon of a CCSN explosion. The ensuing shock wave causes the violent expulsion of the external layers into the interstellar medium. The very high peak temperature achieved by the innermost layers, while the shock front

moves outward, induces a substantial modification of the pre-existing composition; this means that it is not correct to neglect the nucleosynthesis induced by the passage of the shock wave (explosive nucleosynthesis) if one wants to study the contribution of massive stars to the Galactic enrichment and to the ESS composition. Unfortunately, some of the works present in the literature on the ESS radioactivities do not take into account explosive phases. This is in particular the case for some of the scenarios for the sequential contamination of a pre-solar molecular cloud (Gounelle and Meynet 2012; Gounelle et al. 2006). One should therefore look at these results with a bit of caution.

In the external layers of the star, through which the shock wave passes, the relics of core-He- and shell-C-burning are abundant. These zones include *s*-process isotopes, having experienced *n*-captures, mainly from the $^{22}\text{Ne}(\alpha, n)^{25}\text{Mg}$ source, during the quiet evolution of the supernova progenitor. They are actually considered as the main site where the *weak s*-process component is generated (Raiteri et al. 1993; Pignatari et al. 2010), producing isotopes up to those of Sr, sited at the “magic” neutron number $N=50$. Above this mass region, neutron captures in massive stars become rather inefficient, but they might still play a role for the ESS radioactivities, as these last were typically produced in environments with small enhancement factors q^s (see also Section 6.5).

In the scenario of Solar System formation, a massive star forming a CCSN was suggested by several authors as a potential trigger, for inducing the final collapse of the presolar cloud through shock waves (Cameron and Truran 1977; Vanhala and Boss 2002; Boss 2003). This event must have been accompanied by a strong injection of newly formed nuclei into the ESS, including SLRs like ^{26}Al , ^{41}Ca , ^{60}Fe , ^{53}Mn , plus possibly those synthesized in fast and slow *n*-capture processes. Also many stable isotopes of major elements are expected to receive important contributions. Hence, by modelling the processes of hydrostatic and explosive nucleosynthesis in massive pre-supernova and during the final CCSN events, one can predict the isotopic anomalies that such a pollution would have induced in the solar nebula.

As already mentioned, CCSNe are typically the main producers of intermediate-mass elements, from O to Ti; they also synthesize C, iron-peak nuclei and the weak component of the *s*-process. In order to evaluate the possibility that a late Supernova event be responsible for polluting the ESS with the radioactive species not accounted for by the average Galactic enrichment (Section 6.3), it is therefore also necessary to estimate the total variations that this would imply both on the solar abundances of stable elements and on their isotopic admixture. These contributions strongly depend on the initial stellar mass, on the chemical composition and on the rotational properties of the stellar models.

In this work we consider, as possible contaminating candidates, stars that are parents to CCSNe, having a solar metallicity and an initial mass in the range from 13 to 25 M_{\odot} . The models were computed with the FRANEC¹ evolutionary

¹*Software:* Frascati RAphson-Newton Evolutionary Code (Chieffi and Limongi 2013, 2015; Limongi and Chieffi 2018).

Table 6.8: SLRs as predicted by a non-rotating $20 M_{\odot}$ model.

[Fe/H] = 0 – Dilution $d = 1.85 \cdot 10^{-4}$ – Delay time $\Delta = 1.34$ Myr						
Rad.	Ref.	τ_R (Myr)	N^R/N^S	q^S	$\alpha^{R,S}$	$(N^R/N^S)_{Meas.}$
^{26}Al	^{27}Al	1.03	$5.42 \cdot 10^{-3}$	192.2	$5.23 \cdot 10^{-5}$	$(5.23 \pm 0.13) \cdot 10^{-5}$
^{41}Ca	^{40}Ca	0.15	$1.68 \cdot 10^{-3}$	99.52	$4.00 \cdot 10^{-9}$	$4 \cdot 10^{-9}$
^{53}Mn	^{55}Mn	5.3	$5.75 \cdot 10^{-1}$	13.88	$1.15 \cdot 10^{-3}$	$(6.7 \pm 0.56) \cdot 10^{-6}$
^{60}Fe	^{56}Fe	3.75	$3.44 \cdot 10^{-4}$	16.80	$7.48 \cdot 10^{-7}$	$10^{-8} - 10^{-6}$
^{135}Cs	^{133}Cs	3.3	$4.13 \cdot 10^{-2}$	14.43	$6.95 \cdot 10^{-5}$	$4.8 \cdot 10^{-4}$
^{205}Pb	^{204}Pb	22	$1.54 \cdot 10^{-1}$	12.19	$3.27 \cdot 10^{-4}$	10^{-3}

Table 6.9: SLRs as predicted by a $25 M_{\odot}$ model with rotational velocity of 150 km s^{-1} .

[Fe/H] = 0 – Dilution $d = 9.11 \cdot 10^{-5}$ – Delay time $\Delta = 1.41$ Myr						
Rad.	Ref.	τ_R (Myr)	N^R/N^S	q^S	$\alpha^{R,S}$	$(N^R/N^S)_{Meas.}$
^{26}Al	^{27}Al	1.03	$1.08 \cdot 10^{-2}$	209.5	$5.23 \cdot 10^{-5}$	$(5.23 \pm 0.13) \cdot 10^{-5}$
^{41}Ca	^{40}Ca	0.15	$3.01 \cdot 10^{-3}$	179.7	$4.00 \cdot 10^{-9}$	$4 \cdot 10^{-9}$
^{53}Mn	^{55}Mn	5.3	$5.44 \cdot 10^{-1}$	14.08	$5.35 \cdot 10^{-4}$	$(6.7 \pm 0.56) \cdot 10^{-6}$
^{60}Fe	^{56}Fe	3.75	$7.38 \cdot 10^{-4}$	17.80	$8.21 \cdot 10^{-7}$	$10^{-8} - 10^{-6}$
^{135}Cs	^{133}Cs	3.3	$1.43 \cdot 10^{-1}$	18.10	$1.45 \cdot 10^{-4}$	$4.8 \cdot 10^{-4}$
^{205}Pb	^{204}Pb	22	$3.05 \cdot 10^{-1}$	21.63	$5.64 \cdot 10^{-4}$	10^{-3}

code (Chieffi and Limongi 2013, 2015; Limongi and Chieffi 2018) and include the effects of rotation. The main consequence of including rotation is that of increasing the total yields of the elements, because it basically produces additional mixing processes, thus feeding more efficiently the burning layers with fresh fuels. For our purposes, we consider a set of models with masses of 13, 15, 20 and $25 M_{\odot}$ and initial equatorial rotational velocities of 0, 150 and 300 km/s . Each model was evolved from the pre-main sequence up to the onset of the core bounce with the FRANEC code. The explosive phases were then computed by re-processing the structure and composition left after the hydrostatic phases through a hydrodynamical code, which takes into account the passage of the shock wave and the occurrence of explosive nucleosynthesis. The explosion was simulated in each case by considering the mixing and fall back mechanism (Umeda and Nomoto 2002). Within the mixing and fall back scenario, it is assumed that, after the passage of the shock wave, a fraction of the most internal zone of the star is homogeneously mixed before the fallback on the remnant of part of the ejected material occurs. In these models the inner border of the mixed region was set at the layer where $[\text{Ni}/\text{Fe}] = 0.2$, while the outer border was fixed at the base of the O shell ($X(\text{O}) = 0.001$). Then, the mass cut between ejected and non-ejected material is chosen by requiring that $0.07 M_{\odot}$ of ^{56}Ni are ejected, thus reproducing the known iron production from SN1987A (Li et al. 1993).

Tables 6.8 and 6.9 show how all the models considered do produce SLRs,

especially ^{53}Mn and ^{60}Fe . In particular, fixing again the dilution factor d and the time delay Δ so that ^{26}Al and ^{41}Ca are reproduced, we see that the $25 M_{\odot}$ model, in cases characterized by a fast rotation velocity and adopting the highest choices of the $^{60}\text{Fe}/^{56}\text{Fe}$ ratio in the ESS (close to $\simeq 10^{-6}$), would account rather well for ^{60}Fe itself and would imply a ratio $^{205}\text{Pb}/^{204}\text{Pb}$ within a factor-of-two from the measurement. It would however also yield some deficit in ^{135}Cs , which, as seen, cannot be compensated by contributions from the Galactic evolution of r -process nuclei (despite the fact that this isotope is not shielded against fast r -process decays). ^{53}Mn would be overabundant by almost two orders of magnitude and would require a special mass cut, as suggested by Meyer and Clayton (2000). (^{107}Pd and ^{182}Hf were not in the network adopted in the original models and their abundances cannot be checked).

These results are reported also in Figures 6.5 and 6.6, for the two extreme choices of the $^{60}\text{Fe}/^{56}\text{Fe}$ abundance in the ESS (10^{-8} for Figure 6.5 and 10^{-6} for Figure 6.6). As is shown, only in the second case, for a $25 M_{\odot}$ model with a high rotation rate (≥ 150 km/sec) one obtains a reasonable agreement between some of the measurements and predictions. However, ^{53}Mn remains largely overproduced (by two orders of magnitude). In any case, the scenario of Figure 6.6 requires a very large ^{60}Fe abundance in the ESS.

Furthermore, one has to notice that, even fixing ad-hoc the mass cut for accommodating ^{53}Mn , unsolved problems would remain for the abundances of stable isotopes. This is so to the point that we have serious doubts that anyone of the cases studied can be reconciled with the measurements. This includes the models mentioned above, fitting most of the SLRs except for ^{53}Mn . We note that the exercise of adding these ejecta to the forming star in a very simple way, with complete and homogeneous mixing of the two components, would simply shift abundances of stable nuclei without producing isotopic heterogeneities. However, more realistic scenarios that consider the possible clumpiness of ejecta or mass segregation imply the introduction of shifts on stable isotope abundances at levels incompatible with the limits set by actual measurements, as discussed previously. Just to make an example, let's assume that these shifts be of the same order of magnitude of the average variations introduced on stable elements in the mentioned simple exercise. These last are shown in Figure 6.7 for the isotopes ^{16}O , ^{24}Mg , ^{28}Si and ^{40}Ca in term of permil (delta) values. As shown in the plots, the anomalies predicted are at least a few percent. This is much larger than allowed by present uncertainties in the meteoritic data, as discussed in Section 6.2. The fact that the injection process is complex and involves either the formation of clumpy structures or the incorporation of only part of the material ejected was addressed by various authors (Pan et al. 2012; Goswami and Vanhala 2000; Maeda et al. 2008) and seems to be required by the same inhomogeneities of observed SN remnants. Clearly, hydrodynamical models of these mixing processes should be performed considering all the SLRs, to complement the cases recently studied by Dwarkadas et al. (2018) for ^{26}Al and ^{60}Fe .

In view of these complexities, and of the fact that very high shifts are found in Figure 6.7 for elements produced in widely different layers of the star, very

ad-hoc hypotheses seem to be required by any mixing model aiming at eliminating them. We also recall that effects of the same order as found by us were present in the specific model of a $11.8 M_{\odot}$ star by Banerjee et al. (2016). Those authors considered the excesses found on stable isotopes as acceptable; but some of them are well in excess of 1% so that they meet the same problems encountered here.

A crucial and subtle problem concerning the anomalies on stable nuclei introduced by the mixing of freshly added material from an exotic source was underlined years ago by Nichols et al. (1999). Computing such stable shifts involves mixing model yields with measured abundances. Systematic errors in the model yields can give unrealistic estimates of stable isotope anomalies. Nichols et al. (1999) tried to address this issue by mixing stellar ejecta into proxy compositions derived from chemical evolution calculations. These last used the same stellar yields also adopted in the injected matter, to normalize out the errors. According to these calculations by Nichols et al. (1999) expected anomalies in stable isotope abundances are typically at the permil level with only few outliers at the percent level. Overall, inferred anomalies are lower than predicted here (see Figure 6.7) but are in many cases also incompatible with the meteorite data (see Section 6.2).

6.7 Conclusions

In this work we have discussed a series of problems emerging in the attempts of accounting for the presence of isotopic anomalies in early solids of the solar system, induced by the *in situ* decay of SLRs. Such problems become really difficult to handle if one wants to get a comprehensive scenario, indicating a series of Galactic processes capable to account for nuclides with lifetimes in the range of 10-20 Myr, like ^{107}Pd , ^{129}I and ^{182}Hf , and for the shorter-lived isotopes ^{26}Al , ^{41}Ca , ^{53}Mn , ^{60}Fe , and ^{135}Cs . This leads us to conclude that a self-consistent understanding of the astrophysical origins for all the mentioned anomalies is still far from being obtained. In order to limit the uncertainties and update previous works on the subject, for the longer-lived nuclei we have tried to outline possible scenarios emerging from present-day lively debates on the astrophysical sources of the *r*-process, tentatively identifying in NSM nucleosynthesis, or in a complex, short-term granularity of the Galactic admixture of the contributions from different sources, the origin of the low abundance of ^{129}I relative to the other neutron-rich nuclides. We indicate the first hypothesis as the most probable today. For isotopes of lifetime lower than about 5 Myr we have instead pursued our analysis on the basis of very recent calculations of stellar evolution, from 2 to $25 M_{\odot}$. For IMSs, this implies the reference to current physical models for DM processes and to their implications for the activation of the neutron source $^{13}\text{C}(\alpha, n)^{16}\text{O}$. For massive stars, the approach adopted includes up-to-date models with rotation, also accounting in detail for the final explosive phases. We believe that some of the frequently quoted discussions presented so far did not consider adequately the above issues; when this is done properly, several embarrassing

open questions do remain.

In general, we showed that the continuous nuclear evolution of the Galaxy over time scales of the order of 10 Gyr might account for the radioactivities measured in the early solar nebula having lifetimes τ_R longer than about 5 Myr, including ^{53}Mn . As mentioned, it is possible that the inclusion in this picture of peculiar NSM events, yielding large ratios between the abundances of nuclei at the third and second r -process peak, permit also an explanation for the low abundance of ^{129}I . Shorter-lived isotopes cannot however be explained in this way. In particular, in addition to the known problematic cases of ^{26}Al , ^{41}Ca , and (possibly) ^{60}Fe , we showed that also ^{135}Cs requires an ad-hoc, late minute contribution. There is therefore a necessity to assume a late addition of nucleosynthesis products for explaining the presence of very-short lived nuclei, including the exceptionally abundant ^{26}Al , which still poses the mentioned unanswered questions.

In the case of a late massive star, two relevant problems exist, which go beyond its capability of accounting for this or that SLR in a suitable amount. The first is the apparently unavoidable introduction into the forming solar nebula of large anomalies on stable isotopes that are excluded by present measurements. The second difficulty, recognized since a long time, concerns the possibility that the fast winds of a SN explosion can really interact with a star-forming cloud without disrupting it and instead be homogeneously mixed with the cool material of the cloud itself. Also from the point of view of the quantitative yields in SLRs, a late massive star would need very special conditions to avoid introducing enormous excesses in ^{53}Mn , while it might fulfil the requirements posed by ^{26}Al , ^{41}Ca , ^{135}Cs and perhaps also ^{205}Pb .

The problem of mixing fast SN winds with cool condensing matter in a star forming region might be avoided in the case, suggested recently, of a sequential pollution of the molecular cloud where the Sun was born, in which the last contribution might come from a dense shell formed at the external border of a WR wind, transporting cool matter and dust (Gounelle and Meynet 2012; Dwarkadas et al. 2017, 2018). One might guess that these models might or might not encounter the mentioned problems of excesses on stable isotopes, depending on the dilution factor and the degree of homogenization. However, some of the most quoted discussions in the literature do not consider the effects of previous SNe with an adequate and detailed computation of explosive nucleosynthesis; should this be done, we believe that the problems encountered here with a single star pollution would remain. Just to make a simple example, if the Sun was born in a giant molecular cloud similar to the ones we know today (having masses from 10^5 to $3 \times 10^6 M_\odot$, see e.g. Solomon et al. 1979), then the mixing over the whole cloud of typically $20 M_\odot$ of ejecta from a CCSN would yield a dilution factor in the range from 2×10^{-4} (similar to that of Table 6.8) to 0.6×10^{-5} . In the first case, the process of homogenization of the ejecta would probably be incomplete, so that, much like in Figure 6.7, excesses on stable nuclei at levels incompatible with measurements would remain; in the second, the excessive dilution would not explain any SLR except perhaps ^{60}Fe . Possible improvements on the above not encouraging views might come from considerations of asphericities in the SN

ejecta, whose effects on the solar system formation are however at the moment only speculations (Dwarkadas et al. 2017). We stress again that any attempt at obtaining a compromise solution in this field should necessarily be based on quantitative models for explosive processes and for their nucleosynthesis.

Concerning less massive stars, ending their life-cycle with the described TP-AGB phases, their models recently evolved from being fully parameterized to considering the physical mechanisms that can induce non-convective mixing. These mechanisms also control the introduction of proton flows into the He-rich layers at TDU. It is found that all stars, up to at least $7 - 8 M_{\odot}$, would form a reservoir of ^{13}C . This is bound to induce a neutron production through the $^{13}\text{C}(\alpha, n)^{16}\text{O}$ reaction, an occurrence that looks fatal for the old scenario devised by Wasserburg et al. (1994); Busso et al. (2003); Wasserburg et al. (2006). Indeed, the neutron fluences ensuing from it, adding their effects on those from the $^{22}\text{Ne}(\alpha, n)^{25}\text{Mg}$ reaction, always yield large excesses of neutron-capture radioactive isotopes, especially ^{107}Pd , with respect to ^{26}Al . In order to limit model dependencies, this fact was shown to occur with reference to two different treatments for DM mechanisms.

A limited parameter space remains to be explored, in the picture of a single late nucleosynthesis episode, for attempting to explain the shortest-lived radioactivities of the ESS (those with $\tau_R \lesssim 5$ Myr). One possibility resides in the already mentioned Super-AGB stars, objects in a thin mass interval (from about 9 to about $11 M_{\odot}$, variable with the metallicity) between IMSs and Massive Stars. Since the mass of the ^{13}C pocket steadily decreases for increasing initial mass of the parent star, in that mass region it might go essentially to zero, thus avoiding the extra production of neutron-rich nuclei that in the present work appears to hamper the possibilities previously envisaged by Wasserburg et al. (2006) and by Trigo-Rodríguez et al. (2009). An alternative might also be found in the most massive among IMSs ($7 - 8 M_{\odot}$) if HBB calculations, which are still largely model-dependent, were found to be less effective than discussed by Wasserburg et al. (2017), thus allowing to obtain more limited $^{26}\text{Al}/^{107}\text{Pd}$ ratios.

Coming instead to the schemes of the sequential contamination of a pre-solar molecular cloud, one should find a path in the fine-tuning of the many free parameters involved in those models, such that the CCSNe occurred in early epochs of the molecular cloud life do not introduce too large excesses on stable isotopes and nevertheless succeed in producing in adequate quantities, the required SLRs not accounted for by a possible last (and non-exploding) WR event (like e.g. ^{41}Ca , ^{53}Mn , ^{135}Cs , and possibly ^{205}Pb). At the moment of this writing one might also speculate that all SLRs, except ^{26}Al , ^{41}Ca , ^{53}Mn , and ^{60}Fe , might be produced in a burst of nucleosynthesis during a NSM event, which would avoid the excesses on stable isotopes related to CCSNe. The status of our knowledge of these elusive but important phenomena is however still in its infancy and any further guess seems now to be by far premature.

The content of this chapter has been published in Vescovi et al. (2018)². As the first author, I performed all AGB post-process calculations and data analysis, I lead the data interpretation, and I created the vast majority of the figures. I contributed significantly to the writing.

²On the Origin of Early Solar System Radioactivities: Problems with the Asymptotic Giant Branch and Massive Star Scenarios. *ApJ*, 863(2):115. doi: [10.3847/1538-4357/aad191](https://doi.org/10.3847/1538-4357/aad191). Reproduced with permission from The Astrophysical Journal, © AAS

Magnetic-buoyancy-induced mixing in AGB Stars: presolar SiC grains

Isotope ratios can be measured in presolar SiC grains from ancient Asymptotic Giant Branch (AGB) stars at permil-level (0.1%) precision. Such precise grain data permit derivation of more stringent constraints and calibrations on mixing efficiency in AGB models than traditional spectroscopic observations. In this paper we compare SiC heavy-element isotope ratios to a new series of FRUITY models that include the effects of mixing triggered by magnetic fields. Based on 2D and 3D simulations available in the literature, we propose a new formulation, upon which the general features of mixing induced by magnetic fields can be derived. The efficiency of such a mixing, on the other hand, relies on physical quantities whose values are poorly constrained. We present here our calibration by comparing our model results with the heavy-element isotope data of presolar SiC grains from AGB stars. We demonstrate that the isotopic compositions of all measured elements (Ni, Sr, Zr, Mo, Ba) can be simultaneously fitted by adopting a single magnetic field configuration in our new FRUITY models.

7.1 Introduction

Thermally-Pulsing Asymptotic Giant Branch (TP-AGB) stars are among the most efficient polluters of the interstellar medium (Busso et al. 1999; Herwig 2005; Straniero et al. 2006; Karakas and Lattanzio 2014). Those objects present an onion-like structure, with a partially degenerate C-O core, surrounded by two thermonuclear shells, burning He and H alternatively, and an expanded and cool convective envelope, continuously eroded by intense mass-loss phenomena. The products of the rich nucleosynthesis occurring in their interiors are carried to the surface via mixing episodes known as Third Dredge Up (TDU). During a TDU episode, the convective envelope penetrates through the H-shell, which is temporarily switched off due to the expansion triggered by the occurrence of a thermonuclear runaway, named Thermal Pulse (TP). In AGB modelling,

particularly critical is the handling of the convective/radiative interface at the inner border of the convective envelope, whose numerical treatment has dramatic consequences on both the efficiency of TDU and the nucleosynthesis of heavy elements in those objects. AGB stars are the site of the main component of the *slow* neutron capture process (*s*-process; see e.g. Gallino et al. 1998). The major neutron source in AGB stars is the $^{13}\text{C}(\alpha, n)^{16}\text{O}$ reaction (see e.g. Cristallo et al. 2018), which burns in radiative conditions during the interpulse phase between two TPs (Straniero et al. 1995). A ^{13}C -enriched layer is needed to reproduce the observed *s*-process distributions: the so-called ^{13}C pocket (Busso et al. 2001). In order to obtain the ^{13}C pocket, a partial mixing of hydrogen from the envelope to the underlying radiative He-intershell is needed during a TDU episode. Various mechanisms for causing this partial mixing have been proposed in stellar evolutionary codes: diffusive overshoot (Herwig et al. 1997), rotation (Herwig et al. 2003; Siess et al. 2004), gravity waves (Denissenkov and Tout 2003), opacity-induced overshoot (Cristallo et al. 2009), and a combination of overshoot and gravity waves (Battino et al. 2016). None of these treatments, however, have been able to simultaneously reproduce all the *s*-process isotopic anomalies measured in presolar SiC grains in detail (see Zinner 2014 for a review). Presolar SiC grains have been identified in pristine extraterrestrial materials that formed shortly after the solar system birth (about 4.57 Gyr ago), and have remained intact and almost unaltered until the present day. Extensive analyses of presolar SiC grains for their multi-element isotopic compositions show that the majority ($\simeq 90\%$), the so-called mainstream (MS) grains, came from low-mass C-rich AGB stars and exhibit *s*-process isotopic signatures. Recently, the idea that the formation of the ^{13}C pocket can be induced by magnetic buoyancy has been proposed by Trippella et al. 2016 (based on the formalism presented by Nucci and Busso 2014). Such a treatment has been proven to be effective in reproducing many of the features characterizing *s*-process distributions (see Trippella et al. 2016; Palmerini et al. 2018; Vescovi et al. 2018). The inclusion of this process in AGB stellar models, however, is currently confined to post-process techniques. In this work, we present our implementation of mixing triggered by magnetic buoyancy in the FUNS stellar evolutionary code with fully coupled nucleosynthesis (Straniero et al. 2006; Cristallo et al. 2011; Piersanti et al. 2013).

7.2 Updated FRUITY models

Besides the inclusion of mixing triggered by magnetic fields, we made several updates to the FUNS code. Those include the initial solar-scaled composition (Lodders 2019), the mass-loss law (Abia et al. 2020), the Equation Of State (EOS) and many nuclear reaction rates (for these last items we refer to Vescovi & Cristallo, in preparation).

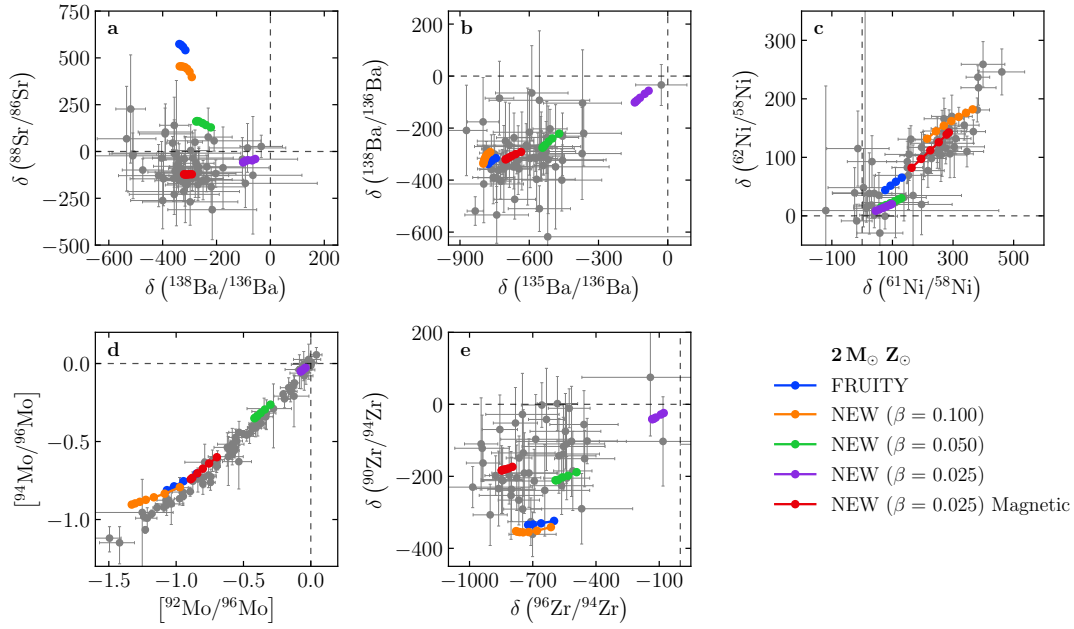


Figure 7.1: Comparison between presolar grain data (see text for details) and theoretical stellar predictions calculated under different physical prescriptions. Plotted are 2σ errors.

7.2.1 Convective overshooting

In FRUITY models previously reported (Cristallo et al. 2011; Piersanti et al. 2013; Cristallo et al. 2015b; available on-line in the FRUITY repository¹), the interface at the inner border of the convective envelope is handled by introducing an exponentially decaying profile of the convective velocities. The velocity of the descending material (ideally braked by viscous friction) appears as:

$$v = v_{\text{cb}} e^{-k\delta r}, \quad (7.1)$$

where v_{cb} is the velocity at the convective border and δr is the corresponding distance. It is common to assume that the convective zone extends over a fraction βH_p beyond the Schwarzschild's limit, where H_p is the pressure scale height at the convective boundary (see e.g. Freytag et al. 1996): for this reason we define $k = (\beta H_p)^{-1}$. The free parameter β regulates the amount of protons mixed beyond the bare convective border, and also affects the TDU efficiency. The introduction of Equation (7.1) has an important by-product, i.e. the formation of a self-consistent ^{13}C pocket, whose size decreases with the shrinking of the He-intershell. Cristallo et al. (2009) tuned β to maximize the production of s -process elements ($\beta = 0.1$). AGB models computed with this value have proven to be effective in roughly reproducing the bulk of the luminosity function of Galactic C-stars (Guandalini and Cristallo 2013) and the solar distribution of s -only isotopes (Prantzos et al. 2020). For this reason we define the FRUITY

¹<http://fruity.oa-teramo.inaf.it/>

Table 7.1: Final enrichments of s -process elements and s -process indexes. See text for details.

	Models				
	FRUITY	NEW	NEW	NEW	NEW Magnetic
Z_{\odot}	0.0138	0.0167	0.0167	0.0167	0.0167
β	0.100	0.100	0.050	0.025	0.025
ΔM_{TDU}	2.91×10^{-2}	6.20×10^{-2}	4.15×10^{-2}	3.28×10^{-2}	3.27×10^{-2}
Yield(C)	5.24×10^{-3}	9.75×10^{-3}	6.51×10^{-3}	5.23×10^{-3}	5.17×10^{-3}
Yield(Ni)	1.61×10^{-7}	1.37×10^{-6}	-1.61×10^{-7}	-1.63×10^{-7}	1.36×10^{-6}
Yield(Sr)	5.81×10^{-7}	9.61×10^{-7}	8.12×10^{-8}	1.07×10^{-8}	5.85×10^{-7}
Yield(Zr)	2.72×10^{-7}	4.66×10^{-7}	3.59×10^{-8}	3.66×10^{-9}	1.76×10^{-7}
Yield(Mo)	4.21×10^{-8}	7.60×10^{-8}	5.73×10^{-9}	5.77×10^{-10}	2.36×10^{-8}
Yield(Ba)	1.72×10^{-7}	3.15×10^{-7}	2.02×10^{-8}	1.43×10^{-9}	6.44×10^{-8}
[ls/Fe] ^a	1.02	1.22	0.37	0.06	0.95
[hs/Fe] ^b	0.96	1.17	0.27	0.02	0.60
[hs/ls] ^c	-0.06	-0.05	-0.10	-0.04	-0.35

^a [ls/Fe] = ([Sr/Fe] + [Y/Fe] + [Zr/Fe]) / 3

^b [hs/Fe] = ([Ba/Fe] + [La/Fe] + [Ce/Fe]) / 3

^c [hs/ls] = [hs/Fe] - [ls/Fe]

models computed with $\beta = 0.1$ as our reference scenario for what concerns the TDU efficiency (blue symbols in Figure 7.1).

In order to evaluate the effects induced by different physical recipes in calculating AGB models, we ran a series of s -process AGB models with an initial mass $M = 2 M_{\odot}$ and $Z = 1.67 \times 10^{-2}$ ($\equiv Z_{\odot}$). We compared the model results to the isotopic ratios of s -elements in presolar SiC grains, which offer precise constraints on the ^{13}C pocket (see Figure 7.1). We included MS grain data for Ni (Trappitsch et al. 2018), Sr (Liu et al. 2015; Stephan et al. 2018), Zr (Nicolussi et al. 1997; Barzyk et al. 2007), Mo (Liu et al. 2017; Stephan et al. 2019) and Ba (Liu et al. 2014b, 2015; Stephan et al. 2018). We also included the Mo isotopic compositions of presolar SiC grains of types Y and Z from Liu et al. (2019), because their Mo isotopic compositions have been demonstrated to be indistinguishable from those of MS grains. Although observations show that C-rich dust can sometimes form in O-rich circumstellar envelopes (see e.g. Millar 2016), we conservatively plot the model data only for the C-rich phase, during which SiC grains most likely form (see also Lodders and Fegley 1999). The presolar SiC data for all elements but Mo are reported in the typical δ -notation, i.e. the deviation in parts per thousand of the isotopic ratio measured in a grain relative to the terrestrial ratio. The Mo isotope data are presented in the usual spectroscopic notation². In Figure 7.1a we focus on ^{88}Sr and ^{138}Ba , both of which have magic numbers of neutrons ($N = 50$ and $N = 82$, respectively). As a consequence, they act as bottlenecks of the s -process and are the most representative isotopes for light and heavy s -elements

²[A/B] = $\log(N(A)/N(B))_{*} - \log(N(A)/N(B))_{\odot}$

(*ls* and *hs*, respectively). In addition, correlations among them were shown to depend strongly on the extension of the ^{13}C reservoir and on the profile of the ^{13}C abundance within the pocket (see e.g. Liu et al. 2015). From Figure 7.1 it clearly emerges that the reference FRUITY model has serious problems in reproducing the presolar grain isotopic ratios. In particular, this model predicts too high $\delta(^{88}\text{Sr}/^{86}\text{Sr})$ and relatively low $\delta(^{90}\text{Zr}/^{94}\text{Zr})$ values, resulting in poor fits to the grains in Figure 7.1a and 7.1e. In fact, both isotope ratios were shown to be sensitive tracers of the ^{13}C pocket structure (Liu et al. 2014a, 2015). Regarding Ni isotopes, the predicted *s*-process enrichments in ^{61}Ni and ^{62}Ni in the envelope fail to explain the grains with the largest δ values. The poor match to the grain data is barely improved by the inclusion of the new inputs (initial composition, mass-loss, EOS and nuclear rates; label “NEW ($\beta = 0.100$)”), apart from a net improvement for the most anomalous grains in Figure 7.1c. An inspection of Figure 7.1, however, is not sufficient. In addition to relative isotopic ratios, the absolute amount of freshly synthesized elements also has to be checked.

In Table 7.1 we report, for the computed models, the following quantities: amount of dredged-up material, net yields³ of some key elements and *s*-process indexes. As we already stressed before, FRUITY models have been demonstrated to be able to grossly reproduce Galactic chemical features. With respect to the FRUITY model, the “NEW ($\beta = 0.100$)” model carries to the surface too much material (see, e.g., the carbon net yield), thus pointing to the need of reducing the mixing efficiency. The test with an intermediate β value of 0.05 improves the situation for both the grains and net element production, but the achieved improvement is still insufficient (due to the fact that the extra-mixed region is too ^{14}N -rich). Therefore, we ran an additional model with $\beta = 0.025$. The “NEW ($\beta = 0.025$)” model shows an amount of dredged-up material similar to the reference FRUITY model⁴, but the production of heavy elements is completely suppressed in this case. This is confirmed by both the close-to-solar values in all the presolar grain isotopic ratios (violet symbols in Figure 7.1) and the extremely reduced net yields. Thus, we conclude that the new FRUITY models, re-calibrated after the inclusion of updated physical inputs, cannot reproduce the amounts of heavy elements required by observations. This calls for an additional mechanism for the production of heavy elements.

³Net yields are defined as $\int_0^{t_{end}} [(X(\text{El}) - X_0(\text{El})) \times \dot{M}] dt$, where t_{end} is the stellar lifetime, \dot{M} is the mass-loss rate, while $X(\text{El})$ and $X_0(\text{El})$ stand for the current and the initial mass fraction of the element, respectively.

⁴It is worth stressing that we could perform a finer calibration, but we believe it is premature at the moment. We will investigate this matter as soon as detailed 3D hydrodynamic simulations of an AGB penetrating envelope become available.

7.3 Mixing triggered by magnetic buoyancy in AGB stars

As in Nucci and Busso (2014), we assume that a toroidal magnetic field is present in the radiative He-intershell region at the beginning of the TDU. We will demonstrate the validity of this assumption in a dedicated forthcoming paper (Vescovi & Cristallo, in preparation). Here we just briefly note that differential rotation may create a strong enough toroidal field ($B \sim 10^5$ G) by stretching a small preexisting poloidal field around the rotation axis (see e.g. Denissenkov et al. 2009). The poloidal field does not need to be preserved from previous phases, since its required small strength ($10 \div 100$ G) can be linked to a local process (such as a convective episode). The energy budget to develop and maintain such a toroidal magnetic field is provided by rotation. Preliminary tests computed by switching on rotation in our new models (see Piersanti et al. 2013 for details) confirm the above-reported statements, even when hypothesizing a large decrease of the core rotation velocity in pre-AGB evolutionary phases (see, e.g., den Hartogh et al. 2019a). In such a situation, mixing triggered by secular rotation instabilities is negligible.

Nucci and Busso (2014) pointed out that a magnetized stellar plasma in quasi-ideal MHD regime, with a density distribution closely following a power law as a function of the radius ($\rho \propto r^k$, with $k < -1$), reaches a dynamic equilibrium and is in radial expansion. The result above is analytically exact and remains so (for the simple but rather typical symmetry adopted by the authors) when the magnetic field B varies in time, as in the case of a toroidal/azimuthal magnetic field amplified by winding-up. Here we assume that magnetic buoyancy is the instability which triggers the plasma expansion. Note that the region below the convective envelope during a TDU fullfills the conditions required by Nucci and Busso 2014, with $\rho \propto r^{-4.6}$ (solid line in Figure 7.2). Moreover, the occurrence of buoyancy instability requires quite strong fields (dashed line in Figure 7.2) and, in such conditions, the magnetic field tends to concentrate in bundles of field lines that are wrapped in a field-free plasma, usually referred to as flux tubes. As a consequence of the magnetic extra-pressure, these tubes are buoyant (see e.g. Parker 1955). Due to the effect of the magnetic buoyancy, a matter flow is pushed from the He-intershell to the envelope. This, in turn, induces a downflow flux, in order to guarantee mass conservation.

A brief outline of the general downflow velocity profile we adopted is presented in Section 2.3. Supposing that magnetic flux tubes, generated in the He-intershell at a distance r_p from the stellar center, start to rise with an initial velocity v_p , then the induced downflow velocity can be expressed (see Equation 2.10) as

$$v_d(r) = u_p \left(\frac{r_p}{r} \right)^{k+2}, \quad (7.2)$$

where $u_p = f \cdot v_p$ acts as an *effective* buoyant velocity. In fact, in radiative zones of evolved stars, the fraction of mass f locked in magnetic flux tubes must be

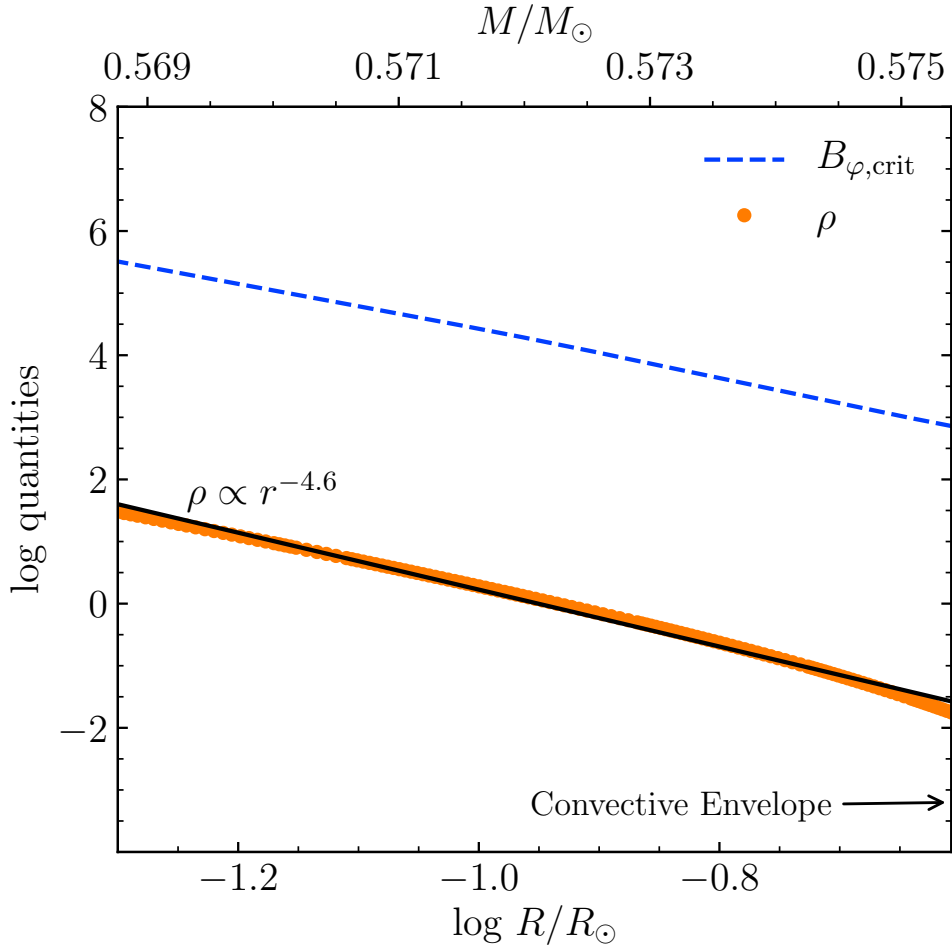


Figure 7.2: Critical toroidal field B_φ for triggering the buoyancy instability (blue dashed curve) and density ρ (orange dots) profiles of the He-intershell up to the inner border of the convective envelope (right edge of the plot), at the epoch of its maximum penetration during the 3rd TDU of a star with $2 M_\odot$ and solar metallicity. Note that the best fit closely follows $\rho \propto r^k$, with $k \simeq -4.6$, which is considerably lower than -1 , as required for the validity of the model by Nucci and Busso (2014).

small, i.e. $f \simeq 10^{-5}$ (see Busso et al. 2007; Trippella et al. 2016). This fact implies that the actual buoyant velocity of the flux tubes is orders of magnitude larger than the corresponding u_p . The downflow velocity relies on two parameters: the radial position r_p of the layer p from which buoyancy (on average) starts and the *effective* buoyant velocity u_p . This is a direct consequence of the solutions derived by Nucci and Busso (2014) for the radial velocity of magnetized structures and also the toroidal component of the magnetic field, as for both these functions we need to fix boundary conditions.

The identification of the critical field necessary for the occurrence of instabilities by magnetic buoyancy allows us to identify the corresponding radial position r_p from which magnetic structures arise. An azimuthal field B_φ is subject to magnetic

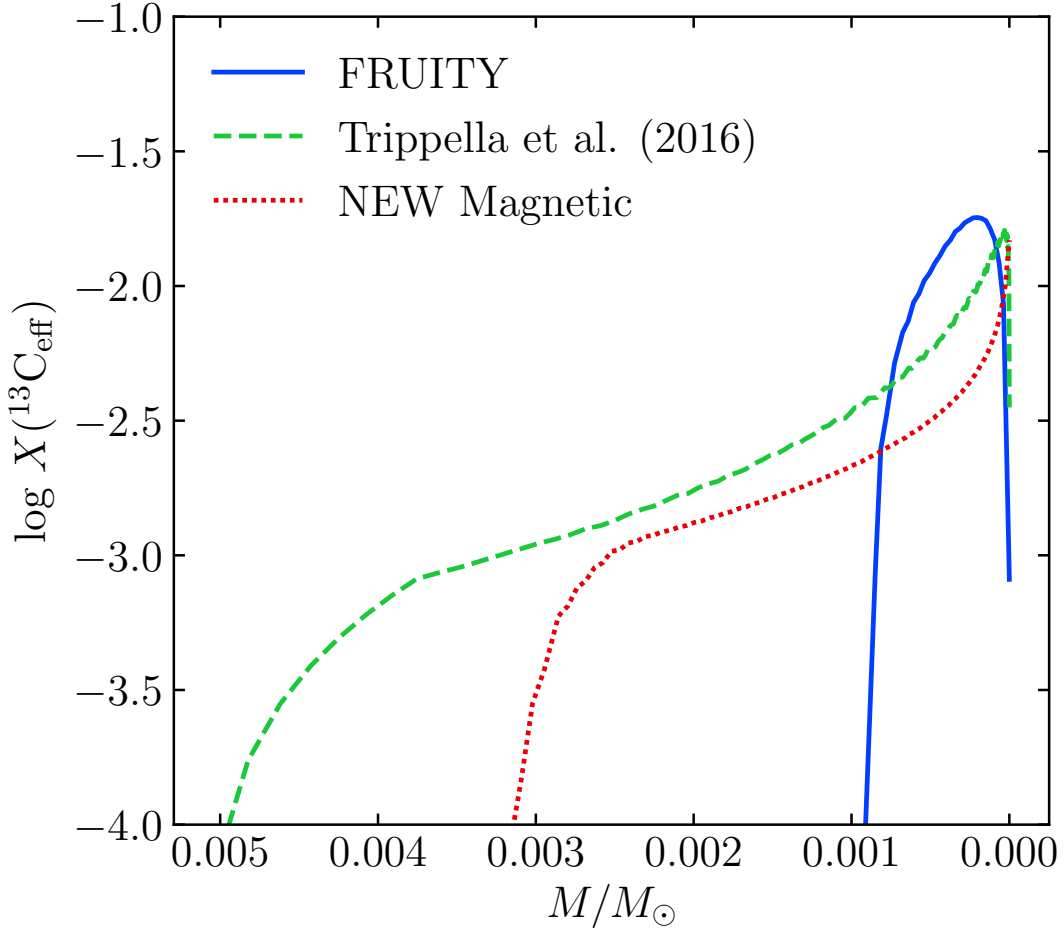


Figure 7.3: *Effective* ^{13}C in the ^{13}C pocket region for models with different physical prescriptions. See text for details.

buoyancy instabilities (Acheson and Gibbons 1978; Spruit 1999; Denissenkov et al. 2009) if:

$$B_\varphi \gtrsim \left(4\pi\rho r N^2 H_p \frac{\eta}{K} \right)^{1/2}, \quad (7.3)$$

provided that the field gradient is smooth, i.e. $\partial \ln B_\varphi / \partial \ln r \sim O(1)$. Here N is the adiabatic Brunt-Väisälä frequency, η the magnetic diffusivity and K the thermal diffusivity.

Figure 7.2 shows the profile of the critical B_φ necessary for the onset of magnetic buoyancy instabilities, in the radiative zone below the convective envelope, at the moment of the maximum penetration of the H-rich envelope during a TDU. B_φ varies from $\sim 10^4$ G to a few 10^5 G, in the region of interest for the formation of the ^{13}C pocket. Different values for B_φ correspond to different values of the free parameter r_p , which determines the extension of the mixed zone and, in turn, of the ^{13}C pocket. Assuming that a fraction of the magnetic energy is converted to the kinetic energy of the magnetic flux tube, we expect that the (*effective*)

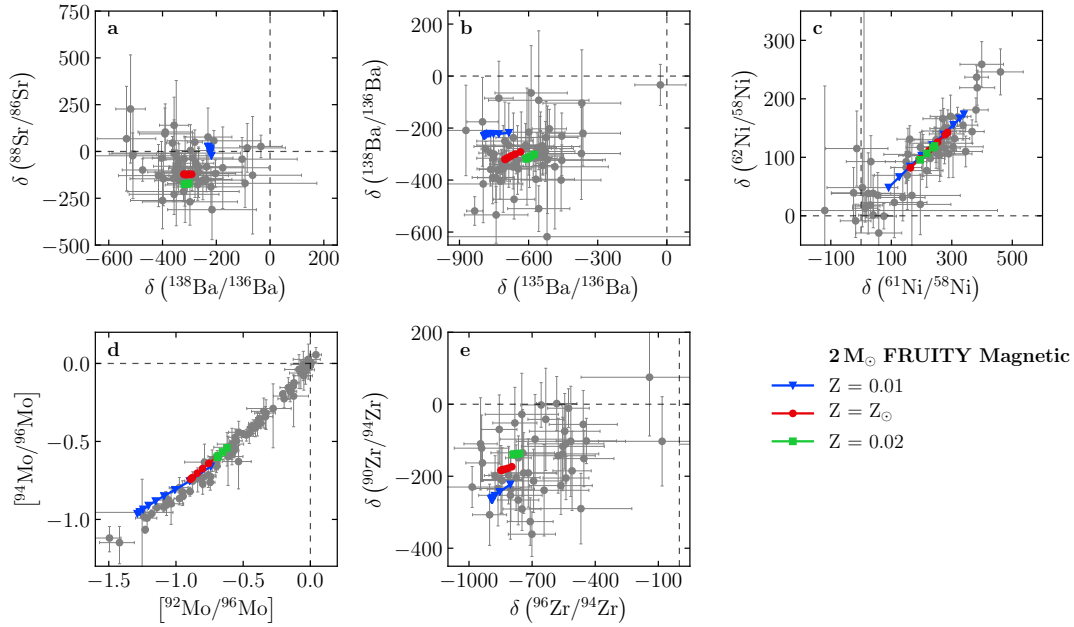


Figure 7.4: Same as Figure 7.1, but with new magnetic $2 M_{\odot}$ models at different metallicities. See text for details.

rising velocity of the flux tubes is proportional to the strength of the magnetic field ($u_p \propto v_p \propto B_{\varphi}$). To calibrate u_p and B_{φ} , we ran various tests with different parameter values ($u_p = 1, 3, 5, 8, 12 \times 10^{-5} \text{ cm s}^{-1}$ and r_p corresponding to $B_{\varphi} = 2, 5, 10, 15 \times 10^4 \text{ G}$). From Equation (7.2) it is straightforward to notice that the velocity of the downward material is proportional to $v_p r_p^{k+2}$ (with k typically < -4 , during a TDU). Thus, the greater the initial velocity of flux tubes is and the deeper the buoyancy starts, the greater the velocity of the material down-flow is. Therefore, larger values of B_{φ} correspond both to larger ^{13}C pockets and to larger mass fractions $X(^{13}\text{C})$. The case that provides the best fit to the presolar SiC grain isotopic ratios was obtained with $B_{\varphi} = 5 \times 10^4 \text{ G}$ and $u_p = 5 \times 10^{-5} \text{ cm s}^{-1}$ (red symbols in Figure 7.1). This u_p value corresponds to a starting buoyant velocity of $v_p = u_p/f \simeq 5 \text{ cm s}^{-1}$, which increases to $\simeq 5 \text{ m s}^{-1}$ at the convective boundary, thus ensuring that magnetic advection acts on timescales much smaller than any dissipative processes (Nucci and Busso 2014).

Figure 7.3 shows the amount of *effective* ^{13}C (i.e. the difference between the number fractions of ^{13}C and ^{14}N in the pocket) obtained by including our new magnetic mixing process after the 3^{rd} TDU in a $2 M_{\odot}$ model with $Z = Z_{\odot}$ (red dotted curve). For comparison, we also show typical ^{13}C pockets obtained in FRUITY models (blue solid curve) and the “magnetic” pocket by Trippella et al. (2016) (green dashed curve). With respect to the FRUITY pocket, our new “Magnetic” pocket shows a lower ^{13}C concentration, with a more extended tail. Our formulation shares the physical principles of Trippella et al. (2016). Adopting the same post-process code by those authors, we have performed a large series of computations to investigate the variability of the magnetic-buoyancy induced

pocket. The results will be presented elsewhere (Busso et al., in preparation). We briefly note that in advanced cycles the ^{13}C pockets shrink somewhat, in almost perfect agreement with the trend observed in the models presented here.

7.4 Presolar SiC grains

In order to test if the new magnetic FRUITY AGB models are able to cover the range defined by the presolar SiC grains, we computed two additional $2 M_{\odot}$ AGB evolutionary sequences with $Z = 1 \times 10^{-2}$ and $Z = 2 \times 10^{-2}$. In Figure 7.4, those models are compared to the same set of data as in Figure 7.1. The inclusion of the “Magnetic” ^{13}C pocket in our new FRUITY models significantly improves the fits to the majority of the grain data in all the panels in Figure 7.4. This is especially true in Figure 7.4a: all the model predictions overlap well with the grain region, in contrast to the poor matches given by the FRUITY models adopting other ^{13}C pockets shown in Figure 7.1a. The $Z = 0.01$ model predicts larger s -process enrichments in the envelope because of the increased neutron-to-seed ratio, thus providing better matches to the grains with extreme Ni and Mo isotopic anomalies. The s -process features detected in presolar grains are, therefore, well reproduced by including our treatment of magnetic-buoyancy induced mixing in our AGB models. It was shown that grain data for Ni, Zr, and Mo suffer from solar and/or terrestrial contamination. This drives their composition toward more normal values and likely results in the large spreads observed in panels c-d-e of Figure 7.4 (Trappitsch et al. 2018; Liu et al. 2018, 2019). Given this caveat, we focus on matching the most anomalous grains in these three cases: the less anomalous grains can be explained by mixing our predicted s -process components with solar and/or terrestrial materials. Alternatively, the less anomalous grains could probably be explained by the models shown in Figure 7.4, if a higher carbon content in the He-intershell is adopted so that the stellar envelope becomes C-rich earlier (see e.g. Battino et al. 2019). In our analysis, we implicitly assumed that the initial mass ($2 M_{\odot}$) and metallicities of the computed models are representative of the population of grain parent stars: this choice is commonly adopted in the literature (see, e.g., Lewis et al. 2013 and Liu et al. 2018). However, it has been recently proposed that more massive AGB stars ($M \simeq 4 M_{\odot}$) with super-solar metallicities ($Z = 2 \times Z_{\odot}$) are the parent stars of presolar SiC grains (Lugaro et al. 2018). We will investigate this subject in a dedicated paper (Cristallo et al., in preparation).

Finally, an important caveat needs to be noted. Theoretically, the physical requirements given by Nucci and Busso (2014) to ensure quasi-ideal MHD conditions still hold slightly deeper inside the star, with respect to the adopted configuration, down to layers with a larger critical magnetic field B_{φ} . Currently, we do not have the means to perform the absolute calibration of the free parameters in our treatment of MHD-induced mixing, and their values were calibrated using the presolar grain data. However, we anticipate that the calibrated values from this study also allow us to obtain an overall reasonable fit to the surface distributions

determined in other s -process enriched objects, including intrinsic C-stars, Ba-stars, CH stars and CEMP-s stars. As a matter of fact, we have hints that the observed s -process spread at a fixed metallicity is connected to the initial mass and/or rotational velocity of the star. According to model simulations, mixing triggered by rotation-induced instabilities is (almost) inhibited in AGB stars that are slowed down to match asteroseismic asteroseismic measurements of core H- and He-burning stars (Piersanti et al. 2013; den Hartogh et al. 2019b). Notwithstanding, the residual angular velocity profile keeps memory of the assigned initial parameters and of the following pre-AGB evolution. All these features will be addressed in a forthcoming paper (Vescovi & Cristallo, in preparation).

7.5 Conclusions

In this work we presented the first numerical simulations of the formation of a magnetically-induced ^{13}C pocket in a stellar evolutionary code with fully coupled nucleosynthesis. We propose that magnetic fields of the order of 10^5 G can induce the formation and buoyant rise of magnetic flux tubes in the He-intershell of AGB stars. Such tubes are fast enough to guarantee, by mass conservation, the downward penetration of a sufficient protons to form a sizable ^{13}C pocket. With a proper choice of the field strength and initial buoyant velocity, our new magnetic FRUITY models provide a consistent explanation to the majority of the heavy-element isotope data detected in presolar SiC grains from AGB stars.

The content of this chapter has been published in Vescovi et al. (2020)⁵. As the first author, I performed all AGB model calculations, data analysis, and interpretation. I contributed significantly to the writing and created all the figures.

⁵Magnetic-buoyancy-induced mixing in AGB stars: Presolar SiC grains. *ApJL*, 897(2):L25. doi: [10.3847/2041-8213/ab9fa1](https://doi.org/10.3847/2041-8213/ab9fa1). Reproduced with permission from The Astrophysical Journal, © AAS

Production of very light elements in kilonovae

We study the production of light elements ($Z < 20$) in the ejecta of binary neutron star mergers by combining detailed nucleosynthesis calculations with the outcome of numerical relativity merger simulations. We explore different microphysical equations of state and binary mass ratios, and find that hydrogen and helium are the most abundant light elements. For both elements, the decay of free neutrons is the driving nuclear reaction. Hydrogen is produced in extremely fast expanding ejecta while helium is synthesized in association with heavy r -process elements. By computing synthetic spectra, we find that the possibility of detecting hydrogen and helium features in kilonova spectra is very unlikely.

8.1 Introduction

Binary neutron star (BNS) mergers are primary sites for the production of heavy elements in the Universe through the rapid neutron capture process (r -process) (Symbalisty and Schramm 1982; Eichler et al. 1989; Freiburghaus et al. 1999). This association was confirmed by the detection of the kilonova AT2017gfo (Arcavi et al. 2017; Coulter et al. 2017; Drout et al. 2017; Evans et al. 2017; Kasliwal et al. 2018; Nicholl et al. 2017; Smartt et al. 2017; Soares-Santos et al. 2017; Tanvir et al. 2017) as electromagnetic counterpart of the BNS gravitational wave (GW) signal GW170817 (Abbott et al. 2017b,c). The luminosity and light curve evolution of the UV/visible/IR transient AT2017gfo are indeed in agreement with the heating rate and opacity expected from a distribution of freshly synthesized r -process elements (Kasen et al. 2017; Tanaka et al. 2017; Rosswog et al. 2018; Wollaeger et al. 2018). While a few days after merger the spectrum reveals absorption features, qualitatively compatible with the forest of lines expected for matter rich in heavy elements (in particular, lanthanides and actinides), the analysis of the spectrum at 1.5 days suggested the presence of strontium (Watson et al. 2019), a light r -process element whose production in the Universe is however

dominated by the slow neutron capture (*s*-process, e.g., Prantzos et al. 2020). *r*-process nucleosynthesis happens in the ejecta expelled during and shortly after the merger. Different mechanisms, acting on different timescales, are responsible for the ejection of several components, characterized by peculiar properties also depending on the still unknown equation of state (EOS) of nuclear matter (see e.g. (Shibata and Hotokezaka 2019; Radice et al. 2020) and references therein). The dynamical ejecta (Korobkin et al. 2012; Hotokezaka et al. 2013; Bauswein et al. 2013; Sekiguchi et al. 2015; Radice et al. 2016; Bovard et al. 2017; Radice et al. 2018) and spiral-wave wind (Nedora et al. 2019, 2020) are the earliest and fastest ejecta, thus becoming transparent within the very first days and possibly providing key spectral features. While heavy elements nucleosynthesis is strongly associated to compact binary mergers, light elements are often observed in astrophysical transients. In this work, we investigate for the first time the production of light elements ($Z < 20$), focusing in particular on hydrogen and helium, we connect the thermodynamics conditions for their production to the binary properties (mass ratio and EOS), and study their early detectability.

8.2 Methods

Nucleosynthesis in BNS mergers depends mainly on three physical parameters: the specific entropy (s), the electron fraction (Y_e), and the expansion timescale (τ) (Hoffman et al. 1997). The ejecta from BNS mergers cannot be characterized by a single value of these parameters. A distribution in the (s, Y_e, τ) space is instead expected. In this work, we consider results of Numerical Relativity (NR) simulations of BNS performed with the `WhiskyTHC` code (Radice et al. 2014a,b). We take three simulations targeted to GW170817: `BLh_equal`, `BLh_unequal`, and `DD2_equal`. The first and the last models have $M_1 = M_2 = 1.364M_\odot$, while the second $M_1 = 1.856M_\odot$ and $M_2 = 1.020M_\odot$. The first two employ the BLh nuclear EOS (Bombaci and Logoteta 2018; Logoteta et al., in preparation), while the third the stiffer HS(DD2) EOS (Typel et al. 2010; Hempel et al. 2012). All models include neutrino radiation and, in particular, neutrino absorption in optically thin conditions. These simulations were extensively presented in (Perego et al. 2019; Nedora et al. 2019; Bernuzzi et al. 2020) where more details can be found. The dynamical ejecta amount to $6.81 \times 10^{-4}M_\odot$, $3.84 \times 10^{-3}M_\odot$, and $1.33 \times 10^{-3}M_\odot$ for the `BLh_equal`, `BLh_unequal`, and `DD2_equal`, respectively. Additionally, the `DD2_equal` simulation was evolved up to ~ 100 ms post merger and shows $6.26 \times 10^{-3}M_\odot$ of (not yet saturated) spiral-wave wind ejecta.

To compute time-dependent yields abundances we use the publicly available nuclear network `SkyNet` that includes 7843 isotopes up to isotope ^{337}Cn (Lippuner and Roberts 2017). We employ the same set-up as in (Lippuner and Roberts 2015), with the exception of the usage of the latest JINA REACLIB database (Cyburt et al. 2010). The time-dependent trajectories of Lagrangian fluid elements input to `SkyNet` are characterized by (s, Y_e, τ) triplets. To cover the relevant intervals we perform extensive nucleosynthesis calculations over wide ranges of s ,

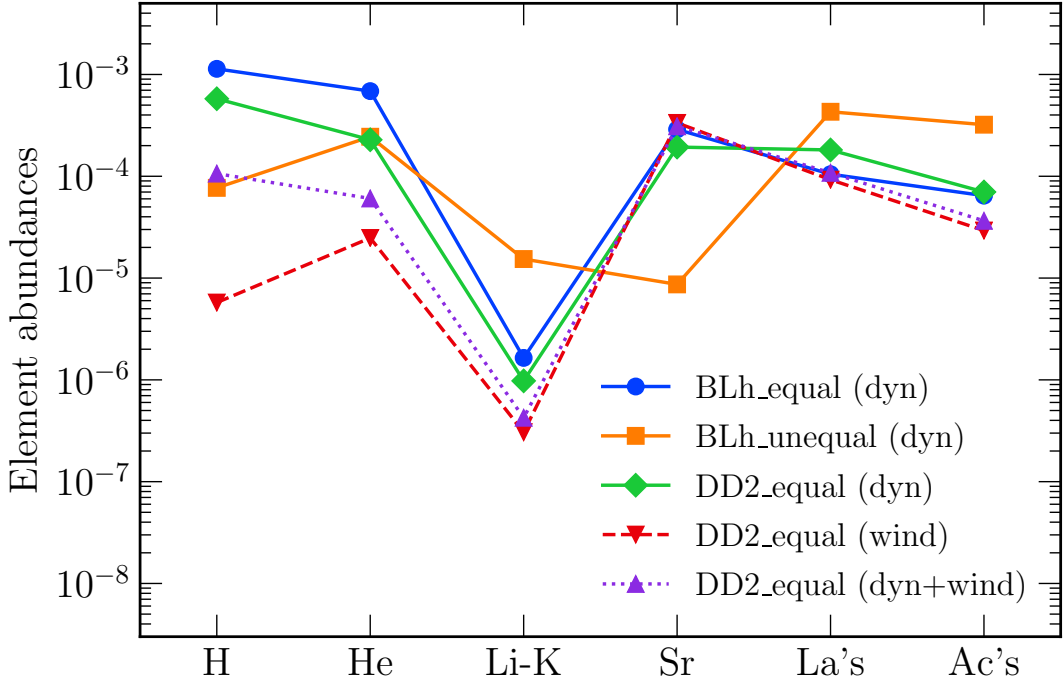


Figure 8.1: Number abundances of very light elements ($Z < 20$), strontium, lanthanides and actinides in the dynamical and spiral wind ejecta of BNS simulations at two days after merger.

Y_e , and τ . From each BNS simulations we extract mass distributions of the ejecta in the s, Y_e, v_∞ space at a coordinate radius of 400 km. We then obtain time dependent abundances from the convolution of the yields tabulated with SkyNet with the distribution of ejecta properties from the simulations. The expansion timescale is computed as $\tau = R/v_\infty$ where $R = 300$ km is a suitable radius obtained by inspecting the late time behavior of publicly available BNS merger tracers (Korobkin et al. 2012), and v_∞ is the velocity at the extraction radius.

The open-source spectral synthesis code TARDIS (Kerzendorf and Sim 2014) is employed to produce spectral models for the predicted abundances and physical conditions. We use it to check whether very light elements can produce recognizable features in kilonova spectra. TARDIS simulations are constrained by the target luminosity and computed for a specific time after merger. The strength of the spectral features depends on many uncertain ingredients, first of all the mass of the ejecta and the ionization/excitation sources.

8.3 Synthesis of hydrogen and helium in BNS mergers

In Figure 8.1 we present number abundances of selected elements in the ejecta of the three considered simulations, two days after merger. Among the lightest

elements ($Z < 20$), H and He are the most abundant species, while all the elements between lithium and potassium are usually several orders of magnitudes less abundant. When considering the dynamical ejecta, the production of H and He appears robust and their abundances vary within one order of magnitude even when changing the EoS stiffness or the binary mass ratio. Unless the binary is very asymmetric, H and He abundances are comparable to Sr abundance, as well as of lanthanides and actinides. Light element production is less significant in the spiral-wave wind ejecta, where the production of the first and second r -process peak element is favored. However, we stress that the spiral-wave wind ejecta (red dashed line) must be combined with the dynamical ejecta (green solid line) emerging first from the merger. Due to the larger spiral-wave wind contribution, H and He are slightly underproduced with respect to Sr and heavy r -process elements in the combined ejecta (purple dotted line).

We investigate the origin of H and He by considering the abundances obtained for individual trajectories characterized by different (s, Y_e, τ) sets. In Figure 8.2 we present the abundances of H, He, lanthanides and actinides for a broad set of Y_e and s , and two expansion timescales that bracket the relevant timescales for dynamical and spiral-wave wind ejecta. The presence of H in the ejecta is related with high- s and low- Y_e matter that expands very rapidly, as visible in the top panels of Figure 8.2 (see also Metzger et al. 2015). Hydrogen is produced as decay product of free neutrons within a few tens of minutes. Indeed the ejecta at NSE freeze-out is composed mostly of free n 's, several percents in mass of α 's and very few heavier seed nuclei ($A \lesssim 100$). Due to the extremely fast density drop, a large fraction of n 's do not participate in the r -process Lippuner and Roberts (2015). The larger the abundance of hydrogen is, the smaller the abundance of heavy elements is, with a narrow intermediate regime where both heavy r -process elements and H have comparable abundances. For $\tau \gtrsim 10$ ms, H production becomes always negligible.

As visible in Figure 8.2, the production of He can happen both in association or in the absence of heavy elements. On the one hand, if $Y_e \gtrsim 0.45$, most neutrons are locked inside strongly bound nuclei (including α 's) at NSE freeze out, and the ratio between free neutrons and seed nuclei is not large enough to guarantee r -process nucleosynthesis beyond the second peak. On the other hand, the simultaneous production of He and heavy r -process elements can take place in two different regimes: i) at high entropy ($s \gtrsim 60k_B$ baryon $^{-1}$) for a broad range of electron fractions ($Y_e \lesssim 0.4$); ii) at low electron fractions ($Y_e \lesssim 0.23$) in low entropy conditions ($s \lesssim 60k_B$ baryon $^{-1}$). The high- s regime was considered for many years as the main scenario for r -process nucleosynthesis in supernova winds (e.g. Woosley et al. 1994; Farouqi et al. 2010). High- s conditions favor the production of α particles and fewer heavier seed nuclei at NSE freeze-out (α -rich freeze-out). Free neutrons are captured by the few seed nuclei to produce the heaviest elements, while for $Y_e \gtrsim 0.40$ the neutron-to-seed ratio becomes too small for this production to occur. In the low- Y_e , low- s regime, the He production correlates with the production of heavy r -process elements, particularly of actinides. To identify which processes are responsible for this correlation, in Figure 8.3 we focus

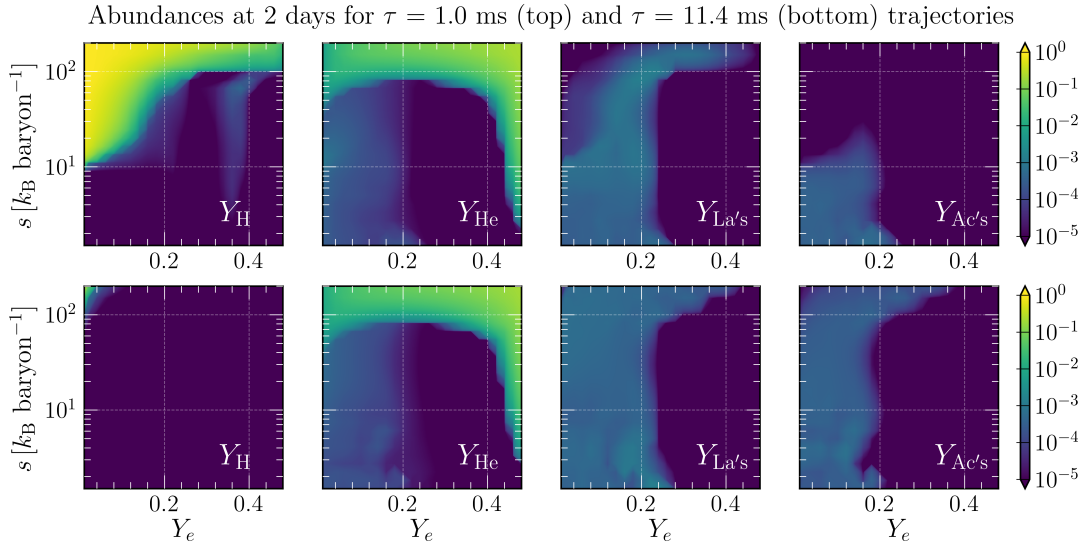


Figure 8.2: Number abundances of hydrogen, helium, lanthanides and actinides as a function of Y_e and s , for $\tau \sim 1.0$ ms (top) and $\tau \sim 10$ ms (bottom), at 2 days after merger, as obtained by our parametric nucleosynthesis calculations.

on a representative low- s , low- Y_e trajectory. In these conditions free neutrons are abundant and provide an almost steady supply of free protons (through n -decay, dashed orange line) and the efficient formation of deuterium (d) and tritium (t). Y_α increases through charge reactions such as $t + t \rightarrow 2n + {}^4\text{He}$ and $d + t \rightarrow n + {}^4\text{He}$, until (n, γ) - (γ, n) equilibrium freezes-out ($Y_n \lesssim 10^{-4}$). This picture is confirmed by the fact that, if n -decay is artificially removed from Skynet’s nuclear network Y_α stays initially frozen (cyan dashed line). At later times ($t \gtrsim 2$ s), α -decay of translead nuclei (if produced) becomes significant and Y_α increases further. Lower initial Y_e (i.e., a larger $Y_n \approx (1 - Y_e)$) results in: i) a wider time window over which t and d can be efficiently produced and converted into α ’s; ii) a larger abundance of α -decaying translead nuclei. The relative importance of the charged reactions and of the α -decays can be found by comparing Y_{He} at neutron freeze-out and at the end of our calculations. For $0.1 \lesssim Y_e \lesssim 0.2$, between ~ 20 and $\sim 40\%$ of the final He is already produced at neutron freeze-out. For $Y_e < 0.1$ the relative amount tends to increase up to $\sim 70\%$. Since many α -decays happen on timescales of several days, $\lesssim 40\%$ ($\lesssim 25\%$) of Y_{He} is produced after the first (10th) day after merger.

We are now in a position to understand in which thermodynamics conditions the abundances presented in Figure 8.1 have been synthesized. For equal mass mergers, in the case of the softer BLh EOS most of the H and He are efficiently synthesized in the high- s , fast expanding tail of the shock-heated component of the dynamical ejecta, while the subdominant He synthesized in low- s , low- Y_e conditions roughly traces the less abundant heavy r -process element distributions. For the stiffer DD2 EOS, the merger is less violent. The high- s tail of the shock-heated dynamical ejecta is thus less relevant and its contribution to the

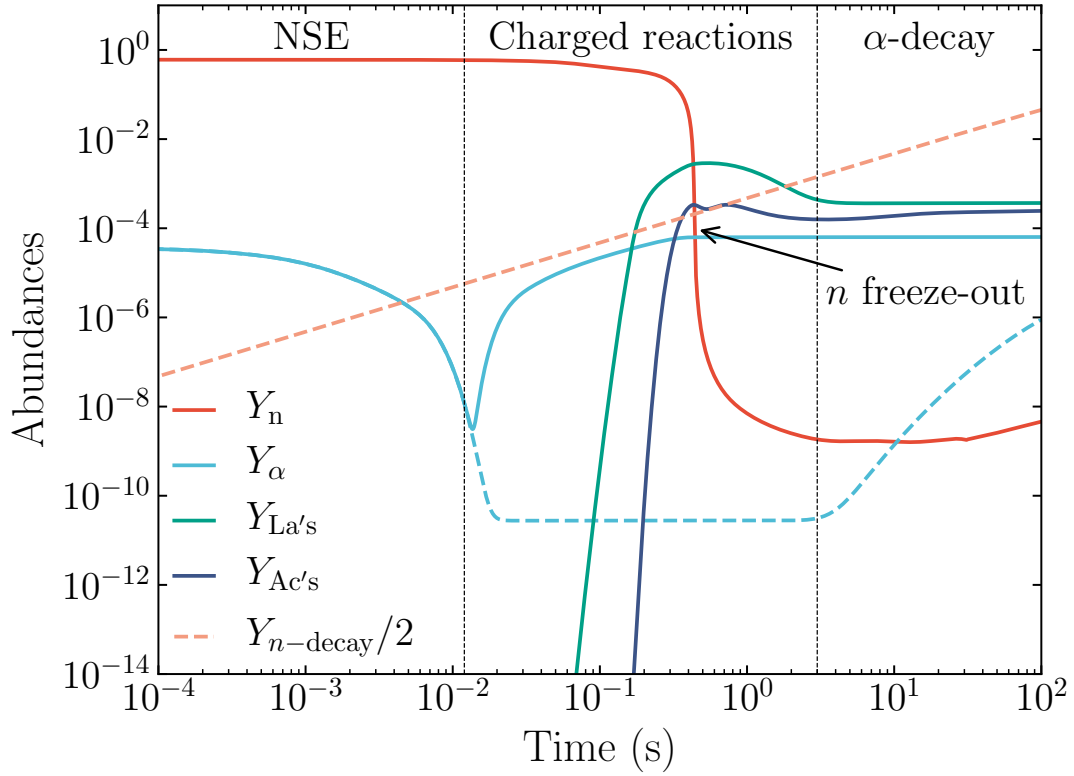


Figure 8.3: Evolution of neutron, helium, lanthanides and actinides abundances for a trajectory with $s = 10 k_B \text{ baryon}^{-1}$, $\tau = 10 \text{ ms}$ and $Y_e = 0.15$.

He production becomes comparable to the low- s , low- Y_e contribution. H is still produced, but slightly less efficiently. For the same merger model, the spiral wind ejecta have a pronounced, narrow peak in the velocity-entropy space, around $\tau = 8 \text{ ms}$ and $s = 20 k_B \text{ baryon}^{-1}$, and a broad Y_e distribution with a peak around $\gtrsim 0.3$, but extending down to 0.1. Thus, the production of H is suppressed while He is synthesized less efficiently than in the dynamical ejecta and in association with the more abundant lanthanides and actinides. For the unequal mass case, because of the lack of the high entropy tail, low- s , low- Y_e matter is the main source of He, tracing the presence of heavy r -process elements, more abundant than He by a few.

Hydrogen and Helium are synthesized in hot conditions as bare nuclei, and electrons recombine as matter expands and cools. Following (Kotelnikov and Milstein 2019), we estimate that the recombination timescale is smaller than the dynamical timescale up to several days for typical expansion conditions. Moreover, the presence of lanthanides and actinides significantly increases matter opacity Kasen et al. (2013) such that radiation drives the expanding ejecta towards local thermodynamical equilibrium (LTE) conditions (Kasen et al. 2017). We thus computed H and He ions abundances in LTE by solving the Saha equation for representative mixtures of atoms and ions. When the temperature drops below the ionization energies recombination occurs: for the density and temperature

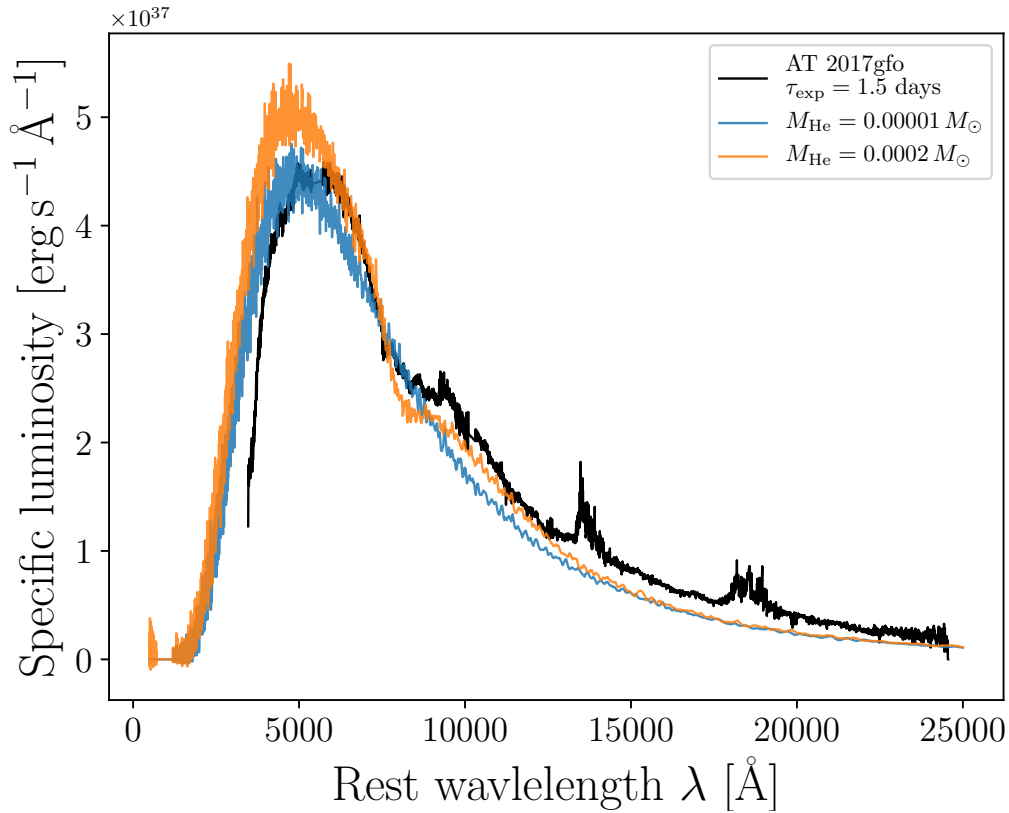


Figure 8.4: Synthetic TARDIS spectra, including non-LTE effects, for different mass of He in an outer ejecta layer, compared with the observed spectrum of AT2017gfo at 1.5d (Pian et al. 2017).

conditions expected during a kilonova, first He and then H could recombine in atomic form after a few hours. In fact, while a few hours after explosions the ejecta temperature reaches 10^5 K, already at 0.5 day the temperature drops to 10^4 K. In these conditions, the small predicted masses of H and He are not expected to produce persistent lines, at least for standard LTE level population. However we cannot exclude the possibility that the H/He lines are boosted by non-LTE effects similar to those observed in the ejecta of supernovae (SNe) (Boyle et al. 2017). In SNe, these effects originate because of the fast electrons from ^{56}Ni radioactive decay. Other radioactive decays or shocks with the circumstellar medium may power a reservoir of fast electrons also in kilonova ejecta.

While the very early spectrum of AT2017gfo (~ 0.5 d) (Shappee et al. 2017) is almost featureless, the 1.5d spectrum (Pian et al. 2017) shows a broad absorption at 810 nm that was explained by a transition of SrII (Watson et al. 2019). We first notice that the amount of Sr required to produce such a feature is compatible with the one predicted in all our equal mass BNS models, see Figure 8.1. However, it is interesting to notice that, based on the velocity profile only, the feature could be consistent with a He 10831 line in the ejecta expanding at $0.25c$. We use TARDIS to test whether this feature can be produced by a high velocity He layer in favorable conditions. We compute a spectrum from a He layer with velocity

$v_\infty = 0.20c - 0.35c$ (compatible with our merger models), adopting a target integrated luminosity $L_0 = 10^8 L_\odot = 3.83 \times 10^{41} \text{ erg s}^{-1}$, that is the observer luminosity of AT2017gfo assuming a distance $d_L = 40 \text{ Mpc}$. We find that with plain LTE treatment a significant He feature never appears even for implausible large ejecta mass (i.e. few solar masses). We also explore the possible impact of non-LTE excitations by using the analytical approximation for the non-LTE He level population developed inside TARDIS for the He rich ejecta of double detonation type Ia SNe (Boyle et al. 2017). The predicted He line strength changes dramatically with the non-LTE treatment. However an acceptable match of the observed spectrum still requires $M_{\text{He}} \simeq 2 \times 10^{-4} M_\odot$ (Fig. 8.4). This is between 1 and 2 orders of magnitude larger than the predicted He mass and therefore we conclude that He is likely not responsible for the observed 810 nm feature, unless non-LTE effects or the He mass are severely underestimated. Similar results were obtained for a H rich ejecta composition although with even larger uncertainties because the current public version of TARDIS is not well suited to treat H-rich ejecta (Vogl et al. 2019) and therefore the strength of the H lines may be underestimated.

8.4 Discussion and conclusions

Dynamical and spiral-wave wind ejecta from BNS mergers are not the only environment where H and He can be synthesized in association with r -process elements. In the case of BH-NS mergers, dynamical ejecta conditions are very similar to the ones observed in very unequal BNS mergers, with possibly larger expansion velocities (Rosswog 2005; Just et al. 2015; Roberts et al. 2017; Fernández et al. 2017; Kyutoku et al. 2018; Brege et al. 2018). Thus, in this case we expect significant He production in association with heavy r -process nucleosynthesis, as visible in some of the nucleosynthesis results of the above papers.

Both in the case of BNS and BH-NS mergers, neutrinos, viscosity and magnetic processes can drive matter ejection from the remnant on the viscous timescale expanding at significantly smaller velocity than dynamical ejecta, $v_\infty \lesssim 0.1c$ (Metzger et al. 2009; Perego et al. 2014; Siegel et al. 2014; Radice et al. 2018). For the bulk of the ejecta, weak interaction increases Y_e above 0.2, especially if a massive NS is present, preventing efficient He nucleosynthesis. Detailed simulations show also in these cases the possible presence of a high- s tail in the ejecta distribution, especially close to the polar axis (Fernández and Metzger 2013; Just et al. 2015; Fujibayashi et al. 2018, 2020). This tail is particularly prominent in the case of GRMHD simulations (Fernández et al. 2019). For BNS mergers, if the central massive NS survives on a timescale comparable to or larger than the viscous timescale, ν -irradiation can increase Y_e even above 0.45, producing efficiently He in α -rich freeze-out conditions. Thus, also these ejecta can host significant He production (Lippuner et al. 2017). Thus we conclude that in the case of BNS and BH-NS mergers H and He can be robustly synthesized, with the He production often associated with the production of heavy r -process elements.

However, these light elements probably never contribute to the kilonova spectrum formation unless strong non-LTE effects appear or a dramatic EOS softening (e.g. for a quark-phase transition at supra-nuclear density) boosts the presence of fast expanding, high- s matter. Our results can be key to organize and prioritize future observational campaigns for the electromagnetic counterparts of GW events.

8.A r -process nucleosynthesis calculations

To perform extensive nucleosynthesis calculations we use the publicly available nuclear network `SkyNet` (Lippuner and Roberts 2015) in its default version (see Section 3.2), with the exception of the usage of the latest JINA REACLIB database (Cyburt et al. 2010). `SkyNet` requires time-dependent trajectories of Lagrangian fluid elements to predict the temporal evolution of the abundances. We initialized all trajectories in NSE at $T_0 = 6$ GK. For a given electron fraction and entropy, the NSE solver determines the corresponding initial density, ρ_0 , by considering a fully ionized ideal gas of ions, electrons and photons. After that, matter density evolves first through an exponential phase and then to a homologous expansion (Lippuner and Roberts 2015):

$$\rho(t) = \begin{cases} \rho_0 e^{-t/\tau} & \text{for } t \leq 3\tau, \\ \rho_0 (3\tau/(et))^3 & \text{otherwise.} \end{cases} \quad (8.1)$$

The tracer temperature is evolved consistently to the expansion, accounting for nuclear heating. The tracer and the abundances of all relevant nuclear species are evolved up to 10^9 s. Given the above initialization procedure, nucleosynthesis in the expanding ejecta of compact binary mergers depends mainly on three physical parameters: the specific entropy (s , measured in units of the Boltzmann constant per baryon), the electron fraction (Y_e), and the expansion timescale (τ) of the ejecta (Hoffman et al. 1997). To compute yields abundances as a function of time we perform extensive nucleosynthesis calculations over wide ranges of s , Y_e , and τ , namely: $0.5 \leq \tau$ [ms] ≤ 200 , $1.5 \leq s$ [k_B baryon $^{-1}$] ≤ 300 , and $0.01 \leq Y_e \leq 0.48$, by constructing a $18 \times 24 \times 24$ regular grid (approximately logarithmic in the two former quantities and linear in the latter). The above ranges span the relevant expected intervals for the ejecta properties of compact binary mergers.

8.B Numerical relativity simulations of binary neutron star mergers

We consider the ejecta obtained by simulations of BNS mergers performed with the `WhiskyTHC` code (Radice et al. 2014a,b). The latter is a NR code that solves the Einstein's equations in the 3+1 Z4c free-evolution scheme coupled to general relativistic hydrodynamics on adaptive mesh-refinement grids. `WhiskyTHC` employs high-resolution shock capturing algorithms. and implements finite-temperature,

composition dependent nuclear EOSs, an approximate neutrino transport scheme and the general-relativistic large eddy simulations method (GRLES) for turbulent viscosity of magnetic origin. The code was specifically designed to model the late inspiral, merger and post-merger phase of BNS mergers. We consider 3 simulations whose chirp mass is targeted to the GW170817 event: BLh_equal, BLh_unequal, and DD2_equal. The first and the third one have $M_1 = M_2 = 1.364M_\odot$, while the second one $M_1 = 1.856M_\odot > M_2 = 1.020M_\odot$. The BLh_equal and BLh_unequal simulations employ the softer BLh nuclear EOS, an hadronic EOS derived using a purely microscopic approach that predicts a maximum mass of $2.10M_\odot$ for a cold, non-rotating NS. The DD2_equal simulation uses the stiffer HS(DD2) EOS. This EOS was derived in the framework of relativistic mean field models and predicts a maximum NS mass of $2.42M_\odot$. Both these EOSs are consistent with present nuclear and astrophysical constraints and bracket uncertainties in the properties of matter above nuclear densities. For all three simulations the adaptive mesh refinement is characterized by seven nested grids with 2:1 refinement level and the linear resolution in the finest level of is 123m. Tidal torques and shock waves produced by the bouncing remnant unbind matter within a few milliseconds (the so-called dynamical ejecta). For equal mass binaries, a softer EOS produces stronger shocks and larger shock-heated ejecta, while tidal ejection within a crescent across the equatorial characterises very unequal mass mergers. The dynamical ejecta (obtained using the geodetic extraction criterion) for the three different runs amount to $3.84 \times 10^{-3}M_\odot$, $6.81 \times 10^{-4}M_\odot$, and $1.33 \times 10^{-3}M_\odot$ for the BLh_equal, BLh_unequal, and DD2_equal, respectively. Additionally, the DD2_equal simulation was extended up to ~ 90 ms after merger showing the development of a $m = 1$ spiral arms in the central remnant. The spiral arms propagate into the disc, transporting angular momentum outwards and producing a matter outflow in the form of a spiral wind. DD2_equal also shows $6.264 \times 10^{-3}M_\odot$ of spiral wind ejecta (obtained using the Bernoulli criterion). The three simulations were presented in Perego et al. (2019); Nedora et al. (2019); Bernuzzi et al. (2020) where more details can be found. In the original papers, the three simulations were referred as BLh_M13641364_M0_LK_SR, BLh_M10201856_M0_LK_SR, and DD2_M13641364_M0_SR.

8.C Conditions of the dynamical and spiral-wave wind ejecta from BNS merger simulations

The nucleosynthesis yields produced in the ejecta of BNS mergers, as predicted by NR simulations and presented in Figure 8.5, is based on/supported by the following analysis of the conditions of ejected matter in the (s, Y_e, τ) space. In Figure 8.5 and Figure 8.6 we present mass weighted histograms as extracted from the three simulations considered in this work. The 3D distributions have been marginalized both with respect to τ and Y_e . Since the ejection of matter in BNS merger is usually anisotropic, we consider two representative polar angles, one close to the polar axis (top panels) and one to the equatorial plane (bottom panels).

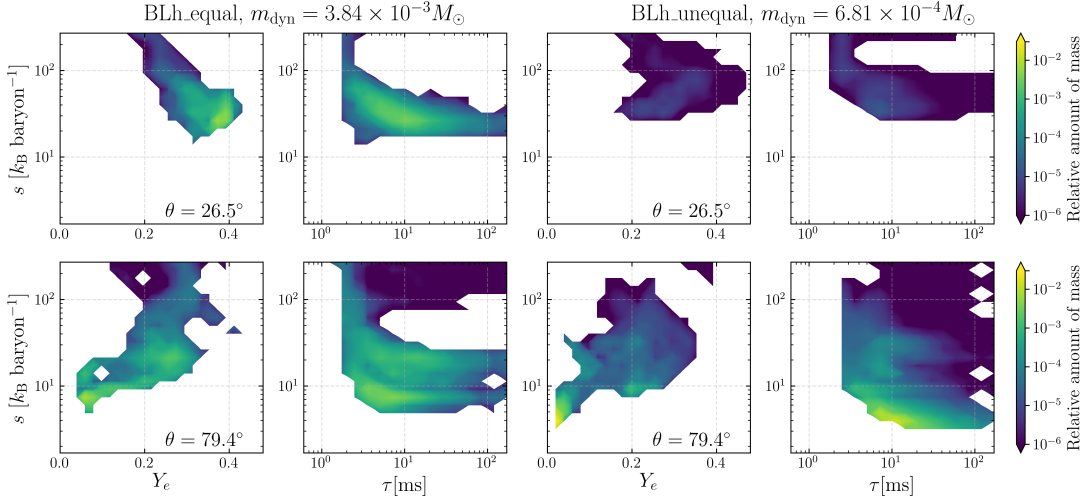


Figure 8.5: Mass weighted histograms of the (Y_e, s, τ) conditions of the dynamical ejecta, as obtained from the dynamical ejecta of the BLh_equal (left four panels), BLh_unequal (right four panels). For each simulation, we distinguish between the (Y_e, s) (left panel) and (τ, s) (right panel) planes, and a high (top panel) and a low (bottom panel) latitude angle.

In the case of an equal mass merger (left panels), significant mass ejection happens over the whole solid angle, even if more matter is expelled at equatorial latitudes. The bulk of the ejecta have low entropy ($s < 40 k_B \text{ baryon}^{-1}$) and is very neutron rich, even if equatorial ejecta are usually characterized by lower Y_e and lower entropy. However, at both angles a high entropy tail (with $s > 60 k_B \text{ baryon}^{-1}$) expanding at high speeds ($\tau \lesssim 5 \text{ ms}$) is visible. This high-entropy, high-velocity tail in the ejecta is a signature of the so-called shock heated ejecta, produced by the bouncing remnant. Qualitative differences characterize the ejecta in the case of very different colliding NS masses. In this case, the dynamical ejecta are mainly produced by the tidal disruption of the lightest NS. Polar ejecta are almost absent and the equatorial ejecta are dominated by low entropy, low Y_e matter that expand with $\tau \sim 10 \text{ ms}$. The high-entropy, high-velocity tail in the ejecta distribution is almost absent.

8.D Helium and heavy elements production in low and high entropy ejecta

For a nucleus (A, Z) of mass number A , atomic number Z and neutron number $N = A - Z$, its abundance $Y_{(A,Z)}$ in NSE is given by

$$Y_{(A,Z)} = Y_p^Z Y_n^N \frac{G_{(A,Z)}(T) A^{3/2}}{2^A} \left(\frac{\rho}{m_u} \right)^{A-1} \left(\frac{2\pi\hbar^2}{m_u k_B T} \right)^{3(A-1)/2} e^{B(A,Z)/k_B T}, \quad (8.2)$$

where $Y_{n,p}$ are the abundances of free n 's and p 's, ρ the matter density, $G_{(A,Z)}(T)$ the nuclear partition function, $B(A, Z)$ the nucleus binding energy, T the matter

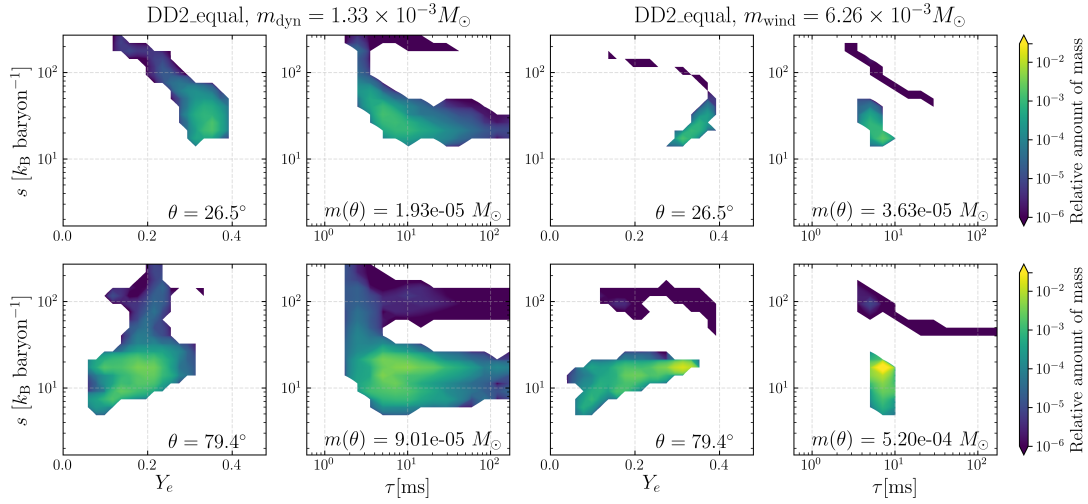


Figure 8.6: Same as in Figure 8.5, but for the DD2_equal simulation. In this case, we consider both dynamical ejecta (left four panels) and spiral-wave wind ejecta (right four panels).

temperature, k_B the Boltzmann constant, m_u the atomic mass unit, and \hbar is the reduced Planck constant. Very high densities favour large nuclei, while photodissociation produces light nuclei (and ultimately free protons and neutrons) in hot conditions. For intermediate regimes, the nuclear binding energy favour the most tightly bound nuclei, i.e. iron group nuclei or α particles among the light nuclei. Ejecta produced by BNS mergers come from high density conditions and experiences high enough temperatures such that it is usually mostly dissociated into free neutrons and protons under NSE conditions at its peak temperature. As temperature drops, neutrons and protons recombine first into α particles. The subsequent building of iron group nuclei depends on the three body reactions responsible for the assembly of heavier nuclei, namely $2\alpha + n \rightarrow {}^9\text{Be} + \gamma$ and $3\alpha \rightarrow {}^{12}\text{C} + \gamma$. If entropy is high, the fluid is radiation-dominated and

$$s \gtrsim s_\gamma = \left(\frac{4\pi^2 k_B^4 m_u}{45c^3 \hbar^3} \right) \frac{T^3}{\rho}, \quad (8.3)$$

where c is the speed of light. Under this assumption, NSE abundances are proportional to

$$Y_{(A,Z)} \propto Y_p^Z Y_n^N \frac{A^{3/2}}{2^A s^{A-1}} \left(\frac{k_B T}{m_u c^2} \right)^{3(A-1)/2} e^{B(A,Z)/k_B T}, \quad (8.4)$$

From this relation it is clear that high entropy conditions favour lighter nuclei and, among them, the most bounded ones (i.e. α particles). The charge-particle freeze-out occurs at low density, see Equation (8.3), such that the corresponding three body reactions involving α 's become soon inefficient. This is the so-called α -rich NSE freeze-out at which matter is composed of neutrons (protons), alphas, and few heavy seed nuclei. Most of the α abundance is preserved in the final

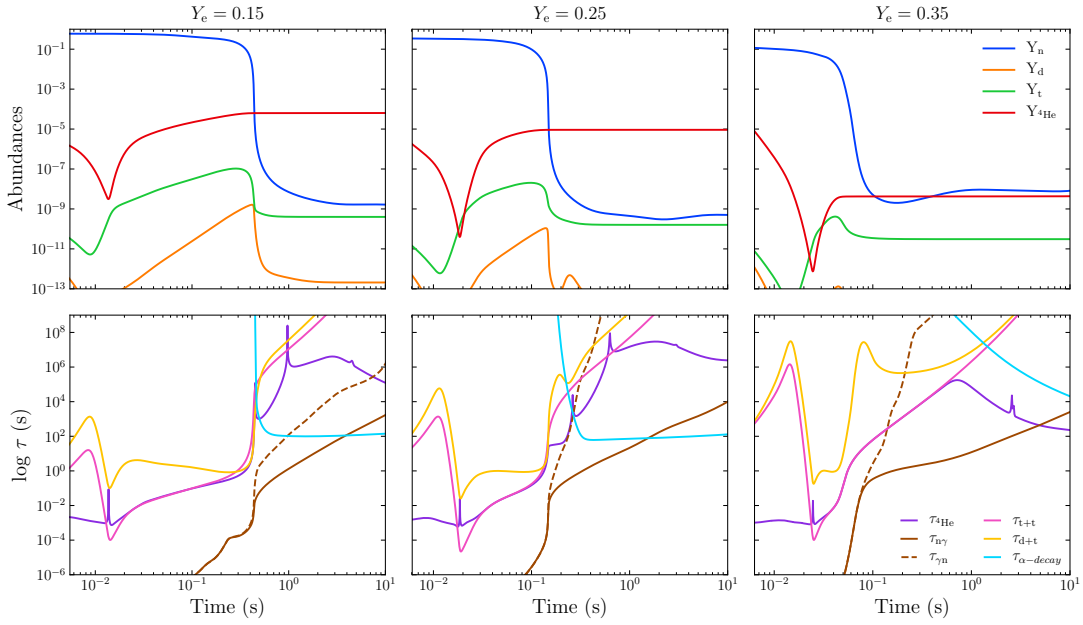


Figure 8.7: Evolution of a few selected abundances (top) and some relevant reaction timescales (bottom) for three low entropy trajectories. For all trajectories, $s = 10 k_B \text{ baryon}^{-1}$ and $\tau = 10 \text{ ms}$, while $Y_e = 0.15, 0.25, 0.35$ moving from left to right. Before n freeze-out, reactions involving deuterium and tritium account for α particle production, while after α -decay of translead nuclei. For $0.2 \lesssim Y_e \lesssim 0.45$ the faster freeze-out and the lack of translead nuclei produce a lower Y_{He} .

composition, but the free neutrons are captured by the few seed nuclei in r -process conditions. The final point of the r -process nucleosynthesis depends on the neutron-to-seed ratio ($\langle A \rangle_{\text{final}} \sim \langle A \rangle_{\text{seed}} + Y_n/Y_{\text{seed}}$), which is larger for lower Y_e , smaller τ and larger s since:

$$\frac{Y_n}{Y_{\text{seed}}} \propto \frac{s^3}{Y_e^3 \tau}. \quad (8.5)$$

In low-entropy neutron-rich conditions, matter stays sufficiently dense while cooling to produce neutron rich iron group nuclei in NSE conditions, see Equation (8.2). For sufficiently neutron rich conditions, not all free neutrons are bound in nuclei so that they can be captured to produce heavy nuclei through the r -process. In order to study in more detail the nuclear processes responsible for the production of He in association with heavy r -process elements in low entropy conditions, we extend the analysis reported in the main text by considering three representative tracers. We fix, in particular, $s = 10 k_B \text{ baryon}^{-1}$ and $\tau = 10 \text{ ms}$, while we consider $Y_e = 0.15, 0.25, 0.35$. In the top panels of Figure 8.7 we represent the abundances of a few selected isotopes as a function of time (measured with respect to the time when $T = 5 \text{ GK}$), including free neutrons (n), deuterium (d), tritium (t), and α particles. Other He isotopes are always subdominant, and will be neglected in the following analysis. In the bottom

panels we report some relevant timescales. The lifetime of α particles is computed as $\tau_\alpha = |(dY_\alpha/dt)/Y_\alpha|^{-1}$. Similarly, we introduce the average radiative neutron capture timescale per nucleus as

$$\tau_{(n,\gamma)} = \frac{\sum_{A,Z} Y_{(A,Z)}}{\sum_{A,Z} Y_{(A,Z)} Y_n \langle \sigma v \rangle_{(A,Z)}}, \quad (8.6)$$

the average photodissociation timescale per nucleus as

$$\tau_{(\gamma,n)} = \frac{\sum_{A,Z} Y_{(A,Z)}}{\sum_{A,Z} Y_{(A,Z)} \lambda_{\gamma,(A,Z)}}, \quad (8.7)$$

the α production timescale through $t + t \rightarrow n + n + \alpha$ reaction as

$$\tau_{t+t} = \frac{Y_\alpha}{Y_t^2 \langle \sigma v \rangle_{t+t}}, \quad (8.8)$$

the Hproduction timescale through $d + t \rightarrow n + \alpha$ reaction as

$$\tau_{d+t} = \frac{Y_\alpha}{Y_d Y_t \langle \sigma v \rangle_{d+t}}, \quad (8.9)$$

and finally the average α -decay timescale per nucleus as

$$\tau_{\alpha\text{-decay}} = \frac{\sum_{A,Z} Y_{(A,Z)}}{\sum_{A,Z} Y_{(A,Z)} \lambda_{\alpha,(A,Z)}}. \quad (8.10)$$

In the previous expressions $Y_{(A,Z)}$ is the number abundance of a nucleus with atomic number Z and mass number A , $\langle \sigma v \rangle_{(A,Z)}$, $\lambda_{\gamma,(A,Z)}$, and $\lambda_{\alpha,(A,Z)}$ are the corresponding neutron capture rate, photodisintegration (γ, n) rate, and α -decay rate, respectively, $\langle \sigma v \rangle_{t+t}$ represents the $t + t$ reaction rate, while $\langle \sigma v \rangle_{d+t}$ the $d + t$ reaction rate. Helium is initially depleted to form heavier iron group nuclei in expanding matter under NSE conditions, up to the point when charged-particle freeze-out occurs ($T \gtrsim 3$ GK). After that, (n, γ) - (γ, n) equilibrium guarantees a high neutron density and neutron-to-seed ratio, and starting from seed nuclei with $A \lesssim 100$ drives the formation of heavier nuclei through the r -process nucleosynthesis, far from the valley of stability. The high abundance of free neutrons provides also an almost steady supply of free protons (through n -decay) and thus the efficient formation of d and t . Reactions such as $t + t \rightarrow n + n + \alpha$ and $d + t \rightarrow n + \alpha$ are not in equilibrium with their inverse. As a consequence α particles accumulate and increase their abundance till (n, γ) - (γ, n) equilibrium freezes-out (visible in the figure when $Y_n \lesssim 10^{-4}$). When Y_n drops, tritium and deuterium are no more produced and the production of He is halted. As visible in the lower panels of Figure 8.7, τ_α is accounted by τ_{d+t} and especially τ_{t+t} in the

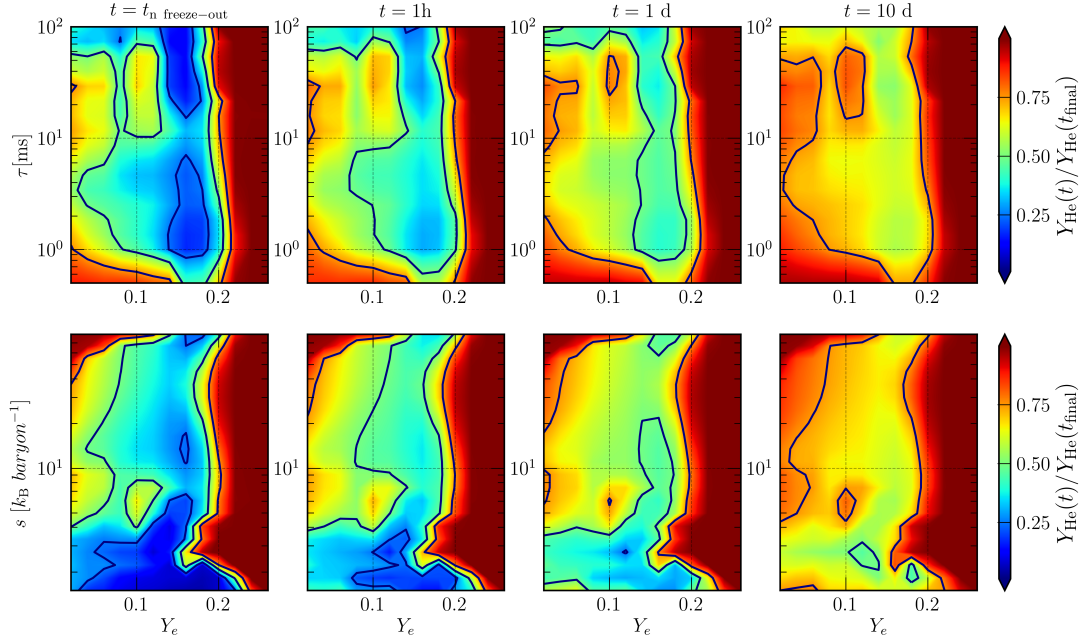


Figure 8.8: Ratio of the helium abundance produced at different times after merger over the final one. The ratios are represented in the (Y_e, τ) (top) and in the (Y_e, s) (bottom) planes. Left panels, referring to the n freeze-out time, represent the ratio of He produced through charged current reactions involving deuterium and tritium. The other three columns show the cumulative He production through α -decays between 1 hour and 10 days. Blue lines refer to 0.25, 0.50 and 0.75.

time window between the end of NSE and the drop of Y_n , clearly demonstrating that these two reactions are the main ${}^4\text{He}$ production channel being other charged-particle reactions frozen. At later times ($t \gtrsim 2$ s), α -decay of translead nuclei (if significantly produced) becomes effective and $Y_{{}^4\text{He}}$ increases again. A direct comparison between the three cases demonstrates that a lower initial Y_e results in: i) a wider time window over which t and d can be efficiently produced and converted into ${}^4\text{He}$; ii) a larger abundance of α -decaying translead nuclei. The relative importance of these two distinct production channels can be computed by comparing $Y_{{}^4\text{He}}$ at neutron freeze-out and at the end of our calculations, see Figure 8.8. For $0.1 \lesssim Y_e \lesssim 0.2$, between ~ 20 and $\sim 40\%$ of the final He is already produced at neutron freeze-out. For $Y_e < 0.1$ the relative amount tends to increase up to $\sim 70\%$. Since many α -decays happen on timescales of several days, $\lesssim 40\%$ ($\lesssim 25\%$) of $Y_{{}^4\text{He}}$ is produced after the first (tenth) day after the merger.

The content of this chapter has appeared in Perego et al. (2020)¹. As the second author, I significantly contributed to setting up the pipeline for the nucleosynthesis calculations and nucleosynthesis data analysis. I significantly contributed to the result interpretation, to the writing, and the figure creation.

¹Production of very light elements in kilonovae. *arXiv e-prints*, page arXiv:2009.08988. <https://arxiv.org/abs/2009.08988>.

Summary and conclusions

In recent years, a large amount of nucleosynthetic data for several different astrophysical environments has been made accessible to the community through improved observational and experimental techniques. In view of this, a *multi-messenger* approach to the study of nuclear astrophysics has increasingly become a key issue for a full understanding of the complex coupling between nuclear burning, mixing processes, and neutrino and radiation emissions occurring in stars.

Besides the need for more precise observations, a huge effort is required from the theoretical side of stellar evolution. In this regard, the recent advances in the input physics required for stellar computations made it possible to construct more accurate evolutionary models, which are an essential tool to investigate and analyze the available observations. Motivated by such recent improvements in the basic knowledge of plasma physics (i.e. EOS, opacity, solar mixture, and nuclear reactions), the FUNS stellar evolutionary code has been updated to the state-of-art of the input physics available. In this framework, we enlightened the importance of the nuclear data activity of the n_TOF collaboration in the last two decades in providing relevant information for the characterization of several aspects of neutron capture nucleosynthesis processes. The n_TOF facility will soon restart its operation and new data are expected from challenging experiments.

Focusing on solar models, we analyzed the main uncertainty sources and quantitatively showed the impact of a revised ${}^7\text{Be}+e^-$ rate on solar structure and expected neutrino fluxes. We found that new SSMs yield a maximum difference in the efficiency of the ${}^7\text{Be}$ channel of about 3 – 4% to what is obtained with the previously adopted rate. Variations in the solar structure and neutrino fluxes are negligible, except for the ${}^8\text{B}$ neutrino flux, whose value increases up to 2.6 – 2.7%, depending on the composition assumed. Both new high- and low-metallicity solar models expectations agree with SNO measurements of the ${}^8\text{B}$ neutrino flux.

Given the degree of uncertainty affecting SSM in predicting neutrino fluxes, model-independent tools for the analysis of solar neutrino data are needed. In this context, we generalized the luminosity constraint by including energy source terms which are commonly neglected and provided a ready-to-use relation for

future solar neutrino analyses. Using experimentally determined beryllium and boron neutrino fluxes, we showed that pp and CNO neutrino fluxes are tightly bound (within 0.2% of uncertainty) by a simple linear relation. Finally, taking advantage of this relationship and adopting the very recent value for the CNO flux measured by the Borexino collaboration, we found that the expected pp neutrino flux is marginally consistent with theoretical predictions for solar models that assume a high abundance of heavy elements. This fact points out that standard solar models may currently predict a too low CNO abundance in the solar core and could give new insights regarding its metal content.

Then we discussed a number of issues resulting from attempts to account for the presence of isotopic anomalies in primitive solids of the solar system. Some of these composition anomalies can be ascribed to *in situ* decay of radioactive isotopes that were present alive in the early solar system. Considering that the proto-sun was previously isolated from Galactic nucleosynthesis for a time around 10 Myr, we found that nuclei with $\tau \gtrsim 5 - 10$ Myr might be explained by Galactic evolution. Instead, shorter-lived isotopes like ^{26}Al , ^{41}Ca , and ^{135}Cs require nucleosynthesis events close in time to the solar formation. We investigated the possibility that both an AGB star or a massive star could have contaminated the solar nebula. Models of final stages of intermediate-mass stars now predict the ubiquitous formation of a ^{13}C pocket, which always implies large excesses in ^{107}Pd with respect to ^{26}Al . Even a late contamination by a massive star meets serious problems, because the inhomogeneous addition of supernova debris yields excesses on stable isotopes that disagree with measurements. Therefore, the possibility that a single, nearby evolved star be at the origin of early solar system radioactivities is in doubt. One possibility still open is that the contamination came from a super-AGB star, where the ^{13}C *n*-source might not be active, avoiding the overproduction of ^{107}Pd . An alternative might also be found in the most massive among intermediate-mass stars ($7 - 8 M_{\odot}$) if hot bottom burning yields were remarkably different from what is currently available in the literature.

Among presolar grains, those classified as mainstream SiC grains came from low-mass C-rich AGB stars and exhibit *s*-process isotopic signatures. However, none of the mechanisms typically adopted in stellar evolutionary codes for the formation of the ^{13}C pocket have been able to simultaneously reproduce all the measured *s*-process isotopic anomalies. Here we have investigated for the first time with a stellar evolutionary code fully coupled to nucleosynthesis, the idea that the formation of the ^{13}C pocket can be induced by magnetic buoyancy. We presented our implementation of mixing triggered by magnetic buoyancy in the FUNS code and found that magnetic fields of the order of 10^5 G can actually induce the formation and buoyant rise of magnetic flux tubes in the He-intershell of AGB stars. Such tubes are fast enough to guarantee, by mass conservation, the downward penetration of sufficient protons to form a sizable ^{13}C pocket. The new “magnetic” pocket exhibits a low concentration of ^{13}C and an extended tail. By adopting a single magnetic field configuration, new magnetic AGB models present isotopic ratios for Ni, Sr, Zr, Mo, and Ba in excellent agreement with grains data. The present models for AGB stars may introduce

improvements in reproducing other observational constraints, e.g. from intrinsic C-stars, Ba-stars, CH stars, and CEMP-s stars. If the toroidal field necessary for the onset of magnetic buoyant instabilities is generated through the dynamo action exerted by differential rotation in the radiative zone of TP-AGB stars, then the typically observed *s*-process spread at a fixed metallicity might be connected to the initial mass and/or rotational velocity of the star. Buoyant magnetized domains may also drive enough radial transport of H-burning ashes to the convective envelopes of AGB stars of mass $\lesssim 2.2 M_{\odot}$ to account for the observational data of CNO and aluminum isotopic ratios that cannot otherwise be accounted for by convective transport in third dredge-up episodes. Another point concerns fluorine nucleosynthesis. The low ^{13}C concentration predicted by our models strongly limits the local formation of ^{14}N , thus inhibiting nuclear channels leading to the synthesis of fluorine. This could alleviate the problem of fluorine overabundance in evolved metal-poor AGB stars predicted by current models.

Finally, we investigated the production of light elements ($Z < 20$) in compact binary mergers, focusing in particular on hydrogen and helium. We considered results of numerical relativity simulations of binary neutron star mergers targeted to GW170817 with different binary properties (mass ratio and EOS) and computed the resulting time-dependent abundances with the nuclear reaction network SkyNet. We found that the presence of hydrogen in the ejecta is related to high-entropy and low- Y_e matter that expands very rapidly. Instead, the production of helium can take place both at high entropy (through α -rich freeze-out) and in low- Y_e , low- s conditions. In the latter regime, the He production correlates with the production of heavy *r*-process elements, particularly of actinides. Although H and He are robustly synthesized, these light elements probably never contribute to the kilonova spectrum formation, unless strong non-LTE effects appear or a dramatic EOS softening boosts the presence of fast expanding and high-entropy matter. In the next future, we plan to systematically extend this kind of study to heavier nuclei, up to to the first *r*-process peak nuclei, in view of prospective observations of electromagnetic counterparts of gravitational wave events.

Bibliography

- Abbott, B. P., Abbott, R., Abbott, T. D., et al. (2017a). Gravitational Waves and Gamma-Rays from a Binary Neutron Star Merger: GW170817 and GRB 170817A. *ApJL*, 848(2):L13. doi: [10.3847/2041-8213/aa920c](https://doi.org/10.3847/2041-8213/aa920c).
- Abbott, B. P., Abbott, R., Abbott, T. D., et al. (2017b). GW170817: Observation of Gravitational Waves from a Binary Neutron Star Inspiral. *PhRvL*, 119(16):161101. doi: [10.1103/PhysRevLett.119.161101](https://doi.org/10.1103/PhysRevLett.119.161101).
- Abbott, B. P., Abbott, R., Abbott, T. D., et al. (2017c). Multi-messenger Observations of a Binary Neutron Star Merger. *ApJL*, 848(2):L12. doi: [10.3847/2041-8213/aa91c9](https://doi.org/10.3847/2041-8213/aa91c9).
- Abdurashitov, J. N., Bowles, T. J., Cherry, M. L., et al. (1999). Measurement of the solar neutrino capture rate by sage and implications for neutrino oscillations in vacuum. *Phys. Rev. Lett.*, 83:4686–4689. doi: [10.1103/PhysRevLett.83.4686](https://doi.org/10.1103/PhysRevLett.83.4686).
- Abe, K., Haga, Y., Hayato, Y., et al. (2016). Solar neutrino measurements in superkamiokande-iv. *Phys. Rev. D*, 94:052010. doi: [10.1103/PhysRevD.94.052010](https://doi.org/10.1103/PhysRevD.94.052010).
- Abia, C., de Laverny, P., Cristallo, S., Kordopatis, G., and Straniero, O. (2020). Properties of carbon stars in the solar neighbourhood based on Gaia DR2 astrometry. *A&A*, 633:A135. doi: [10.1051/0004-6361/201936831](https://doi.org/10.1051/0004-6361/201936831).
- Acheson, D. J. and Gibbons, M. P. (1978). On the Instability of Toroidal Magnetic Fields and Differential Rotation in Stars. *Philosophical Transactions of the Royal Society of London Series A*, 289(1363):459–500. doi: [10.1098/rsta.1978.0066](https://doi.org/10.1098/rsta.1978.0066).
- Adelberger, E. G., Austin, S. M., Bahcall, J. N., et al. (1998). Solar fusion cross sections. *Rev. Mod. Phys.*, 70:1265–1291. doi: [10.1103/RevModPhys.70.1265](https://doi.org/10.1103/RevModPhys.70.1265).
- Adelberger, E. G., García, A., Robertson, R. G. H., et al. (2011). Solar fusion cross sections. II. The pp chain and CNO cycles. *Reviews of Modern Physics*, 83:195–246. doi: [10.1103/RevModPhys.83.195](https://doi.org/10.1103/RevModPhys.83.195).
- Adsley, P., Battino, U., Best, A., Caciolli, A., Guglielmetti, A., Imbriani, G., Jayatissa, H., La Cognata, M., Lamia, L., Masha, E., Massimi, C., Palmerini, S., Tattersall, A., and Hirschi, R. (2020). Re-evaluation of the $^{22}\text{Ne}(\alpha, \gamma)^{26}\text{Mg}$

- and $^{22}\text{Ne}(\alpha, n)^{25}\text{Mg}$ reaction rates. *arXiv e-prints*, page arXiv:2005.14482. <https://arxiv.org/abs/2005.14482>.
- Aerts, C. (2019). Probing the interior physics of stars through asteroseismology. *arXiv e-prints*, page arXiv:1912.12300. <https://arxiv.org/abs/1912.12300>.
- Aerts, C., Mathis, S., and Rogers, T. M. (2019). Angular Momentum Transport in Stellar Interiors. *ARA&A*, 57:35–78. doi: [10.1146/annurev-astro-091918-104359](https://doi.org/10.1146/annurev-astro-091918-104359).
- Agostini, M., Altenmüller, K., Appel, S., et al. (2019). Simultaneous precision spectroscopy of p p , ^7Be , and p e p solar neutrinos with Borexino Phase-II. *PhRvD*, 100(8):082004. doi: [10.1103/PhysRevD.100.082004](https://doi.org/10.1103/PhysRevD.100.082004).
- Agostini, M., Altenmüller, K., Appel, S., et al. (2020a). First Direct Experimental Evidence of CNO neutrinos. *arXiv e-prints*, page arXiv:2006.15115. <https://arxiv.org/abs/2006.15115>.
- Agostini, M., Altenmüller, K., Appel, S., et al. (2020b). Sensitivity to neutrinos from the solar CNO cycle in Borexino. *arXiv e-prints*, page arXiv:2005.12829. <https://arxiv.org/abs/2005.12829>.
- Agostini, M., Altenmüller, K., and Appel, S. (2018). Comprehensive measurement of pp-chain solar neutrinos. *Nature*, 562(7728):505–510. doi: [10.1038/s41586-018-0624-y](https://doi.org/10.1038/s41586-018-0624-y).
- Aharmim, B., Ahmed, S. N., Anthony, A. E., Barros, N., Beier, E. W., Bellerive, A., Beltran, B., Bergevin, M., Biller, S. D., Boudjemline, K., and et al. (2013). Combined analysis of all three phases of solar neutrino data from the sudbury neutrino observatory. *Physical Review C*, 88(2). doi: [10.1103/physrevc.88.025501](https://doi.org/10.1103/physrevc.88.025501).
- Aharmim, B., Ahmed, S. N., Anthony, A. E., et al. (2020). A search for *hep* solar neutrinos and the diffuse supernova neutrino background using all three phases of the sudbury neutrino observatory. <https://arxiv.org/abs/2007.08018>.
- Aharmim, B., Ahmed, S. N., and Anthony and others (2013). Combined analysis of all three phases of solar neutrino data from the Sudbury Neutrino Observatory. *Phys. Rev. C*, 88(2):025501. doi: [10.1103/PhysRevC.88.025501](https://doi.org/10.1103/PhysRevC.88.025501).
- Ahmad, Q. R., Allen, R. C., Andersen, T. C., et al. (2002). Measurement of day and night neutrino energy spectra at sno and constraints on neutrino mixing parameters. *Phys. Rev. Lett.*, 89:011302. doi: [10.1103/PhysRevLett.89.011302](https://doi.org/10.1103/PhysRevLett.89.011302).
- Alimonti, G., Arpesella, C., Back, H., et al. (2009). The borexino detector at the laboratori nazionali del gran sasso. *Nuclear Instruments and Methods in Physics Research Section A: Accelerators, Spectrometers, Detectors and Associated Equipment*, 600(3):568–593. doi: [10.1016/j.nima.2008.11.076](https://doi.org/10.1016/j.nima.2008.11.076).

- Allen, C. W. (1963). *Astrophysical quantities*. London: University of London, Athlone Press, 1963, 2nd ed.
- Angulo, C., Arnould, M., Rayet, M., et al. (1999). A compilation of charged-particle induced thermonuclear reaction rates. *Nuclear Physics A*, 656:3–183. doi: [10.1016/S0375-9474\(99\)00030-5](https://doi.org/10.1016/S0375-9474(99)00030-5).
- Arcavi, I. et al. (2017). Optical emission from a kilonova following a gravitational-wave-detected neutron-star merger. *Nature*, 551:64. doi: [10.1038/nature24291](https://doi.org/10.1038/nature24291).
- Arcones, A. and Montes, F. (2011). Production of Light-element Primary Process Nuclei in Neutrino-driven Winds. *ApJ*, 731(1):5. doi: [10.1088/0004-637X/731/1/5](https://doi.org/10.1088/0004-637X/731/1/5).
- Arlandini, C., Käppeler, F., Wisshak, K., Gallino, R., Lugaro, M., Busso, M., and Straniero, O. (1999). Neutron Capture in Low-Mass Asymptotic Giant Branch Stars: Cross Sections and Abundance Signatures. *ApJ*, 525(2):886–900. doi: [10.1086/307938](https://doi.org/10.1086/307938).
- Asplund, M. (2005). New Light on Stellar Abundance Analyses: Departures from LTE and Homogeneity. *ARA&A*, 43:481–530. doi: [10.1146/annurev.astro.42.053102.134001](https://doi.org/10.1146/annurev.astro.42.053102.134001).
- Asplund, M., Grevesse, N., and Sauval, A. J. (2005). *The Solar Chemical Composition*, volume 336 of *Astronomical Society of the Pacific Conference Series*, page 25. Barnes, Thomas G., III and Bash, Frank N.
- Asplund, M., Grevesse, N., Sauval, A. J., and Scott, P. (2009). The Chemical Composition of the Sun. *ARA&A*, 47(1):481–522. doi: [10.1146/annurev.astro.46.060407.145222](https://doi.org/10.1146/annurev.astro.46.060407.145222).
- Atanasov, D., Ascher, P., Blaum, K., Cakirli, R. B., Cocolios, T. E., George, S., Goriely, S., Herfurth, F., Janka, H. T., Just, O., Kowalska, M., Kreim, S., Kisler, D., Litvinov, Y. A., Lunney, D., Manea, V., Neidherr, D., Rosenbusch, M., Schweikhard, L., Welker, A., Wienholtz, F., Wolf, R. N., and Zuber, K. (2015). Precision Mass Measurements of $^{Cd-131}_{129}$ and Their Impact on Stellar Nucleosynthesis via the Rapid Neutron Capture Process. *PhRvL*, 115(23):232501. doi: [10.1103/PhysRevLett.115.232501](https://doi.org/10.1103/PhysRevLett.115.232501).
- Bahcall, J. N. (1962). Beta Decay in Stellar Interiors. *PhRv*, 126:1143–1149. doi: [10.1103/PhysRev.126.1143](https://doi.org/10.1103/PhysRev.126.1143).
- Bahcall, J. N. (1994). ^7Be solar neutrino line: A reflection of the central temperature distribution of the Sun. *PhRvD*, 49(8):3923–3945. doi: [10.1103/PhysRevD.49.3923](https://doi.org/10.1103/PhysRevD.49.3923).
- Bahcall, J. N. (2002). The luminosity constraint on solar neutrino fluxes. *PhRvC*, 65(2):025801. doi: [10.1103/PhysRevC.65.025801](https://doi.org/10.1103/PhysRevC.65.025801).

- Bahcall, J. N., Basu, S., Pinsonneault, M., and Serenelli, A. M. (2005a). Helioseismological implications of recent solar abundance determinations. *ApJ*, 618(2):1049. <http://stacks.iop.org/0004-637X/618/i=2/a=1049>.
- Bahcall, J. N., Brown, L. S., Gruzinov, A., and Sawyer, R. F. (2002). The Salpeter plasma correction for solar fusion reactions. *A&A*, 383:291–295. doi: [10.1051/0004-6361:20011715](https://doi.org/10.1051/0004-6361:20011715).
- Bahcall, J. N., Huebner, W. F., Lubow, S. H., Parker, P. D., and Ulrich, R. K. (1982). Standard solar models and the uncertainties in predicted capture rates of solar neutrinos. *Reviews of Modern Physics*, 54:767–799. doi: [10.1103/RevModPhys.54.767](https://doi.org/10.1103/RevModPhys.54.767).
- Bahcall, J. N. and Krastev, P. I. (1996). How well do we (and will we) know solar neutrino fluxes and oscillation parameters? *PhRvD*, 53(8):4211–4225. doi: [10.1103/PhysRevD.53.4211](https://doi.org/10.1103/PhysRevD.53.4211).
- Bahcall, J. N. and Moeller, C. P. (1969). The ${}^7\text{Be}$ Electron-Capture Rate. *ApJ*, 155:511. doi: [10.1086/149887](https://doi.org/10.1086/149887).
- Bahcall, J. N. and Pinsonneault, M. H. (2004). What Do We (Not) Know Theoretically about Solar Neutrino Fluxes? *PhRvL*, 92(12):121301. doi: [10.1103/PhysRevLett.92.121301](https://doi.org/10.1103/PhysRevLett.92.121301).
- Bahcall, J. N., Pinsonneault, M. H., and Basu, S. (2001). Solar Models: Current Epoch and Time Dependences, Neutrinos, and Helioseismological Properties. *ApJ*, 555:990–1012. doi: [10.1086/321493](https://doi.org/10.1086/321493).
- Bahcall, J. N., Pinsonneault, M. H., and Wasserburg, G. J. (1995). Solar models with helium and heavy-element diffusion. *Reviews of Modern Physics*, 67(4):781–808. doi: [10.1103/RevModPhys.67.781](https://doi.org/10.1103/RevModPhys.67.781).
- Bahcall, J. N. and Serenelli, A. M. (2005). How Do Uncertainties in the Surface Chemical Composition of the Sun Affect the Predicted Solar Neutrino Fluxes? *ApJ*, 626:530–542. doi: [10.1086/429883](https://doi.org/10.1086/429883).
- Bahcall, J. N., Serenelli, A. M., and Basu, S. (2005b). New solar opacities, abundances, helioseismology, and neutrino fluxes. *The Astrophysical Journal Letters*, 621(1):L85. <http://stacks.iop.org/1538-4357/621/i=1/a=L85>.
- Bahcall, J. N., Serenelli, A. M., and Basu, S. (2006). 10,000 Standard Solar Models: A Monte Carlo Simulation. *ApJS*, 165:400–431. doi: [10.1086/504043](https://doi.org/10.1086/504043).
- Bahcall, J. N., Serenelli, A. M., and Pinsonneault, M. (2004). How Accurately Can We Calculate the Depth of the Solar Convective Zone? *ApJ*, 614:464–471. doi: [10.1086/423027](https://doi.org/10.1086/423027).
- Bahcall, J. N. and Ulmer, A. (1996). Temperature dependence of solar neutrino fluxes. *Phys. Rev. D*, 53:4202–4210. doi: [10.1103/PhysRevD.53.4202](https://doi.org/10.1103/PhysRevD.53.4202).

- Bahcall, J. N. and Ulrich, R. K. (1988). Solar models, neutrino experiments, and helioseismology. *Reviews of Modern Physics*, 60(2):297–372. doi: [10.1103/RevModPhys.60.297](https://doi.org/10.1103/RevModPhys.60.297).
- Baker, R. G. A., Schönbachler, M., Rehkämper, M., Williams, H. M., and Halliday, A. N. (2010). The thallium isotope composition of carbonaceous chondrites — New evidence for live ^{205}Pb in the early solar system. *Earth and Planetary Science Letters*, 291(1-4):39–47. doi: [10.1016/j.epsl.2009.12.044](https://doi.org/10.1016/j.epsl.2009.12.044).
- Banerjee, P., Qian, Y.-Z., Heger, A., and Haxton, W. C. (2016). Evidence from stable isotopes and ^{10}Be for solar system formation triggered by a low-mass supernova. *Nature Communications*, 7:13639. doi: [10.1038/ncomms13639](https://doi.org/10.1038/ncomms13639).
- Bao, Z. Y., Beer, H., Käppeler, F., Voss, F., Wisshak, K., and Rauscher, T. (2000). Neutron Cross Sections for Nucleosynthesis Studies. *Atomic Data and Nuclear Data Tables*, 76(1):70–154. doi: [10.1006/adnd.2000.0838](https://doi.org/10.1006/adnd.2000.0838).
- Barzyk, J. G., Savina, M. R., Davis, A. M., Gallino, R., Gyngard, F., Amari, S., Zinner, E., Pellin, M. J., Lewis, R. S., and Clayton, R. N. (2007). Constraining the ^{13}C neutron source in agb stars through isotopic analysis of trace elements in presolar sic. *Meteoritics & Planetary Science*, 42(7-8):1103–1119. doi: [10.1111/j.1945-5100.2007.tb00563.x](https://doi.org/10.1111/j.1945-5100.2007.tb00563.x).
- Basu, S. and Antia, H. M. (2004). Constraining Solar Abundances Using Helioseismology. *ApJL*, 606(1):L85–L88. doi: [10.1086/421110](https://doi.org/10.1086/421110).
- Battino, U., Pignatari, M., Ritter, C., Herwig, F., Denisenkov, P., Den Hartogh, J. W., Trappitsch, R., Hirschi, R., Freytag, B., Thielemann, F., and Paxton, B. (2016). Application of a Theory and Simulation-based Convective Boundary Mixing Model for AGB Star Evolution and Nucleosynthesis. *ApJ*, 827(1):30. doi: [10.3847/0004-637X/827/1/30](https://doi.org/10.3847/0004-637X/827/1/30).
- Battino, U., Tattersall, A., Lederer-Woods, C., Herwig, F., Denissenkov, P., Hirschi, R., Trappitsch, R., den Hartogh, J. W., Pignatari, M., and NuGrid Collaboration (2019). NuGrid stellar data set - III. Updated low-mass AGB models and s-process nucleosynthesis with metallicities $Z=0.01$, $Z=0.02$, and $Z=0.03$. *MNRAS*, 489(1):1082–1098. doi: [10.1093/mnras/stz2158](https://doi.org/10.1093/mnras/stz2158).
- Bauswein, A., Goriely, S., and Janka, H. T. (2013). Systematics of Dynamical Mass Ejection, Nucleosynthesis, and Radioactively Powered Electromagnetic Signals from Neutron-star Mergers. *ApJ*, 773(1):78. doi: [10.1088/0004-637X/773/1/78](https://doi.org/10.1088/0004-637X/773/1/78).
- Becker, S. A. and Iben, I., J. (1979). The asymptotic giant branch evolution of intermediate-mass stars as a function of mass and composition. I. Through the second dredge-up phase. *ApJ*, 232:831–853. doi: [10.1086/157345](https://doi.org/10.1086/157345).

- Beer, H., Sedyshev, P. V., Rochow, W., Rauscher, T., and Mohr, P. (2002). Neutron capture of ^{30}Si . *NuPhA*, 709(1):453–466. doi: [10.1016/S0375-9474\(02\)01030-8](https://doi.org/10.1016/S0375-9474(02)01030-8).
- Bellerive, A., Klein, J., McDonald, A., Noble, A., and Poon, A. (2016). The sudbury neutrino observatory. *Nuclear Physics B*, 908:30 – 51. Neutrino Oscillations: Celebrating the Nobel Prize in Physics 2015, doi: <https://doi.org/10.1016/j.nuclphysb.2016.04.035>.
- Bellini, G., Benziger, J., Bick, D., et al. (2014). Neutrinos from the primary proton-proton fusion process in the Sun. *Nature*, 512(7515):383–386. doi: [10.1038/nature13702](https://doi.org/10.1038/nature13702).
- Bergström, J., Gonzalez-Garcia, M. C., Maltoni, M., Peña-Garay, C., Serenelli, A. M., and Song, N. (2016). Updated determination of the solar neutrino fluxes from solar neutrino data. *Journal of High Energy Physics*, 2016(3). doi: [10.1007/jhep03\(2016\)132](https://doi.org/10.1007/jhep03(2016)132).
- Bernuzzi, S., Breschi, M., Daszuta, B., Endrizzi, A., Logoteta, D., Nedora, V., Perego, A., Radice, D., Schianchi, F., Zappa, F., Bombaci, I., and Ortiz, N. (2020). Accretion-induced prompt black hole formation in asymmetric neutron star mergers, dynamical ejecta and kilonova signals. *MNRAS*. doi: [10.1093/mnras/staa1860](https://doi.org/10.1093/mnras/staa1860).
- Best, A., Beard, M., Görres, J., et al. (2013). Measurement of the reaction $^{17}\text{O}(\alpha, n)^{20}\text{Ne}$ and its impact on the *s* process in massive stars. *Phys. Rev. C*, 87:045805. doi: [10.1103/PhysRevC.87.045805](https://doi.org/10.1103/PhysRevC.87.045805).
- Best, A., Falahat, S., Görres, J., Couder, M., deBoer, R., Güray, R. T., Kontos, A., Kratz, K. L., LeBlanc, P. J., Li, Q., O’Brien, S., Özkan, N., Sonnabend, K., Talwar, R., Uberseder, E., and Wiescher, M. (2013). Measurement of the reaction $^{18}\text{O}(\alpha, n)^{21}\text{Ne}$. *PhRvC*, 87(4):045806. doi: [10.1103/PhysRevC.87.045806](https://doi.org/10.1103/PhysRevC.87.045806).
- Best, A., Pantaleo, F. R., Boeltzig, A., et al. (2019). Cross section of the reaction $^{18}\text{O}(p, \gamma)^{19}\text{F}$ at astrophysical energies: The 90 keV resonance and the direct capture component. *Physics Letters B*, 797:134900. doi: [10.1016/j.physletb.2019.134900](https://doi.org/10.1016/j.physletb.2019.134900).
- Bisterzo, S., Gallino, R., Käppeler, F., Wiescher, M., Imbriani, G., Straniero, O., Cristallo, S., Görres, J., and deBoer, R. J. (2015). The branchings of the main *s*-process: their sensitivity to α -induced reactions on ^{13}C and ^{22}Ne and to the uncertainties of the nuclear network. *MNRAS*, 449(1):506–527. doi: [10.1093/mnras/stv271](https://doi.org/10.1093/mnras/stv271).
- Bisterzo, S., Travaglio, C., Gallino, R., Wiescher, M., and Käppeler, F. (2014). Galactic Chemical Evolution and Solar *s*-process Abundances: Dependence on the ^{13}C -pocket Structure. *ApJ*, 787(1):10. doi: [10.1088/0004-637X/787/1/10](https://doi.org/10.1088/0004-637X/787/1/10).

- Boger, J., Hahn, R., Rowley, J., Carter, A., Hollebhone, B., Kessler, D., Blevis, I., Dalnoki-Veress, F., DeKok, A., Farine, J., and et al. (2000). The sudbury neutrino observatory. *Nuclear Instruments and Methods in Physics Research Section A: Accelerators, Spectrometers, Detectors and Associated Equipment*, 449(1-2):172–207. doi: [10.1016/S0168-9002\(99\)01469-2](https://doi.org/10.1016/S0168-9002(99)01469-2).
- Böhm-Vitense, E. (1958). Über die Wasserstoffkonvektionszone in Sternen verschiedener Effektivtemperaturen und Leuchtkräfte. Mit 5 Textabbildungen. *ZA*, 46:108.
- Bojazi, M. J. and Meyer, B. S. (2017). Short-Lived Radioactivities in the Context of Full Galactic Chemical Evolution. In *Lunar and Planetary Science Conference*, Lunar and Planetary Science Conference, page 3010.
- Bojazi, M. J. and Meyer, B. S. (2018). Neutron Star Mergers and the Short-Lived r-Process Radioactivities. In *Lunar and Planetary Science Conference*, Lunar and Planetary Science Conference, page 2890.
- Bombaci, I. and Logoteta, D. (2018). Equation of state of dense nuclear matter and neutron star structure from nuclear chiral interactions. *A&A*, 609:A128. doi: [10.1051/0004-6361/201731604](https://doi.org/10.1051/0004-6361/201731604).
- Bondarenko, V. et al. (2002). Interplay of quasiparticle and phonon excitations in ^{181}Hf observed through (n, γ) and $(d \rightarrow \alpha, p)$ reactions. *Nucl. Phys. A*, 709:3–59. doi: [10.1016/S0375-9474\(02\)00646-2](https://doi.org/10.1016/S0375-9474(02)00646-2).
- Boss, A. P. (2003). Triggered Collapse, Magnetic Fields, and Very Low Mass Star Formation (Invited Review). In De Buizer, J. M. and van der Bliek, N. S., editors, *Galactic Star Formation Across the Stellar Mass Spectrum*, volume 287 of *Astronomical Society of the Pacific Conference Series*, pages 281–291.
- Boss, A. P. (2017). Triggering Collapse of the Presolar Dense Cloud Core and Injecting Short-lived Radioisotopes with a Shock Wave. V. Nonisothermal Collapse Regime. *ApJ*, 844(2):113. doi: [10.3847/1538-4357/aa7cf4](https://doi.org/10.3847/1538-4357/aa7cf4).
- Bovard, L., Martin, D., Guercilena, F., Arcones, A., Rezzolla, L., and Korobkin, O. (2017). r-process nucleosynthesis from matter ejected in binary neutron star mergers. *Phys. Rev.*, D96(12):124005. doi: [10.1103/PhysRevD.96.124005](https://doi.org/10.1103/PhysRevD.96.124005).
- Boyle, A., Sim, S. A., Hachinger, S., and Kerzendorf, W. (2017). Helium in double-detonation models of type Ia supernovae. *A&A*, 599:A46. doi: [10.1051/0004-6361/201629712](https://doi.org/10.1051/0004-6361/201629712).
- Braithwaite, J. and Spruit, H. C. (2017). Magnetic fields in non-convective regions of stars. *Royal Society Open Science*, 4(2):160271. doi: [10.1098/rsos.160271](https://doi.org/10.1098/rsos.160271).
- Branch, D. and Wheeler, J. C. (2017). *Supernova Explosions*. Springer Berlin Heidelberg. doi: [10.1007/978-3-662-55054-0](https://doi.org/10.1007/978-3-662-55054-0).

- Brege, W., Duez, M. D., Foucart, F., Deaton, M. B., Caro, J., Hemberger, D. A., Kidder, L. E., O'Connor, E., Pfeiffer, H. P., and Scheel, M. A. (2018). Black hole-neutron star mergers using a survey of finite-temperature equations of state. *PhRvD*, 98(6):063009. doi: [10.1103/PhysRevD.98.063009](https://doi.org/10.1103/PhysRevD.98.063009).
- Brennecka, G. A., Weyer, S., Wadhwa, M., Janney, P. E., Zipfel, J., and Anbar, A. D. (2010). $^{238}\text{U}/^{235}\text{U}$ Variations in Meteorites: Extant ^{247}Cm and Implications for Pb-Pb Dating. *Science*, 327(5964):449. doi: [10.1126/science.1180871](https://doi.org/10.1126/science.1180871).
- Brown, L. S. and Sawyer, R. F. (1997). Nuclear Electron Capture in a Plasma. *ApJ*, 489:968–975. doi: [10.1086/304828](https://doi.org/10.1086/304828).
- Bruno, C. G., Aliotta, M., Descouvemont, P., et al. (2019). Improved astrophysical rate for the $^{18}\text{O}(p,\alpha)^{15}\text{N}$ reaction by underground measurements. *Physics Letters B*, 790:237–242. doi: [10.1016/j.physletb.2019.01.017](https://doi.org/10.1016/j.physletb.2019.01.017).
- Bruno, C. G., Scott, D. A., Aliotta, M., et al. (2016). Improved direct measurement of the 64.5 keV resonance strength in the $^{17}\text{O}(p,\alpha)^{14}\text{N}$ reaction at luna. *Phys. Rev. Lett.*, 117:142502. doi: [10.1103/PhysRevLett.117.142502](https://doi.org/10.1103/PhysRevLett.117.142502).
- Buckner, M. Q., Iliadis, C., Cesaratto, J. M., Howard, C., Clegg, T. B., Champagne, A. E., and Daigle, S. (2012). Thermonuclear reaction rate of $^{18}\text{O}(p,\gamma)^{19}\text{F}$. *Phys. Rev. C*, 86:065804. doi: [10.1103/PhysRevC.86.065804](https://doi.org/10.1103/PhysRevC.86.065804).
- Buckner, M. Q., Iliadis, C., Kelly, K. J., Downen, L. N., Champagne, A. E., Cesaratto, J. M., Howard, C., and Longland, R. (2015). High-intensity-beam study of $^{17}\text{O}(p,\gamma)^{18}\text{F}$ and thermonuclear reaction rates for $^{17}\text{O} + p$. *Phys. Rev. C*, 91:015812. doi: [10.1103/PhysRevC.91.015812](https://doi.org/10.1103/PhysRevC.91.015812).
- Burkhardt, C., Kleine, T., Bourdon, B., Palme, H., Zipfel, J., Friedrich, J. M., and Ebel, D. S. (2008). Hf W mineral isochron for Ca,Al-rich inclusions: Age of the solar system and the timing of core formation in planetesimals. *GeoCoA*, 72(24):6177–6197. doi: [10.1016/j.gca.2008.10.023](https://doi.org/10.1016/j.gca.2008.10.023).
- Busso, M. (2011). The early solar system. In Diehl, R., Hartmann, D. H., and Prantzos, N., editors, *Astronomy with Radioactivities*, pages 309–344. Springer Berlin Heidelberg, Berlin, Heidelberg. doi: [10.1007/978-3-642-12698-7_6](https://doi.org/10.1007/978-3-642-12698-7_6).
- Busso, M. (2018). The early solar system. In Diehl, R., Hartmann, D. H., and Prantzos, N., editors, *Astrophysics with Radioactive Isotopes*, pages 379–425. Springer International Publishing, Cham. doi: [10.1007/978-3-319-91929-4_6](https://doi.org/10.1007/978-3-319-91929-4_6).
- Busso, M., Gallino, R., Lambert, D. L., Travaglio, C., and Smith, V. V. (2001). Nucleosynthesis and Mixing on the Asymptotic Giant Branch. III. Predicted and Observed s-Process Abundances. *ApJ*, 557(2):802–821. doi: [10.1086/322258](https://doi.org/10.1086/322258).

- Busso, M., Gallino, R., and Wasserburg, G. J. (1999). Nucleosynthesis in Asymptotic Giant Branch Stars: Relevance for Galactic Enrichment and Solar System Formation. *ARA&A*, 37:239–309. doi: [10.1146/annurev.astro.37.1.239](https://doi.org/10.1146/annurev.astro.37.1.239).
- Busso, M., Gallino, R., and Wasserburg, G. J. (2003). Short-Lived Nuclei in the Early Solar System: A Low Mass Stellar Source? *PASA*, 20(4):356–370. doi: [10.1071/AS03035](https://doi.org/10.1071/AS03035).
- Busso, M., Palmerini, S., Maiorca, E., Cristallo, S., Straniero, O., Abia, C., Gallino, R., and La Cognata, M. (2010). On the Need for Deep-mixing in Asymptotic Giant Branch Stars of Low Mass. *ApJL*, 717(1):L47–L51. doi: [10.1088/2041-8205/717/1/L47](https://doi.org/10.1088/2041-8205/717/1/L47).
- Busso, M., Vescovi, D., Palmerini, S., Cristallo, S., and Antonuccio Delogu, V. (2020). s-Processing in AGB Stars Revisited. III. Neutron captures from MHD mixing at different metallicities and observational constraints. *arXiv e-prints*, page arXiv:2011.07469. <https://arxiv.org/abs/2011.07469>.
- Busso, M., Wasserburg, G. J., Nollett, K. M., and Calandra, A. (2007). Can Extra Mixing in RGB and AGB Stars Be Attributed to Magnetic Mechanisms? *ApJ*, 671(1):802–810. doi: [10.1086/522616](https://doi.org/10.1086/522616).
- Buzzoni, A., Patelli, L., Bellazzini, M., Pecci, F. F., and Oliva, E. (2010). Bolometric correction and spectral energy distribution of cool stars in Galactic clusters. *MNRAS*, 403(3):1592–1610. doi: [10.1111/j.1365-2966.2009.16223.x](https://doi.org/10.1111/j.1365-2966.2009.16223.x).
- Caffau, E., Ludwig, H. G., Steffen, M., Freytag, B., and Bonifacio, P. (2011). Solar Chemical Abundances Determined with a CO5BOLD 3D Model Atmosphere. *SoPh*, 268(2):255–269. doi: [10.1007/s11207-010-9541-4](https://doi.org/10.1007/s11207-010-9541-4).
- Cameron, A. G. W., Thielemann, F. K., and Cowan, J. J. (1993). s- and r-process contributions to extinct radioactivities. *PhR*, 227(1-5):283–291. doi: [10.1016/0370-1573\(93\)90073-M](https://doi.org/10.1016/0370-1573(93)90073-M).
- Cameron, A. G. W. and Truran, J. W. (1977). The Supernova Trigger for Formation of the Solar System. *Icarus*, 30(3):447–461. doi: [10.1016/0019-1035\(77\)90101-4](https://doi.org/10.1016/0019-1035(77)90101-4).
- Cesaratto, J. M., Champagne, A. E., Buckner, M. Q., Clegg, T. B., Daigle, S., Howard, C., Iliadis, C., Longland, R., Newton, J. R., and Oginni, B. M. (2013). Measurement of the $E_r^{c.m.} = 138$ keV resonance in the $^{23}\text{Na}(p,\gamma)^{24}\text{Mg}$ reaction and the abundance of sodium in agb stars. *Phys. Rev. C*, 88:065806. doi: [10.1103/PhysRevC.88.065806](https://doi.org/10.1103/PhysRevC.88.065806).
- Charbonnel, C. and Lagarde, N. (2010). Thermohaline instability and rotation-induced mixing. I. Low- and intermediate-mass solar metallicity stars up to the end of the AGB. *A&A*, 522:A10. doi: [10.1051/0004-6361/201014432](https://doi.org/10.1051/0004-6361/201014432).

- Charbonnel, C. and Zahn, J. P. (2007). Inhibition of thermohaline mixing by a magnetic field in Ap star descendants: implications for the Galactic evolution of ^3He . *A&A*, 476(3):L29–L32. doi: [10.1051/0004-6361:20078740](https://doi.org/10.1051/0004-6361:20078740).
- Chaussidon, M., Robert, F., and McKeegan, K. D. (2006). Li and B isotopic variations in an Allende CAI: Evidence for the in situ decay of short-lived ^{10}Be and for the possible presence of the short-lived nuclide ^7Be in the early solar system. *GeoCoA*, 70(1):224–245. doi: [10.1016/j.gca.2005.08.016](https://doi.org/10.1016/j.gca.2005.08.016).
- Chieffi, A., Domínguez, I., Limongi, M., and Straniero, O. (2001). Evolution and Nucleosynthesis of Zero-Metal Intermediate-Mass Stars. *ApJ*, 554(2):1159–1174. doi: [10.1086/321387](https://doi.org/10.1086/321387).
- Chieffi, A. and Limongi, M. (2013). Pre-supernova Evolution of Rotating Solar Metallicity Stars in the Mass Range 13-120 M_{\odot} and their Explosive Yields. *ApJ*, 764(1):21. doi: [10.1088/0004-637X/764/1/21](https://doi.org/10.1088/0004-637X/764/1/21).
- Chieffi, A. and Limongi, M. (2015). The advanced phases of massive stars and the explosive yields. In Meynet, G., Georgy, C., Groh, J., and Stee, P., editors, *New Windows on Massive Stars*, volume 307 of *IAU Symposium*, pages 1–8. doi: [10.1017/S174392131400619X](https://doi.org/10.1017/S174392131400619X).
- Christensen-Dalsgaard, J. (2020). Solar structure and evolution. *arXiv e-prints*, page arXiv:2007.06488. <https://arxiv.org/abs/2007.06488>.
- Christensen-Dalsgaard, J., di Mauro, M. P., Houdek, G., and Pijpers, F. (2009). On the opacity change required to compensate for the revised solar composition. *A&A*, 494(1):205–208. doi: [10.1051/0004-6361:200810170](https://doi.org/10.1051/0004-6361:200810170).
- Clayton, R. N. (2003). Oxygen Isotopes in Meteorites. *Treatise on Geochemistry*, 1:711. doi: [10.1016/B0-08-043751-6/01063-X](https://doi.org/10.1016/B0-08-043751-6/01063-X).
- Cleveland, B. T., Daily, T., Davis, Raymond, J., Distel, J. R., Lande, K., Lee, C. K., Wildenhain, P. S., and Ullman, J. (1998). Measurement of the Solar Electron Neutrino Flux with the Homestake Chlorine Detector. *ApJ*, 496(1):505–526. doi: [10.1086/305343](https://doi.org/10.1086/305343).
- Colonna, N., Gusing, F., and Käppeler, F. (2018). Neutron physics with accelerators. *Progress in Particle and Nuclear Physics*, 101:177 – 203. doi: <https://doi.org/10.1016/j.pnpnp.2018.02.002>.
- Colonna, N., Tsinganis, A., Vlastou, R., Patronis, N., Diakaki, M., Amaducci, S., Barbagallo, M., Bennett, S., Berthoumieux, E., Bacak, M., Cosentino, G., Cristallo, S., Finocchiaro, P., Heyse, J., Lewis, D., Manna, A., Massimi, C., Mendoza, E., Mirea, M., Moens, A., Nolte, R., Pirovano, E., Sabaté-Gilarte, M., Sibbens, G., Smith, A. G., Sosnin, N., Stamatopoulos, A., Tarrío, D., Tassan-Got, L., Vanleeuw, D., Ventura, A., Vescovi, D., Wright, T., Žugec, P., and n TOF Collaboration (2020). The fission experimental programme at the

- CERN n_TOF facility: status and perspectives. *European Physical Journal A*, 56(2):48. doi: [10.1140/epja/s10050-020-00037-8](https://doi.org/10.1140/epja/s10050-020-00037-8).
- Costantini, H., deBoer, R. J., Azuma, R. E., Couder, M., Görres, J., Hammer, J. W., LeBlanc, P. J., Lee, H. Y., O'Brien, S., Palumbo, A., Simpson, E. C., Stech, E., Tan, W., Uberseder, E., and Wiescher, M. (2010). $^{16}\text{O}(\alpha, \gamma)^{20}\text{Ne}$ s factor: Measurements and r -matrix analysis. *Phys. Rev. C*, 82:035802. doi: [10.1103/PhysRevC.82.035802](https://doi.org/10.1103/PhysRevC.82.035802).
- Coulter, D. A. et al. (2017). Swope Supernova Survey 2017a (SSS17a), the Optical Counterpart to a Gravitational Wave Source. *Science*. [Science358,1556(2017)], doi: [10.1126/science.aap9811](https://doi.org/10.1126/science.aap9811).
- Cowan, J. J., Sneden, C., Lawler, J. E., Aprahamian, A., Wiescher, M., Langanke, K., Martínez-Pinedo, G., and Thielemann, F.-K. (2019). Origin of the Heaviest Elements: the Rapid Neutron-Capture Process. *arXiv e-prints*, page arXiv:1901.01410. <https://arxiv.org/abs/1901.01410>.
- Cox, J. P. and Giuli, R. T. (1968). *Principles of stellar structure*. Gordon and Breach.
- Cravens, J. P., Abe, K., Iida, T., et al. (2008). Solar neutrino measurements in Super-Kamiokande-II. *PhRvD*, 78(3):032002. doi: [10.1103/PhysRevD.78.032002](https://doi.org/10.1103/PhysRevD.78.032002).
- Cristallo, S., Abia, C., Straniero, O., and Piersanti, L. (2015a). On the Need for the Light Elements Primary Process (LEPP). *ApJ*, 801(1):53. doi: [10.1088/0004-637X/801/1/53](https://doi.org/10.1088/0004-637X/801/1/53).
- Cristallo, S., Karinkuzhi, D., Goswami, A., Piersanti, L., and Gobrecht, D. (2016). Constraints of the Physics of Low-mass AGB Stars from CH and CEMP Stars. *ApJ*, 833(2):181. doi: [10.3847/1538-4357/833/2/181](https://doi.org/10.3847/1538-4357/833/2/181).
- Cristallo, S., La Cognata, M., Massimi, C., Best, A., Palmerini, S., Straniero, O., Trippella, O., Busso, M., Ciani, G. F., Mingrone, F., Piersanti, L., and Vescovi, D. (2018). The Importance of the $^{13}\text{C}(\alpha, n)^{16}\text{O}$ Reaction in Asymptotic Giant Branch Stars. *ApJ*, 859(2):105. doi: [10.3847/1538-4357/aac177](https://doi.org/10.3847/1538-4357/aac177).
- Cristallo, S., Nanni, A., Cescutti, G., Minchev, I., Liu, N., Vescovi, D., Gobrecht, D., and Piersanti, L. (2020). Mass and metallicity distribution of parent AGB stars of presolar SiC. *A&A*, 644:A8. doi: [10.1051/0004-6361/202039492](https://doi.org/10.1051/0004-6361/202039492).
- Cristallo, S., Piersanti, L., Straniero, O., Gallino, R., Domínguez, I., Abia, C., Di Rico, G., Quintini, M., and Bisterzo, S. (2011). Evolution, Nucleosynthesis, and Yields of Low-mass Asymptotic Giant Branch Stars at Different Metallicities. II. The FRUITY Database. *ApJS*, 197:17. doi: [10.1088/0067-0049/197/2/17](https://doi.org/10.1088/0067-0049/197/2/17).

- Cristallo, S., Straniero, O., Gallino, R., Piersanti, L., Domínguez, I., and Lederer, M. T. (2009). Evolution, Nucleosynthesis, and Yields of Low-Mass Asymptotic Giant Branch Stars at Different Metallicities. *ApJ*, 696:797–820. doi: [10.1088/0004-637X/696/1/797](https://doi.org/10.1088/0004-637X/696/1/797).
- Cristallo, S., Straniero, O., Lederer, M. T., and Aringer, B. (2007). Molecular Opacities for Low-Mass Metal-poor AGB Stars Undergoing the Third Dredge-up. *ApJ*, 667(1):489–496. doi: [10.1086/520833](https://doi.org/10.1086/520833).
- Cristallo, S., Straniero, O., Piersanti, L., and Gobrecht, D. (2015b). Evolution, Nucleosynthesis, and Yields of AGB Stars at Different Metallicities. III. Intermediate-mass Models, Revised Low-mass Models, and the ph-FRUITY Interface. *ApJS*, 219(2):40. doi: [10.1088/0067-0049/219/2/40](https://doi.org/10.1088/0067-0049/219/2/40).
- Cristallo, S. and Vescovi, D. (2019). Nuclear astrophysics at the n_TOF facility: Some key cases in low mass star evolution and Neutron Star Mergers. *Nuovo Cim. C*, 42(2-3-3):117. doi: [10.1393/ncc/i2019-19117-7](https://doi.org/10.1393/ncc/i2019-19117-7).
- Cyburt, R. H., Amthor, A. M., Ferguson, R., Meisel, Z., Smith, K., Warren, S., Heger, A. e., Hoffman, R. D., Rauscher, T., Sakharuk, A. e., Schatz, H., Thielemann, F. K., and Wiescher, M. (2010). The JINA REACLIB Database: Its Recent Updates and Impact on Type-I X-ray Bursts. *ApJS*, 189(1):240–252. doi: [10.1088/0067-0049/189/1/240](https://doi.org/10.1088/0067-0049/189/1/240).
- D’Agata, G., Pizzone, R. G., La Cognata, M., Indelicato, I., Spitaleri, C., Palmerini, S., Trippella, O., Vescovi, D., et al. (2018). The $^{19}\text{F}(\alpha, p)^{22}\text{Ne}$ Reaction at Energies of Astrophysical Relevance by Means of the Trojan Horse Method and Its Implications in AGB Stars. *ApJ*, 860:61. doi: [10.3847/1538-4357/aac207](https://doi.org/10.3847/1538-4357/aac207).
- Dauphas, N., John, S. G., and Rouxel, O. (2017). Iron Isotope Systematics. *Reviews in Mineralogy and Geochemistry*, 82(1):415–510. doi: [10.2138/rmg.2017.82.11](https://doi.org/10.2138/rmg.2017.82.11).
- Dauphas, N. and Schauble, E. A. (2016). Mass Fractionation Laws, Mass-Independent Effects, and Isotopic Anomalies. *Annual Review of Earth and Planetary Sciences*, 44:709–783. doi: [10.1146/annurev-earth-060115-012157](https://doi.org/10.1146/annurev-earth-060115-012157).
- Davies, M. B., Adams, F. C., Armitage, P., Chambers, J., Ford, E., Morbidelli, A., Raymond, S. N., and Veras, D. (2014). The Long-Term Dynamical Evolution of Planetary Systems. In Beuther, H., Klessen, R. S., Dullemond, C. P., and Henning, T., editors, *Protostars and Planets VI*, page 787. doi: [10.2458/azu_uapress_9780816531240-ch034](https://doi.org/10.2458/azu_uapress_9780816531240-ch034).
- Davis, A. and McKeegan, K. (2014). 1.11 - short-lived radionuclides and early solar system chronology. In Holland, H. D. and Turekian, K. K., editors, *Treatise on Geochemistry (Second Edition)*, pages 361 – 395. Elsevier, Oxford, second edition edition. doi: <https://doi.org/10.1016/B978-0-08-095975-7.00113-3>.

- Davis, R., Harmer, D. S., and Hoffman, K. C. (1968). Search for Neutrinos from the Sun. *PhRvL*, 20(21):1205–1209. doi: [10.1103/PhysRevLett.20.1205](https://doi.org/10.1103/PhysRevLett.20.1205).
- den Hartogh, J. W., Eggenberger, P., and Hirschi, R. (2019a). Constraining transport of angular momentum in stars. Combining asteroseismic observations of core helium burning stars and white dwarfs. *A&A*, 622:A187. doi: [10.1051/0004-6361/201834330](https://doi.org/10.1051/0004-6361/201834330).
- den Hartogh, J. W., Hirschi, R., Lugaro, M., Doherty, C. L., Battino, U., Herwig, F., Pignatari, M., and Eggenberger, P. (2019b). The s process in rotating low-mass AGB stars. Nucleosynthesis calculations in models matching asteroseismic constraints. *A&A*, 629:A123. doi: [10.1051/0004-6361/201935476](https://doi.org/10.1051/0004-6361/201935476).
- Denissenkov, P. A., Herwig, F., Truran, J. W., and Paxton, B. (2013). The C-flame Quenching by Convective Boundary Mixing in Super-AGB Stars and the Formation of Hybrid C/O/Ne White Dwarfs and SN Progenitors. *ApJ*, 772(1):37. doi: [10.1088/0004-637X/772/1/37](https://doi.org/10.1088/0004-637X/772/1/37).
- Denissenkov, P. A. and Merryfield, W. J. (2011). Thermohaline Mixing: Does it Really Govern the Atmospheric Chemical Composition of Low-mass Red Giants? *ApJL*, 727(1):L8. doi: [10.1088/2041-8205/727/1/L8](https://doi.org/10.1088/2041-8205/727/1/L8).
- Denissenkov, P. A., Pinsonneault, M., and MacGregor, K. B. (2009). Magneto-Thermohaline Mixing in Red Giants. *ApJ*, 696(2):1823–1833. doi: [10.1088/0004-637X/696/2/1823](https://doi.org/10.1088/0004-637X/696/2/1823).
- Denissenkov, P. A. and Tout, C. A. (2003). Partial mixing and formation of the ^{13}C pocket by internal gravity waves in asymptotic giant branch stars. *MNRAS*, 340(3):722–732. doi: [10.1046/j.1365-8711.2003.06284.x](https://doi.org/10.1046/j.1365-8711.2003.06284.x).
- Depalo, R., Cavanna, F., Aliotta, M., et al. (2016). Direct measurement of low-energy $^{22}\text{Ne}(p, \gamma)^{23}\text{Na}$ resonances. *Phys. Rev. C*, 94(5):055804. doi: [10.1103/PhysRevC.94.055804](https://doi.org/10.1103/PhysRevC.94.055804).
- Di Leva, A., Scott, D. A., Cacioli, A., Formicola, A., et al. (2014). Underground study of the $^{17}\text{O}(p, \gamma)^{18}\text{F}$ reaction relevant for explosive hydrogen burning. *Phys. Rev. C*, 89:015803. doi: [10.1103/PhysRevC.89.015803](https://doi.org/10.1103/PhysRevC.89.015803).
- Diehl, R., Haloïn, H., Kretschmer, K., Lichti, G. G., Schönfelder, V., Strong, A. W., von Kienlin, A., Wang, W., Jean, P., Knödseder, J., Roques, J.-P., Weidenspointner, G., Schanne, S., Hartmann, D. H., Winkler, C., and Wunderer, C. (2006). Radioactive ^{26}Al from massive stars in the Galaxy. *Nature*, 439(7072):45–47. doi: [10.1038/nature04364](https://doi.org/10.1038/nature04364).
- Dillmann, I. (2014). The new KADoNiS v1.0 and its influence on the s-process. In *XIII Nuclei in the Cosmos (NIC XIII)*, page 57.

- Dillmann, I., Domingo-Pardo, C., Heil, M., Käppeler, F., Wallner, A., Forstner, O., Golser, R., Kutschera, W., Priller, A., Steier, P., Mengoni, A., Gallino, R., Paul, M., and Vockenhuber, C. (2009). Determination of the stellar (n,γ) cross section of Ca40 with accelerator mass spectrometry. *PhRvC*, 79(6):065805. doi: [10.1103/PhysRevC.79.065805](https://doi.org/10.1103/PhysRevC.79.065805).
- Dillmann, I., Domingo-Pardo, C., Heil, M., Käppeler, F., Walter, S., Dababneh, S., Rauscher, T., and Thielemann, F. K. (2010). Stellar (n,γ) cross sections of p-process isotopes Part I: Pd102, Te120, Ba130,132, and Dy156. *PhRvC*, 81(1):015801. doi: [10.1103/PhysRevC.81.015801](https://doi.org/10.1103/PhysRevC.81.015801).
- Dillmann, I., Kratz, K. L., Wöhr, A., Arndt, O., Brown, B. A., Hoff, P., Hjorth-Jensen, M., Köster, U., Ostrowski, A. N., Pfeiffer, B., Seweryniak, D., Shergur, J., and Walters, W. B. (2003). N=82 Shell Quenching of the Classical r-Process “Waiting-Point” Nucleus ^{130}Cd . *PhRvL*, 91(16):162503. doi: [10.1103/PhysRevLett.91.162503](https://doi.org/10.1103/PhysRevLett.91.162503).
- Dillmann, I., Plag, R., Käppeler, F., and Rauscher, T. (2009). Efnudat fast neutrons-scientific workshop on neutron measurements, theory & applications. *JRC-IRMM*, online at <http://www.kadonis.org>.
- Doherty, C. L., Gil-Pons, P., Siess, L., and Lattanzio, J. C. (2017). Super-AGB Stars and their Role as Electron Capture Supernova Progenitors. *PASA*, 34:e056. doi: [10.1017/pasa.2017.52](https://doi.org/10.1017/pasa.2017.52).
- Domingo-Pardo, C., Abbondanno, U., Aerts, G., et al. (2006a). New measurement of neutron capture resonances in Bi209. *PhRvC*, 74(2):025807. doi: [10.1103/PhysRevC.74.025807](https://doi.org/10.1103/PhysRevC.74.025807).
- Domingo-Pardo, C., Abbondanno, U., Aerts, G., et al. (2006b). Resonance capture cross section of Pb207. *PhRvC*, 74(5):055802. doi: [10.1103/PhysRevC.74.055802](https://doi.org/10.1103/PhysRevC.74.055802).
- Domingo-Pardo, C., Abbondanno, U., Aerts, G., et al. (2007a). Measurement of the neutron capture cross section of the s-only isotope Pb204 from 1 eV to 440 keV. *PhRvC*, 75(1):015806. doi: [10.1103/PhysRevC.75.015806](https://doi.org/10.1103/PhysRevC.75.015806).
- Domingo-Pardo, C., Abbondanno, U., Aerts, G., et al. (2007b). Measurement of the radiative neutron capture cross section of Pb206 and its astrophysical implications. *PhRvC*, 76(4):045805. doi: [10.1103/PhysRevC.76.045805](https://doi.org/10.1103/PhysRevC.76.045805).
- Drout, M. R. et al. (2017). Light Curves of the Neutron Star Merger GW170817/SSS17a: Implications for R-Process Nucleosynthesis. *Science*. doi: [10.1126/science.aaq0049](https://doi.org/10.1126/science.aaq0049).
- Duprat, J. and Tatischeff, V. (2007). Energetic Constraints on In Situ Production of Short-Lived Radionuclei in the Early Solar System. *ApJL*, 671(1):L69–L72. doi: [10.1086/524297](https://doi.org/10.1086/524297).

- Dwarkadas, V. V., Dauphas, N., Meyer, B., Boyajian, P., and Bojazi, M. (2017). Triggered Star Formation inside the Shell of a Wolf-Rayet Bubble as the Origin of the Solar System. *ApJ*, 851(2):147. doi: [10.3847/1538-4357/aa992e](https://doi.org/10.3847/1538-4357/aa992e).
- Dwarkadas, V. V., Dauphas, N., Meyer, B., Boyajian, P., and Bojazi, M. (2018). Triggered Star Formation at the Periphery of the Shell of a Wolf-Rayet Bubble as the Origin of the Solar System. In *Lunar and Planetary Science Conference*, Lunar and Planetary Science Conference, page 1304.
- Eggleton, P. P., Dearborn, D. S. P., and Lattanzio, J. C. (2006). Deep Mixing of ^3He : Reconciling Big Bang and Stellar Nucleosynthesis. *Science*, 314(5805):1580. doi: [10.1126/science.1133065](https://doi.org/10.1126/science.1133065).
- Eggleton, P. P., Dearborn, D. S. P., and Lattanzio, J. C. (2008). Compulsory Deep Mixing of ^3He and CNO Isotopes in the Envelopes of Low-Mass Red Giants. *ApJ*, 677(1):581–592. doi: [10.1086/529024](https://doi.org/10.1086/529024).
- Eichler, D., Livio, M., Piran, T., and Schramm, D. N. (1989). Nucleosynthesis, neutrino bursts and γ -rays from coalescing neutron stars. *Nature*, 340(6229):126–128. doi: [10.1038/340126a0](https://doi.org/10.1038/340126a0).
- Eichler, M., Arcones, A., Kelic, A., Korobkin, O., Langanke, K., Marketin, T., Martinez-Pinedo, G., Panov, I., Rauscher, T., Rosswog, S., Winteler, C., Zinner, N. T., and Thielemann, F. K. (2015). The Role of Fission in Neutron Star Mergers and Its Impact on the r-Process Peaks. *ApJ*, 808(1):30. doi: [10.1088/0004-637X/808/1/30](https://doi.org/10.1088/0004-637X/808/1/30).
- Elliott, S. R., Wilkerson, J. F., and Abdurashitov, J. N. (1995). The Russian-American gallium solar neutrino experiment. NASA STI/Recon Technical Report N.
- Evans, P. A. et al. (2017). Swift and NuSTAR observations of GW170817: detection of a blue kilonova. *Science*. doi: [10.1126/science.aap9580](https://doi.org/10.1126/science.aap9580).
- Farouqi, K., Kratz, K. L., Cowan, J. J., Mashonkina, L. I., Pfeiffer, B., Sneden, C., Thielemann, F. K., and Truran, J. W. (2008a). Nucleosynthesis Modes in the High-Entropy-Wind Scenario of Type II Supernovae. In O’Shea, B. W. and Heger, A., editors, *First Stars III*, volume 990 of *American Institute of Physics Conference Series*, pages 309–314. doi: [10.1063/1.2905568](https://doi.org/10.1063/1.2905568).
- Farouqi, K., Kratz, K. L., Mashonkina, L. I., Pfeiffer, B., and Thielemann, F. K. (2008b). News from r-Process Nucleosynthesis: Consequences from the ESS to Early Stars. In Guandalini, R., Palmerini, S., and Busso, M., editors, *Evolution and Nucleosynthesis in AGB Stars*, volume 1001 of *American Institute of Physics Conference Series*, pages 245–253. doi: [10.1063/1.2916971](https://doi.org/10.1063/1.2916971).
- Farouqi, K., Kratz, K. L., and Pfeiffer, B. (2009). Co-Production of Light p-, s- and r-Process Isotopes in the High-Entropy Wind of Type II Supernovae. *PASA*, 26(3):194–202. doi: [10.1071/AS08075](https://doi.org/10.1071/AS08075).

- Farouqi, K., Kratz, K. L., Pfeiffer, B., Rauscher, T., Thielemann, F. K., and Truran, J. W. (2010). Charged-particle and Neutron-capture Processes in the High-entropy Wind of Core-collapse Supernovae. *ApJ*, 712(2):1359–1377. doi: [10.1088/0004-637X/712/2/1359](https://doi.org/10.1088/0004-637X/712/2/1359).
- Ferguson, J. W., Alexander, D. R., Allard, F., Barman, T., Bodnarik, J. G., Hauschildt, P. H., Heffner-Wong, A., and Tamanai, A. (2005). Low-Temperature Opacities. *ApJ*, 623:585–596. doi: [10.1086/428642](https://doi.org/10.1086/428642).
- Fernández, R., Foucart, F., Kasen, D., Lippuner, J., Desai, D., and Roberts, L. F. (2017). Dynamics, nucleosynthesis, and kilonova signature of black hole—neutron star merger ejecta. *Classical and Quantum Gravity*, 34(15):154001. doi: [10.1088/1361-6382/aa7a77](https://doi.org/10.1088/1361-6382/aa7a77).
- Fernández, R. and Metzger, B. D. (2013). Delayed outflows from black hole accretion tori following neutron star binary coalescence. *MNRAS*, 435(1):502–517. doi: [10.1093/mnras/stt1312](https://doi.org/10.1093/mnras/stt1312).
- Fernández, R., Tchekhovskoy, A., Quataert, E., Foucart, F., and Kasen, D. (2019). Long-term GRMHD simulations of neutron star merger accretion discs: implications for electromagnetic counterparts. *MNRAS*, 482(3):3373–3393. doi: [10.1093/mnras/sty2932](https://doi.org/10.1093/mnras/sty2932).
- Frankel, S. and Metropolis, N. (1947). Calculations in the Liquid-Drop Model of Fission. *Physical Review*, 72(10):914–925. doi: [10.1103/PhysRev.72.914](https://doi.org/10.1103/PhysRev.72.914).
- Frebel, A. and Beers, T. C. (2018). The formation of the heaviest elements. *Physics Today*, 71(1):30–37. doi: [10.1063/PT.3.3815](https://doi.org/10.1063/PT.3.3815).
- Freiburghaus, C., Rosswog, S., and Thielemann, F.-K. (1999). R-Process in Neutron Star Mergers. *Astrophys. J. Letters*, 525:L121–L124. doi: [10.1086/312343](https://doi.org/10.1086/312343).
- Freytag, B., Ludwig, H.-G., and Steffen, M. (1996). Hydrodynamical models of stellar convection. The role of overshoot in DA white dwarfs, A-type stars, and the Sun. *A&A*, 313:497–516.
- Fröhlich, C., Hix, W. R., Martínez-Pinedo, G., Liebendörfer, M., Thielemann, F. K., Bravo, E., Langanke, K., and Zinner, N. T. (2006). Nucleosynthesis in neutrino-driven supernovae. *NewAR*, 50(7-8):496–499. doi: [10.1016/j.newar.2006.06.003](https://doi.org/10.1016/j.newar.2006.06.003).
- Frost, C. A. and Lattanzio, J. C. (1996). On the Numerical Treatment and Dependence of the Third Dredge-up Phenomenon. *ApJ*, 473:383. doi: [10.1086/178152](https://doi.org/10.1086/178152).
- Fujibayashi, S., Kiuchi, K., Nishimura, N., Sekiguchi, Y., and Shibata, M. (2018). Mass Ejection from the Remnant of a Binary Neutron Star Merger: Viscous-radiation Hydrodynamics Study. *ApJ*, 860(1):64. doi: [10.3847/1538-4357/aabafd](https://doi.org/10.3847/1538-4357/aabafd).

- Fujibayashi, S., Wanajo, S., Kiuchi, K., Kyutoku, K., Sekiguchi, Y., and Shibata, M. (2020). Post-merger Mass Ejection of Low-mass Binary Neutron Stars. *arXiv e-prints*, page arXiv:2007.00474. <https://arxiv.org/abs/2007.00474>.
- Fukuda, Y. et al. (2003). The Super-Kamiokande detector. *Nucl. Instrum. Meth.*, A501:418–462. doi: [10.1016/S0168-9002\(03\)00425-X](https://doi.org/10.1016/S0168-9002(03)00425-X).
- Gallino, R., Arlandini, C., Busso, M., Lugaro, M., Travaglio, C., Straniero, O., Chieffi, A., and Limongi, M. (1998). Evolution and Nucleosynthesis in Low-Mass Asymptotic Giant Branch Stars. II. Neutron Capture and the S-Process. *ApJ*, 497(1):388–403. doi: [10.1086/305437](https://doi.org/10.1086/305437).
- Gallo Rosso, A., Mascaretti, C., Palladino, A., and Vissani, F. (2018). Introduction to neutrino astronomy. *European Physical Journal Plus*, 133(7):267. doi: [10.1140/epjp/i2018-12143-6](https://doi.org/10.1140/epjp/i2018-12143-6).
- Gamow, G. (1928). Zur Quantentheorie des Atomkernes. *Zeitschrift für Physik*, 51(3-4):204–212. doi: [10.1007/BF01343196](https://doi.org/10.1007/BF01343196).
- Gilroy, K. K. (1989). Carbon Isotope Ratios and Lithium Abundances in Open Cluster Giants. *ApJ*, 347:835. doi: [10.1086/168173](https://doi.org/10.1086/168173).
- Goriely, S. (1999). Uncertainties in the solar system r-abundance distribution. *A&A*, 342:881–891.
- Goriely, S. and Janka, H. T. (2016). Solar r-process-constrained actinide production in neutrino-driven winds of supernovae. *MNRAS*, 459(4):4174–4182. doi: [10.1093/mnras/stw946](https://doi.org/10.1093/mnras/stw946).
- Goriely, S. and Martínez Pinedo, G. (2015). The production of transuranium elements by the r-process nucleosynthesis. *NuPhA*, 944:158–176. doi: [10.1016/j.nuclphysa.2015.07.020](https://doi.org/10.1016/j.nuclphysa.2015.07.020).
- Goriely, S., Sida, J. L., Lemaître, J. F., Panebianco, S., Dubray, N., Hilaire, S., Bauswein, A., and Janka, H. T. (2013). New Fission Fragment Distributions and r-Process Origin of the Rare-Earth Elements. *PhRvL*, 111(24):242502. doi: [10.1103/PhysRevLett.111.242502](https://doi.org/10.1103/PhysRevLett.111.242502).
- Goswami, J. N. and Vanhala, H. A. T. (2000). Extinct Radionuclides and the Origin of the Solar System. In Mannings, V., Boss, A. P., and Russell, S. S., editors, *Protostars and Planets IV*, page 963.
- Gough, D. O. (2019). Anticipating the Sun’s heavy-element abundance. *MNRAS*, 485(1):L114–L115. doi: [10.1093/mnrasl/slz044](https://doi.org/10.1093/mnrasl/slz044).
- Gounelle, M. and Meynet, G. (2012). Solar system genealogy revealed by extinct short-lived radionuclides in meteorites. *A&A*, 545:A4. doi: [10.1051/0004-6361/201219031](https://doi.org/10.1051/0004-6361/201219031).

- Gounelle, M., Shu, F. H., Shang, H., Glassgold, A. E., Rehm, K. E., and Lee, T. (2006). The Irradiation Origin of Beryllium Radioisotopes and Other Short-lived Radionuclides. *ApJ*, 640(2):1163–1170. doi: [10.1086/500309](https://doi.org/10.1086/500309).
- Grevesse, N. and Sauval, A. J. (1998). Standard Solar Composition. *Space Sci. Rev.*, 85:161–174. doi: [10.1023/A:1005161325181](https://doi.org/10.1023/A:1005161325181).
- Gruzinov, A. V. and Bahcall, J. N. (1997). The ${}^7\text{Be}$ Electron Capture Rate in the Sun. *ApJ*, 490(1):437–441. doi: [10.1086/304854](https://doi.org/10.1086/304854).
- Gruzinov, A. V. and Bahcall, J. N. (1998). Screening in Thermonuclear Reaction Rates in the Sun. *ApJ*, 504:996–1001. doi: [10.1086/306116](https://doi.org/10.1086/306116).
- Guandalini, R. and Cristallo, S. (2013). Luminosities of carbon-rich asymptotic giant branch stars in the Milky Way. *A&A*, 555:A120. doi: [10.1051/0004-6361/201321225](https://doi.org/10.1051/0004-6361/201321225).
- Guardo, G. L., Spitaleri, C., Lamia, L., Gulino, M., La Cognata, M., Tang, X., deBoer, R., Fang, X., Goldberg, V., Mrazek, J., Mukhamedzhanov, A., Notani, M., Pizzone, R. G., Rapisarda, G. G., Sergi, M. L., and Wiescher, M. (2017). Assessing the near threshold cross section of the ${}^{17}\text{O}(n, \alpha){}^{14}\text{C}$ reaction by means of the Trojan horse method. *PhRvC*, 95(2):025807. doi: [10.1103/PhysRevC.95.025807](https://doi.org/10.1103/PhysRevC.95.025807).
- Guber, K. H., Derrien, H., Leal, L. C., Arbanas, G., Wiarda, D., Koehler, P. E., and Harvey, J. A. (2010). Astrophysical reaction rates for $\text{Ni}58,60(n, \gamma)$ from new neutron capture cross section measurements. *PhRvC*, 82(5):057601. doi: [10.1103/PhysRevC.82.057601](https://doi.org/10.1103/PhysRevC.82.057601).
- Guerrero, C., Leredegui-Marco, J., Paul, M., et al. (2020). Neutron capture on the s -process branching point ${}^{171}\text{Tm}$ via time-of-flight and activation. *Phys. Rev. Lett.*, 125:142701. doi: [10.1103/PhysRevLett.125.142701](https://doi.org/10.1103/PhysRevLett.125.142701).
- Guerrero, C., Tsinganis, A., Berthoumieux, E., et al. (2013). Performance of the neutron time-of-flight facility n_TOF at CERN. *European Physical Journal A*, 49:27. doi: [10.1140/epja/i2013-13027-6](https://doi.org/10.1140/epja/i2013-13027-6).
- Hampel, W., Handt, J., Heusser, G., et al. (1999). Gallex solar neutrino observations: results for gallex iv. *Physics Letters B*, 447(1):127 – 133. doi: [https://doi.org/10.1016/S0370-2693\(98\)01579-2](https://doi.org/10.1016/S0370-2693(98)01579-2).
- Hansen, C. J., Primas, F., Hartman, H., Kratz, K. L., Wanajo, S., Leibundgut, B., Farouqi, K., Hallmann, O., Christlieb, N., and Nilsson, H. (2012). Silver and palladium help unveil the nature of a second r -process. *A&A*, 545:A31. doi: [10.1051/0004-6361/201118643](https://doi.org/10.1051/0004-6361/201118643).
- Hansen, T. T., Holmbeck, E. M., Beers, T. C., Placco, V. M., Roederer, I. U., Frebel, A., Sakari, C. M., Simon, J. D., and Thompson, I. B. (2018). The R-process Alliance: First Release from the Southern Search for R-process-enhanced Stars in the Galactic Halo. *ApJ*, 858(2):92. doi: [10.3847/1538-4357/aabacc](https://doi.org/10.3847/1538-4357/aabacc).

- Haxton, W., Robertson, R. H., and Serenelli, A. M. (2013). Solar neutrinos: Status and prospects. *Annual Review of Astronomy and Astrophysics*, 51(1):21–61. doi: [10.1146/annurev-astro-081811-125539](https://doi.org/10.1146/annurev-astro-081811-125539).
- Haxton, W. C. and Serenelli, A. M. (2008). CN Cycle Solar Neutrinos and the Sun’s Primordial Core Metallicity. *ApJ*, 687(1):678–691. doi: [10.1086/591787](https://doi.org/10.1086/591787).
- Heil, M., Käppeler, F., Uberseder, E., Gallino, R., Bisterzo, S., and Pignatari, M. (2008a). Stellar (n, γ) cross sections for Br and Rb: Matching the weak and main s-process components. *PhRvC*, 78(2):025802. doi: [10.1103/PhysRevC.78.025802](https://doi.org/10.1103/PhysRevC.78.025802).
- Heil, M., Käppeler, F., Uberseder, E., Gallino, R., and Pignatari, M. (2008b). Neutron capture cross sections for the weak s process in massive stars. *PhRvC*, 77(1):015808. doi: [10.1103/PhysRevC.77.015808](https://doi.org/10.1103/PhysRevC.77.015808).
- Heil, M., Plag, R., Uberseder, E., Bisterzo, S., Käppeler, F., Mengoni, A., and Pignatari, M. (2016). Stellar neutron capture cross sections of ^{41}K and ^{45}Sc . *PhRvC*, 93(5):055807. doi: [10.1103/PhysRevC.93.055807](https://doi.org/10.1103/PhysRevC.93.055807).
- Heil, M., Plag, R., Uberseder, E., Gallino, R., Bisterzo, S., Juseviciute, A., Käppeler, F., Lederer, C., Mengoni, A., and Pignatari, M. (2014). Stellar neutron capture cross sections of $^{20,21,22}\text{Ne}$. *PhRvC*, 90(4):045804. doi: [10.1103/PhysRevC.90.045804](https://doi.org/10.1103/PhysRevC.90.045804).
- Hempel, M., Fischer, T., Schaffner-Bielich, J., and Liebendorfer, M. (2012). New Equations of State in Simulations of Core-Collapse Supernovae. *Astrophys. J.*, 748:70. doi: [10.1088/0004-637X/748/1/70](https://doi.org/10.1088/0004-637X/748/1/70).
- Herwig, F. (2000). The evolution of AGB stars with convective overshoot. *A&A*, 360:952–968. <https://arxiv.org/abs/astro-ph/0007139>.
- Herwig, F. (2005). Evolution of Asymptotic Giant Branch Stars. *ARA&A*, 43(1):435–479. doi: [10.1146/annurev.astro.43.072103.150600](https://doi.org/10.1146/annurev.astro.43.072103.150600).
- Herwig, F., Bloeker, T., Schoenberner, D., and El Eid, M. (1997). Stellar evolution of low and intermediate-mass stars. IV. Hydrodynamically-based overshoot and nucleosynthesis in AGB stars. *A&A*, 324:L81–L84.
- Herwig, F., Freytag, B., Fuchs, T., Hansen, J. P., Hueckstaedt, R. M., Porter, D. H., Timmes, F. X., and Woodward, P. R. (2007). Convective and Non-Convective Mixing in AGB Stars. In Kerschbaum, F., Charbonnel, C., and Wing, R. F., editors, *Why Galaxies Care About AGB Stars: Their Importance as Actors and Probes*, volume 378 of *Astronomical Society of the Pacific Conference Series*, page 43. <https://arxiv.org/abs/0709.0197>.
- Herwig, F., Langer, N., and Lugaro, M. (2003). The s-Process in Rotating Asymptotic Giant Branch Stars. *ApJ*, 593(2):1056–1073. doi: [10.1086/376726](https://doi.org/10.1086/376726).

- Hidaka, H. and Yoneda, S. (2013). Radioactive Cs capture in the early solar system. *Scientific Reports*, 3:1330. doi: [10.1038/srep01330](https://doi.org/10.1038/srep01330).
- Higdon, J. C., Lingenfelter, R. E., and Rothschild, R. E. (2004). The Galactic ^{26}Al Problem and the Close Binary Type Ib/c Supernova Solution? *ApJL*, 611(1):L29–L32. doi: [10.1086/423616](https://doi.org/10.1086/423616).
- Hill, V., Christlieb, N., Beers, T. C., Barklem, P. S., Kratz, K. L., Nordström, B., Pfeiffer, B., and Farouqi, K. (2017). The Hamburg/ESO R-process Enhanced Star survey (HERES). XI. The highly r-process-enhanced star CS 29497-004. *A&A*, 607:A91. doi: [10.1051/0004-6361/201629092](https://doi.org/10.1051/0004-6361/201629092).
- Hirata, K. S., Kajita, T., Kifune, T., et al. (1989). Observation of ^8B solar neutrinos in the Kamiokande-II detector. *Phys. Rev. Lett.*, 63:16–19. doi: [10.1103/PhysRevLett.63.16](https://doi.org/10.1103/PhysRevLett.63.16).
- Hoffman, R. D., Woosley, S. E., and Qian, Y. Z. (1997). Nucleosynthesis in Neutrino-driven Winds. II. Implications for Heavy Element Synthesis. *ApJ*, 482(2):951–962. doi: [10.1086/304181](https://doi.org/10.1086/304181).
- Höfner, S. and Olofsson, H. (2018). Mass loss of stars on the asymptotic giant branch. Mechanisms, models and measurements. *A&A Rv*, 26(1):1. doi: [10.1007/s00159-017-0106-5](https://doi.org/10.1007/s00159-017-0106-5).
- Honda, S., Aoki, W., Ishimaru, Y., Wanajo, S., and Ryan, S. G. (2006). Neutron-Capture Elements in the Very Metal Poor Star HD 122563. *ApJ*, 643(2):1180–1189. doi: [10.1086/503195](https://doi.org/10.1086/503195).
- Hotokezaka, K., Kiuchi, K., Kyutoku, K., Okawa, H., Sekiguchi, Y.-i., et al. (2013). The mass ejection from the merger of binary neutron stars. *Phys.Rev.*, D87:024001. doi: [10.1103/PhysRevD.87.024001](https://doi.org/10.1103/PhysRevD.87.024001).
- Huss, G. R., Goswami, J. N., Meyer, B. S., Sahijpal, S., and Wasserburg, G. J. (2007). Stellar Sources of Short-lived Radionuclides. In *Chronology of Meteorites and the Early Solar System*, pages 71–72.
- Huss, G. R., Meyer, B. S., Srinivasan, G., Goswami, J. N., and Sahijpal, S. (2009). Stellar sources of the short-lived radionuclides in the early solar system. *GeoCoA*, 73(17):4922–4945. doi: [10.1016/j.gca.2009.01.039](https://doi.org/10.1016/j.gca.2009.01.039).
- Iben, Jr., I., Kalata, K., and Schwartz, J. (1967). The Effect of Be^{7} K-Capture on the Solar Neutrino Flux. *ApJ*, 150:1001. doi: [10.1086/149399](https://doi.org/10.1086/149399).
- Iben, I., J. (1985). The life and times of an intermediate mass star - In isolation/in a close binary. *QJRAS*, 26:1–39.
- Iglesias, C. A. and Rogers, F. J. (1996). Updated Opal Opacities. *ApJ*, 464:943. doi: [10.1086/177381](https://doi.org/10.1086/177381).

- Iliadis, C., Longland, R., Champagne, A. E., Coc, A., and Fitzgerald, R. (2010). Charged-particle thermonuclear reaction rates: II. Tables and graphs of reaction rates and probability density functions. *Nuclear Physics A*, 841:31–250. doi: [10.1016/j.nuclphysa.2010.04.009](https://doi.org/10.1016/j.nuclphysa.2010.04.009).
- Indelicato, I., La Cognata, M., and Spitaleri and others (2017). New Improved Indirect Measurement of the $^{19}\text{F}(p, \alpha)^{16}\text{O}$ Reaction at Energies of Astrophysical Relevance. *ApJ*, 845:19. doi: [10.3847/1538-4357/aa7de7](https://doi.org/10.3847/1538-4357/aa7de7).
- Ji, A. P., Frebel, A., Ezzeddine, R., and Casey, A. R. (2016a). Chemical Diversity in the Ultra-faint Dwarf Galaxy Tucana II. *ApJL*, 832(1):L3. doi: [10.3847/2041-8205/832/1/L3](https://doi.org/10.3847/2041-8205/832/1/L3).
- Ji, A. P., Frebel, A., Simon, J. D., and Chiti, A. (2016b). Complete Element Abundances of Nine Stars in the r-process Galaxy Reticulum II. *ApJ*, 830(2):93. doi: [10.3847/0004-637X/830/2/93](https://doi.org/10.3847/0004-637X/830/2/93).
- Johnson, C. W., Kolbe, E., Koonin, S. E., and Langanke, K. (1992). The fate of Be-7 in the sun. *ApJ*, 392:320–327. doi: [10.1086/171431](https://doi.org/10.1086/171431).
- Johnson, E. D., Rogachev, G. V., Mitchell, J., Miller, L., and Kemper, K. W. (2009). $\text{C}^{14}(\alpha, \gamma)$ reaction rate. *PhRvC*, 80(4):045805. doi: [10.1103/PhysRevC.80.045805](https://doi.org/10.1103/PhysRevC.80.045805).
- Just, O., Bauswein, A., Ardevol Pulpillo, R., Goriely, S., and Janka, H. T. (2015). Comprehensive nucleosynthesis analysis for ejecta of compact binary mergers. *MNRAS*, 448(1):541–567. doi: [10.1093/mnras/stv009](https://doi.org/10.1093/mnras/stv009).
- Kajino, T. and Mathews, G. J. (2017). Impact of new data for neutron-rich heavy nuclei on theoretical models for r-process nucleosynthesis. *Reports on Progress in Physics*, 80(8):084901. doi: [10.1088/1361-6633/aa6a25](https://doi.org/10.1088/1361-6633/aa6a25).
- Kappeler, F., Beer, H., and Wisshak, K. (1989). s-process nucleosynthesis-nuclear physics and the classical model. *Reports on Progress in Physics*, 52(8):945–1013. doi: [10.1088/0034-4885/52/8/002](https://doi.org/10.1088/0034-4885/52/8/002).
- Käppeler, F., Gallino, R., Bisterzo, S., and Aoki, W. (2011). The s process: Nuclear physics, stellar models, and observations. *Reviews of Modern Physics*, 83(1):157–194. doi: [10.1103/RevModPhys.83.157](https://doi.org/10.1103/RevModPhys.83.157).
- Karakas, A. I. and Lattanzio, J. C. (2014). The Dawes Review 2: Nucleosynthesis and Stellar Yields of Low- and Intermediate-Mass Single Stars. *PASA*, 31:e030. doi: [10.1017/pasa.2014.21](https://doi.org/10.1017/pasa.2014.21).
- Kasen, D., Badnell, N. R., and Barnes, J. (2013). Opacities and Spectra of the r-process Ejecta from Neutron Star Mergers. *ApJ*, 774(1):25. doi: [10.1088/0004-637X/774/1/25](https://doi.org/10.1088/0004-637X/774/1/25).

- Kasen, D., Metzger, B., Barnes, J., Quataert, E., and Ramirez-Ruiz, E. (2017). Origin of the heavy elements in binary neutron-star mergers from a gravitational-wave event. *Nature*, 551(7678):80–84. doi: [10.1038/nature24453](https://doi.org/10.1038/nature24453).
- Kasliwal, M. M. et al. (2018). Spitzer Mid-Infrared Detections of Neutron Star Merger GW170817 Suggests Synthesis of the Heaviest Elements. *MNRAS*. doi: [10.1093/mnrasl/slz007](https://doi.org/10.1093/mnrasl/slz007).
- Kastner, J. H. and Myers, P. C. (1994). An Observational Estimate of the Probability of Encounters between Mass-losing Evolved Stars and Molecular Clouds. *ApJ*, 421:605. doi: [10.1086/173676](https://doi.org/10.1086/173676).
- Kerzendorf, W. E. and Sim, S. A. (2014). A spectral synthesis code for rapid modelling of supernovae. *MNRAS*, 440:387–404. doi: [10.1093/mnras/stu055](https://doi.org/10.1093/mnras/stu055).
- Koehler, P. E. and Guber, K. H. (2013). Improved $^{192,194,195,196}\text{Pt}(n,\gamma)$ and $^{192}\text{Ir}(n,\gamma)$ astrophysical reaction rates. *PhRvC*, 88(3):035802. doi: [10.1103/PhysRevC.88.035802](https://doi.org/10.1103/PhysRevC.88.035802).
- Koehler, P. E., Winters, R. R., Guber, K. H., Rauscher, T., Harvey, J. A., Raman, S., Spencer, R. R., Blackmon, J. C., Larson, D. C., Bardayan, D. W., and Lewis, T. A. (2000). High-resolution neutron capture and transmission measurements, and the stellar neutron-capture cross section of ^{88}Sr . *PhRvC*, 62(5):055803. doi: [10.1103/PhysRevC.62.055803](https://doi.org/10.1103/PhysRevC.62.055803).
- Korobkin, O., Rosswog, S., Arcones, A., and Winteler, C. (2012). On the astrophysical robustness of the neutron star merger r-process. *MNRAS*, 426(3):1940–1949. doi: [10.1111/j.1365-2966.2012.21859.x](https://doi.org/10.1111/j.1365-2966.2012.21859.x).
- Kotelnikov, I. A. and Milstein, A. I. (2019). Electron radiative recombination with a hydrogen-like ion. *PhyS*, 94(5):055403. doi: [10.1088/1402-4896/ab060a](https://doi.org/10.1088/1402-4896/ab060a).
- Kratz, K.-L., Bitouzet, J.-P., Thielemann, F.-K., Moeller, P., and Pfeiffer, B. (1993). Isotopic r-Process Abundances and Nuclear Structure Far from Stability: Implications for the r-Process Mechanism. *ApJ*, 403:216. doi: [10.1086/172196](https://doi.org/10.1086/172196).
- Kratz, K. L., Farouqi, K., Hallmann, O., Pfeiffer, B., and Ott, U. (2014a). Origin of anomalous Xe-H in nanodiamond stardust. In *American Institute of Physics Conference Series*, volume 1595 of *American Institute of Physics Conference Series*, pages 62–68. doi: [10.1063/1.4875291](https://doi.org/10.1063/1.4875291).
- Kratz, K. L., Farouqi, K., Mashonkina, L. I., and Pfeiffer, B. (2008). Nucleosynthesis modes in the high-entropy-wind of type II supernovae. *NewAR*, 52(7-10):390–395. doi: [10.1016/j.newar.2008.06.015](https://doi.org/10.1016/j.newar.2008.06.015).
- Kratz, K.-L., Farouqi, K., and Möller, P. (2014b). A High-entropy-wind r-process Study Based on Nuclear-structure Quantities from the New Finite-range Droplet Model Frdm(2012). *ApJ*, 792(1):6. doi: [10.1088/0004-637X/792/1/6](https://doi.org/10.1088/0004-637X/792/1/6).

- Kratz, K. L., Pfeiffer, B., Cowan, J. J., and Sneden, C. (2004). r-process chronometers. *NewAR*, 48(1-4):105–108. doi: [10.1016/j.newar.2003.11.014](https://doi.org/10.1016/j.newar.2003.11.014).
- Kunz, R., Fey, M., Jaeger, M., Mayer, A., Hammer, J. W., Staudt, G., Harissopoulos, S., and Paradellis, T. (2002). Astrophysical Reaction Rate of $^{12}\text{C}(\alpha, \gamma)^{16}\text{O}$. *ApJ*, 567(1):643–650. doi: [10.1086/338384](https://doi.org/10.1086/338384).
- Kyutoku, K., Kiuchi, K., Sekiguchi, Y., Shibata, M., and Taniguchi, K. (2018). Neutrino transport in black hole-neutron star binaries: Neutrino emission and dynamical mass ejection. *PhRvD*, 97(2):023009. doi: [10.1103/PhysRevD.97.023009](https://doi.org/10.1103/PhysRevD.97.023009).
- La Cognata, M., Spitaleri, C., and Mukhamedzhanov, A. M. (2010). Effect of High-energy Resonances on the $^{18}\text{O}(\text{p}, \alpha)^{15}\text{N}$ Reaction Rate at AGB and Post-AGB Relevant Temperatures. *ApJ*, 723:1512–1522. doi: [10.1088/0004-637X/723/2/1512](https://doi.org/10.1088/0004-637X/723/2/1512).
- Lamia, L., Spitaleri, C., La Cognata, M., Palmerini, S., and Pizzone, R. G. (2012). Recent evaluation of the $^7\text{Li}(\text{p}, \alpha)^4\text{He}$ reaction rate at astrophysical energies via the Trojan Horse method. *A&A*, 541:A158. doi: [10.1051/0004-6361/201219014](https://doi.org/10.1051/0004-6361/201219014).
- Lamia, L., Spitaleri, C., Tognelli, E., Degl’Innocenti, S., Pizzone, R. G., and Prada Moroni, P. G. (2015). Astrophysical Impact of the Updated $^9\text{Be}(\text{p}, \alpha)^6\text{Li}$ and $^{10}\text{B}(\text{p}, \alpha)^7\text{Be}$ Reaction Rates As Deduced By THM. *ApJ*, 811:99. doi: [10.1088/0004-637X/811/2/99](https://doi.org/10.1088/0004-637X/811/2/99).
- Langer, N., Heger, A., Wellstein, S., and Herwig, F. (1999). Mixing and nucleosynthesis in rotating TP-AGB stars. *A&A*, 346:L37–L40. <https://arxiv.org/abs/astro-ph/9904257>.
- Lattimer, J. M., Schramm, D. N., and Grossman, L. (1977). Supernovae, grains and the formation of the solar system. *Nature*, 269:116–118. doi: [10.1038/269116a0](https://doi.org/10.1038/269116a0).
- LeBlanc, P. J., Imbriani, G., Görres, J., et al. (2010). Constraining the s factor of $^{15}\text{N}(\text{p}, \gamma)^{16}\text{O}$ at astrophysical energies. *Phys. Rev. C*, 82:055804. doi: [10.1103/PhysRevC.82.055804](https://doi.org/10.1103/PhysRevC.82.055804).
- Lederer, C., Massimi, C., Altstadt, S., et al. (2013). Neutron Capture Cross Section of Unstable Ni63: Implications for Stellar Nucleosynthesis. *PhRvL*, 110(2):022501. doi: [10.1103/PhysRevLett.110.022501](https://doi.org/10.1103/PhysRevLett.110.022501).
- Lederer, C., Massimi, C., Berthoumieux, E., et al. (2015). Erratum: $^{62}\text{Ni}(\text{n}, \gamma)$ and $^{63}\text{Ni}(\text{n}, \gamma)$ cross sections measured at the n_TOF facility at CERN [Phys. Rev. C 89, 025810 (2014)]. *PhRvC*, 92(1):019903. doi: [10.1103/PhysRevC.92.019903](https://doi.org/10.1103/PhysRevC.92.019903).

- Lederer-Woods, C., Battino, U., Ferreira, P., et al. (2019). Measurement of $^{73}\text{Ge}(n,\gamma)$ cross sections and implications for stellar nucleosynthesis. *Physics Letters B*, 790:458–465. doi: [10.1016/j.physletb.2019.01.045](https://doi.org/10.1016/j.physletb.2019.01.045).
- Lee, T., Papanastassiou, D. A., and Wasserburg, G. J. (1976). Correction [to “Demonstration of ^{26}Mg excess in Allende and evidence for ^{26}Al ”]. *Geophys. Res. Lett.*, 3(2):109–112. doi: [10.1029/GL003i002p00109](https://doi.org/10.1029/GL003i002p00109).
- Lewis, K. M., Lugaro, M., Gibson, B. K., and Pilkington, K. (2013). Decoding the Message from Meteoritic Stardust Silicon Carbide Grains. *ApJL*, 768(1):L19. doi: [10.1088/2041-8205/768/1/L19](https://doi.org/10.1088/2041-8205/768/1/L19).
- Li, H., McCray, R., and Sunyaev, R. A. (1993). Iron, Cobalt, and Nickel in SN 1987A. *ApJ*, 419:824. doi: [10.1086/173534](https://doi.org/10.1086/173534).
- Limongi, M. and Chieffi, A. (2018). Presupernova Evolution and Explosive Nucleosynthesis of Rotating Massive Stars in the Metallicity Range $-3 \leq [\text{Fe}/\text{H}] \leq 0$. *ApJS*, 237(1):13. doi: [10.3847/1538-4365/aacb24](https://doi.org/10.3847/1538-4365/aacb24).
- Lippuner, J. (2018). *r-Process nucleosynthesis in neutron star mergers with the new nuclear reaction network SkyNet*. PhD thesis, California Institute of Technology.
- Lippuner, J., Fernández, R., Roberts, L. F., Foucart, F., Kasen, D., Metzger, B. D., and Ott, C. D. (2017). Signatures of hypermassive neutron star lifetimes on r-process nucleosynthesis in the disc ejecta from neutron star mergers. *MNRAS*, 472(1):904–918. doi: [10.1093/mnras/stx1987](https://doi.org/10.1093/mnras/stx1987).
- Lippuner, J. and Roberts, L. F. (2015). r-process Lanthanide Production and Heating Rates in Kilonovae. *ApJ*, 815(2):82. doi: [10.1088/0004-637X/815/2/82](https://doi.org/10.1088/0004-637X/815/2/82).
- Lippuner, J. and Roberts, L. F. (2017). SkyNet: A Modular Nuclear Reaction Network Library. *ApJS*, 233(2):18. doi: [10.3847/1538-4365/aa94cb](https://doi.org/10.3847/1538-4365/aa94cb).
- Liu, M.-C., Chaussidon, M., Srinivasan, G., and McKeegan, K. D. (2012). A Lower Initial Abundance of Short-lived ^{41}Ca in the Early Solar System and Its Implications for Solar System Formation. *ApJ*, 761(2):137. doi: [10.1088/0004-637X/761/2/137](https://doi.org/10.1088/0004-637X/761/2/137).
- Liu, N., Gallino, R., Bisterzo, S., Davis, A. M., Savina, M. R., and Pellin, M. J. (2014a). The ^{13}C -Pocket Structure in AGB Models: Constraints from Zirconium Isotope Abundances in Single Mainstream SiC Grains. *ApJ*, 788(2):163. doi: [10.1088/0004-637X/788/2/163](https://doi.org/10.1088/0004-637X/788/2/163).
- Liu, N., Gallino, R., Cristallo, S., Bisterzo, S., Davis, A. M., Trappitsch, R., and Nittler, L. R. (2018). New Constraints on the Major Neutron Source in Low-mass AGB Stars. *ApJ*, 865(2):112. doi: [10.3847/1538-4357/aad9f3](https://doi.org/10.3847/1538-4357/aad9f3).

- Liu, N., Savina, M. R., Davis, A. M., Gallino, R., Straniero, O., Gyngard, F., Pellin, M. J., Willingham, D. G., Dauphas, N., Pignatari, M., Bisterzo, S., Cristallo, S., and Herwig, F. (2014b). Barium Isotopic Composition of Mainstream Silicon Carbides from Murchison: Constraints for s-process Nucleosynthesis in Asymptotic Giant Branch Stars. *ApJ*, 786(1):66. doi: [10.1088/0004-637X/786/1/66](https://doi.org/10.1088/0004-637X/786/1/66).
- Liu, N., Savina, M. R., Gallino, R., Davis, A. M., Bisterzo, S., Gyngard, F., Käppeler, F., Cristallo, S., Dauphas, N., Pellin, M. J., and Dillmann, I. (2015). Correlated Strontium and Barium Isotopic Compositions of Acid-cleaned Single Mainstream Silicon Carbides from Murchison. *ApJ*, 803(1):12. doi: [10.1088/0004-637X/803/1/12](https://doi.org/10.1088/0004-637X/803/1/12).
- Liu, N., Stephan, T., Boehnke, P., Nittler, L. R., O'D. Alexander, C. M., Wang, J., Davis, A. M., Trappitsch, R., and Pellin, M. J. (2017). J-type Carbon Stars: A Dominant Source of ^{14}N -rich Presolar SiC Grains of Type AB. *ApJL*, 844(1):L12. doi: [10.3847/2041-8213/aa7d4c](https://doi.org/10.3847/2041-8213/aa7d4c).
- Liu, N., Stephan, T., Cristallo, S., Gallino, R., Boehnke, P., Nittler, L. R., O'D. Alexander, C. M., Davis, A. M., Trappitsch, R., Pellin, M. J., and Dillmann, I. (2019). Presolar Silicon Carbide Grains of Types Y and Z: Their Molybdenum Isotopic Compositions and Stellar Origins. *ApJ*, 881(1):28. doi: [10.3847/1538-4357/ab2d27](https://doi.org/10.3847/1538-4357/ab2d27).
- Lodders, K. (2003). Solar System Abundances and Condensation Temperatures of the Elements. *ApJ*, 591(2):1220–1247. doi: [10.1086/375492](https://doi.org/10.1086/375492).
- Lodders, K. (2019). Solar Elemental Abundances. *arXiv e-prints*, page arXiv:1912.00844. <https://arxiv.org/abs/1912.00844>.
- Lodders, K. and Fegley, B., J. (1999). Condensation Chemistry of Circumstellar Grains. In Le Bertre, T., Lebre, A., and Waelkens, C., editors, *Asymptotic Giant Branch Stars*, volume 191 of *IAU Symposium*, page 279.
- Lodders, K. and Palme, H. (2009). Solar System Elemental Abundances in 2009. *Meteoritics and Planetary Science Supplement*, 72:5154.
- Loll, A. M., Desch, S. J., Scowen, P. A., and Foy, J. P. (2013). Observations of the Crab Nebula's Asymmetrical Development. *ApJ*, 765(2):152. doi: [10.1088/0004-637X/765/2/152](https://doi.org/10.1088/0004-637X/765/2/152).
- Lugaro, M., Doherty, C. L., Karakas, A. I., Maddison, S. T., Liffman, K., García-Hernández, D. A., Siess, L., and Lattanzio, J. C. (2012). Short-lived radioactivity in the early solar system: The Super-AGB star hypothesis. *Meteoritics and Planetary Science*, 47(12):1998–2012. doi: [10.1111/j.1945-5100.2012.01411.x](https://doi.org/10.1111/j.1945-5100.2012.01411.x).

- Lugaro, M., Heger, A., Osrin, D., Goriely, S., Zuber, K., Karakas, A. I., Gibson, B. K., Doherty, C. L., Lattanzio, J. C., and Ott, U. (2014). Stellar origin of the ^{182}Hf cosmochronometer and the presolar history of solar system matter. *Science*, 345(6197):650–653. doi: [10.1126/science.1253338](https://doi.org/10.1126/science.1253338).
- Lugaro, M., Karakas, A. I., Pető, M., and Plachy, E. (2018). Do meteoritic silicon carbide grains originate from asymptotic giant branch stars of super-solar metallicity? *GeoCoA*, 221:6–20. doi: [10.1016/j.gca.2017.06.006](https://doi.org/10.1016/j.gca.2017.06.006).
- Macias, P. and Ramirez-Ruiz, E. (2018). A Stringent Limit on the Mass Production Rate of r-process Elements in the Milky Way. *ApJ*, 860(2):89. doi: [10.3847/1538-4357/aac3e0](https://doi.org/10.3847/1538-4357/aac3e0).
- Maeda, K., Kawabata, K., Mazzali, P. A., Tanaka, M., Valenti, S., Nomoto, K., Hattori, T., Deng, J., Pian, E., Taubenberger, S., Iye, M., Matheson, T., Filippenko, A. V., Aoki, K., Kosugi, G., Ohyama, Y., Sasaki, T., and Takata, T. (2008). Asphericity in Supernova Explosions from Late-Time Spectroscopy. *Science*, 319(5867):1220. doi: [10.1126/science.1149437](https://doi.org/10.1126/science.1149437).
- Maeder, A. (2009). *Physics, Formation and Evolution of Rotating Stars*. Springer-Verlag Berlin Heidelberg. doi: [10.1007/978-3-540-76949-1](https://doi.org/10.1007/978-3-540-76949-1).
- Mamajek, E. E., Prsa, A., Torres, G., Harmanec, P., Asplund, M., Bennett, P. D., Capitaine, N., Christensen-Dalsgaard, J., Depagne, E., Folkner, W. M., Haberleiter, M., Hekker, S., Hilton, J. L., Kostov, V., Kurtz, D. W., Laskar, J., Mason, B. D., Milone, E. F., Montgomery, M. M., Richards, M. T., Schou, J., and Stewart, S. G. (2015). IAU 2015 Resolution B3 on Recommended Nominal Conversion Constants for Selected Solar and Planetary Properties. *arXiv e-prints*, page arXiv:1510.07674. <https://arxiv.org/abs/1510.07674>.
- Mamdouh, A., Pearson, J. M., Rayet, M., and Tondeur, F. (2001). Fission barriers of neutron-rich and superheavy nuclei calculated with the ETFSI method. *NuPhA*, 679(3-4):337–358. doi: [10.1016/S0375-9474\(00\)00358-4](https://doi.org/10.1016/S0375-9474(00)00358-4).
- Marcucci, L. E., Schiavilla, R., and Viviani, M. (2013). Proton-Proton Weak Capture in Chiral Effective Field Theory. *Physical Review Letters*, 110(19):192503. doi: [10.1103/PhysRevLett.110.192503](https://doi.org/10.1103/PhysRevLett.110.192503).
- Marcucci, L. E., Schiavilla, R., and Viviani, M. (2019). Erratum: Proton-Proton Weak Capture in Chiral Effective Field Theory [Phys. Rev. Lett. 110, 192503 (2013)]. *PhRvL*, 123(1):019901. doi: [10.1103/PhysRevLett.123.019901](https://doi.org/10.1103/PhysRevLett.123.019901).
- Marganec, J., Dillmann, I., Domingo-Pardo, C., and Käppeler, F. (2014). Stellar (n, γ) cross sections of neutron-rich nuclei: Completing the isotope chains of Yb, Os, Pt, and Hg. *PhRvC*, 90(6):065801. doi: [10.1103/PhysRevC.90.065801](https://doi.org/10.1103/PhysRevC.90.065801).
- Marganec, J., Dillmann, I., Pardo, C. D., and Käppeler, F. (2009a). Neutron capture cross sections of W184 and W186. *PhRvC*, 80(2):025804. doi: [10.1103/PhysRevC.80.025804](https://doi.org/10.1103/PhysRevC.80.025804).

- Marganiec, J., Dillmann, I., Pardo, C. D., Käppeler, F., Reifarth, R., Gallino, R., Pignatari, M., and Grabmayr, P. (2009b). Neutron capture cross sections of Ge74, Ge76, and As75 at 25 keV. *PhRvC*, 79(6):065802. doi: [10.1103/PhysRevC.79.065802](https://doi.org/10.1103/PhysRevC.79.065802).
- Marganiec, J., Dillmann, I., Pardo, C. D., Käppeler, F., and Walter, S. (2010). Stellar (n, γ) cross sections of p-process isotopes. II. Yb168, W180, Os184, Pt190, and Hg196. *PhRvC*, 82(3):035806. doi: [10.1103/PhysRevC.82.035806](https://doi.org/10.1103/PhysRevC.82.035806).
- Marigo, P. (2002). Asymptotic Giant Branch evolution at varying surface C/O ratio: effects of changes in molecular opacities. *A&A*, 387:507–519. doi: [10.1051/0004-6361:20020304](https://doi.org/10.1051/0004-6361:20020304).
- Marigo, P. and Aringer, B. (2009). Low-temperature gas opacity. \AA SOPUS: a versatile and quick computational tool. *A&A*, 508(3):1539–1569. doi: [10.1051/0004-6361/200912598](https://doi.org/10.1051/0004-6361/200912598).
- Marrone, S., Abbondanno, U., Aerts, G., Alvarez-Velarde, F., Alvarez-Pol, H., Andriamonje, S., Andrzejewski, J., Badurek, G., Baumann, P., Bečvář, F., Benlliure, J., Berthomieux, E., Calviño, F., Cano-Ott, D., Capote, R., Cennini, P., Chepel, V., Chiaveri, E., Colonna, N., Cortes, G., Cortina, D., Couture, A., Cox, J., Dababneh, S., Dahlfors, M., David, S., Dolfini, R., Domingo-Pardo, C., Duran-Escribano, I., Embid-Segura, M., Ferrant, L., Ferrari, A., Ferreira-Marques, R., Frais-Koelbl, H., Fujii, K., Furman, W. I., Gallino, R., Goncalves, I. F., Gonzalez-Romero, E., Goverdovski, A., Gramegna, F., Griesmayer, E., Gunsing, F., Haas, B., Haight, R., Heil, M., Herrera-Martinez, A., Isaev, S., Jericha, E., Käppeler, F., Kadi, Y., Karadimos, D., Kerveno, M., Ketlerov, V., Koehler, P. E., Konovalov, V., Kritčeka, M., Lamboudis, C., Leeb, H., Lindote, A., Lopes, M. I., Lozano, M., Lukic, S., Marganiec, J., Martinez-Val, J., Mastinu, P. F., Mengoni, A., Milazzo, P. M., Molina-Coballes, A., Moreau, C., Mosconi, M., Neves, F., Oberhummer, H., O'Brien, S., Pancin, J., Papaevangelou, T., Paradela, C., Pavlik, A., Pavlopoulos, P., Perlado, J. M., Perrot, L., Pignatari, M., Pigni, M. T., Plag, R., Plompen, A., Plukis, A., Poch, A., Policarpo, A., Pretel, C., Quesada, J. M., Raman, S., Rapp, W., Rauscher, T., Reifarth, R., Rosetti, M., Rubbia, C., Rudolf, G., Rullhusen, P., Salgado, J., Soares, J. C., Stephan, C., Tagliente, G., Tain, J. L., Tassan-Got, L., Tavora, L. M. N., Terlizzi, R., Vannini, G., Vaz, P., Ventura, A., Villamarin-Fernandez, D., Vincente-Vincente, M., Vlachoudis, V., Voss, F., Wendler, H., Wiescher, M., and Wisshak, K. (2006). Measurement of the Sm151(n, γ) cross section from 0.6 eV to 1 MeV via the neutron time-of-flight technique at the CERN n_TOF facility. *PhRvC*, 73(3):034604. doi: [10.1103/PhysRevC.73.034604](https://doi.org/10.1103/PhysRevC.73.034604).
- Marta, M., Formicola, A., and Bemmerer and others (2011). The N14(p, γ)O15 reaction studied with a composite germanium detector. *PhRvC*, 83(4):045804. doi: [10.1103/PhysRevC.83.045804](https://doi.org/10.1103/PhysRevC.83.045804).

- Martínez-Pinedo, G., Fischer, T., Langanke, K., Lohs, A., Sieverding, A., and Wu, M.-R. (2017). Neutrinos and their impact on core-collapse supernova nucleosynthesis. In Alsabti, A. W. and Murdin, P., editors, *Handbook of Supernovae*, pages 1805–1841. Springer International Publishing, Cham. doi: [10.1007/978-3-319-21846-5_78](https://doi.org/10.1007/978-3-319-21846-5_78).
- Massimi, C., Aberle, O., Alcaÿne, V., , and other 125 authors including Vescovi, D. (2019). Data for the s Process from n_TOF. In *Nuclei in the Cosmos XV*, volume 219, pages 63–70. doi: [10.1007/978-3-030-13876-9_11](https://doi.org/10.1007/978-3-030-13876-9_11).
- Massimi, C., Altstadt, S., Andrzejewski, J., et al. (2017). Neutron spectroscopy of ^{26}Mg states: Constraining the stellar neutron source $^{22}\text{Ne}(\alpha, n)^{25}\text{Mg}$. *Physics Letters B*, 768:1–6. doi: [10.1016/j.physletb.2017.02.025](https://doi.org/10.1016/j.physletb.2017.02.025).
- Massimi, C., Becker, B., Dupont, E., Kopecky, S., Lampoudis, C., Massarczyk, R., Moxon, M., Pronyaev, V., Schillebeeckx, P., Sirakov, I., and Wynants, R. (2014). Neutron capture cross section measurements for ^{197}Au from 3.5 to 84 keV at GELINA. *European Physical Journal A*, 50:124. doi: [10.1140/epja/i2014-14124-8](https://doi.org/10.1140/epja/i2014-14124-8).
- Massimi, C., Koehler, P., Bisterzo, S., et al. (2012). Resonance neutron-capture cross sections of stable magnesium isotopes and their astrophysical implications. *PhRvC*, 85(4):044615. doi: [10.1103/PhysRevC.85.044615](https://doi.org/10.1103/PhysRevC.85.044615).
- Mathews, G. J., Snedden, A., Phillips, L. A., Suh, I. S., Coughlin, J., Bhattacharya, A., Zhao, X., and Lan, N. Q. (2014). Origin and evolution of structure and nucleosynthesis for galaxies in the local group. *Modern Physics Letters A*, 29(14):1430012–118. doi: [10.1142/S0217732314300122](https://doi.org/10.1142/S0217732314300122).
- Mazzone, A., Cristallo, S., Aberle, O., and other 128 authors including Vescovi, D. (2020). Measurement of the $^{154}\text{Gd}(n, \gamma)$ cross section and its astrophysical implications. *Physics Letters B*, 804:135405. doi: [10.1016/j.physletb.2020.135405](https://doi.org/10.1016/j.physletb.2020.135405).
- McKeegan, K. D., Kallio, A. P. A., Heber, V. S., Jarzebinski, G., Mao, P. H., Coath, C. D., Kunihiro, T., Wiens, R. C., Nordholt, J. E., Moses, R. W., Reisenfeld, D. B., Jurewicz, A. J. G., and Burnett, D. S. (2011). The Oxygen Isotopic Composition of the Sun Inferred from Captured Solar Wind. *Science*, 332(6037):1528. doi: [10.1126/science.1204636](https://doi.org/10.1126/science.1204636).
- Metzger, B. D. (2019). Kilonovae. *Living Reviews in Relativity*, 23(1):1. doi: [10.1007/s41114-019-0024-0](https://doi.org/10.1007/s41114-019-0024-0).
- Metzger, B. D., Bauswein, A., Goriely, S., and Kasen, D. (2015). Neutron-powered precursors of kilonovae. *Mon. Not. Roy. Astron. Soc.*, 446:1115–1120. doi: [10.1093/mnras/stu2225](https://doi.org/10.1093/mnras/stu2225).

- Metzger, B. D., Piro, A. L., and Quataert, E. (2009). Neutron-rich freeze-out in viscously spreading accretion discs formed from compact object mergers. *MNRAS*, 396(1):304–314. doi: [10.1111/j.1365-2966.2008.14380.x](https://doi.org/10.1111/j.1365-2966.2008.14380.x).
- Meyer, B. S. (1989). Decompression of Initially Cold Neutron Star Matter: A Mechanism for the r-Process? *ApJ*, 343:254. doi: [10.1086/167702](https://doi.org/10.1086/167702).
- Meyer, B. S. and Clayton, D. D. (2000). Short-Lived Radioactivities and the Birth of the sun. *SSRv*, 92:133–152. doi: [10.1023/A:1005282825778](https://doi.org/10.1023/A:1005282825778).
- Millar, T. J. (2016). Chemistry in AGB stars: successes and challenges. In *Journal of Physics Conference Series*, volume 728 of *Journal of Physics Conference Series*, page 052001. doi: [10.1088/1742-6596/728/5/052001](https://doi.org/10.1088/1742-6596/728/5/052001).
- Möller, P., Myers, W. D., Sagawa, H., and Yoshida, S. (2012). New Finite-Range Droplet Mass Model and Equation-of-State Parameters. *PhRvL*, 108(5):052501. doi: [10.1103/PhysRevLett.108.052501](https://doi.org/10.1103/PhysRevLett.108.052501).
- Möller, P., Sierk, A. J., Ichikawa, T., and Sagawa, H. (2016). Nuclear ground-state masses and deformations: FRDM(2012). *Atomic Data and Nuclear Data Tables*, 109:1–204. doi: [10.1016/j.adt.2015.10.002](https://doi.org/10.1016/j.adt.2015.10.002).
- Mosconi, M., Fujii, K., Mengoni, A., et al. (2010). Neutron physics of the Re/Os clock. I. Measurement of the (n, γ) cross sections of Os186,187,188 at the CERN n_TOF facility. *PhRvC*, 82(1):015802. doi: [10.1103/PhysRevC.82.015802](https://doi.org/10.1103/PhysRevC.82.015802).
- Mostefaoui, S., Lugmair, G. W., and Hoppe, P. (2005). ^{60}Fe : A Heat Source for Planetary Differentiation from a Nearby Supernova Explosion. *ApJ*, 625(1):271–277. doi: [10.1086/429555](https://doi.org/10.1086/429555).
- Mumpower, M. R., Kawano, T., Sprouse, T. M., Vassh, N., Holmbeck, E. M., Surman, R., and Möller, P. (2018). β -delayed Fission in r-process Nucleosynthesis. *ApJ*, 869(1):14. doi: [10.3847/1538-4357/aaeaca](https://doi.org/10.3847/1538-4357/aaeaca).
- Nedora, V., Bernuzzi, S., Radice, D., Daszuta, B., Endrizzi, A., Perego, A., Prakash, A., Safarzadeh, M., Schianchi, F., and Logoteta, D. (2020). Numerical Relativity Simulations of the Neutron Star Merger GW170817: Long-Term Remnant Evolutions, Winds, Remnant Disks, and Nucleosynthesis. *arXiv e-prints*, page arXiv:2008.04333. <https://arxiv.org/abs/2008.04333>.
- Nedora, V., Bernuzzi, S., Radice, D., Perego, A., Endrizzi, A., and Ortiz, N. (2019). Spiral-wave Wind for the Blue Kilonova. *ApJL*, 886(2):L30. doi: [10.3847/2041-8213/ab5794](https://doi.org/10.3847/2041-8213/ab5794).
- Nicholl, M. et al. (2017). The Electromagnetic Counterpart of the Binary Neutron Star Merger LIGO/VIRGO GW170817. III. Optical and UV Spectra of a Blue Kilonova From Fast Polar Ejecta. *Astrophys. J.*, 848:L18. doi: [10.3847/2041-8213/aa9029](https://doi.org/10.3847/2041-8213/aa9029).

- Nichols, R. H., J., Podosek, F. A., Meyer, B. S., and Jennings, C. L. (1999). Collateral Consequences of Inhomogeneous Distribution of Short-lived Radionuclides in the Solar Nebula. In *Lunar and Planetary Science Conference*, Lunar and Planetary Science Conference, page 1790.
- Nicolussi, G. K., Davis, A. M., Pellin, M. J., Lewis, R. S., Clayton, R. N., and Amari, S. (1997). s-process zirconium in presolar silicon carbide grains. *Science*, 277(5330):1281–1284. doi: [10.1126/science.277.5330.1281](https://doi.org/10.1126/science.277.5330.1281).
- Nishimura, N., Sawai, H., Takiwaki, T., Yamada, S., and Thielemann, F. K. (2017). The Intermediate r-process in Core-collapse Supernovae Driven by the Magnetorotational Instability. *ApJL*, 836(2):L21. doi: [10.3847/2041-8213/aa5dee](https://doi.org/10.3847/2041-8213/aa5dee).
- Nollett, K. M., Busso, M., and Wasserburg, G. J. (2003). Cool Bottom Processes on the Thermally Pulsing Asymptotic Giant Branch and the Isotopic Composition of Circumstellar Dust Grains. *ApJ*, 582(2):1036–1058. doi: [10.1086/344817](https://doi.org/10.1086/344817).
- Nomoto, K. (1984). Evolution of 8-10 solar mass stars toward electron capture supernovae. I - Formation of electron-degenerate O + NE + MG cores. *ApJ*, 277:791–805. doi: [10.1086/161749](https://doi.org/10.1086/161749).
- Nordhaus, J., Busso, M., Wasserburg, G. J., Blackman, E. G., and Palmerini, S. (2008). Magnetic Mixing in Red Giant and Asymptotic Giant Branch Stars. *ApJL*, 684:L29. doi: [10.1086/591963](https://doi.org/10.1086/591963).
- Nucci, M. C. and Busso, M. (2014). Magnetohydrodynamics and Deep Mixing in Evolved Stars. I. Two- and Three-dimensional Analytical Models for the Asymptotic Giant Branch. *ApJ*, 787:141. doi: [10.1088/0004-637X/787/2/141](https://doi.org/10.1088/0004-637X/787/2/141).
- Oda, T., Hino, M., Muto, K., Takahara, M., and Sato, K. (1994). Rate Tables for the Weak Processes of sd-Shell Nuclei in Stellar Matter. *Atomic Data and Nuclear Data Tables*, 56:231–403. doi: [10.1006/adnd.1994.1007](https://doi.org/10.1006/adnd.1994.1007).
- Ott, U. and Kratz, K.-L. (2008). Meteoritic evidence for two r-processes and the HEW scenario. *NewAR*, 52(7-10):396–400. doi: [10.1016/j.newar.2008.05.001](https://doi.org/10.1016/j.newar.2008.05.001).
- Palme, H., Lodders, K., and Jones, A. (2014). 2.2 - solar system abundances of the elements. In Holland, H. D. and Turekian, K. K., editors, *Treatise on Geochemistry (Second Edition)*, pages 15 – 36. Elsevier, Oxford, second edition edition. doi: <https://doi.org/10.1016/B978-0-08-095975-7.00118-2>.
- Palmerini, S., Cristallo, S., Busso, M., Abia, C., Uttenthaler, S., Gialanella, L., and Maiorca, E. (2011a). Deep Mixing in Evolved Stars. II. Interpreting Li Abundances in Red Giant Branch and Asymptotic Giant Branch Stars. *ApJ*, 741(1):26. doi: [10.1088/0004-637X/741/1/26](https://doi.org/10.1088/0004-637X/741/1/26).

- Palmerini, S., La Cognata, M., Cristallo, S., and Busso, M. (2011b). Deep Mixing in Evolved Stars. I. The Effect of Reaction Rate Revisions from C to Al. *ApJ*, 729(1):3. doi: [10.1088/0004-637X/729/1/3](https://doi.org/10.1088/0004-637X/729/1/3).
- Palmerini, S., Trippella, O., and Busso, M. (2017). A deep mixing solution to the aluminum and oxygen isotope puzzles in pre-solar grains. *MNRAS*, 467:1193–1201. doi: [10.1093/mnras/stx137](https://doi.org/10.1093/mnras/stx137).
- Palmerini, S., Trippella, O., Busso, M., Vescovi, D., Petrelli, M., Zucchini, A., and Frondini, F. (2018). s-Processing from MHD-induced mixing and isotopic abundances in presolar SiC grains. *GeoCoA*, 221:21–36. doi: [10.1016/j.gca.2017.05.030](https://doi.org/10.1016/j.gca.2017.05.030).
- Pan, L., Desch, S. J., Scannapieco, E., and Timmes, F. X. (2012). Mixing of Clumpy Supernova Ejecta into Molecular Clouds. *ApJ*, 756(1):102. doi: [10.1088/0004-637X/756/1/102](https://doi.org/10.1088/0004-637X/756/1/102).
- Panov, I. V., Korneev, I. Y., Rauscher, T., Martínez-Pinedo, G., Kelić-Heil, A., Zinner, N. T., and Thielemann, F. K. (2010). Neutron-induced astrophysical reaction rates for translead nuclei. *A&A*, 513:A61. doi: [10.1051/0004-6361/200911967](https://doi.org/10.1051/0004-6361/200911967).
- Parker, E. N. (1955). The Formation of Sunspots from the Solar Toroidal Field. *ApJ*, 121:491. doi: [10.1086/146010](https://doi.org/10.1086/146010).
- Parker, E. N. (1960). The Hydrodynamic Theory of Solar Corpuscular Radiation and Stellar Winds. *ApJ*, 132:821. doi: [10.1086/146985](https://doi.org/10.1086/146985).
- Pastorello, A., Pumo, M. L., Navasardyan, H., Zampieri, L., Turatto, M., Sollerman, J., Taddia, F., Kankare, E., Mattila, S., Nicolas, J., Prosperi, E., San Segundo Delgado, A., Taubenberger, S., Boles, T., Bachini, M., Benetti, S., Bufano, F., Cappellaro, E., Cason, A. D., Cetrulo, G., Ergon, M., Germany, L., Harutyunyan, A., Howerton, S., Hurst, G. M., Patat, F., Stritzinger, M., Strolger, L. G., and Wells, W. (2012). SN 2009E: a faint clone of SN 1987A. *A&A*, 537:A141. doi: [10.1051/0004-6361/201118112](https://doi.org/10.1051/0004-6361/201118112).
- Pavetich, S., Wallner, A., Martschini, M., Akhmadaliev, S., Dillmann, I., Fifield, K., Halfon, S., Heftrich, T., Käppeler, F., Lederer-Woods, C., Merchel, S., Paul, M., Reifarth, R., Rugel, G., Steier, P., Tessler, M., Tims, S., Weigand, M., and Weissman, L. (2019). Accelerator mass spectrometry measurement of the reaction $^{35}\text{Cl}(n, \gamma)^{36}\text{Cl}$ at keV energies. *PhysRevC*, 99(1):015801. doi: [10.1103/PhysRevC.99.015801](https://doi.org/10.1103/PhysRevC.99.015801).
- Pellin, M. J., Savina, M. R., Calaway, W. F., Tripa, C. E., Barzyk, J. G., Davis, A. M., Gyngard, F., Amari, S., Zinner, E., Lewis, R. S., and Clayton, R. N. (2006). Heavy Metal Isotopic Anomalies in Supernovae Presolar Grains. In Mackwell, S. and Stansbery, E., editors, *37th Annual Lunar and Planetary Science Conference*, Lunar and Planetary Science Conference, page 2041.

- Perego, A., Bernuzzi, S., and Radice, D. (2019). Thermodynamics conditions of matter in neutron star mergers. *European Physical Journal A*, 55(8):124. doi: [10.1140/epja/i2019-12810-7](https://doi.org/10.1140/epja/i2019-12810-7).
- Perego, A., Rosswog, S., Cabezón, R. M., Korobkin, O., Käppeli, R., Arcones, A., and Liebendörfer, M. (2014). Neutrino-driven winds from neutron star merger remnants. *MNRAS*, 443(4):3134–3156. doi: [10.1093/mnras/stu1352](https://doi.org/10.1093/mnras/stu1352).
- Perego, A., Vescovi, D., Fiore, A., Benetti, S., Bernuzzi, S., Branchesi, M., Cristallo, S., Cappellaro, E., and Radice, D. (2020). Production of very light elements in kilonovae. *arXiv e-prints*, page arXiv:2009.08988. <https://arxiv.org/abs/2009.08988>.
- Pfeiffer, B., Ott, U., and Kratz, K. L. (2001). Stellar and nuclear-physics constraints on two r-process components in the early Galaxy. *NuPhA*, 688(1-2):575–577. doi: [10.1016/S0375-9474\(01\)00792-8](https://doi.org/10.1016/S0375-9474(01)00792-8).
- Pian, E. et al. (2017). Spectroscopic identification of r-process nucleosynthesis in a double neutron-star merger. *Nature*, 551(7678):67–70. doi: [10.1038/nature24298](https://doi.org/10.1038/nature24298).
- Piersanti, L., Cristallo, S., and Straniero, O. (2013). The Effects of Rotation on s-process Nucleosynthesis in Asymptotic Giant Branch Stars. *ApJ*, 774(2):98. doi: [10.1088/0004-637X/774/2/98](https://doi.org/10.1088/0004-637X/774/2/98).
- Piersanti, L., Straniero, O., and Cristallo, S. (2007). A method to derive the absolute composition of the Sun, the solar system, and the stars. *A&A*, 462:1051–1062. doi: [10.1051/0004-6361:20054505](https://doi.org/10.1051/0004-6361:20054505).
- Pignatari, M., Gallino, R., Heil, M., Wiescher, M., Käppeler, F., Herwig, F., and Bisterzo, S. (2010). The Weak s-Process in Massive Stars and its Dependence on the Neutron Capture Cross Sections. *ApJ*, 710(2):1557–1577. doi: [10.1088/0004-637X/710/2/1557](https://doi.org/10.1088/0004-637X/710/2/1557).
- Podosek, F. A. and Nichols, R. H. (1997). Short-lived radionuclides in the solar nebula. In Bernatowicz, T. J. and Zinner, E., editors, *Astrophysical implications of the laboratory study of presolar materials*, volume 402 of *American Institute of Physics Conference Series*, pages 617–647. doi: [10.1063/1.53321](https://doi.org/10.1063/1.53321).
- Poitrasson, F. (2017). Silicon Isotope Geochemistry. *Reviews in Mineralogy and Geochemistry*, 82(1):289–344. doi: [10.2138/rmg.2017.82.8](https://doi.org/10.2138/rmg.2017.82.8).
- Potekhin, A. Y., Baiko, D. A., Haensel, P., and Yakovlev, D. G. (1999). Transport properties of degenerate electrons in neutron star envelopes and white dwarf cores. *A&A*, 346:345–353. <https://arxiv.org/abs/astro-ph/9903127>.
- Prada Moroni, P. G. and Straniero, O. (2002). Calibration of White Dwarf Cooling Sequences: Theoretical Uncertainty. *ApJ*, 581:585–597. doi: [10.1086/344052](https://doi.org/10.1086/344052).

- Prantzos, N., Abia, C., Cristallo, S., Limongi, M., and Chieffi, A. (2020). Chemical evolution with rotating massive star yields II. A new assessment of the solar s- and r-process components. *MNRAS*, 491(2):1832–1850. doi: [10.1093/mnras/stz3154](https://doi.org/10.1093/mnras/stz3154).
- Prantzos, N., Abia, C., Limongi, M., Chieffi, A., and Cristallo, S. (2018). Chemical evolution with rotating massive star yields - I. The solar neighbourhood and the s-process elements. *MNRAS*, 476(3):3432–3459. doi: [10.1093/mnras/sty316](https://doi.org/10.1093/mnras/sty316).
- Prokop, C. J., Couture, A., Jones, S., Mosby, S., Rusev, G., Ullmann, J., and Kr̆tička, M. (2019). Measurement of the $^{65}\text{Cu}(n, \gamma)$ cross section using the Detector for Advanced Neutron Capture Experiments at LANL. *PhRvC*, 99(5):055809. doi: [10.1103/PhysRevC.99.055809](https://doi.org/10.1103/PhysRevC.99.055809).
- Qian, Y. Z. and Wasserburg, G. J. (2000). Stellar abundances in the early galaxy and two /r-process components. *PhR*, 333:77–108. doi: [10.1016/S0370-1573\(00\)00017-X](https://doi.org/10.1016/S0370-1573(00)00017-X).
- Radice, D., Bernuzzi, S., and Perego, A. (2020). The Dynamics of Binary Neutron Star Mergers and of GW170817. *Annu. Rev. Nucl. Part. Sci.* doi: [10.1146/annurev-nucl-013120-114541](https://doi.org/10.1146/annurev-nucl-013120-114541).
- Radice, D., Galeazzi, F., Lippuner, J., Roberts, L. F., Ott, C. D., and Rezzolla, L. (2016). Dynamical Mass Ejection from Binary Neutron Star Mergers. *Mon. Not. Roy. Astron. Soc.*, 460(3):3255–3271. doi: [10.1093/mnras/stw1227](https://doi.org/10.1093/mnras/stw1227).
- Radice, D., Perego, A., Bernuzzi, S., and Zhang, B. (2018). Long-lived remnants from binary neutron star mergers. *MNRAS*, 481(3):3670–3682. doi: [10.1093/mnras/sty2531](https://doi.org/10.1093/mnras/sty2531).
- Radice, D., Perego, A., Hotokezaka, K., Fromm, S. A., Bernuzzi, S., and Roberts, L. F. (2018). Binary Neutron Star Mergers: Mass Ejection, Electromagnetic Counterparts and Nucleosynthesis. *Astrophys. J.*, 869(2):130. doi: [10.3847/1538-4357/aaf054](https://doi.org/10.3847/1538-4357/aaf054).
- Radice, D., Rezzolla, L., and Galeazzi, F. (2014a). Beyond second-order convergence in simulations of binary neutron stars in full general relativity. *MNRAS*, 437(1):L46–L50. doi: [10.1093/mnrasl/slt137](https://doi.org/10.1093/mnrasl/slt137).
- Radice, D., Rezzolla, L., and Galeazzi, F. (2014b). High-order fully general-relativistic hydrodynamics: new approaches and tests. *Classical and Quantum Gravity*, 31(7):075012. doi: [10.1088/0264-9381/31/7/075012](https://doi.org/10.1088/0264-9381/31/7/075012).
- Raiteri, C. M., Gallino, R., Busso, M., Neuberger, D., and Kaeppler, F. (1993). The Weak s-Component and Nucleosynthesis in Massive Stars. *ApJ*, 419:207. doi: [10.1086/173476](https://doi.org/10.1086/173476).

- Rapp, W., Heil, M., Hentschel, D., Käppeler, F., Reifarth, R., Brede, H. J., Klein, H., and Rauscher, T. (2002). α - and neutron-induced reactions on ruthenium isotopes. *PhRvC*, 66(1):015803. doi: [10.1103/PhysRevC.66.015803](https://doi.org/10.1103/PhysRevC.66.015803).
- Rauscher, T. and Thielemann, F.-K. (2000). Astrophysical Reaction Rates From Statistical Model Calculations. *Atomic Data and Nuclear Data Tables*, 75:1–351. doi: [10.1006/adnd.2000.0834](https://doi.org/10.1006/adnd.2000.0834).
- Reifarth, R., Dababneh, S., Heil, M., Käppeler, F., Plag, R., Sonnabend, K., and Uberseder, E. (2012). Neutron activation of natural zinc samples at $kT=25$ keV. *PhRvC*, 85(3):035802. doi: [10.1103/PhysRevC.85.035802](https://doi.org/10.1103/PhysRevC.85.035802).
- Reynolds, J. H. (1960). Isotopic Composition of Primordial Xenon. *PhRvL*, 4(7):351–354. doi: [10.1103/PhysRevLett.4.351](https://doi.org/10.1103/PhysRevLett.4.351).
- Roberts, L. F., Lippuner, J., Duez, M. D., Faber, J. A., Foucart, F., Lombardi, James C., J., Ning, S., Ott, C. D., and Ponce, M. (2017). The influence of neutrinos on r-process nucleosynthesis in the ejecta of black hole-neutron star mergers. *MNRAS*, 464(4):3907–3919. doi: [10.1093/mnras/stw2622](https://doi.org/10.1093/mnras/stw2622).
- Roberts, L. F., Reddy, S., and Shen, G. (2012). Medium modification of the charged-current neutrino opacity and its implications. *PhRvC*, 86(6):065803. doi: [10.1103/PhysRevC.86.065803](https://doi.org/10.1103/PhysRevC.86.065803).
- Roberts, L. F., Woosley, S. E., and Hoffman, R. D. (2010). Integrated Nucleosynthesis in Neutrino-driven Winds. *ApJ*, 722(1):954–967. doi: [10.1088/0004-637X/722/1/954](https://doi.org/10.1088/0004-637X/722/1/954).
- Roederer, I. U., Cowan, J. J., Karakas, A. I., Kratz, K.-L., Lugaro, M., Simmerer, J., Farouqi, K., and Sneden, C. (2010). The Ubiquity of the Rapid Neutron-capture Process. *ApJ*, 724(2):975–993. doi: [10.1088/0004-637X/724/2/975](https://doi.org/10.1088/0004-637X/724/2/975).
- Roederer, I. U., Kratz, K.-L., Frebel, A., Christlieb, N., Pfeiffer, B., Cowan, J. J., and Sneden, C. (2009). The End of Nucleosynthesis: Production of Lead and Thorium in the Early Galaxy. *ApJ*, 698(2):1963–1980. doi: [10.1088/0004-637X/698/2/1963](https://doi.org/10.1088/0004-637X/698/2/1963).
- Roederer, I. U., Mateo, M., Bailey, John I., I., Song, Y., Bell, E. F., Crane, J. D., Loebman, S., Nidever, D. L., Olszewski, E. W., Shectman, S. A., Thompson, I. B., Valluri, M., and Walker, M. G. (2016). Detailed Chemical Abundances in the r-process-rich Ultra-faint Dwarf Galaxy Reticulum 2. *AJ*, 151(3):82. doi: [10.3847/0004-6256/151/3/82](https://doi.org/10.3847/0004-6256/151/3/82).
- Rogers, F. J., Swenson, F. J., and Iglesias, C. A. (1996). OPAL Equation-of-State Tables for Astrophysical Applications. *ApJ*, 456:902. doi: [10.1086/176705](https://doi.org/10.1086/176705).
- Roig, O., Jandel, M., Méot, V., Bond, E. M., Bredeweg, T. A., Couture, A. J., Haight, R. C., Keksis, A. L., Rundberg, R. S., Ullmann, J. L., and Vieira, D. J.

- (2016). Radiative neutron capture cross sections on ^{176}Lu at DANCE. *PhRvC*, 93(3):034602. doi: [10.1103/PhysRevC.93.034602](https://doi.org/10.1103/PhysRevC.93.034602).
- Rosswog, S. (2005). Mergers of Neutron Star-Black Hole Binaries with Small Mass Ratios: Nucleosynthesis, Gamma-Ray Bursts, and Electromagnetic Transients. *ApJ*, 634(2):1202–1213. doi: [10.1086/497062](https://doi.org/10.1086/497062).
- Rosswog, S., Sollerman, J., Feindt, U., Goobar, A., Korobkin, O., Wollaeger, R., Fremling, C., and Kasliwal, M. M. (2018). The first direct double neutron star merger detection: implications for cosmic nucleosynthesis. *Astron. Astrophys.*, 615:A132. doi: [10.1051/0004-6361/201732117](https://doi.org/10.1051/0004-6361/201732117).
- Rubin, M., Altwegg, K., Balsiger, H., Berthelier, J. J., Bieler, A., Calmonte, U., Combi, M., De Keyser, J., Engrand, C., Fiethe, B., Fuselier, S. A., Gasc, S., Gombosi, T. I., Hansen, K. C., Hässig, M., Le Roy, L., Mezger, K., Tzou, C. Y., Wampfler, S. F., and Wurz, P. (2017). Evidence for depletion of heavy silicon isotopes at comet 67P/Churyumov-Gerasimenko. *A&A*, 601:A123. doi: [10.1051/0004-6361/201730584](https://doi.org/10.1051/0004-6361/201730584).
- Rugel, G., Faestermann, T., Knie, K., Korschinek, G., Poutivtsev, M., Schumann, D., Kivel, N., Günther-Leopold, I., Weinreich, R., and Wohlmuther, M. (2009). New Measurement of the Fe60 Half-Life. *PhRvL*, 103(7):072502. doi: [10.1103/PhysRevLett.103.072502](https://doi.org/10.1103/PhysRevLett.103.072502).
- Sahijpal, S., Goswami, J. N., Davis, A. M., Grossman, L., and Lewis, R. S. (1998). A stellar origin for the short-lived nuclides in the early Solar System. *Nature*, 391(6667):559–561. doi: [10.1038/35325](https://doi.org/10.1038/35325).
- Sakamoto, N., Seto, Y., Itoh, S., Kuramoto, K., Fujino, K., Nagashima, K., Krot, A. N., and Yurimoto, H. (2007). Remnants of the Early Solar System Water Enriched in Heavy Oxygen Isotopes. *Science*, 317(5835):231. doi: [10.1126/science.1142021](https://doi.org/10.1126/science.1142021).
- Sallaska, A. L., Iliadis, C., Champagne, A. E., Goriely, S., Starrfield, S., and Timmes, F. X. (2013). STARLIB: A Next-generation Reaction-rate Library for Nuclear Astrophysics. *ApJS*, 207(1):18. doi: [10.1088/0067-0049/207/1/18](https://doi.org/10.1088/0067-0049/207/1/18).
- Sawyer, R. F. (2011). Electron capture rates in a plasma. *PhRvC*, 83(6):065804. doi: [10.1103/PhysRevC.83.065804](https://doi.org/10.1103/PhysRevC.83.065804).
- Schönbächler, M., Carlson, R. W., Horan, M. F., Mock, T. D., and Hauri, E. H. (2008). Silver isotope variations in chondrites: Volatile depletion and the initial ^{107}Pd abundance of the solar system. *GeoCoA*, 72(21):5330–5341. doi: [10.1016/j.gca.2008.07.032](https://doi.org/10.1016/j.gca.2008.07.032).
- Schou, J., Antia, H. M., and Basu and others (1998). Helioseismic Studies of Differential Rotation in the Solar Envelope by the Solar Oscillations Investigation Using the Michelson Doppler Imager. *ApJ*, 505:390–417. doi: [10.1086/306146](https://doi.org/10.1086/306146).

- Schuessler, M. (1977). On buoyant magnetic flux tube in the solar convection zone. *A&A*, 56(3):439–442.
- Seeger, P. A., Fowler, W. A., and Clayton, D. D. (1965). Nucleosynthesis of Heavy Elements by Neutron Capture. *ApJS*, 11:121. doi: [10.1086/190111](https://doi.org/10.1086/190111).
- Sekiguchi, Y., Kiuchi, K., Kyutoku, K., and Shibata, M. (2015). Dynamical mass ejection from binary neutron star mergers: Radiation-hydrodynamics study in general relativity. *Phys.Rev.*, D91(6):064059. doi: [10.1103/PhysRevD.91.064059](https://doi.org/10.1103/PhysRevD.91.064059).
- Serenelli, A. M., Haxton, W. C., and Peña-Garay, C. (2011). Solar models with accretion. i. application to the solar abundance problem. *ApJ*, 743(1):24. <http://stacks.iop.org/0004-637X/743/i=1/a=24>.
- Shappee, B. J. et al. (2017). Early spectra of the gravitational wave source GW170817: Evolution of a neutron star merger. *Science*, 358(6370):1574–1578. doi: [10.1126/science.aag0186](https://doi.org/10.1126/science.aag0186).
- Shibagaki, S., Kajino, T., Mathews, G. J., Chiba, S., Nishimura, S., and Lorusso, G. (2016). Relative Contributions of the Weak, Main, and Fission-recycling r-process. *ApJ*, 816(2):79. doi: [10.3847/0004-637X/816/2/79](https://doi.org/10.3847/0004-637X/816/2/79).
- Shibata, M. and Hotokezaka, K. (2019). Merger and Mass Ejection of Neutron-Star Binaries. *Ann. Rev. Nucl. Part. Sci.*, 69:41–64. doi: [10.1146/annurev-nucl-101918-023625](https://doi.org/10.1146/annurev-nucl-101918-023625).
- Shternin, P. S. and Yakovlev, D. G. (2006). Electron thermal conductivity owing to collisions between degenerate electrons. *Phys. Rev. D*, 74:043004. doi: [10.1103/PhysRevD.74.043004](https://doi.org/10.1103/PhysRevD.74.043004).
- Siegel, D. M., Ciolfi, R., and Rezzolla, L. (2014). Magnetically Driven Winds from Differentially Rotating Neutron Stars and X-Ray Afterglows of Short Gamma-Ray Bursts. *ApJL*, 785(1):L6. doi: [10.1088/2041-8205/785/1/L6](https://doi.org/10.1088/2041-8205/785/1/L6).
- Siegel, D. M. and Metzger, B. D. (2017). Three-Dimensional General-Relativistic Magnetohydrodynamic Simulations of Remnant Accretion Disks from Neutron Star Mergers: Outflows and r -Process Nucleosynthesis. *PhRvL*, 119(23):231102. doi: [10.1103/PhysRevLett.119.231102](https://doi.org/10.1103/PhysRevLett.119.231102).
- Siess, L., Goriely, S., and Langer, N. (2004). Nucleosynthesis of s-elements in rotating AGB stars. *A&A*, 415:1089–1097. doi: [10.1051/0004-6361:20034281](https://doi.org/10.1051/0004-6361:20034281).
- Simonucci, S., Taioli, S., Palmerini, S., and Busso, M. (2013). Theoretical estimates of stellar e – captures. i. the half-life of ${}^7\text{Be}$ in evolved stars. *ApJ*, 764(2):118. <http://stacks.iop.org/0004-637X/764/i=2/a=118>.
- Smartt, S. J. et al. (2017). A kilonova as the electromagnetic counterpart to a gravitational-wave source. *Nature*. doi: [10.1038/nature24303](https://doi.org/10.1038/nature24303).

- Sneden, C., Cowan, J. J., and Gallino, R. (2008). Neutron-capture elements in the early galaxy. *ARA&A*, 46:241–288. doi: [10.1146/annurev.astro.46.060407.145207](https://doi.org/10.1146/annurev.astro.46.060407.145207).
- Sneden, C., McWilliam, A., Preston, G. W., Cowan, J. J., Burris, D. L., and Armosky, B. J. (1996). The Ultra–Metal-poor, Neutron-Capture–rich Giant Star CS 22892-052. *ApJ*, 467:819. doi: [10.1086/177656](https://doi.org/10.1086/177656).
- Soares-Santos, M. et al. (2017). The Electromagnetic Counterpart of the Binary Neutron Star Merger LIGO/Virgo GW170817. I. Dark Energy Camera Discovery of the Optical Counterpart. *Astrophys. J.*, 848(2):L16. doi: [10.3847/2041-8213/aa9059](https://doi.org/10.3847/2041-8213/aa9059).
- Solomon, P. M., Sanders, D. B., and Scoville, N. Z. (1979). Giant Molecular Clouds in the Galaxy; Distribution, Mass, Size and Age. In Burton, W. B., editor, *The Large-Scale Characteristics of the Galaxy*, volume 84 of *IAU Symposium*, page 35.
- Sossi, P. A., Moynier, F., Chaussidon, M., Villeneuve, J., Kato, C., and Gounelle, M. (2017). Early Solar System irradiation quantified by linked vanadium and beryllium isotope variations in meteorites. *Nature Astronomy*, 1:0055. doi: [10.1038/s41550-017-0055](https://doi.org/10.1038/s41550-017-0055).
- Spite, F., Spite, M., Barbuy, B., Bonifacio, P., Caffau, E., and François, P. (2018). Abundance patterns of the light neutron-capture elements in very and extremely metal-poor stars. *A&A*, 611:A30. doi: [10.1051/0004-6361/201732096](https://doi.org/10.1051/0004-6361/201732096).
- Spitzer, L. (1956). *Physics of fully ionized gases; 1st ed.* Internat. Sci. Tracts Phys. Astron. Interscience, New York, NY. <https://cds.cern.ch/record/106370>.
- Spruit, H. C. (1999). Differential rotation and magnetic fields in stellar interiors. *A&A*, 349:189–202. <https://arxiv.org/abs/astro-ph/9907138>.
- Srinivasan, G., Sahijpal, S., Ulyanov, A. A., and Goswami, J. N. (1996). Ion microprobe studies of Efremovka CAIs: II. Potassium isotope composition and ^{41}Ca in the early Solar System. *GeoCoA*, 60(10):1823–1835. doi: [10.1016/0016-7037\(96\)00054-3](https://doi.org/10.1016/0016-7037(96)00054-3).
- Srinivasan, G., Ulyanov, A. A., and Goswami, J. N. (1994). ^{41}Ca in the Early Solar System. *ApJL*, 431:L67. doi: [10.1086/187474](https://doi.org/10.1086/187474).
- Stephan, T., Trappitsch, R., Davis, A. M., Pellin, M. J., Rost, D., Savina, M. R., Jadhav, M., Kelly, C. H., Gyngard, F., Hoppe, P., and Dauphas, N. (2018). Strontium and barium isotopes in presolar silicon carbide grains measured with chili—two types of x grains. *Geochimica et Cosmochimica Acta*, 221:109 – 126. Astrophysical Implications of Extraterrestrial Materials: A Special issue for Ernst K. Zinner, doi: <https://doi.org/10.1016/j.gca.2017.05.001>.

- Stephan, T., Trappitsch, R., Hoppe, P., Davis, A. M., Pellin, M. J., and Pardo, O. S. (2019). Molybdenum Isotopes in Presolar Silicon Carbide Grains: Details of s-process Nucleosynthesis in Parent Stars and Implications for r- and p-processes. *ApJ*, 877(2):101. doi: [10.3847/1538-4357/ab1c60](https://doi.org/10.3847/1538-4357/ab1c60).
- Straniero, O. (1988). A tabulation of thermodynamical properties of fully ionized matter in stellar interiors. *A&AS*, 76:157–184.
- Straniero, O., Cristallo, S., and Piersanti, L. (2014). Heavy Elements in Globular Clusters: The Role of Asymptotic Giant Branch Stars. *ApJ*, 785(1):77. doi: [10.1088/0004-637X/785/1/77](https://doi.org/10.1088/0004-637X/785/1/77).
- Straniero, O., Gallino, R., Busso, M., Chiefei, A., Raiteri, C. M., Limongi, M., and Salaris, M. (1995). Radiative ^{13}C Burning in Asymptotic Giant Branch Stars and s-Processing. *ApJL*, 440:L85. doi: [10.1086/187767](https://doi.org/10.1086/187767).
- Straniero, O., Gallino, R., and Cristallo, S. (2006). s process in low-mass asymptotic giant branch stars. *Nuclear Physics A*, 777:311–339. doi: [10.1016/j.nuclphysa.2005.01.011](https://doi.org/10.1016/j.nuclphysa.2005.01.011).
- Straniero, O., Imbriani, G., Strieder, F., et al. (2013). Impact of a Revised $^{25}\text{Mg}(p, \gamma)^{26}\text{Al}$ Reaction Rate on the Operation of the Mg-Al Cycle. *ApJ*, 763:100. doi: [10.1088/0004-637X/763/2/100](https://doi.org/10.1088/0004-637X/763/2/100).
- Symbalysty, E. and Schramm, D. N. (1982). Neutron star collisions and the r-process. *Astrophys. J. Letters*, 22:143–145.
- Tagliente, G., Fujii, K., Milazzo, P. M., et al. (2008a). Neutron capture cross section of Zr90: Bottleneck in the s-process reaction flow. *PhRvC*, 77(3):035802. doi: [10.1103/PhysRevC.77.035802](https://doi.org/10.1103/PhysRevC.77.035802).
- Tagliente, G., Milazzo, P. M., Fujii, K., et al. (2008b). Experimental study of the Zr91(n, γ) reaction up to 26 keV. *PhRvC*, 78(4):045804. doi: [10.1103/PhysRevC.78.045804](https://doi.org/10.1103/PhysRevC.78.045804).
- Tagliente, G., Milazzo, P. M., Fujii, K., et al. (2011a). $^{96}\text{Zr}(n, \gamma)$ measurement at the n_TOF facility at CERN. *PhRvC*, 84(5):055802. doi: [10.1103/PhysRevC.84.055802](https://doi.org/10.1103/PhysRevC.84.055802).
- Tagliente, G., Milazzo, P. M., Fujii, K., et al. (2011b). Neutron capture on Zr94: Resonance parameters and Maxwellian-averaged cross sections. *PhRvC*, 84(1):015801. doi: [10.1103/PhysRevC.84.015801](https://doi.org/10.1103/PhysRevC.84.015801).
- Tagliente, G., Milazzo, P. M., Fujii, K., et al. (2013). The $^{93}\text{Zr}(n, \gamma)$ reaction up to 8 keV neutron energy. *PhRvC*, 87(1):014622. doi: [10.1103/PhysRevC.87.014622](https://doi.org/10.1103/PhysRevC.87.014622).
- Takahashi, K. and Yokoi, K. (1987). Beta-Decay Rates of Highly Ionized Heavy Atoms in Stellar Interiors. *ADNDT*, 36:375. doi: [10.1016/0092-640X\(87\)90010-6](https://doi.org/10.1016/0092-640X(87)90010-6).

- Takigawa, A., Miki, J., Tachibana, S., Huss, G. R., Tominaga, N., Umeda, H., and Nomoto, K. (2008). Injection of Short-Lived Radionuclides into the Early Solar System from a Faint Supernova with Mixing Fallback. *ApJ*, 688(2):1382–1387. doi: [10.1086/592184](https://doi.org/10.1086/592184).
- Tanaka, M. et al. (2017). Kilonova from post-merger ejecta as an optical and near-infrared counterpart of GW170817. *Publ. Astron. Soc. Jap.* doi: [10.1093/pasj/psx121](https://doi.org/10.1093/pasj/psx121).
- Tang, H. and Dauphas, N. (2012). Abundance, distribution, and origin of ^{60}Fe in the solar protoplanetary disk. *Earth and Planetary Science Letters*, 359:248–263. doi: [10.1016/j.epsl.2012.10.011](https://doi.org/10.1016/j.epsl.2012.10.011).
- Tanvir, N. R. et al. (2017). The Emergence of a Lanthanide-Rich Kilonova Following the Merger of Two Neutron Stars. *Astrophys. J.*, 848:L27. doi: [10.3847/2041-8213/aa90b6](https://doi.org/10.3847/2041-8213/aa90b6).
- Tatischeff, V., Duprat, J., and de Séréville, N. (2014). Light-element Nucleosynthesis in a Molecular Cloud Interacting with a Supernova Remnant and the Origin of Beryllium-10 in the Protosolar Nebula. *ApJ*, 796(2):124. doi: [10.1088/0004-637X/796/2/124](https://doi.org/10.1088/0004-637X/796/2/124).
- Telus, M., Huss, G. R., Oglione, R. C., Nagashima, K., Howard, D. L., Newville, M. G., and Tomkins, A. G. (2016). Mobility of iron and nickel at low temperatures: Implications for ^{60}Fe - ^{60}Ni systematics of chondrules from unequilibrated ordinary chondrites. *GeoCoA*, 178:87–105. doi: [10.1016/j.gca.2015.11.046](https://doi.org/10.1016/j.gca.2015.11.046).
- Teng, F.-Z. (2017). Magnesium Isotope Geochemistry. *Reviews in Mineralogy and Geochemistry*, 82(1):219–287. doi: [10.2138/rmg.2017.82.7](https://doi.org/10.2138/rmg.2017.82.7).
- Terluzzi, R., Abbondanno, U., Aerts, G., et al. (2007). The $\text{La}139(n,\gamma)$ cross section: Key for the onset of the s-process. *PhRvC*, 75(3):035807. doi: [10.1103/PhysRevC.75.035807](https://doi.org/10.1103/PhysRevC.75.035807).
- Thielemann, F. K., Eichler, M., Panov, I. V., and Wehmeyer, B. (2017). Neutron Star Mergers and Nucleosynthesis of Heavy Elements. *Annual Review of Nuclear and Particle Science*, 67:253–274. doi: [10.1146/annurev-nucl-101916-123246](https://doi.org/10.1146/annurev-nucl-101916-123246).
- Thielemann, F.-K., Isern, J., Perego, A., and von Ballmoos, P. (2018). Nucleosynthesis in Supernovae. *SSRv*, 214(3):62. doi: [10.1007/s11214-018-0494-5](https://doi.org/10.1007/s11214-018-0494-5).
- Thompson, T. A. and ud-Doula, A. (2018). High-entropy ejections from magnetized proto-neutron star winds: implications for heavy element nucleosynthesis. *MNRAS*, 476(4):5502–5515. doi: [10.1093/mnras/sty480](https://doi.org/10.1093/mnras/sty480).
- Thoul, A. A., Bahcall, J. N., and Loeb, A. (1994). Element diffusion in the solar interior. *ApJ*, 421:828–842. doi: [10.1086/173695](https://doi.org/10.1086/173695).

- Trappitsch, R., Stephan, T., Savina, M. R., Davis, A. M., Pellin, M. J., Rost, D., Gyngard, F., Gallino, R., Bisterzo, S., Cristallo, S., and Dauphas, N. (2018). Simultaneous iron and nickel isotopic analyses of presolar silicon carbide grains. *Geochimica et Cosmochimica Acta*, 221:87 – 108. Astrophysical Implications of Extraterrestrial Materials: A Special issue for Ernst K. Zinner, doi: <https://doi.org/10.1016/j.gca.2017.05.031>.
- Trigo-Rodríguez, J. M., García-Hernández, D. A., Lugaro, M., Karakas, A. I., van Raai, M., García Lario, P., and Manchado, A. (2009). The role of massive AGB stars in the early solar system composition. *Meteoritics and Planetary Science*, 44(5):627–641. doi: [10.1111/j.1945-5100.2009.tb00758.x](https://doi.org/10.1111/j.1945-5100.2009.tb00758.x).
- Trippella, O., Busso, M., Maiorca, E., Käppeler, F., and Palmerini, S. (2014). s-Processing in AGB Stars Revisited. I. Does the Main Component Constrain the Neutron Source in the ^{13}C Pocket? *ApJ*, 787(1):41. doi: [10.1088/0004-637X/787/1/41](https://doi.org/10.1088/0004-637X/787/1/41).
- Trippella, O., Busso, M., Palmerini, S., Maiorca, E., and Nucci, M. C. (2016). s-Processing in AGB Stars Revisited. II. Enhanced ^{13}C Production through MHD-induced Mixing. *ApJ*, 818:125. doi: [10.3847/0004-637X/818/2/125](https://doi.org/10.3847/0004-637X/818/2/125).
- Trippella, O. and La Cognata, M. (2017). Concurrent Application of ANC and THM to assess the $^{13}\text{C}(\alpha, n)^{16}\text{O}$ Absolute Cross Section at Astrophysical Energies and Possible Consequences for Neutron Production in Low-mass AGB Stars. *ApJ*, 837(1):41. doi: [10.3847/1538-4357/aa5eb5](https://doi.org/10.3847/1538-4357/aa5eb5).
- Troja, E., Piro, L., van Eerten, H., Wollaeger, R. T., Im, M., Fox, O. D., Butler, N. R., Cenko, S. B., Sakamoto, T., Fryer, C. L., Ricci, R., Lien, A., Ryan, R. E., Korobkin, O., Lee, S. K., Burgess, J. M., Lee, W. H., Watson, A. M., Choi, C., Covino, S., D’Avanzo, P., Fontes, C. J., González, J. B., Khandrika, H. G., Kim, J., Kim, S. L., Lee, C. U., Lee, H. M., Kuttyrev, A., Lim, G., Sánchez-Ramírez, R., Veilleux, S., Wieringa, M. H., and Yoon, Y. (2017). The X-ray counterpart to the gravitational-wave event GW170817. *Nature*, 551(7678):71–74. doi: [10.1038/nature24290](https://doi.org/10.1038/nature24290).
- Tsujimoto, T., Matsuno, T., Aoki, W., Ishigaki, M. N., and Shigeyama, T. (2017). Enrichment in r-process Elements from Multiple Distinct Events in the Early Draco Dwarf Spheroidal Galaxy. *ApJL*, 850(1):L12. doi: [10.3847/2041-8213/aa9886](https://doi.org/10.3847/2041-8213/aa9886).
- Tsujimoto, T. and Shigeyama, T. (2001). SN 1987A Revisited as a Major Production Site for r-Process Elements. *ApJL*, 561(1):L97–L100. doi: [10.1086/324441](https://doi.org/10.1086/324441).
- Typel, S., Ropke, G., Klahn, T., Blaschke, D., and Wolter, H. H. (2010). Composition and thermodynamics of nuclear matter with light clusters. *Phys. Rev.*, C81:015803. doi: [10.1103/PhysRevC.81.015803](https://doi.org/10.1103/PhysRevC.81.015803).

- Uberseder, E., Heil, M., Käppeler, F., Görres, J., and Wiescher, M. (2007). New measurements of the $F19(n,\gamma)F20$ cross section and their implications for the stellar reaction rate. *PhRvC*, 75(3):035801. doi: [10.1103/PhysRevC.75.035801](https://doi.org/10.1103/PhysRevC.75.035801).
- Uberseder, E., Heil, M., Käppeler, F., Lederer, C., Mengoni, A., Bisterzo, S., Pignatari, M., and Wiescher, M. (2017). Stellar (n, γ) cross sections of ^{23}Na . *PhRvC*, 95(2):025803. doi: [10.1103/PhysRevC.95.025803](https://doi.org/10.1103/PhysRevC.95.025803).
- Uberseder, E., Reifarth, R., Schumann, D., Dillmann, I., Pardo, C. D., Görres, J., Heil, M., Käppeler, F., Marganiec, J., Neuhausen, J., Pignatari, M., Voss, F., Walter, S., and Wiescher, M. (2009). Measurement of the $^{60}\text{Fe}(n, \gamma)^{61}\text{Fe}$ cross section at stellar temperatures. *Phys. Rev. Lett.*, 102:151101. doi: [10.1103/PhysRevLett.102.151101](https://doi.org/10.1103/PhysRevLett.102.151101).
- Umeda, H. and Nomoto, K. (2002). Nucleosynthesis of Zinc and Iron Peak Elements in Population III Type II Supernovae: Comparison with Abundances of Very Metal Poor Halo Stars. *ApJ*, 565(1):385–404. doi: [10.1086/323946](https://doi.org/10.1086/323946).
- Utrobin, V. P. and Chugai, N. N. (2005). Strong effects of time-dependent ionization in early SN 1987A. *A&A*, 441(1):271–281. doi: [10.1051/0004-6361:20042599](https://doi.org/10.1051/0004-6361:20042599).
- Vanhala, H. A. T. and Boss, A. P. (2002). Injection of Radioactivities into the Forming Solar System. *ApJ*, 575(2):1144–1150. doi: [10.1086/341356](https://doi.org/10.1086/341356).
- Vassiliadis, E. and Wood, P. R. (1993). Evolution of Low- and Intermediate-Mass Stars to the End of the Asymptotic Giant Branch with Mass Loss. *ApJ*, 413:641. doi: [10.1086/173033](https://doi.org/10.1086/173033).
- Ventura, P., Karakas, A. I., Dell’Agli, F., Boyer, M. L., García-Hernández, D. A., Di Criscienzo, M., and Schneider, R. (2015). The Large Magellanic Cloud as a laboratory for hot bottom burning in massive asymptotic giant branch stars. *MNRAS*, 450(3):3181–3190. doi: [10.1093/mnras/stv918](https://doi.org/10.1093/mnras/stv918).
- Ventura, P. and Marigo, P. (2010). Asymptotic giant branch stars at low metallicity: the challenging interplay between the mass-loss and molecular opacities. *MNRAS*, 408(4):2476–2486. doi: [10.1111/j.1365-2966.2010.17304.x](https://doi.org/10.1111/j.1365-2966.2010.17304.x).
- Vescovi, D., Busso, M., Palmerini, S., Trippella, O., Cristallo, S., Piersanti, L., Chieffi, A., Limongi, M., Hoppe, P., and Kratz, K. L. (2018). On the Origin of Early Solar System Radioactivities: Problems with the Asymptotic Giant Branch and Massive Star Scenarios. *ApJ*, 863(2):115. doi: [10.3847/1538-4357/aad191](https://doi.org/10.3847/1538-4357/aad191).
- Vescovi, D., Cristallo, S., Busso, M., and Liu, N. (2020). Magnetic-buoyancy-induced mixing in AGB stars: Presolar SiC grains. *ApJL*, 897(2):L25. doi: [10.3847/2041-8213/ab9fa1](https://doi.org/10.3847/2041-8213/ab9fa1).

- Vescovi, D., Mascaretti, C., Vissani, F., Piersanti, L., and Straniero, O. (2021). The luminosity constraint in the era of precision solar physics. *Journal of Physics G Nuclear Physics*, 48(1):015201. doi: [10.1088/1361-6471/abb784](https://doi.org/10.1088/1361-6471/abb784).
- Vescovi, D., Piersanti, L., Cristallo, S., Busso, M., Vissani, F., Palmerini, S., Simonucci, S., and Taioli, S. (2019). Effects of a revised ${}^7\text{Be}$ e^- -capture rate on solar neutrino fluxes. *A&A*, 623:A126. doi: [10.1051/0004-6361/201834993](https://doi.org/10.1051/0004-6361/201834993).
- Villante, F. L. (2010). Constraints on the Opacity Profile of the Sun from Helioseismic Observables and Solar Neutrino Flux Measurements. *ApJ*, 724(1):98–110. doi: [10.1088/0004-637X/724/1/98](https://doi.org/10.1088/0004-637X/724/1/98).
- Villante, F. L., Ianni, A., Lombardi, F., Pagliaroli, G., and Vissani, F. (2011). A step toward CNO solar neutrino detection in liquid scintillators. *Physics Letters B*, 701(3):336–341. doi: [10.1016/j.physletb.2011.05.068](https://doi.org/10.1016/j.physletb.2011.05.068).
- Villante, F. L. and Ricci, B. (2010). Linear Solar Models. *ApJ*, 714(1):944–959. doi: [10.1088/0004-637X/714/1/944](https://doi.org/10.1088/0004-637X/714/1/944).
- Villeneuve, J., Chaussidon, M., and Libourel, G. (2009). Homogeneous Distribution of ${}^{26}\text{Al}$ in the Solar System from the Mg Isotopic Composition of Chondrules. *Science*, 325(5943):985. doi: [10.1126/science.1173907](https://doi.org/10.1126/science.1173907).
- Vinyoles, N., Serenelli, A. M., Villante, F. L., Basu, S., Bergström, J., Gonzalez-Garcia, M. C., Maltoni, M., Peña-Garay, C., and Song, N. (2017). A New Generation of Standard Solar Models. *ApJ*, 835:202. doi: [10.3847/1538-4357/835/2/202](https://doi.org/10.3847/1538-4357/835/2/202).
- Vissani, F. (2019). Luminosity constraint and entangled solar neutrino signals. In *Solar Neutrinos*, pages 121–141. doi: [10.1142/9789811204296_0006](https://doi.org/10.1142/9789811204296_0006).
- Vockenhuber, C., Dillmann, I., Heil, M., Käppeler, F., Winckler, N., Kutschera, W., Wallner, A., Bichler, M., Dababneh, S., Bisterzo, S., and Gallino, R. (2007). Stellar (n,γ) cross sections of Hf174 and radioactive Hf182. *PhRvC*, 75(1):015804. doi: [10.1103/PhysRevC.75.015804](https://doi.org/10.1103/PhysRevC.75.015804).
- Vogl, C., Sim, S. A., Noebauer, U. M., Kerzendorf, W. E., and Hillebrandt, W. (2019). Spectral modeling of type II supernovae. I. Dilution factors. *A&A*, 621:A29. doi: [10.1051/0004-6361/201833701](https://doi.org/10.1051/0004-6361/201833701).
- Žugec, P., Barbagallo, M., Colonna, N., et al. (2014). Experimental neutron capture data of ${}^{58}\text{Ni}$ from the CERN n_TOF facility. *PhRvC*, 89(1):014605. doi: [10.1103/PhysRevC.89.014605](https://doi.org/10.1103/PhysRevC.89.014605).
- Wadhwa, M., Amelin, Y., Davis, A. M., Lugmair, G. W., Meyer, B., Gounelle, M., and Desch, S. J. (2007). From Dust to Planetesimals: Implications for the Solar Protoplanetary Disk from Short-lived Radionuclides. In Reipurth, B., Jewitt, D., and Keil, K., editors, *Protostars and Planets V*, page 835.

- Wahl, A. C. (2002). Systematics of fission-product yields. Technical report, Los Alamos National Lab. doi: [10.2172/809946](https://doi.org/10.2172/809946).
- Wallner, A., Bichler, M., Buczak, K., Dillmann, I., Käppeler, F., Karakas, A., Lederer, C., Lugaro, M., Mair, K., Mengoni, A., Schätzel, G., Steier, P., and Trautvetter, H. P. (2016). Accelerator mass spectrometry measurements of the $^{13}\text{C}(n, \gamma)^{14}\text{C}$ and $^{14}\text{N}(n, p)^{14}\text{C}$ cross sections. *PhRvC*, 93(4):045803. doi: [10.1103/PhysRevC.93.045803](https://doi.org/10.1103/PhysRevC.93.045803).
- Wallner, A., Buczak, K., Belgya, T., Bichler, M., Coquard, L., Dillmann, I., Golser, R., Käppeler, F., Karakas, A., Kutschera, W., Lederer, C., Mengoni, A., Pignatari, M., Priller, A., Reifarh, R., Steier, P., and Szentmiklosi, L. (2017). Precise measurement of the thermal and stellar $^{54}\text{Fe}(n, \gamma)^{55}\text{Fe}$ cross sections via accelerator mass spectrometry. *PhRvC*, 96(2):025808. doi: [10.1103/PhysRevC.96.025808](https://doi.org/10.1103/PhysRevC.96.025808).
- Wanajo, S. and Janka, H.-T. (2012). The r-process in the Neutrino-driven Wind from a Black-hole Torus. *ApJ*, 746(2):180. doi: [10.1088/0004-637X/746/2/180](https://doi.org/10.1088/0004-637X/746/2/180).
- Wanajo, S., Sekiguchi, Y., Nishimura, N., Kiuchi, K., Kyutoku, K., and Shibata, M. (2014). Production of All the r-process Nuclides in the Dynamical Ejecta of Neutron Star Mergers. *ApJL*, 789(2):L39. doi: [10.1088/2041-8205/789/2/L39](https://doi.org/10.1088/2041-8205/789/2/L39).
- Wasserburg, G. J., Boothroyd, A. I., and Sackmann, I. J. (1995a). Deep Circulation in Red Giant Stars: A Solution to the Carbon and Oxygen Isotope Puzzles? *ApJL*, 447:L37. doi: [10.1086/309555](https://doi.org/10.1086/309555).
- Wasserburg, G. J., Busso, M., and Gallino, R. (1996). Abundances of Actinides and Short-lived Nonactinides in the Interstellar Medium: Diverse Supernova Sources for the r-Processes. *ApJL*, 466:L109. doi: [10.1086/310177](https://doi.org/10.1086/310177).
- Wasserburg, G. J., Busso, M., Gallino, R., and Nollett, K. M. (2006). Short-lived nuclei in the early Solar System: Possible AGB sources. *NuPhA*, 777:5–69. doi: [10.1016/j.nuclphysa.2005.07.015](https://doi.org/10.1016/j.nuclphysa.2005.07.015).
- Wasserburg, G. J., Busso, M., Gallino, R., and Raiteri, C. M. (1994). Asymptotic Giant Branch Stars as a Source of Short-lived Radioactive Nuclei in the Solar Nebula. *ApJ*, 424:412. doi: [10.1086/173899](https://doi.org/10.1086/173899).
- Wasserburg, G. J., Gallino, R., and Busso, M. (1998). A Test of the Supernova Trigger Hypothesis with ^{60}Fe and ^{26}Al . *ApJL*, 500(2):L189–L193. doi: [10.1086/311414](https://doi.org/10.1086/311414).
- Wasserburg, G. J., Gallino, R., Busso, M., Goswami, J. N., and Raiteri, C. M. (1995b). Injection of Freshly Synthesized ^{41}Ca in the Early Solar Nebula by an Asymptotic Giant Branch Star. *ApJL*, 440:L101. doi: [10.1086/187771](https://doi.org/10.1086/187771).

- Wasserburg, G. J., Karakas, A. I., and Lugaro, M. (2017). Intermediate-mass Asymptotic Giant Branch Stars and Sources of ^{26}Al , ^{60}Fe , ^{107}Pd , and ^{182}Hf in the Solar System. *ApJ*, 836(1):126. doi: [10.3847/1538-4357/836/1/126](https://doi.org/10.3847/1538-4357/836/1/126).
- Wasserburg, G. J., Trippella, O., and Busso, M. (2015). Isotope Anomalies in the Fe-group Elements in Meteorites and Connections to Nucleosynthesis in AGB Stars. *ApJ*, 805(1):7. doi: [10.1088/0004-637X/805/1/7](https://doi.org/10.1088/0004-637X/805/1/7).
- Watson, D., Hansen, C. J., Selsing, J., Koch, A., Malesani, D. B., Andersen, A. C., Fynbo, J. P. U., Arcones, A., Bauswein, A., Covino, S., Grado, A., Heintz, K. E., Hunt, L., Kouveliotou, C., Leloudas, G., Levan, A. J., Mazzali, P., and Pian, E. (2019). Identification of strontium in the merger of two neutron stars. *Nature*, 574(7779):497–500. doi: [10.1038/s41586-019-1676-3](https://doi.org/10.1038/s41586-019-1676-3).
- Weigand, M., Beinrucker, C., Couture, A., Fiebiger, S., Fonseca, M., Göbel, K., Heftrich, M., Heftrich, T., Jandel, M., Käppeler, F., Krása, A., Lederer, C., Lee, H. Y., Plag, R., Plompen, A., Reifarh, R., Schmidt, S., Sonnabend, K., and Ullmann, J. L. (2017). $^{63}\text{Cu}(n, \gamma)$ cross section measured via 25 keV activation and time of flight. *PhRvC*, 95(1):015808. doi: [10.1103/PhysRevC.95.015808](https://doi.org/10.1103/PhysRevC.95.015808).
- Whitelock, P. A., Feast, M. W., van Loon, J. T., and Zijlstra, A. A. (2003). Obscured asymptotic giant branch variables in the Large Magellanic Cloud and the period-luminosity relation. *MNRAS*, 342(1):86–104. doi: [10.1046/j.1365-8711.2003.06514.x](https://doi.org/10.1046/j.1365-8711.2003.06514.x).
- Wisshak, K., Voss, F., Käppeler, F., Kazakov, L., Bečvář, F., Krutička, M., Gallino, R., and Pignatari, M. (2006). Fast neutron capture on the Hf isotopes: Cross sections, isomer production, and stellar aspects. *PhRvC*, 73(4):045807. doi: [10.1103/PhysRevC.73.045807](https://doi.org/10.1103/PhysRevC.73.045807).
- Wollaeger, R. T., Korobkin, O., Fontes, C. J., Rosswog, S. K., Even, W. P., Fryer, C. L., Sollerman, J., Hungerford, A. L., van Rossum, D. R., and Wollaber, A. B. (2018). Impact of ejecta morphology and composition on the electromagnetic signatures of neutron star mergers. *Mon. Not. Roy. Astron. Soc.*, 478(3):3298–3334. doi: [10.1093/mnras/sty1018](https://doi.org/10.1093/mnras/sty1018).
- Woosley, S. E., Wilson, J. R., Mathews, G. J., Hoffman, R. D., and Meyer, B. S. (1994). The r-Process and Neutrino-heated Supernova Ejecta. *ApJ*, 433:229. doi: [10.1086/174638](https://doi.org/10.1086/174638).
- Zhang, Q.-S., Li, Y., and Christensen-Dalsgaard, J. (2019). Solar models with convective overshoot, solar-wind mass loss, and pms disk accretion: Helioseismic quantities, li depletion, and neutrino fluxes. *The Astrophysical Journal*, 881(2):103. doi: [10.3847/1538-4357/ab2f77](https://doi.org/10.3847/1538-4357/ab2f77).
- Zhang, X., Nollett, K. M., and Phillips, D. R. (2015). Halo effective field theory constrains the solar $^7\text{Be} + \text{p} \rightarrow ^8\text{B} + \gamma$ rate. *Physics Letters B*, 751:535–540. doi: [10.1016/j.physletb.2015.11.005](https://doi.org/10.1016/j.physletb.2015.11.005).

- Zhu, Y., Wollaeger, R. T., Vassh, N., Surman, R., Sprouse, T. M., Mumpower, M. R., Möller, P., McLaughlin, G. C., Korobkin, O., Kawano, T., Jaffke, P. J., Holmbeck, E. M., Fryer, C. L., Even, W. P., Couture, A. J., and Barnes, J. (2018). Californium-254 and Kilonova Light Curves. *ApJL*, 863(2):L23. doi: [10.3847/2041-8213/aad5de](https://doi.org/10.3847/2041-8213/aad5de).
- Zinner, E. (2014). 1.4 - presolar grains. In Holland, H. D. and Turekian, K. K., editors, *Treatise on Geochemistry (Second Edition)*, pages 181 – 213. Elsevier, Oxford, second edition edition. doi: <https://doi.org/10.1016/B978-0-08-095975-7.00101-7>.